Advanced Structured Materials

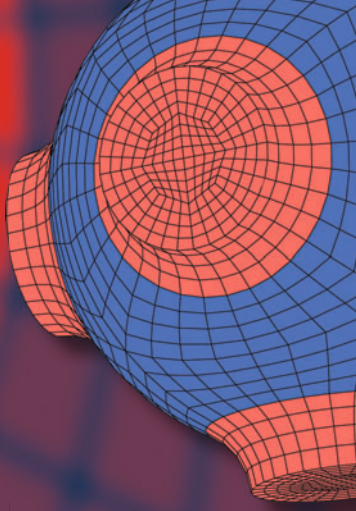

Ku Zilati Ku Shaari
Mokhtar Awang *Editors*

Engineering Applications of Computational Fluid Dynamics

Springer

Advanced Structured Materials

Volume 44

More information about this series at http://www.springer.com/series/8611

Ku Zilati Ku Shaari · Mokhtar Awang
Editors

Engineering Applications of Computational Fluid Dynamics

Springer

Editors
Ku Zilati Ku Shaari
Chemical Engineering Department
Universiti Teknologi Petronas
Seri Iskandar
Malaysia

Mokhtar Awang
Mechanical Engineering Department
Universiti Teknologi Petronas
Seri Iskandar
Malaysia

ISSN 1869-8433 ISSN 1869-8441 (electronic)
ISBN 978-3-319-02835-4 ISBN 978-3-319-02836-1 (eBook)
DOI 10.1007/978-3-319-02836-1

Library of Congress Control Number: 2014954099

Springer Cham Heidelberg New York Dordrecht London

Printed on acid-free paper

Springer is part of Springer Science+Business Media (www.springer.com)

Acknowledgments

We would like to acknowledge our university (Universiti Teknologi Petronas) for giving financial support during the ACEX conferences.

We also would like to acknowledge the following reviewers for their efforts and time reviewing the manuscripts:

1. Dr. Timothy Ganesan
2. Dr. T.M. Yusoff Shah Tuan Ya
3. Dr. Hussain Al Kayiem
4. Dr. William Pao
5. Dr. Mohammad Shakir Nasif
6. M. Zamri Abdullah
7. Dr. Lau Kok Keong

Contents

Reaction Modeling for Prediction of Hydrogen Production During Biomass Gasification

Athirah bt Mohd. Tamidi, K.Z.K. Shaari and T. Ganesan

Abstract The principal aim of this work is to model a steady reactive flow in a gasification reactor using the Finite-Rate Approach within a computational fluid dynamics (CFD) framework. Using this model, the optimal conditions for hydrogen production during biomass steam gasification were determined. In addition, this model was utilized to simulate the effects of the reaction parameters (e.g. gasification temperature, steam to biomass ratio and adsorbent to biomass ratio) for the production of hydrogen. In this work, the hydrodynamic and reaction models were developed concurrently. The reaction model which was empirically validated was developed and implemented using ANSYS Fluent® V6.3. Some comparative analyses were carried out between the simulated and experimental results.

Keywords Computational fluid dynamics (CFD) · Large eddy simulation (LES) and finite volume method · Turbulence · Navier–Stokes equations

1 Introduction

It is widely known that combustion of fossil fuel contributes to the build-up of carbon dioxide (CO_2) in the atmosphere which in effect contributes to global warming. Hence, the search towards cleaner and renewable alternative energy is attracting more attention in various research areas. Hydrogen (H_2) is among the most viable potential alternative energy sources that could be used to replace existing fossil fuels. Hydrogen is an important substance in several chemical, petroleum and energy industries where it is mainly used for the manufacture of

A.bt.Mohd. Tamidi · K.Z.K. Shaari (✉) · T. Ganesan
Department of Chemical Engineering, Universiti Teknologi Petronas,
31750 Seri Iskandar, Perak, Malaysia
e-mail: kuzilati_kushaari@petronas.com

K.Z.K. Shaari and M. Awang (eds.), *Engineering Applications of Computational Fluid Dynamics*, Advanced Structured Materials 44,
DOI 10.1007/978-3-319-02836-1_1

ammonia (NH_3) and methanol. It is also widely used in petroleum-related processes involving hydrotreating. Besides, hydrogen is expected to become a prominent energy carrier for stationary and mobile power generation applications such as in transport, industrial, commercial and residential applications [1–3]. Current energy supplies in the world are dominated by fossil fuel which is around 400 EJ/annum [4]. Nevertheless, 10–15 % of this demand is covered by biomass resources making biomass by far the most important renewable energy source [4]. Recently there are abundant of biomass that exists in the form of waste materials [5, 6]. Biomass can be converted into useful forms of energy using the gasification process. Furthermore, biomass gasification is greatly appealing for hydrogen generation and hot fuel cell applications [7].

There are several potential gasifying agents that can be used to gasify biomass which includes air, oxygen-rich air, steam and a mixture of air and steam [8]. Steam gasification is also capable of producing high heating value (HHV) gas with 30–60 % H_2 content [8, 9]. Steam gasification has become an area of growing interest as it produces higher hydrogen product gas [7, 10]. Furthermore steam gasification is capable of maximizing the gas product with higher heating rate, advantageous residence time characteristic and efficient char and tar reduction. However, steam gasification processes are endothermic. Therefore, sufficient heat needs to be provided to the system [2, 8, 11, 12]. One effective reactor that has been applied widely for gasification applications is the fluidized bed reactor [13–15].

The increasing availability of computational power has enhanced the development of mathematical models of particulate solids which in effect has enabled researchers to simulate the behavior of fluidized biomass particles with considerable accuracy [16]. Thus, the link between fundamental particle properties and the particle behavior can be attained for the prediction of the particle-fluids interactions [16, 17]. In this work, computational fluid dynamic (CFD) approaches in tandem with the reaction rate mode [18] were used for predicting the fluid flow, energy transfer, chemical reactions and other gasification characteristics.

In current times, biomass steam gasification has emerged as a clean and efficient way of producing hydrogen. Nevertheless, experimental studies involving biomass gasification are costly and may be detrimental to the safety of the human experimenter. Simulation and modelling approaches are more cost saving, safe and easy to scale up in order to study the biomass gasification process [19–21]. In this work, a computational fluid dynamics (CFD) approach using the commercial software, ANSYS Fluent® V6.3 has been utilized to simulate and study the gasification reactions in the fluidized bed gasifier.

This chapter is organized as follows: Sect. 2 presents the reactive species transport model while Sect. 3 provides the chemical components and reactions used in the CFD simulation. Section 4 describes the details on the results and analysis with some comparative studies. Finally, this paper ends with some conclusions and recommendations for future work.

2 Reactive Species Transport Models

In Fluent® the mixing and transport of chemical species can be modelled by solving several conservation equations related to convection, diffusion and reaction sources for each component species. In the volumetric reaction model, the model was used to solve several equations related to continuity balance equation, mass and momentum balance equation and also to predict the hydrogen production from the gasifier. The assumption employed during modeling procedures are as follows:

- The steady-state process is considered.
- All gases are uniformly distributed in the gasifier.
- Reactions are not dependent on pressure.
- The gasifying agent is pure steam.
- Fluid in the system is incompressible.

The continuity equation derived from first principles (mass conservation laws) is as follows:

$$\frac{\partial \rho}{\partial t} + \nabla(\rho \vec{u}) = S_m \tag{1}$$

where ρ is the fluid density, u is the velocity vector in the x, y and z-direction respectively and S_{m} is the source term. The momentum conservation principles then form the Navier–Stokes' equation. The solution to this partial differential equation would describe the behavior of the momentum in the flow. The final form of the momentum equation will be as the following:

$$\frac{\partial(\rho \vec{u})}{\partial t} + \nabla(\rho \vec{u}\vec{u}) = \nabla p + \nabla(\bar{\tau}) + \rho g + \vec{F} \tag{2}$$

where $\vec{F}$ is the total external body forces, p is the static pressure and g is the gravitational acceleration. The stress tensor is given as follows:

$$\bar{\tau} = \mu\left[(\nabla \vec{u} + \nabla \vec{u}^T) - \frac{2}{3}\nabla \cdot \vec{u} I\right] \tag{3}$$

where μ is the molecular viscosity and I is the unit tensor of the radiation intensity. Fluent® solve the energy equation in the following form:

$$\frac{\partial(\rho E)}{\partial t} + \nabla \cdot (\vec{u}(\rho E + p)) = \nabla \cdot \left(k_{eff} \Delta T - \sum_j h_j \vec{J}_j + (\bar{\tau}_{eff} \cdot \vec{u})\right) + S_h \tag{4}$$

where E is the total energy, p is the static pressure, T is the fluid temperature, S_h is the source terms for the heat of the chemical reaction, h_j enthalpy formation for

species j, and J_j is the diffusion flux for species j and k_{eff} is the effective fluid thermal conductivity.

This energy equation includes pressure work and kinetic energy terms. However, for incompressible flow, these two terms are often negligible. Therefore, in this model pressure-based solver was used because in the pressure-based solver by default does not include the pressure work or kinetic energy for incompressible flow. From Eq. 4:

$$E = h - \frac{p}{\rho} + \frac{\vec{v}^2}{2}$$

$$h = \sum_j Y_j h_j$$

$$h_j = \int_{T_{ref}}^{T} c_{r,j} dt \tag{5}$$

where $c_{p,j}$ is the molar concentration of species j in reaction r. The source term, S_h, in the energy equation include the source of energy due to chemical reaction, $S_{h,rxn}$ is written as follows:

$$S_{h,rxn} = -\sum_j \frac{h_j^o}{M_j} R_j \tag{6}$$

where R_j is the volumetric rate of creation of species j, Y_j is the third-body efficiency of species j and M_j is the mass of species j. The source term also includes the energy source from radiation heat transfer. In this model, Rosseland radiation model [22], from Fluent® has been used to simulate the heating of incompressible fluid in the gasifier. The general radiative transfer equation used in Fluent® is as follows:

$$\frac{dI(\vec{r},\vec{s})}{ds} + (a + \sigma_S) I(\vec{r},\vec{s}) = an^2 \frac{\sigma T^4}{\pi} + \frac{\sigma_s}{4\pi} \int_0^{4\pi} I(\vec{r},\vec{s}') \Phi(\vec{s},\vec{s}') d\Omega' \tag{7}$$

where σ_S is the scattering coefficient, n is the refractive index, $\vec{s}$ is the direction of scattering and Φ is the phase function and Ω is the solid angle. For Rosseland radiation model, radiative heat flux vector, q_r can be approximated by the following equation:

$$q_r = -\Gamma \nabla G \tag{8}$$

where G is the incident radiation and Γ is the conduction coefficient given as follows:

$$\Gamma = \frac{1}{(3(a+\sigma_s)) - C\sigma_s} \tag{9}$$

where a and C are empirical parameters. The incident radiation from Eq. 8 can be calculated from the equation:

$$G = 4\sigma n^2 \Gamma^4 \tag{10}$$

Replacing G into Eq. 8 yield:

$$q_r = -16\sigma\Gamma n^2 T^3 \nabla T \tag{11}$$

Since Eq. 11 has the same form as the Fourier conduction law, it is possible to write it as Eq. 12. This equation is use in the energy equation to compute the temperature field.

$$q = q_c + q_r = -(k + k_r)\nabla T \tag{12}$$

$$k_r = 16\sigma\Gamma n^2 T^3 \tag{13}$$

where q_c is the heat flux through conduction and k_r is the radiative heat coefficient. Fluent® models anisotropic scattering by means of a linear-anisotropic scattering phase function:

$$\Phi(\vec{s}', \vec{s}) = 1 + C\vec{s}' \cdot \vec{s} \tag{14}$$

The reaction rate source term, R_i, in the species transport equation is computed by laminar finite-rate model in Fluent®. This model neglect the effect of turbulent fluctuations and reaction rates are determined by Arrhenius expressions. The net source of chemical species, i due to the reaction is computed as the sum of the Arrhenius reaction source over the NR reactions which the species participates:

$$R_i = M_{w,i} \sum_{i=1}^{N_R} \hat{R}_{i,r} \tag{15}$$

where $M_{w,i}$ is the molecular weight of species i and $\hat{R}_{i,r}$ net rate of production of species i by chemical reaction r. Consider the rth reaction is written in general form as follows:

$$\sum_{i=1}^{N} v_{i,r} M_i \overleftrightarrow{k}_{b,r/f,r} \sum_{i=1}^{N_R} v'_{i,r} M_i \tag{16}$$

where $\overleftrightarrow{k}_{b,r/f,r}$ is the backward and forward rate constant for reaction, $v_{i,r}$ is the stoichiometric coefficient for product i in reaction r and $v'_{i,r}$ is the stoichiometric coefficient for reactant i in reaction r.

For non-reversible reaction, the backward rate constant is simply omitted. The summations in the above equation are for all chemical species in the system, but only species that appears as reactants or products will have non-zero stoichiometric coefficient. Hence, species that are not involved will drop out of the equation. For non-reversible reaction, the molar rate of creation/destruction of species i in the reaction r, $\hat{R}_{i,r}$, is given as the following:

$$\hat{R}_{i,r} = \Gamma(v'_{i,r} - v_{i,r})(k_{f,r} \prod_{J=1}^{N} [C_{j,r}]^{(n_{j,r}+n'_{j,r})} \tag{17}$$

where $k_{f,r}$ is forward rate constant for reaction r, $C_{j,r}$ is the molar concentration of species j in reaction r, $n_{j,r}$ is the rate exponent for product species j in reaction r and $n'_{j,r}$ is the rate exponent for reactant species j in reaction r. The term Γ represents the net effect of third bodies on the reaction rate. This term is given by:

$$\Gamma = \sum_{j}^{N} Y_{j,r} C_j \tag{18}$$

For this study, the third body effect is not included in the reaction rate calculation.

The forward rate constant for reaction r, $k_{f,r}$ is computed using the following Arrhenius expression:

$$k_{f,r} = A_r T^{\beta_r} e^{-E_r/RT} \tag{19}$$

where A_r is the pre-exponential factor, E_r is the activation energy, R is the gas constant and β_r is the temperature exponent.

3 Chemical Components and Reactions

Biomass gasification involves the reactions of multiple species of reactants as well as products. All these species are defined as components of the mixture template in the reaction model. For this model, the mixture components consists of chemical species as listed in Table 1.

The physical properties for the mixture material are defined in Fluent®. The physical properties required are density, viscosity, thermal conductivity, specific heat capacity and mass diffusion coefficients. As part of the reaction model, the complex biomass gasification reactions were simulated as the source term of the species transport equations when the reactants were consumed and the products

Table 1 Chemical species of mixture

Compound	Formula
Biomass	C
Steam	H_2O
Hydrogen	H_2
Carbon monoxide	CO
Carbon dioxide	CO_2
Methane	CH_4
Calcium oxide	CaO
Calcium carbonate	$CaCO_3$
Nitrogen	N_2

Table 2 Chemical reaction

Compound	Formula
Biomass gasification	$C + H_2O \rightarrow CO + H_2$
Boudouard	$C + CO_2 \rightarrow 2CO$
Water–gas shift	$CO + H_2O \rightarrow CO_2 + H_2$
Methanation	$C + 2H_2 \rightarrow CH_4$
Methane reforming	$CH_4 + H_2O \rightarrow CO + 3H_2$
Adsorption	$CaO + CO_2 \rightarrow CaCO_3$

were created. In this work there are six main reactions, which were assumed to occur in the fluidized bed gasifier including the CO_2 adsorption reaction. These six reactions are shown in Table 2.

In this work, all reactions were solved using the laminar finite-rate reaction model. In laminar finite-rate reaction model, the kinetic parameters such as the Pre-exponential factor and activation energy are required in order to calculate the Arrhenius rate. Therefore, the kinetic parameters from pass works have been developed from experiments using coal, cellulose and various types of biomasses. The kinetic parameters used in this work are shown in Table 3.

Table 3 Kinetic data for reaction model

Reaction	Pre-exponential factor	Activation energy (kJ/mol)
Biomass gasification	2×10^5	6,000
Boudouard	1×10^6	6,370
Water–gas shift	4.4	1.62×10^8
Methanation	0.12	17,921
Methane reforming	3×10^5	15,000
Adsorption	10.2	44.5

4 Results and Analysis

The reaction model developed in Fluent® was validated with experimental and simulation data from previous works. In Busciglio et al. [17], direct experimental or simulation on biomass gasification reactions were not performed rather other data from available literature were used for model validation. The simulated hydrogen production using the model in the work Busciglio et al. [17] was validated with results obtained by Lv et al. [23] and Gao et al. [24]. Busciglio et al. [17] had developed a comprehensive process model for biomass gasification in ASPEN PLUS software. Lv et al. [23] have investigated biomass air gasification in a small scale fluidized bed and Gao et al. [24] performed experiments on biomass air-steam gasification. The details of simulation parameters for model validation used in this work are as shown in Table 4.

Figure 1 shows the comparison of estimated hydrogen production from the reaction model in this work with previous works:

The hydrogen concentration in term of mol% is the facet average value taken at the 'Outlet' line surface of the two-dimensional domain of the gasifier. From the graph, it is observed that the reaction model can accurately predict the hydrogen production from biomass gasification (at 800 °C and steam to biomass ratio of 2).

Table 4 Simulation parameters for model validation

Parameters	Value
Biomass mass flow rate (kg/s)	1.25×10^{-3}
Steam mass flow rate (kg/s)	2.5×10^{-3}
Gasifier temperature (°C)	800
Gasifier pressure (kPa)	101.325
Steam temperature (°C)	250

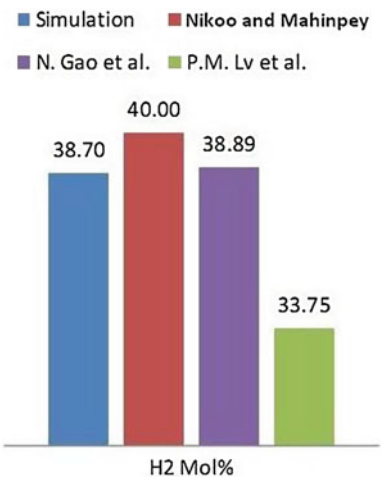

Fig. 1 Comparison of estimated H_2 production

The prediction of hydrogen from the model is close to the predicted hydrogen production by Nikoo and Mahinpey [14] (from ASPEN PLUS process simulation software) and from the steam gasification experimental study by Gao et al. [24]. The experimental hydrogen production from Lv et al. [23] is lower as compared to the predicted production from the reaction model. This is due to the utilization of air as the gasifying agent and the low hydrogen concentration which results from the 'dilution effect' by nitrogen from air. Based on this comparison, it can be inferred that simulated hydrogen production by the reaction model is in good agreement with the literature data. In addition, the model can be further employed to predict the effect of other reaction parameters on hydrogen production from the biomass gasification process.

The fluidized bed gasifier temperature is one of the most important operating variables for biomass gasification. In this work, the reactions were simulated at gasifier temperature ranging from 700 to 900 °C in 50 °C increments. Figure 2 shows the effect of fluidized bed reaction temperature on hydrogen production from biomass gasification process at steam to biomass ratio of 2.

From Fig. 2, it is observed that the hydrogen production increases with temperature. This finding is similar to the experimental data obtained by Lv et al. [23] and Wu et al. [3]. This is because biomass gasification is an endothermic reaction. Therefore high temperatures are more favorable for the reaction to occur. Estimated hydrogen production from the reaction model is also compared with the data from previous works. Based on the comparison, it is observed that the model is able to accurately predict hydrogen production from biomass gasification. It can be observed that the concentration of hydrogen and trend of hydrogen production is in good agreement with the data from literature. The highest hydrogen production is observed to occur at the temperature of 850 °C which was approximately 48 mol%. Figure 3 shows the effect of gasification temperature on product gas composition.

From the Fig. 3, it is observed that as temperature increases, the concentration of carbon monoxide also increases while the concentration of carbon dioxide decreases. This is because at temperatures higher than 800 °C, carbon dioxide is

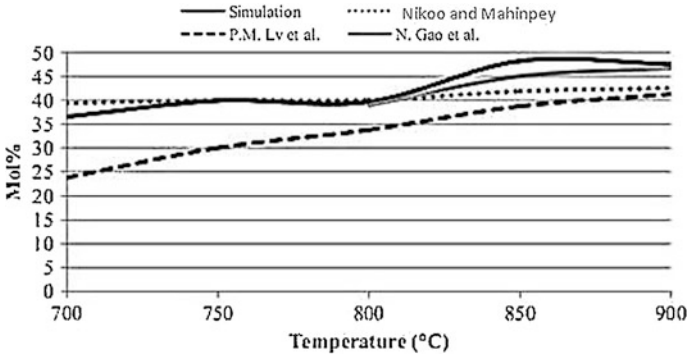

Fig. 2 The effect of fluidized bed reaction temperature on hydrogen production

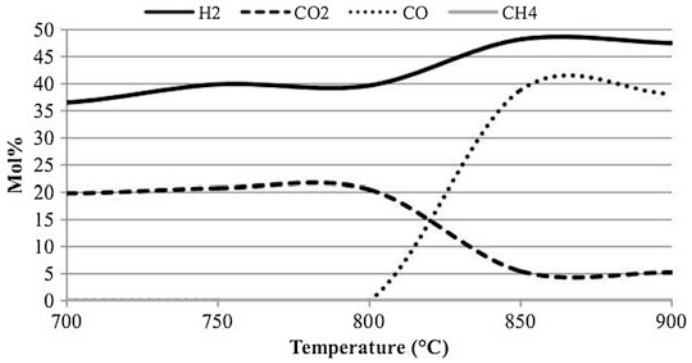

Fig. 3 The effect of gasification temperature on product gas composition

further cracked to carbon monoxide making carbon monoxide concentration to increase. Kalinci et al. [25] also claimed that at high gasification temperatures (800–850 °C), product gas which is rich in hydrogen and carbon monoxide is produced. The concentration of methane remains low in the product gas since methane is continuously produced and consumed simultaneously during the gasification process. Hydrogen profile from the Fig. 3 shows that gasification is effectively occurring at temperatures higher than 800 °C since there is a significant jump in the hydrogen concentration from 800 °C onwards. Therefore, to obtain the best performance of biomass gasification with maximum concentration of hydrogen (without the presence of the carbon dioxide adsorbent), the gasifier should be operated at temperatures ranging from 800 to 900 °C. Figure 4 shows the effect of gasification temperature on hydrogen yield during gasification.

The hydrogen yield predicted from the reaction model is also compared with experimental data from previous works as shown in Table 5.

From the comparison in Table 5, it is observed that the predicted hydrogen yield obtained from the reaction model is similar with the experimental data obtained by

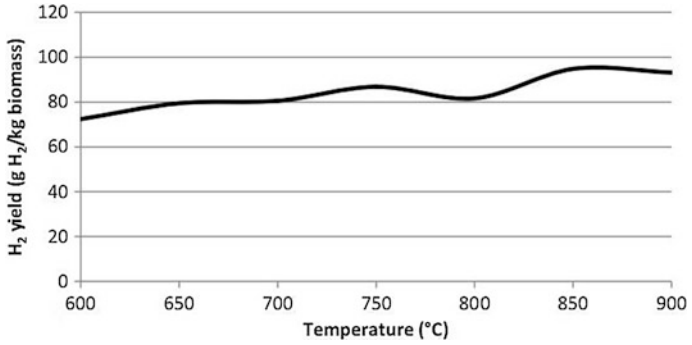

Fig. 4 The effect of gasification temperature on hydrogen yield

Table 5 Comparison of hydrogen yield and other properties

	Simulation	Shen et al. [8]	Gao et al. [24]
Carbon content in biomass (%)	50	36.57	44.75
Temperature (^{o}C)	850	850	850
Gasifying agent	Steam	Steam	Air–steam
Steam to biomass ratio	2	0.6	1.4
Adsorbent	No	No	No
Hydrogen yield (g H_2/kg biomass)	94.75	62	99.55

Gao et al. [24] at 850 °C. This shows that the assumptions made on biomass carbon content is valid in order to predict hydrogen production from biomass gasification process using the reaction model. The predicted hydrogen yield from the simulation is higher compared to the experimental data obtain by Shen et al. [8]. This is because the biomass used in Shen et al. [8] has lower carbon content and much lower steam to biomass ratio. In Shen et al. [8], it was reported that the increase of steam in the fluidized bed gasifier has the same effect as increasing gasifier temperature. In this work, the effect of increasing steam to biomass ratio on product gas composition from biomass gasification was analyzed. Steam to biomass ratio in the range of 1–4 is simulated using the reaction model. Figure 5 shows the effect of steam to biomass ratio on product gas composition in the gasifier.

In Fig. 5, it can be observed that the hydrogen concentration decreases as steam to biomass ratio increases. This is due to the dilution effect from the excess steam which does not completely react with the biomass. The excess steam further reacts with carbon monoxide to produce carbon dioxide. This explains the increase of carbon dioxide and decrease of carbon monoxide as the steam to biomass ratio increases. The same observation was obtained by Wu et al. [3] in their experimental study. The increase of steam to biomass ratio also shows an increase in water production by the gasifier. The increase of water production means there is a need of an additional downstream system in order to increase the purity of the hydrogen in the product gas. The highest hydrogen concentration produced is observed at

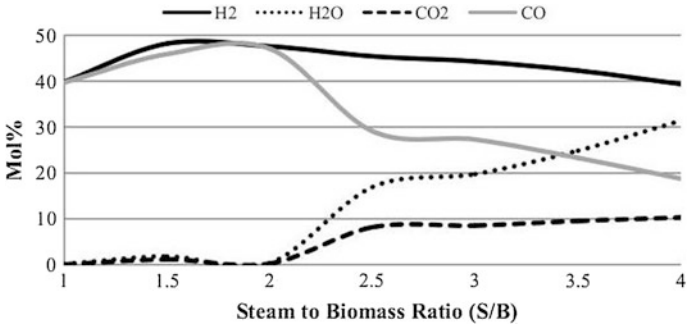

Fig. 5 The effect of steam to biomass ratio on product gas composition

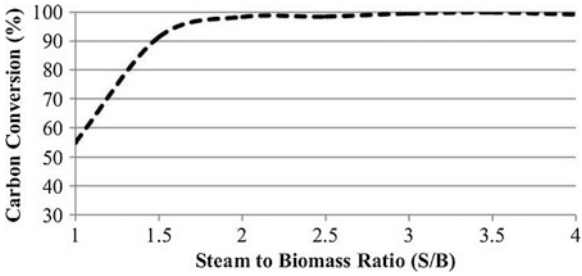

Fig. 6 The effect of steam to biomass ratio on carbon conversion

steam to biomass ratios of 1.5–2. Therefore, in order to achieve high purity of hydrogen from the gasifier, it is best to operate the gasifier at steam to biomass ratios of 1.5–2. Figure 6 shows the effect of steam to biomass ratio on biomass carbon conversion during the gasification process.

From Fig. 6, it is observed that the biomass carbon conversion increases as the steam to biomass ratio increases from 1 to 4. A drastic increase in carbon conversion is observed as steam to biomass ratio increases from 1 to 1.5. The carbon conversion becomes almost constant and reaches approximately 100 % when the steam to biomass ratio reaches to 2 and beyond. This shows that high carbon conversion could be achieved as more steam is added into the system because the surplus steam further pushes the gasification reaction forward making the biomass as the limiting reactant. Figure 7 shows the predicted hydrogen yield from the simulation.

From the graph, it is observed that the hydrogen yield increases with the increment of the steam to biomass ratio. This shows that increasing steam input to the system has the same effect as increasing the gasification temperature. Based on the Le Chatelier's principle, as more steam (reactant) is added into the system, the gasification reactions are further pushed forward towards producing more hydrogen. This occurs as the reactive system strives to achieve equilibrium. Thus, hydrogen yield increases further as more steam is added into the system. The same concept applies as gasification temperatures increase. Since gasification reactions are endothermic, increasing temperatures also further pushes the reactions forward and more hydrogen could be produced from the system. Hence, increasing steam input has the same effect as increasing the gasification temperature. Based on

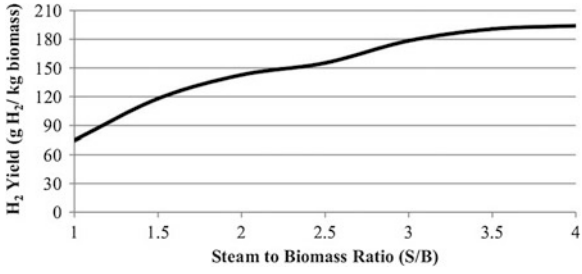

Fig. 7 The effect of steam to biomass ratio on hydrogen yield

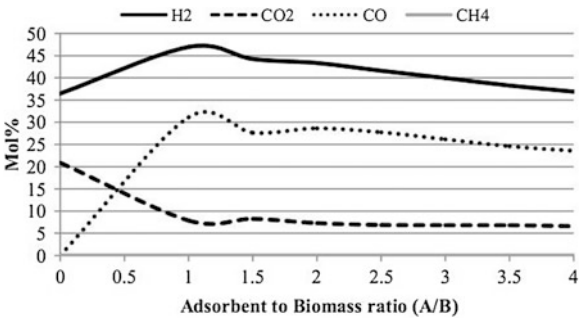

Fig. 8 The effect of adsorbent to biomass ratio (*A/B*) on product gas composition

simulation results, the optimum steam to biomass ratio for the biomass steam gasification system is 2. This is because at steam to biomass ratio of 2, high concentrations of hydrogen could be obtained from the system and at the same time high carbon conversion could be achieved. Even though higher hydrogen yield could be obtained at higher steam to biomass ratios, adding more steam into the system will not be economical since more energy is required for stream generation. Therefore, in order to have an economical process while simultaneously maintaining high gasifier performance, it is best to keep the steam to biomass ratio at 2. In this work, the effect of carbon dioxide adsorbent on hydrogen production was studied. The simulation was done in order to observe the effect of adsorbent to biomass ratio (A/B) and adsorbent temperature on hydrogen production during biomass gasification. Figure 8 shows the comparison of hydrogen concentrations in the product gas at different reaction temperatures with and without the carbon dioxide adsorbent.

From Fig. 8, it is observed that at lower temperatures, the concentration of hydrogen produced from gasification with carbon dioxide adsorbent is higher than gasification without adsorbent. However, the opposite trend is seen at temperatures 850 °C and higher. This is because at higher temperatures, the exothermic adsorption reaction reverses to calcination reactions where hydrogen becomes the reactant to produce calcium oxide. This in effect reduces the hydrogen concentration. Figure 9 shows the comparison of hydrogen yield from biomass gasification with and without the adsorbent in the system.

Figure 9 shows the comparison of hydrogen yield from biomass gasification with and without adsorbent in the system. From the comparison, it is observed that the hydrogen yield from the gasification system with in situ carbon dioxide adsorbent is much higher compared to the gasification system without the adsorbent. The hydrogen yield increases more than two folds especially at the lower temperatures (600–750 °C). This is because the exothermic adsorption reaction is much more favorable at lower temperatures. The highest hydrogen yield is observed at 600 °C which is 195.3 g H_2/kg biomass. For optimal performance of biomass gasification with in situ carbon dioxide adsorbent, the gasifier should be operated at a temperature range of 600–750 °C.

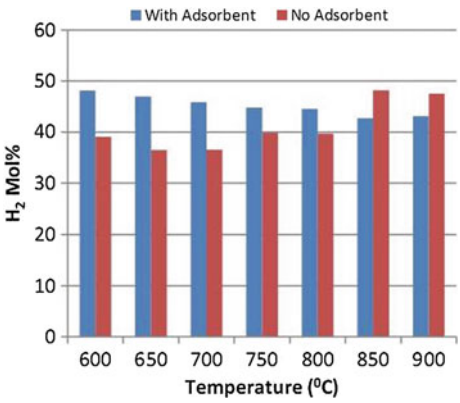

Fig. 9 Comparison of hydrogen yield from biomass gasification with and without adsorbent in the system

5 Concluding Remarks and Recommendations

In this work, the optimization of biomass fluidized bed gasifier with respect to different reaction parameters has been investigated via the computational fluid dynamics framework. Using Fluent®, the reaction model (the finite-rate model) has been successfully validated with empirical results and implemented in this work to predict hydrogen production from biomass gasification. From the reaction model, gasification temperature of 850 °C and steam to biomass ratio of 2 gave the highest concentration and yield of hydrogen which were 48 mol% and 94.75 g H_2/kg respectively. The addition of the carbon dioxide adsorbent in the gasifier highly improves the hydrogen production. At adsorbent to biomass ratio of 1 and at gasification temperatures as low as 600–750 °C, high concentration and yield of hydrogen could be obtained (47 mol% and 195.3 g H_2/kg biomass respectively).

In order to improve the quality of product gas prediction from the gasifier it is recommended to use the kinetic data that is specifically developed from local biomass gasification reaction. For example kinetic data from actual gasification experimental data using TGA, micro-reactor or bench scale gasifier would be much more reliable than kinetic data from literature. Results of hydrogen production from experimental data also could be used as model validation. Biomass is represented as pure carbon (C) in this current work in order to resemble the actual biomass. It is best to use the empirical chemical formula for biomass which consists of C, H and O according to the actual biomass proximate and ultimate analysis.

References

1. Florin, N.H., Harris, A.T.: Enhanced hydrogen production from biomass with in situ carbon dioxide capture using calcium oxide sorbents. Chem. Eng. Sci. **63**, 287–316 (2008)
2. Mahishi, M.R., Sadrameli, M.S., Vijayaraghavan, S., Goswami, Y.D.: A novel approach to enhance the hydrogen yield of biomass gasification using CO_2 adsorbent. J. Eng. Gas Turbines Power **130**, 1–8 (2008)

3. Wu, W., Kawamoto, K., Kuramochi, H.: Hydrogen-rich synthesis gas production from waste wood via gasification and reforming technology for fuel cell application. J. Mater Cycl. Waste Manag. **8**, 70–77 (2006)
4. Faaij, A.: Modern biomass conversion technologies. Mitig. Adapt. Strat. Glob. Change **11**, 343–375 (2006)
5. Bender, R.J., Tomassi, J.P., Asplund, F.: Variable moisture biomass gasification heating system and method. US Patent 6485296 (2002)
6. Kaneko, S., Sato, S., Kobayashi, Y., Kabata, T., Kobayashi, K., Takeuchi, Y., Takuda, K., Hashimoto, A., Shinoda, K., Takeno, K., Matsumoto, S., Ohta, H., Yamamoto, T., Sakai, M., Takegawa, T. and Seike, Y.: Biomass gasification furnace and system for methanol synthesis using gas produced by gasifying biomass. US Patent 6991769 B2 (2006)
7. Miccio, F., Svoboda, K., Schosger, J., Baxter, D.: Biomass gasification in internal circulating fluidized beds: a thermodynamic predictive tool. Korean J. Chem. Eng. **25**, 721–726 (2008)
8. Shen, L., Gao, Y., Xiao, J.: Simulation of hydrogen production from biomass gasification in interconnected fluidized beds. Biomass Bioenergy **32**, 120–127 (2008)
9. Koppatz, S., Pfeifer, C., Rauch, R., Hofbauer, H., Marquard-Moellenstedt, T., Specht, M.: H_2 rich product gas by steam gasification of biomass with in situ CO_2 adsorption in a dual fluidized bed system of 8 MW fuel input. Fuel Process. Technol. **90**, 914–921 (2009)
10. Ajilkumar, A., Sundararajan, T., Shet, U.S.P.: Numerical modeling of a steam-assisted tubular coal gasifier. Int. J. Therm. Sci. **48**, 308–321 (2009)
11. Marquard-Mollenstedt, T., Sichler, P., Specht, M., Michel, M., Berger, R., Hein, K.R.G., Hoftberger, E., Rauch, R., Hofbauer, H.: New approach for biomass gasification to hydrogen. In: 2nd World Conference on Biomass for Energy, Industry & Climate Protection, Rome, Italy (2004)
12. Pfeifer, C., Hofbauer, H.: Development of catalytic tar decomposition downstream from a dual fluidized bed biomass steam gasifier. Powder Technol. **180**, 9–16 (2008)
13. Nemtsov, D.A., Zabaniotou, A.: Mathematical modelling and simulation approaches of agricultural residue air gasification in a bubbling fluidized bed reactor. Chem. Eng. J. **143**, 10–31 (2008)
14. Nikoo, M.B., Mahinpey, N.: Simulation of biomass gasification in fluidized bed reactor using ASPEN PLUS. Biomass Bioenergy **32**, 1245–1254 (2008)
15. Sadaka, S.S., Ghaly, A.E., Sabbah, M.A.: Two phase biomass air-steam gasification model for fluidized bed reactors: Part I-model development. Biomass Bioenergy **22**, 439–462 (2002)
16. Wang, Y., Yan, L.: CFD simulation on biomass thermochemical conversion. Int. J. Mol. Sci. **9**, 1108–1130 (2008)
17. Busciglio, A., Vella, G., Micale, G., Rizzuti, L.: Analysis of the bubbling behavior of 2D gas solid fluidized beds Part II. Comparison between experiments and numerical simulations via digital image analysis technique. Chem. Eng. J. **148**, 145–163 (2009)
18. Fletcher, D.F., Haynes, B.S., Christo, F.C., Joseph, S.D.: A CFD based combustion model of an entrained flow biomass gasifier. Appl. Math. Model. **24**, 165–182 (2000)
19. Deng, Z., Xiao, R., Jin, B., Huang, H., Shen, L., Song, Q., Li, Q.J.: Computational fluid dynamics modeling of coal gasification in a pressurized spout-fluid bed. Energy Fuels **22**, 1560–1569 (2008)
20. Ji, P., Feng, W., Chen, B.: Production of ultrapure hydrogen from biomass gasification with air. Chem. Eng. Sci. **64**, 582–592 (2009)
21. Wang, X., Jin, B., Zhong, W.: Three-dimensional simulation of fluidized bed coal gasification. Chem. Eng. Process. **48**, 695–705 (2009)
22. Murthy, S., Fedorov, A.G.: Radiation heat transfer analysis of the monolith type solid oxide fuel cell. J. Power Source **124**(24), 453–458 (2003)

23. Lv, P.M., Xiong, Z.H., Chang, J., Wu, C.Z., Chen, Y., Zhu, J.X.: An experimental study on biomass air-steam gasification in fluidized bed. Bioresour. Technol. **95**, 95–101 (2004)
24. Gao, N., Li, A., Quan, C., Gao, F.: Hydrogen-rich gas production from biomass steam gasification in an updraft fixed-bed gasifier combined with a porous ceramic reformer. Int. J. Hydrogen Energy **33**, 5430–5438 (2008)
25. Kalinci, Y., Hepbasli, A., Dincer, I.: Biomass-based hydrogen production: a review and analysis. Int. J. Hydrogen Energy **34**, 8799–8817 (2009)

Large Eddy Simulation (LES) for Steady-State Turbulent Flow Prediction

T. Ganesan and M. Awang

Abstract The aim of this work is to simulate a steady turbulent flow using the Large Eddy Simulation (LES) technique in computational fluid dynamics (CFD). The simulation was done using an in-house code developed in the programming platform of Visual C++. The Finite Volume Method was used to compute numerically the solutions of the Navier-Stokes equation under turbulent conditions. The Quadratic Upstream Interpolation for Convective Kinetics (QUICK) numerical scheme was utilized with the Semi-Implicit Pressure Linked Equations (SIMPLE) as an algorithm. The code consists of a steady three-dimensional turbulent solver using the Large Eddy Simulation (LES) turbulent model. The simulated velocity flow profile was then compared against experimental data.

Keywords Computational fluid dynamics (CFD) · Large eddy simulation (LES) · Finite volume method · Turbulence · Navier-Stokes equations

1 Introduction

Large eddy simulation (LES) has been used in myriad studies to analyse turbulent flows in simple geometries and boundary conditions over the past 25 years [1, 2]. In the recent 5–10 years LES has been applied to predict increasingly complex flows [2]. These research efforts pioneered the idea of using the flow characteristics from the smallest resolved scales to predict the subgrid scale (SGS) stresses. This idea

T. Ganesan
Department of Chemical Engineering, Universiti Teknologi Petronas,
31750 Seri Iskandar, Perak, Malaysia
e-mail: tim.ganesan@gmail.com

M. Awang (✉)
Department of Mechanical Engineering, Universiti Teknologi Petronas,
31750 Seri Iskandar, Perak, Malaysia
e-mail: mokhtar_awang@petronas.com.my

K.Z.K. Shaari and M. Awang (eds.), *Engineering Applications of Computational Fluid Dynamics*, Advanced Structured Materials 44,
DOI 10.1007/978-3-319-02836-1_2

then gave rise to the scale similarity model and the mixed model. This way the required information from the smallest resolved scales were obtained mathematically by applying the filter operation twice. Bardina et al. [3] performed this method to rotating turbulent and to homogeneous isotropic flows. The follow-up work from Bardina et al. [3] was carried out by Germano et al. [4] who then proceeded to develop the dynamic subgrid scale model (DM).

Some simulations were done on the analysis of flows through cylindrical geometries using LES. For instance, Chang et al. [5] studied multiphase turbulent flows in pipes and Eggels and Nieuwstadt [6] used the Smagorinsky model to calculate flow properties in an axially rotating pipe. Besides that, the LES and DNS approaches were used to model a temporally evolving round jet at a low Reynolds number by Fatica et al. [7]. In this study, the Reynolds number was 800 (which was based on the radius and the centerline velocity of the jet) where the Smagorinsky model and the DM model were utilized.

In another study, the dynamic subgrid scale model (DM) model was used by Yang and Ferziger [8] to calculate the flow characteristics of a low Reynolds number turbulent flow in a channel with a two-dimensional obstacle mounted on one wall. The results were compared with another calculation performed using the Smagorinsky model with as well as the results from the DNS model. The overall results of the DM model were more consistent with the DNS solution as compared to the results from the Smagorinsky model. These comparisons conclude that the DM model is an improvement over the Smagorinsky model.

Hoffmann and Benocci [9] modelled a jet issuing from a two-dimensional slit onto a flat plate using LES. The DM model was modified to take into account the SGS stresses. The DM model was modified to utilizing test filtered variables (in contrast to the commonly used grid filtered variables) in the equation for the modelled parameter C. In these computations, no comparison against experimental data was carried out. However, the main physical features in the flow were captured.

Some work on the development of the LES method has been carried out in recent times [3, 6–8, 10]. These works were mainly on the modifications and development of the filtering component in the LES model used during the spatial averaging procedure.

The LES modelling method has gone through significant changes and improvements in the 1980s and in the 1990s. This is mainly due to the radical improvement in the advancement of computer systems. Besides that, these changes could also be attributed in the very rapid evolution of the SGS models where the DM model is proving to be quite promising. In a nutshell, there is a continuous and strong effort to advance the LES modelling approach to produce more realistic results for predicting characteristics of turbulent flows especially in engineering applications.

In this work, a solver was developed using the Finite Volume Method. The Quadratic Upstream Interpolation for Convective Kinetics (QUICK) numerical scheme [11] was used with the Semi-Implicit Pressure Linked Equations (SIMPLE) algorithm. The Large Eddy Simulation (LES) static turbulent model developed in

Smagorinsky [12] was used to compute the subgrid scale (SGS) stresses. Many simple experiments have been done in the past to observe turbulent flow phenomenon and to outline its characteristics. In this paper, two three-dimensional steady turbulent flow phenomenon was simulated and compared against the experimental results by Martinuzzi and Tropea [13] and Driver and Seegmiller [14].

This paper is organized as follows: Sect. 2 presents the Mathematical Formulation and Computational Techniques while Sect. 3 provides the solver parameters used in the LES simulation. Section 4 describes the experimental details of the flow application at which the LES simulation was implemented and Sect. 5 consists of the analysis of the results and some comparative studies. Section 6 provides some discussions on the error distribution between the simulation and the experimental results. Finally, this paper ends with some conclusions and recommendations for future work.

2 Mathematical Formulation and Computational Techniques

The mass flow rate across the faces of the fluid element is the product of density, area and the velocity component normal to the face. The summation will be in the form of a differential which will result as the following:

$$\frac{\partial \rho}{\partial t} + \frac{\partial(\rho u)}{\partial x} + \frac{\partial(\rho v)}{\partial y} + \frac{\partial(\rho w)}{\partial z} = 0 \tag{1}$$

where u, v and w are the velocity components in the x, y and z—direction respectively.

The momentum conservation principles are required in order to form a partial differential equation (Navier-Stokes). The solution to this partial differential equation would describe the behavior of the momentum in the flow. The final form of the momentum equation will be as the following:

$$\frac{\partial(\rho u)}{\partial t} + div(\rho u v) = div(\Gamma \cdot gradu) + S_u \tag{2}$$

where the $\partial(\rho u)/\partial t$ is the unsteady term, $div(\rho u v)$ is the convective term, $div(\Gamma \cdot gradu)$ is the diffusive term and S_u is the source term. The Γ in the diffusion term is the diffusion coefficient which is a function of the viscosity. The SIMPLE algorithm was employed in this simulation and it is shown in Fig. 1.

The LES model computes the subgrid scale stresses. Large eddies depend and extract energy from the bulk flow, their behavior is more anisotropic than small eddies (which are isotropic at high Reynolds number flows). A model such as the Reynolds Averaged Navier-Stokes (RANS) equations also describe the solution that comprises of the behavior of eddies in a time-averaged fashion. However, the

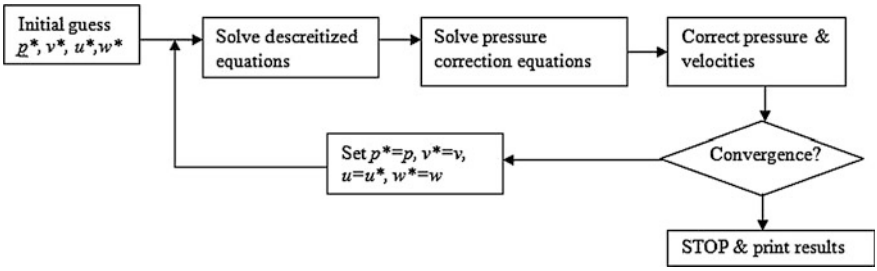

Fig. 1 The SIMPLE algorithm

LES model provides a means to compute a certain range of eddy scales (large eddies) through a statistical filtering procedure (spatial-averaging).

The filtering procedure is done by performing a convolution on the Navier-Stokes equation and the filter function (Gaussian filter, Fourier filter or the Tophat filter) producing the spatial-averaged Navier-Stokes equation.

The convolution averages-off the small eddies (which effects are estimated using semi-empirical models called sub- grid scale (SGS) models) where computation is only done on the large eddies. The LES model gives spatial-filtered Navier-Stokes equations:

$$\frac{\partial(\rho\bar{u}_i)}{\partial t} + div\left(\rho\bar{u}_i\bar{u}_j\right) = -\frac{\partial(\bar{p}_i)}{\partial x_i} + div(\Gamma \cdot grad\bar{u}_i) - \frac{\partial\tau_{ij}}{\partial x_j} \tag{3}$$

$$\tau_{ij} = \overline{\rho u_i u_j} + \rho\bar{u}_i\bar{u}_j \tag{4}$$

The terms $\bar{u}_i$ are the filtered velocities, $\bar{p}$ is the filtered pressure, the term τ_{ij} is the stress tensor that results from the statistical procedure (analogous to the Reynolds stresses in the RANS equations).

The LES Reynolds stresses arise due to the convective momentum transport which is a result of the interactions among SGS eddies per se and is modelled with a SGS turbulence model. The SGS turbulence model used in this computer code is the Smagorinsky-Lilly SGS model. In this computation, the Cross stress C_{ij}, Leonard stresses, L_{ij} and Reynold stresses, R_{ij} are implemented together in the finite volume method:

$$L_{ij} = (\rho\bar{u}_i\bar{u}_j - \rho\bar{u}_i\bar{u}_j) \tag{5}$$

$$C_{ij} = (\rho\bar{u}_i u'_j - \rho u'_i\bar{u}_j \tag{6}$$

$$R_{ij} = \rho u'_i u'_j \tag{7}$$

Thus, resulting in one SGS turbulence model which can be formulated as the following:

$$\tau_{ij} = -2\mu_{SGS}\bar{S}_{ij} + \frac{1}{3}\tau_{ii}\delta_{ij} \tag{8}$$

Where μ_{SGS} is the artificial or the sub-grid scale viscosity which acts as the constant of proportionality and $\bar{S}_{ij}$ is the average strain rate. The size of the SGS eddies are determined by the filter choice as well as the filter cut-off width which is used during the averaging operation. The SGS viscosity can be obtained by the following semi-empirical formulation:

$$\mu_{SGS} = \rho(C_{SGS}\Delta)^2\left|\sqrt{2\bar{S}_{ij}\bar{S}_{ij}}\right| \tag{9}$$

where Δ is the filter cut-off width and is an CSGS empirical constant which is usually specified in a range, $0.19 < C_{\mathrm{SGS}} < 0.24$.

3 Solver Parameters

Prior to execution of the numerical solver, a number of parameters are required to be specified. These parameters are the numerical coefficients that are employed in the numerical scheme and the algorithm. These parameters influence the number of iterations, computational time, stability of computations and the convergence rate. The parameter types and the values that are used in this work can be summarized as in Table 1:

Table 1 Numerical setting for solver parameters

Properties	Experiment 1	Experiment 2
	Parameters	Parameters
Iterations for velocity and pressure	3,496	3,470
Relaxation factor for velocity	0.9	0.9
Relaxation factor for pressure	0.9	0.9
Convergence criterion for pressure correction matrix	1 %	1 %
Mesh size (x, y, z) in (meters)	(0.032, 0.05, 0.04)	(0.02, 0.0034, 0.0051)
C_{SGS}, SGS Constant	0.2	0.2

4 Experimental Descriptions

4.1 Experiment 1: Flow Over a Surface-Mounted Cubicle Obstacle

The experimental data from this experiment which was performed by Martinuzzi and Tropea [13] was compared against the simulation results. The fluid used in this experiment was water (incompressible flow) with the density of 1,000 kg/m^3 and viscosity of 0.001 kg/ms. The experiment was performed in a rectangular channel with a single cubicle obstacle mounted on the surface of the channel (internal flow). The Reynolds number (which is based on the channel height) was 12,000 with the inlet velocity of 0.467 m/s.

The experiment was conducted at atmospheric pressure. The length (x-direction), height (y-direction) and width (z-direction) are respectively 1.6 × 0.16 × 1.0 m^3. The obstacle was mounted at 0.8 m from the inlet (x-direction) and 0.46 m in the z-direction. This experiment was performed in a fully developed turbulent channel flow. The cubicle obstacle was placed at 5 times the channel height from the inlet (x-direction) and at the centerline of the width (z-direction). A detailed description of the experimental technique can be found in Dimaczek et al. [15]. A schematic illustration of the setup is shown in Fig. 2:

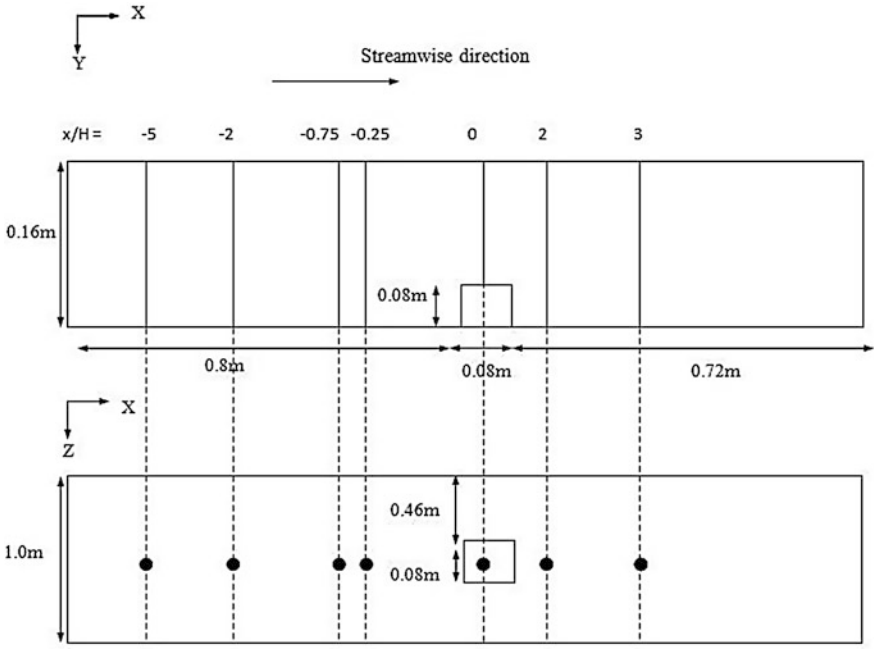

Fig. 2 Schematic representation of the setup in Experiment 1

4.2 Experiment 2: Flow Over a Backward-Facing Step with Opposite Wall

The experimental results from this experiment which was performed by Driver and Seegmiller [14] are used for the second validation of the LES solver. The fluid used in this experiment was air (incompressible at the Mach number of 0.128) with the density of 1.0 kg/m^3 and viscosity of 1.02×10^{-5} kg/ms at ambient temperature. This experiment was performed in a rectangular channel with a backward-facing step that diverges the channel. The Reynolds number based on momentum thickness with the boundary layer thickness of 0.019 m was 5,000 with the inlet velocity of 44.2 m/s. Hence, the fluid at the inlet is incompressible and undergoes fully turbulent flow. The experiment was conducted at atmospheric pressure. The length (x-direction), height (y-direction) and width (z-direction) are respectively $1.0 \times 0.101 \times 0.152$ m^3. The backward step begins at 0.06 m from the inlet (in the x-direction). A schematic illustration of the setup is shown in Fig. 3:

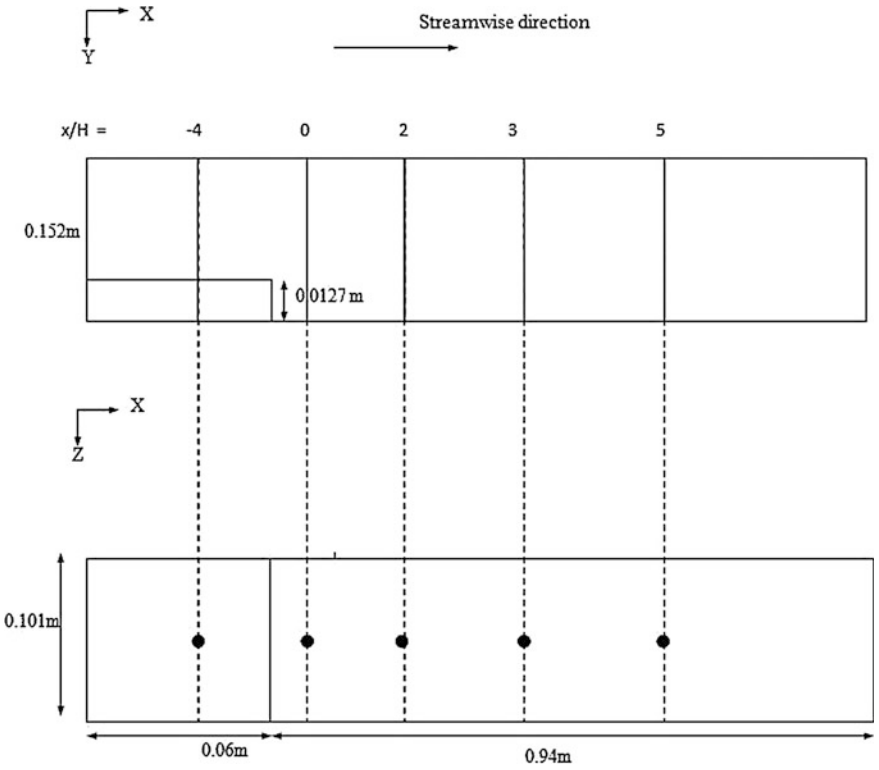

Fig. 3 Schematic representation of the setup in Experiment 2

5 Results Analysis

5.1 *Experiment 1: Flow Over a Surface-Mounted Cubicle Obstacle*

The velocity distributions obtained by the solver is compared with that obtained from the experiment. For the purpose of comparison, the most significant velocity gradients that influence the flow behaviour are taken. To identify the significant velocity gradients, a scaling argument was used. From the analysis, the velocity gradients, was identified as the most significant term for the given dimensions of the setup and the flow conditions. Thus, the u-velocities (streamwise velocities) are taken with respect to the y-axis at different points in the x-direction.

The velocity distributions in the experimental results are normalized to the inlet velocity that is U/U_0. Similarly the distances in the experimental results are also normalized to the height of the obstacle which is respectively x/H, y/H, and z/H.

Seven sets of experimental results of the u-velocity distributions are obtained throughout the test section. Four sets of velocity distributions are used in the comparison at the region before the obstacle, one set right above the obstacle and two sets at the flow after the obstacle (the dissipation region). The normalized distances in the x, y and z -direction (x/H, y/H, and z/H) is at (0, 0, 0) is right above the obstacle. The following are the first four sets of velocity distributions which are taken for comparison. These sets are taken at the upstream region before the obstacle at x/H = −5, x/H = −2, x/H = −0.75 and x/H = −0.25 which is shown in Figs. 4, 5, 6 and 7:

The computed streamwise velocities when compared with the experimental data at the near-wall region are seen to have deviations (Fig. 4 and 5). It can be seen that the usage of non-uniform grid produces more realistic results than a uniform grid for such cases. In Arnal and Friedrich [16] finer was used grid at the near-wall region. The simulations produced more accurate results as compared to the calculation done with a uniform grid which can be observed in Friedrich and Arnal [17]. Similar to Friedrich and Arnal [17], this work used a uniform grid which may be one of the reasons for inconsistencies mentioned above.

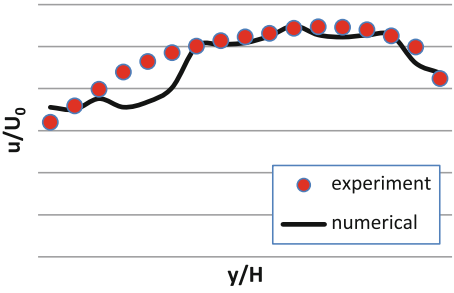

Fig. 4 Comparison of velocity distributions at *x/H* = −5

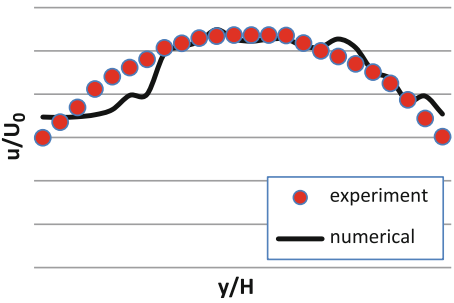

Fig. 5 Comparison of velocity distributions at $x/H = -2$

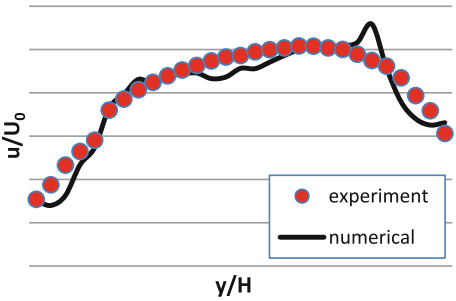

Fig. 6 Comparison of velocity distributions at $x/H = -0.75$

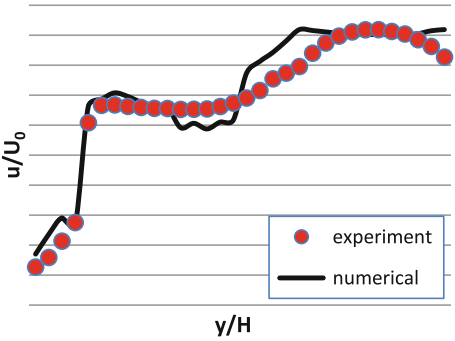

Fig. 7 Comparison of velocity distributions at $x/H = -0.25$

In Figs. 6 and 7, it can be observed that the simulation results produce a qualitatively similar trend as compared with that of the experiment. However, the velocity profile produced by the simulation appears to have slight irregularities ('wiggles'). Similar occurrences have been observed in Krajnovic and Davidson [18] while performing LES simulation on flow over a bluff body. In Krajnovic and Davidson [19], it was stated that these wiggles can be attributed to a combination of two factors, the coarseness of the mesh and the numerical scheme applied. Krajnovic and Davidson [18] also experienced these similar wiggles in the streamwise velocities in their simulation. Therefore, in Krajnovic and Davidson [19], it was suggested that a finer grid and a better numerical scheme may produce smoother trend in the streamwise velocities and hence eliminate these wiggles.

Figures 8, 9 and 10 are the velocity distributions which are taken right above the obstacle (at $x/H = 0$) and at the flow after the obstacle (the dissipation region at $x/H = 2$ and $x/H = 3$):

The solver had difficulty in accurately computing the flow behavior at the recirculation region (see Fig. 8). This may be attributed to the inability of the SGS model (Smagorinsky's model) to compute accurately the SGS stresses that heavily influences the flow during the recirculation phenomenon. One method to enhance the SGS model's accuracy is to modify it by including approximate boundary conditions. This was done in Morinishi and Kobayashi [20] where this method was stated to improve the accuracy of the computed SGS stresses. Another method was

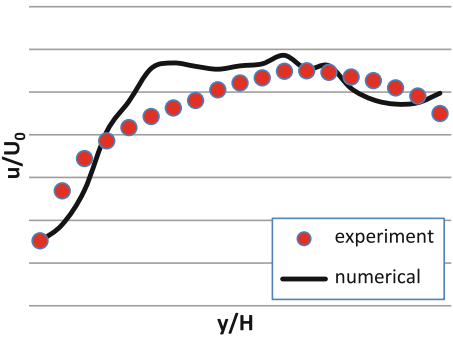

Fig. 8 Comparison of velocity distributions at $x/H = 0$

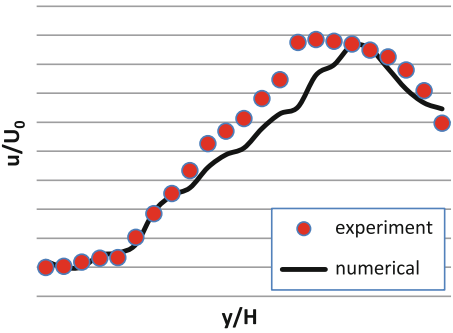

Fig. 9 Comparison of velocity distributions at $x/H = 2$

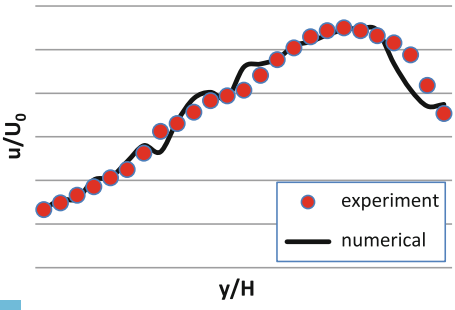

Fig. 10 Comparison of velocity distributions at $x/H = 3$

proposed in Yoshizawa [21] where a new parameter was introduced and was said to improve the accuracy of the Smagorinsky's model.

There are also slight inconsistencies for the velocities at the recirculation and the recovery region (refer to Figs. 9 and 10). To trace the vortex, the vortex center can be used where the velocity is zero. In this work, it can be observed that dissipation occurs gradually downstream after the obstacle or the step. Hence heading further downstream the vortex structure disappears which is consistent with the physical data. A similar work on identifying vortex dissipation downstream of flows was done in Roquemore [22]. The dynamic Smagorinsky's model (DM model) was also stated to give more realistic results as compared with the static Smagorinsky's model.

5.2 *Experiment 2: Flow Over a Backward-Facing Step with Opposite Wall*

The velocity distributions obtained by the solver is compared with that obtained from the experiment. Similar to experiment 1, for the purpose of validation, the identification of the most significant velocity gradients is necessary and thus, the scaling argument was used. From the analysis, the velocity gradients, was identified as the most significant term for the given dimensions of the setup and the flow conditions. Therefore, the u-velocities (streamwise velocities) are taken with respect to the y-axis at different points in the x-direction.

The velocity distributions in the experimental results are normalized to the inlet velocity that is U/U_0 (dimensionless). Similarly, the distances in the experimental results are also normalized to the height of the backward-step which is respectively x/H, y/H, and z/H (dimensionless).

Seven sets of experimental results of the u-velocity distributions (velocities in the x-direction) are obtained throughout the test sections. Four sets of velocity distributions are used in the comparison at the region after the backward-step (the dissipation region) and before the backward-step. The following are the five sets of velocity distributions which are taken for comparison. These sets are taken at x/H = −4, x/H = 0, x/H = 2, x/H = 3 and x/H = 5 which are shown in Figs. 11, 12, 13, 14 and 15:

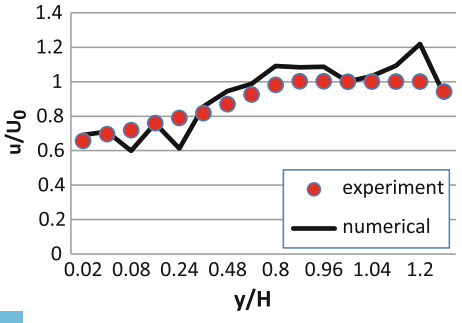

Fig. 11 Comparison of velocity distributions at *x/H* = −4

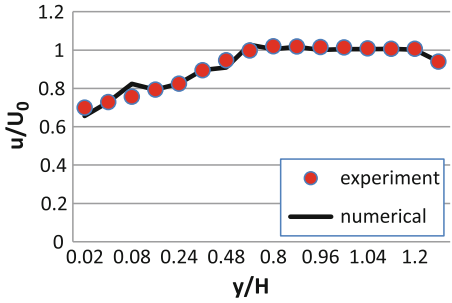

Fig. 12 Comparison of velocity distributions at $x/H = 0$

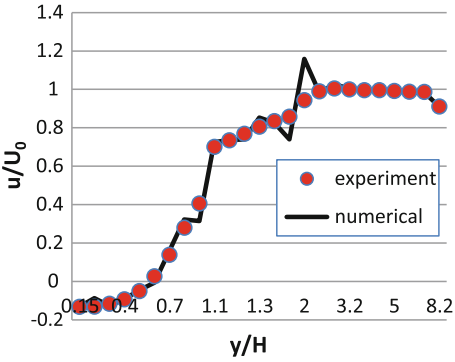

Fig. 13 Comparison of velocity distributions at $x/H = 2$

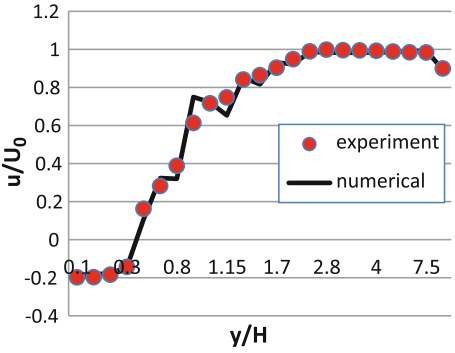

Fig. 14 Comparison of velocity distributions at $x/H = 3$

It can be seen in Fig. 11 that the wiggles have manifested themselves once more in the solver similar to experiment 1. However, these inconsistencies do not appear in Fig. 12. The factors of grid type and coarseness together with the numerical scheme play a critical role for the existence of these wiggles [18, 19].

The reattachment locations (the points where the wall-normal gradient of the stream wise velocity changes sign) obtained by the solver for experiment 2 is rather consistent with the physical results. This can be observed in Figs. 13, 14 and 15. Therefore, the incoherent vortex or the vortex stretching phenomenon is accurately

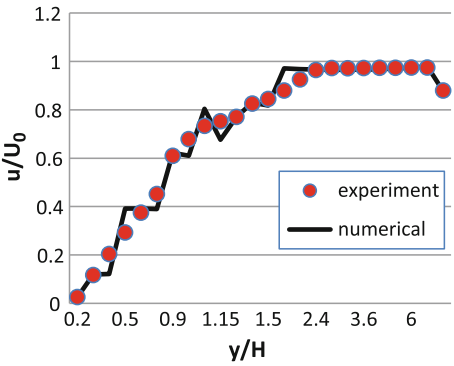

Fig. 15 Comparison of velocity distributions at $x/H = 5$

captured by the solver. The results of the solver capturing this phenomenon are not only consistent with the physical data but also similar to computational results of Balaras et al. [23]. To trace the vortex, the vortex center can be used where the velocity is zero. In this work for both experiments it can be observed that dissipation occurs gradually downstream after the obstacle or the step. Hence heading further downstream the vortex structure disappears which is consistent with the physical data. This can be observed in Figs. 13, 14 and 15. A similar work on identifying vortex dissipation downstream of flows was done by Roquemore et al. [22].

6 Deviation Analysis

The error in percentage (%) between the velocity distributions obtained by the numerical solver and the experimental results was computed using the following formulation:

$$error\ (\%) = \left|\frac{u - u'}{u'}\right| \times 100\ \% \tag{10}$$

where u' is the velocity obtained by the experimental results and u is the velocity obtained by the numerical solver. The average error obtained for the sets of velocity distributions in experiment 1 are as in Fig. 16:

In Fig. 16, as the flow approaches the obstacle, the average error is observed to increase. The average error at $x/H = -0.25$ which is right before the obstacle is at 15.545 %. This may be attributed to flow reversal, as could be observed in Fig. 5 (negative velocity values) when the fluid encounters the mounted-obstacle. This phenomenon is not accurately captured by the numerical solver and hence results in higher error values. The average error in the velocity distribution is observed to reduce as compared with that in the flow reversal region in front of the obstacle. This may be explained by the fact that the flow above the obstacle exhibits comparatively higher stability as the mean flow direction is preserved. The average error

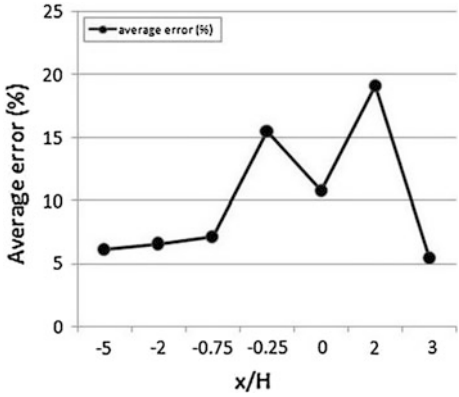

Fig. 16 The average error distribution in the streamwise direction (For Experiment 1)

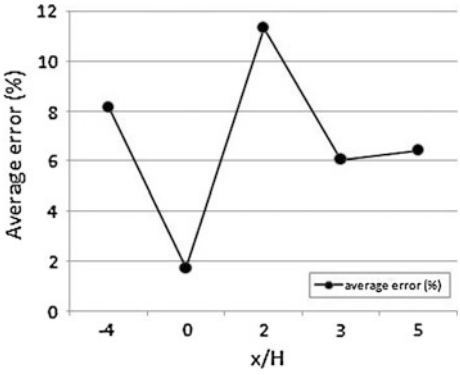

Fig. 17 The average error distribution in the stream wise direction (For Experiment 2)

at $x/H = 2$ has a higher value of 19.14 % due to inability of the numerical solver to capture the finer details of the flow recirculation phenomenon. Finally at $x/H = 3$, is can be observed that the average error reduces again during flow recovery. Thus the solver computes the velocity profile with fair amount accuracy.

The average error distribution in the streamwise direction for Experiment 2 can be seen in Fig. 17:

In Fig. 17, the average error is observed to reduce radically from $x/H = -4$ to $x/H = 0$. This is because at $x/H = 0$, the distribution at the velocity profile becomes more regular as compared to the profile near the inlet. However, at $x/H = 2$, it can be observed that the average error retains a high value of 11.34 %. This can be due to the numerical discrepancies in the solver which may give rise to difficulties in accurately capturing the flow recirculation phenomenon. Finally at $x/H = 3$ and at $x/H = 5$, it can be observed that the average error reduces and maintains a stable value. The intensity of backflow gradually reduces as the dissipation occurs. As the flow recovers and regains its stability, the solver computes the velocity profile more accurately.

The type of SGS stresses existing in turbulent flows are Reynolds stresses. Since stresses such as Leonard and Cross stresses are the result from the statistical

operation and thus, not measurable, the dominant SGS stresses which has any effect on the flow is assumed to be the Reynolds stresses. As can be observed in Fig. 17, the computational results in experiment 2 agree fairly well with the experimental data quantitatively and qualitatively with a less than 12 % average error at each measurement as compared to experiment 1 (Fig. 16). This is because; the complexity of the geometry of the experimental setup in experiment 2 is much lower than experiment 1. Hence, the Reynolds stresses from the flow is more intense in experiment 1 as compared to experiment 2 such that the simulation encountered more difficulties when predicting the flow in experiment 1 as compared to experiment 2.

7 Concluding Remarks

Based on the analysis performed it can be concluded that the results produced by the simulation are fairly consistent with the experimental results. Although the in-house source code equipped with the LES turbulence model is complete, further advancement and validation with empirical results with different flow conditions are necessary. For instance, the numerical scheme of the solver can be upgraded to third order QUICK or other UPWIND schemes to cut down the approximation errors during numerical operation. Besides that, based on recent work [18] the static Smagorinsky's model in this solver can be upgraded to the Dynamic Smagorinsky's model to accurately capture the flow fluctuations due to turbulence. The option for more meshing techniques could also be included as one of the features in the solver. These upgrades and testing will increase the capacity of the simulator to solve a greater variation of flow cases with optimum accuracy.

References

1. Rogallo, R.S., Moin, P.: Numerical simulations of turbulent flow. Annu. Rev. Fluid Mech. **16**, 99–137 (1984)
2. Moin, P., Jimenez, P.: Large eddy simulations of complex turbulent flows. AIAA, Paper No. 93-3099, Orlando, Florida, U.S (1993)
3. Bardina, J., Ferziger, J.H., Reynolds, W.C.: Improved turbulence models based on large eddy simulation of homogeneous, incompressible turbulent flows. Report TF-19, Thermosciences Division, Department of Mechanical Engineering, Stanford University, Stanford, (1983)
4. Germano, M., Piomelli, U., Moin, P., Cabot, W.H.: A dynamic subgrid scale eddy viscosity model. Phys. Fluids A **3**(7), 1760–1765 (1991)
5. Chang, Y.S.H., Ganesan, T., Lau, K.K.: Comparison between empirical correlation and computational fluid dynamics simulation for the pressure gradient of multiphase flow. Lect. Notes Eng. Comput. Sci. **2172**(1), 1814–1818 (2008). ISSN: 20780958
6. Eggels, J.G.M., Nieuwstadt, F.T.M.: Large eddy simulation of a turbulent flow in an axially rotating pipe. In: Ninth Symposium on "Turbulent Shear Flows", Kyoto, Japan, 16–18 Aug 1993
7. Fatica, M., Orlandi, P., Verzicco, R.: Direct numerical simulation of round jets. In: Ninth AGARD Symposium on Direct and Large Eddy Simulation to Transition and Turbulence, Chania, Crete, Greece, 18–21 April 1994

8. Yang, K.S., Ferziger, J.H.: Large-eddy simulation of turbulent obstacle flow using dynamic subgrid scale model. AIAA J. **31**(8), 1406–1413 (1993)
9. Hoffmann, G., Benocci, C.: Numerical simulation of a spatially-developing planar jets. In: AGARD Symposium on Direct and Large Eddy Simulation to Transition and Turbulence, Chania, Crete, Greece, 18–21 April 1994
10. Winckelmans, G.S., Wray, A.A., Vasilyev, O.V., Jeanmart, H.: Explicit-filtering large eddy simulation using tensor diffusivity model supplemented by a dynamic Smagorinsky term. Phys. Fluids **12**(7), (2000)
11. Leonard, B.P.: A stable and accurate convective modeling procedure based on quadratic upwind interpolation. Comput. Methods Appl. Mech. Eng. **19**, 59–98 (1979)
12. Smagorinsky, J.: General circulation experiments with the primitive equations I. The basic experiment. Mon. Weather Rev. **91**(3), 99–164 (1963)
13. Martinuzzi, R., Tropea, C.: The flow around surface-mounted, prismatic obstacles placed in a fully developed channel flow. J. Fluid Eng. **1**, 85–86 (1993)
14. Driver, D.M., Seegmiller, H.L.: Features of a reattaching turbulent shear layer in divergent channel flow. AIAA J. **23**, 163–164 (1985)
15. Dimaczek, G., Tropea, C., Wang, A.B.: Turbulent flow over two-dimensional, surface-mounted obstacles: plane and axisymmetric geometries. In: 2nd European Turbulence Conference, Berlin (1988)
16. Arnal, M., Friedrich, R.: On the effects of spatial-resolution and subgrid scale modelling in large eddy simulation of a recirculating flow. In: Proceedings of the 9th GAMM-Conference on Numerical Methods in Fluid Mechanics, Lausanne (1991)
17. Friedrich, R., Arnal, M.: Analyzing turbulent backward-facing step flow with the low-pass filtered Navier-Stokes equations. J. Wind Eng. Ind. Aerodyn. **35**, 101–128 (1990)
18. Krajnovic, S., Davidson, L.: Large eddy simulation of the flow around a bluff body. AIAA J. **40**(5), 927–936 (2002)
19. Krajnovic S., Davidson, L.: Large-eddy simulation of the flow around a ground vehicle body. Society of Automotive Engineers, SAE Paper 2001-01-0702 (2001)
20. Morinishi, Y., Kobayashi, T.: Large eddy simulation of backward-facing step flow. In: International Symposium of Engineering Turbulence Modelling and Measurement, Dubrovnik, Yugoslavia (1990)
21. Yoshizawa, A.: Subgrid scale modelling with a variable length scale. Phys. Fluids A **1** (7),1293–1295 (1989)
22. Roquemore, W.M., Chen, L., Goss, L.P., Lynn, W.F.: Joint US-France Workshop on Turbulent Reacting Flows, Rouen, France (1987)
23. Balaras, E., Benocci, C., Piomelli, U.: Two-layer approximate boundary conditions for large-eddy simulations. AIAA J. **34**, 1111–1119 (1996)

Numerical Simulations of Lid-Driven Cavity Flows Using Multi-relaxation Time Lattice Boltzmann Method

S.J. Almalowi, D.E. Oztekin and A. Oztekin

Abstract Lattice Boltzmann method is implemented to study two and three dimensional flows in a square cavity. D2Q9 is used to predict the velocity field in a two dimensional cavity while both D3Q15 and D3Q19 lattice arrangements are employed to predict three dimensional flows in a cavity. The second order and non-equilibrium type of boundary conditions are used to discretize the conditions imposed on the velocity field at both moving and stationary walls. Multi-relaxation time method is applied for two dimensional lattice arrangements while single relaxation time method is employed for three dimensional arrangements. Multi relaxation time provides an accurate and stable simulations at high Re flows. The velocity field predicted here for both two and three dimensional cavity flows agrees well with those documented by previous investigators. It has been shown here that the Lattice Boltzmann method is an effective computational fluid dynamics tool to study high Re flows.

1 Introduction

The Lattice Boltzmann method is a tool from statistical mechanics which is used to predict macroscopic properties of fluids such as viscosity, thermal conductivity, and diffusion coefficient from the microscopic properties of atoms and molecules. The method has been investigated by several investigators [1–4] and has been increasing in popularity since its development in the early nineties. It has been shown to have accuracy comparable with that of traditional CFD methods. In the present work we will be studying the classical lid driven cavity flow as an example. It should be noted that the Lattice Boltzmann method has been applied to very complicated flows, including high Reynolds number flows and viscoelastic flows [5].

S.J. Almalowi (✉) · D.E. Oztekin · A. Oztekin
Department of Mechanical Engineering and Mechanics, Lehigh University, Bethlehem, PA 18015, USA
e-mail: sja210@lehigh.edu

K.Z.K. Shaari and M. Awang (eds.), *Engineering Applications of Computational Fluid Dynamics*, Advanced Structured Materials 44,
DOI 10.1007/978-3-319-02836-1_3

The Lattice Boltzmann method can be easily applied to one, two, or three dimensions and can be applied to many lattice arrangements. The number associated with lattice arrangement is the number of directions involved. These lattice directions can be imagined as the paths the fluid can flow. In any Lattice Boltzmann method the first lattice direction is the node itself, this represents the fluid remaining stationary. The other directions vary depending on the arrangement. A common arrangement in two dimensions is a nine directional arrangement, where directions two through five are the cardinal directions and directions 6 though nine are the diagonals. The terminology D2Q9 is used as shorthand for 2 dimensions and 9 lattice directions. In the present work D2Q9 and D3Q19 will be studied.

Some relevant investigations in lid driven cavity flow and in the Lattice Boltzmann method are listed here. Barragy and Carey [6] have used a finite element method with a fine sized mesh. They have obtained highly accurate solutions for steady cavity flow up to Reynolds number of 12,500. Botella and Peyret [7] have used a Chebyshev collocation method to examine a similar flow. Erturk et al. [8] studied the 2-D steady incompressible lid driven cavity flow by using stream function and vorticity formulation and was able to obtain solutions up to Reynolds number of 21,000.

Mei et al. [9] studied the 3-D flows with curved boundary condition using the Lattice Boltzmann method with D3Q15 and D3Q19. They obtained solutions for steady cavity flows up to Reynolds numbers of 400. Hou et al. [10] investigated 2-D cavity flows using the Lattice Boltzmann method. They utilized D2Q9 arrangements using single relaxation time. They had success up to Reynolds numbers of 7,500.

2 Governing Equations

The Lattice Boltzmann method (LBM) was developed from the Lattice Gas Automaton method (LGA). In LGA imaginary particles are placed on the lattice and are given velocities. At each time step the particles will move along the lattice to their next position based on their velocities, this is the propagation step. Then, if multiple particles are on the same node in the lattice, certain collision rules are followed. This is called the collision step and it is in this step that the velocities are updated for the next time step. This easily conserves mass and momentum. Mass is conserved by maintaining the same number of imaginary particles throughout the simulation and momentum is conserved by the rules set in the collision step. However, there are serious errors in this method. The imaginary particles in the LGA method are representing a large number of particles and are being limited to movement along certain angles. The LBM uses Boltzmann's density distribution function to create a continuous model for the particles. Because LBM uses a

distributed function, instead of discrete particles at each node, the fluid at the node is capable of following multiple branches of the lattice, as opposed to the discrete particle which had to choose one branch as a path. With this change the fluid can move in a natural way along the lattice in contrast to the jerky motions seen in LGA [11].

In LBM we have the evolution equation which is the combination of the propagation and collision steps

$$f_k(\boldsymbol{x} + \boldsymbol{e}_k\delta_t, t + \delta_t) - f_k(\boldsymbol{x}, t) = -\frac{1}{\tau}\left[f_k(\boldsymbol{x}, t) - f_k^{eq}(\boldsymbol{x}, t)\right] \tag{1}$$

In this equation the left hand side represents propagation and the right hand side represents the collision. Where the function $f_k(\boldsymbol{x}, t)$ is the density distribution function along the lattice branch k. x is the spatial coordinate and t is time. $\boldsymbol{e}_k$ is the expression for the discrete velocities along each branch k. τ is the lattice relaxation time. $f_k^{eq}(\boldsymbol{x}, t)$ is the equilibrium distribution. This is a very important term, since the appropriate selection of this function guarantees that the evolution equation satisfies the Navier-Stokes equation. The selection of this function is shown below.

In LGA the conservation laws are clear but in LBM it takes a bit more work to show that the Navier-Stokes equation is upheld. To start let D_t be the operator $(\partial_t + \boldsymbol{e}_k \cdot \nabla)$ and let $\in = \delta_t$ be a small parameter. It is know that this is the Taylor Series expansion.

$$f_k(\boldsymbol{x} + \boldsymbol{e}_k\delta_t, t + \delta_t) = \sum_{n=0}^{\infty} \frac{\in^n}{n!} D_t^{(n)} f_k(\boldsymbol{x}, t) \tag{2}$$

The following relations are from perturbation analysis [11]. The function $f_k(\boldsymbol{x}, t)$ and the operator ∂_t can be expanded in terms of powers of $\in$ as

$$f_k = \sum_{n=0}^{\infty} \in^n f_k^{[n]} \quad \partial_t = \sum_{n=0}^{\infty} \in^n \partial_{t_n} \tag{3}$$

Substituting Eqs. 2 and 3 into the evolution equation (Eq. 1), and extracting terms with coefficient $\in$ of order n, $O(\in^n)$ for n of zero, one, and two yields

$$O(\in^0) : f_k^{[0]} = f_k^{eq} \tag{4}$$

$$O(\in^1) : D_{t_0} f_k^{[0]} = -\frac{1}{\tau} f_k^{[1]} \tag{5}$$

$$O(\in^2) : \partial_{t_1} f_k^{[0]} + \left(\frac{2\tau - 1}{2\tau}\right) D_{t_0} f_k^{[1]} = -\frac{1}{\tau} f_k^{[2]} \tag{6}$$

Now apply these critical constraints to satisfy the conservation laws

$$\begin{aligned} \sum_k f_k^{[0]} &= \rho \qquad (a) \\ \sum_k f_k^{[0]} \boldsymbol{e_k} &= \rho \boldsymbol{u} \qquad (b) \\ \sum_k f_k^{[n]} &= 0 \quad \mathrm{n} > 0 \quad (c) \\ \sum_k f_k^{[n]} \boldsymbol{e_k} &= 0 \qquad (d) \end{aligned} \tag{7}$$

Using these constraints an expression for f_k^{eq} can be derived using the Chapman-Enskog expansion; details will be given in a 2D example below. With this expression for f_k^{eq} we can get solve the zeroth-order momentum flux tensor

$$\Pi^{[0]} = \sum_k \boldsymbol{e}_k \boldsymbol{e}_k f_k^{eq} \tag{8}$$

Now multiply Eq. 5 by $\boldsymbol{e_k}$ and sum over k. Since D_t is a linear operator the result can be written as

$$D_{t_0} \sum_k f_k^{[0]} \boldsymbol{e}_k = -\frac{1}{\tau} \sum_k f_k^{[1]} \boldsymbol{e}_k \tag{9}$$

Applying the constraint 7d we see

$$D_{t_0} \sum_k f_k^{[0]} \boldsymbol{e}_k = 0 \tag{10}$$

Now expanding the operator we get

$$\partial_{t_0} (\rho_0 \boldsymbol{u}) + \nabla \cdot \Pi^{[0]} = 0 \tag{11}$$

Which will be the Euler momentum equation for incompressible fluid when the expression for $\Pi^{[0]}$ is solved.

Similarly, by summing Eq. 5 over k the conservation of mass is satisfied exactly.

The following is an example derivation done with the lattice arrangement D2Q9. Using the general method above this can be extended to other lattice arraignments. First we must note what is given from our lattice arrangement. The definition of $\boldsymbol{e}_k$ yields

$$\boldsymbol{e}_k = \begin{cases} (0,0) & \text{for } k = 0 \\ \left(c * \cos\left(\frac{(k-1)\pi}{2}\right), c * \sin\left(\frac{(k-1)\pi}{2}\right)\right) & \text{for } k = 1,2,3,4 \\ \left(c\sqrt{2}\cos\left[\frac{(k-5)\pi}{2} + \frac{\pi}{4}\right], c\sqrt{2}\sin\left[\frac{(k-5)\pi}{2} + \frac{\pi}{4}\right]\right) & \text{for } k = 5,6,7,8 \end{cases} \tag{12}$$

Here c is a lattice speed. Similarly we can find the weighting function as

$$w = \begin{cases} \frac{4}{9} & \text{for } k = 0 \\ \frac{1}{9} & \text{for } k = 1,2,3,4 \\ \frac{1}{36} & \text{for } k = 5,6,7,8 \end{cases} \tag{13}$$

Next we can derive $f_k^{eq}(\boldsymbol{x}, t)$ by knowing this is 2D. Starting with the Chapman-Enskog expansion for 2D we have

$$f_k^{eq} = C\left\{1 + C_1 \boldsymbol{e}_k \cdot \boldsymbol{u} + C_2\left[(\boldsymbol{e}_k \cdot \boldsymbol{u})^2 - \frac{1}{2}|\boldsymbol{u}|^2\right] + \cdots\right\} \tag{14}$$

The higher order terms of the expansion are unnecessary for incompressible fluid. This leaves us with the three constants and which need to be selected. We know that f_k^{eq} must satisfy the constraints 7a and 7b. This provides us with the three equations; you will note that 7b are in fact 2 equations in the 2D case, to fit our three unknowns. The result of which will be

$$f_k^{eq} = w_k\left\{\rho + \rho\left[3\frac{\boldsymbol{e}_k \cdot \boldsymbol{u}}{c^2}\right] + \frac{9(\boldsymbol{e}_k \cdot \boldsymbol{u})^2}{2c^4} - \frac{3|\boldsymbol{u}|^2}{2c^2}\right\} \tag{15}$$

Now plug the solved f_k^{eq} into the zeroth-order momentum flux tensor and get Π

$$\Pi^{[0]} = \sum_k e_k e_k f_k^{[0]}{}_k = \frac{c^2\rho}{3} I + \rho u_i u_j \tag{16}$$

where i and j are the axial directions.

With the definition of pressure as $P = \frac{c^2\rho}{3}$, Eq. (10) becomes the Euler momentum equation.

A similar procedure can be applied to Eq. 6 to get the Navier-Stokes equations. However this proof becomes too tedious to include here. It should be noted that to Eq. 6 into the form of the Navier-Stokes equation you will have to eliminate terms of order M^3. Where M is the Mach number.

2.1 Multiple Relaxation Time

The single relaxation time method above is known to have several problems, which include: stability issues, fixed Prandtl number, and a fixed ratio between the kinematic and bulk viscosities [2]. The solution to these problems lies in the Multiple-relaxation time Lattice Boltzmann method. This method has been described as "creating a self-contained mathematical object representing a dynamical system with a finite number of moments in discrete space and time" [12]. The objective here is to create a system of evolution equations which where each equation satisfies a certain conserved quantity. As such the evolution equation now becomes

$$f_k(\boldsymbol{x} + \boldsymbol{e}_k\delta_t, t + \delta_t) - f_k(\boldsymbol{x}, t) = \boldsymbol{S}\left[f_k(\boldsymbol{x}, t) - f_k^{eq}(\boldsymbol{x}, t)\right] \tag{17}$$

where S is a k by k matrix. The issue now becomes, how to construct S. It can be immediately seen that the eigenvalues of S must be between 0 and 2 or the relaxation times for the non-conserved properties would be faster than the hydrodynamic time scales. If the eigenvalues are selected to equal the set of Hermite tensor polynomials in continues velocity space, the problem can be simplified to

$$f_k(x + e_k\delta_t, t + \delta_t) - f_k(x, t) = -M^{-1}\widehat{S}\left[m_k(x, t) - m_k^{eq}(x, t)\right] \tag{18}$$

where M is the linear mapping from velocity space to momentum space and $\widehat{S} = \boldsymbol{M} \cdot \boldsymbol{S} \cdot \boldsymbol{M}^{-1}$. Note that in this equation $\widehat{S}$ is diagonalized and m_k^{eq} is the equilibrium value of the corresponding moment m_k. For greater detail see D'Humieres et al. [12].

2.2 Lid Driven Cavity Flow

Below is the schematic of the two dimensional lid-driven cavity flow inside a square shaped system (Fig. 1). The present study also considers a three dimensional lid-driven cavity flow inside a cube shaped system. D2Q9, D3Q15 and D3Q19 lattice Boltzmann arrangement are employed in the present study. D2Q9 lattice arrangement on the boundary, as discussed earlier and is shown in Fig. 2.

The present study uses the multi-relaxation time technique described in the previous section. For the D2Q9 case the nine m^{eq} values have been chosen to be

$$\begin{aligned} &m_1^{eq} = \rho, m_2^{eq} = -2\rho + 3 \times \left(\kappa_x^2 + \kappa_y^2\right), m_3^{eq} = \rho - 3 \times \left(\kappa_x^2 + \kappa_y^2\right), \\ &m_4^{eq} = \kappa_x, m_5^{eq} = -\kappa_x, m_6^{eq} = \kappa_y, m_7^{eq} = -\kappa_y, m_8^{eq} = \kappa_x^2 - \kappa_y^2 \text{ and } m_9^{eq} = \kappa_x\kappa_y \end{aligned} \tag{19}$$

where $\kappa_i = \sum_{k=1}^{9} f_k \boldsymbol{e}_{ki}$ where i is an axial direction.

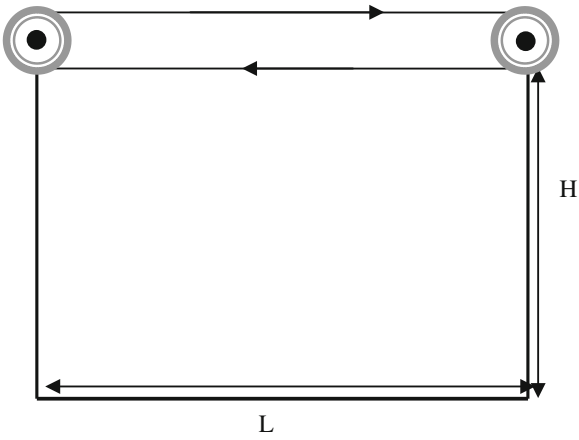

Fig. 1 The 2-D cavity flow

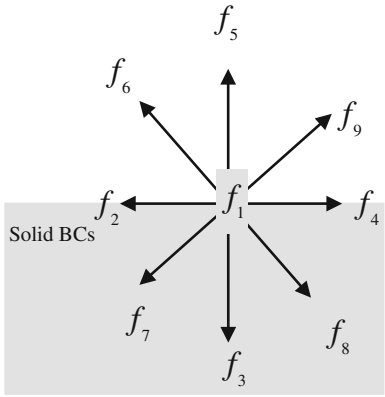

Fig. 2 D2Q9 lattice arrangement

Proper treatment of boundary conditions is essential in Lattice Boltzmann method as Chai Zhen et al. reported [1]. It affects the accuracy of the predictions especially in the complex flows with high Reynolds number. Therefore, finding an optimum discretization scheme for the boundary condition that is compatible with MRT model is important. For D2Q9 model the equilibrium and non-equilibrium schemes are

$$f_k(r,t) = f_k^{eq}(r,t) + f_k^{neq}(r,t) \tag{20}$$

Here, f_k^{eq} *and* f_k^{neq} are equilibrium and non-equilibrium distribution functions, respectively. The Eq. (20) can be defined as

$$f_k(r,t)_{at\,BCS} = f_k^{eq}(r,t)_{inside\,flow\,domain} + \left(f_k^{eq}(r,t)_{at\,BCS} - f_k^{eq}(r,t)_{inside\,flow\,domain}\right) \tag{21}$$

The details of the discretized boundary conditions for all the lattice arrangement are described elsewhere by the present authors.

3 Results and Discussions

First the numerical simulations are presented for two dimensional lid-driven cavity flows for various values of Reynolds number. The stream lines, vorticity contours, and the velocity profiles are presented for Reynolds numbers of 1,000, 12,500, 20,000 and 30,000. The velocity field presented here for each value of Reynolds number represents the long time solution obtained from transient simulations and it agrees well with the results documented previously [7] for steady state simulations.

3.1 Validity and Convergence Test

The spectral convergence test was conducted by obtaining results using 500 by 500 and 600 by 600 lattices. Figure 3 displays the x component of the velocity profile along the y direction for each grid resolution at Reynolds number of 3,000. The results show that there is no difference between the two grid resolutions. This implies that a 500 by 500 lattice is sufficient to ensure spectral convergence. The results presented for two dimensional lid driven cavity flow are obtained using 500 by 500 grids.

The validation of numerical method has been conducted by comparing the present results with those reported by previous investigators. For two-dimensional lid-driven cavity flow, the results are compared with those obtained by Erturk et al. [7] for Reynolds numbers of 12,500 and 20,000, as shown in Fig. 4. For both Reynolds number our results agree well with Erturk et al. validating the Lattice

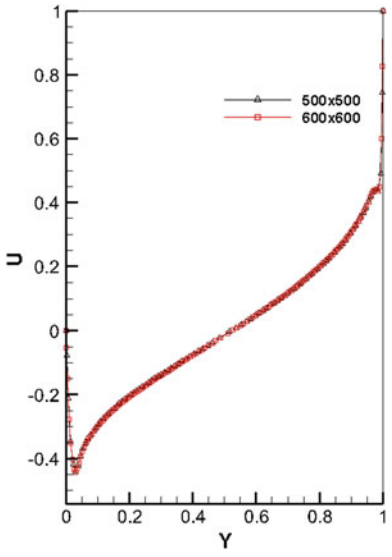

Fig. 3 The x component of the velocity profile along the y direction at x = 0.5 normalized by the speed of the moving lid

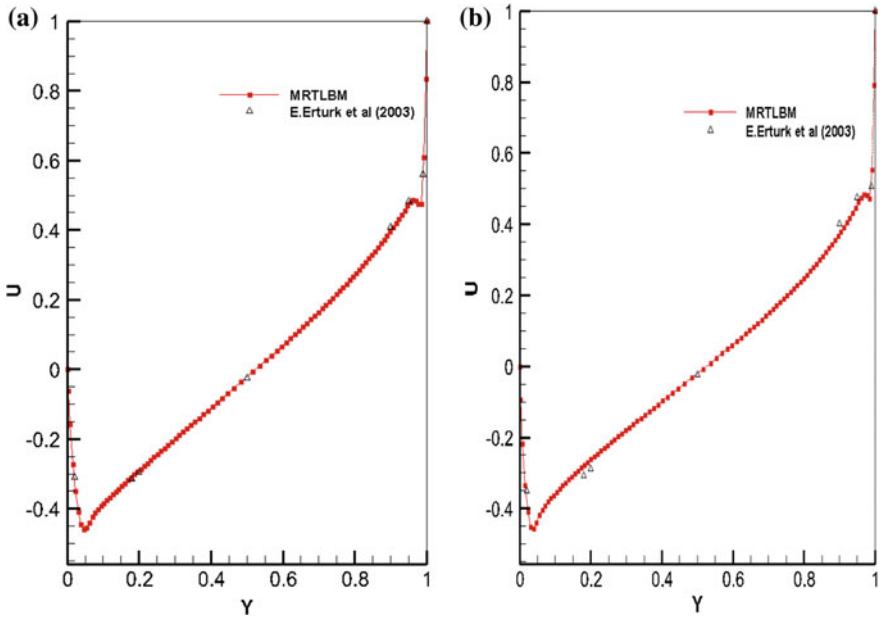

Fig. 4 The x component of the velocity profile along the y direction at x = 0.5 for Re **a** 12,500 **b** 20,000. Our results are displayed by the *red squares* and Erturk's results are displayed by the *black triangles*

Boltzmann method utilized. Figure 5 depicts the x-component of the velocity as a function of y at x = 0.5 for Re = 1,000, 12,500, 20,000 and 30,000. The velocity profiles indicate the presence of a short boundary layer attached to each boundary at top and bottom surfaces. Near the center of the cavity the x-component of the velocity varies linearly with y, as shown in Fig. 5.

The next six figures (Figs. 6, 7, 8, 9, 10, 11) are displaying the streamlines and vorticity contours at various Reynolds number from 10,000 to 30,000. One prevailing feature of the flow is the large primary recirculating vortex rotating in the clockwise direction. The other common feature is the smaller secondary vortices in each corner except the corner the sliding boundary is moving towards. As the Reynolds number increases tertiary vortices form and begin to grow. For the two bottom corners the tertiary vortices form directly in the corners; however, for the top corner the ternary vortex forms on the side boundary away from the sliding boundary. The overall size of the corner eddies including both secondary and tertiary vortices do not vary as much as Re increases, as depicted in Figs. 6, 7, 8 and 9.

For flows at each Re, in the region at the center of the cavity the vorticity gradient is smaller; indicating nearly rigid body rotation. There is a larger vorticity gradient present near the boundaries. The center of the low vorticity region shifts first toward the top right corner as Re increases to 12,500, but returns to nearly the center of the cavity for Re = 20,000. As Re increases to 30,000 the center of the low

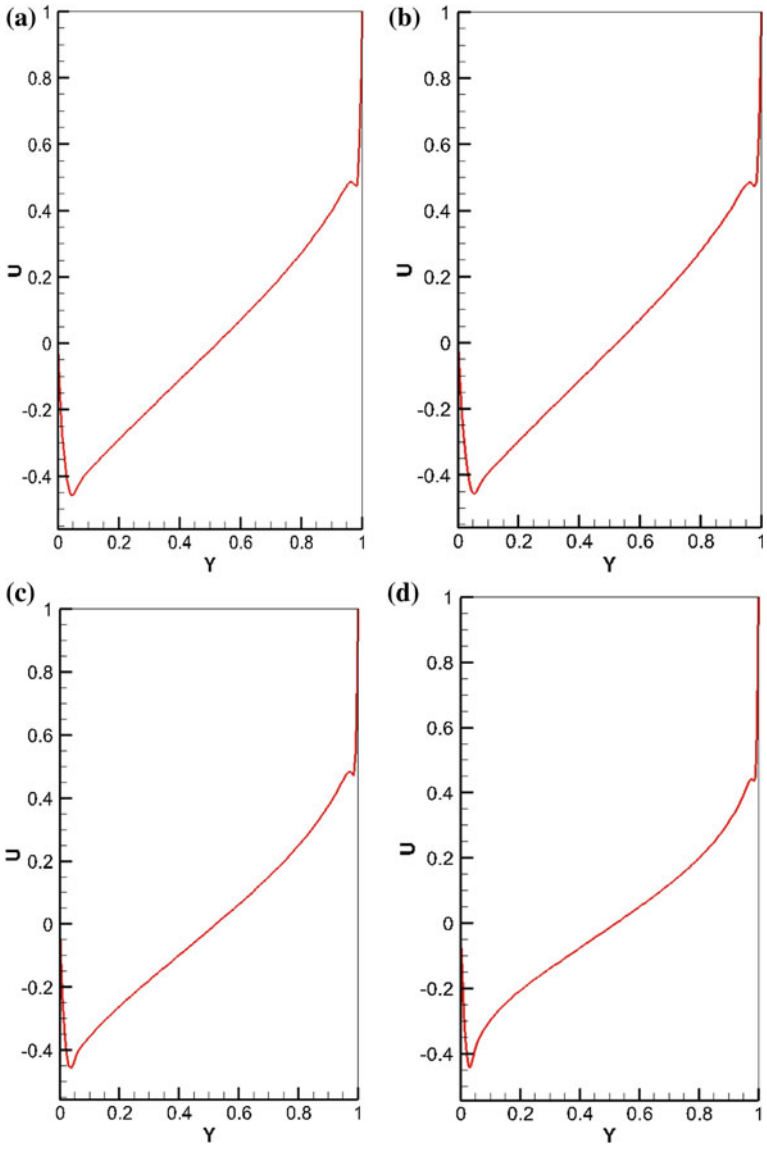

Fig. 5 The x component of the velocity profile along the y direction at x = 0.5 for **a** Re = 10,000 **b** Re = 12,500, **c** Re = 20,000, and **d** Re = 30,000

vorticity gradient region gets much closer to the top right corner. Vorticity contours indicate the complexity of the lid-driven cavity flows.

Next, results are presented for three dimensional lid-driven cavity flows.

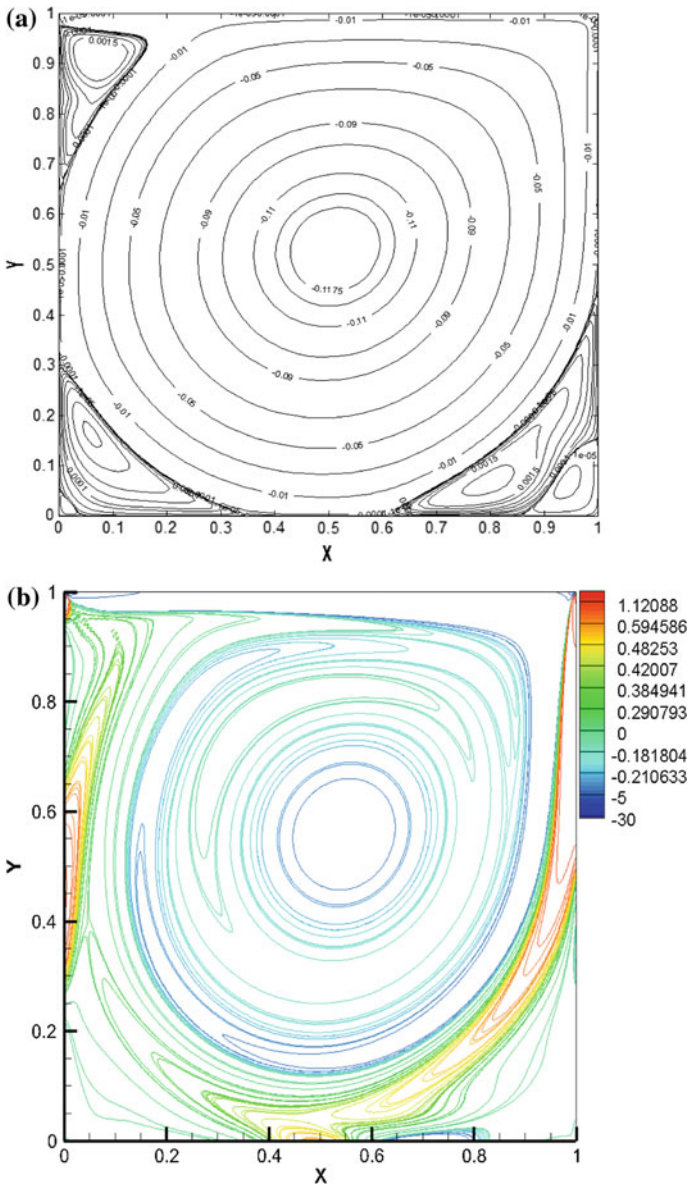

Fig. 6 **a** The streamlines **b** the vorticity contour for Re = 10,000

The x component of the velocity profiles in the y-direction at the center plane are depicted in Fig. 10 for Re = 50 and 500. The velocity of the fluid is measured in units of the wall speed. These profiles are obtained using single relaxation time Lattice Boltzmann method with D3Q15 and D3Q19 lattice arrangements. The velocity profiles obtained by both lattice arrangements agree well for Re = 50, while they

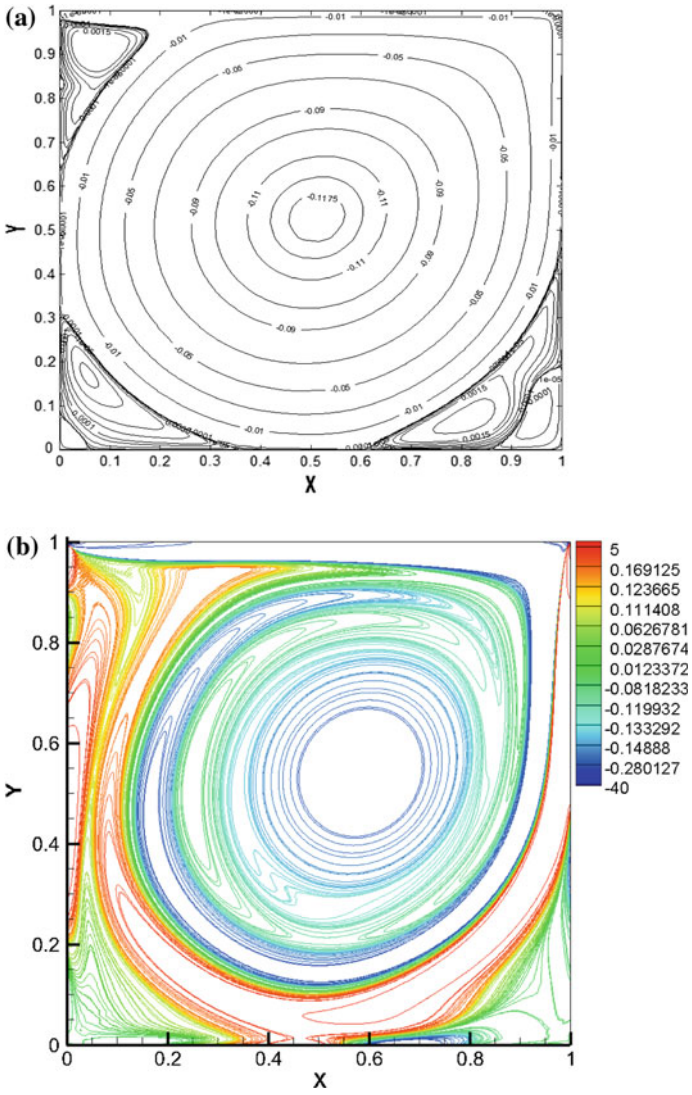

Fig. 7 **a** The streamlines **b** the vorticity contour for Re = 12,500

differs significantly for Re = 500, as depicted in Fig. 8. D3Q19 should provide a more accurate representation of the flow field which is verified by the work of Mei et al. [8]. For D3Q19 lattice arrangements, discretization, utilizing the second order-bounce back approach, for the boundary conditions results in stable and accurate simulation of the flow field up to Re = 800. The uniform grid of 31 × 31 × 16 for Re = 50 and 40 × 40 × 20 for Re = 500 are used for simulations. The x- and y-components of the velocity at various cross-sections are plotted in Fig. 11 for Re = 40. Near the wall the boundary layer type of flow structure is noticed.

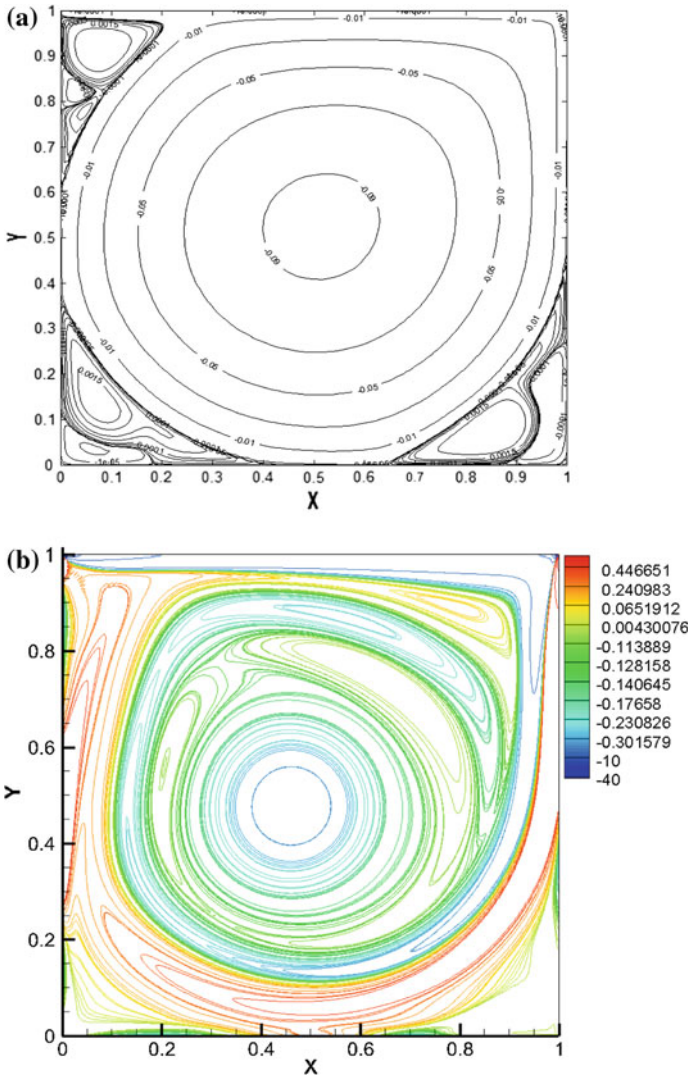

Fig. 8 **a** The streamlines **b** the vorticity contour for Re = 20,000

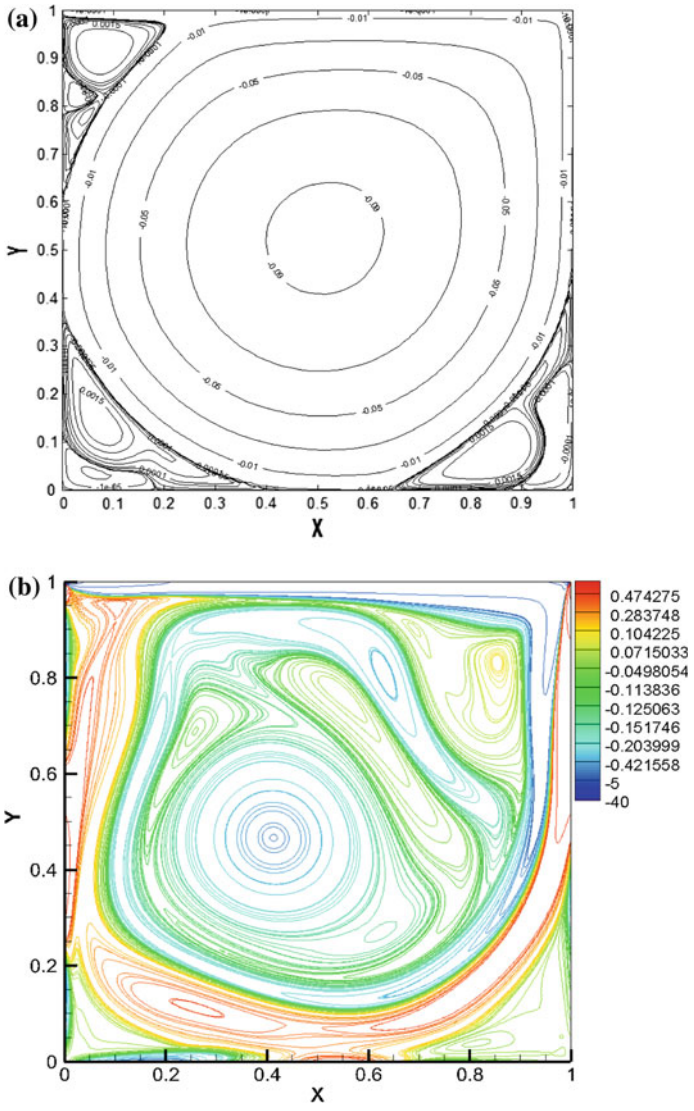

Fig. 9 **a** The streamlines **b** the vorticity contour for Re = 30,000

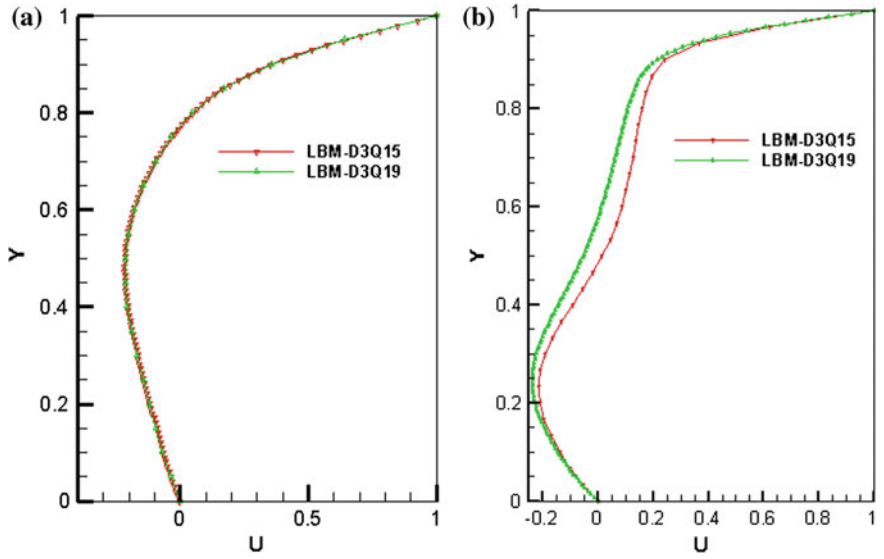

Fig. 10 The x component of the velocity profile along the y direction at the center plane for **a** Re = 50 **b** Re = 500

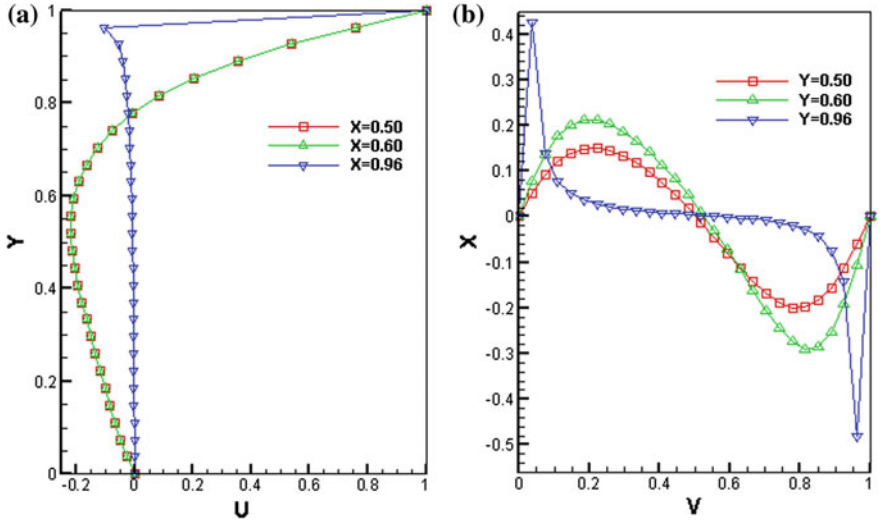

Fig. 11 **a** The x component of the velocity profile along the y direction and **b** the y component of the velocity profile along the x direction at the center plane for Re = 40

4 Conclusion

Two and three dimensional lid-driven cavity flows have been investigated using different arrangements and different forms of Lattice Boltzmann method. Multi relaxation time Lattice Boltzmann method provides accurate results for the two dimensional cavity. Both D3Q15 and D3Q19 lattice arrangements for three dimensional flows are employed with the single relaxation time Lattice Boltzmann method. It has been proven here that LBM can be used as a computational fluid dynamics tool to simulate two and three dimensional steady or transient flows.

Acknowledgments The author, SJA, would like to thank Saudi Arabia government and the College of Engineering at Taibah University—KSA for their support.

References

1. Chai, Z.-H., Shi, B-C., Lin, Z.: Simulating high Reynolds number flow in two-dimensional lid-driven cavity by MRT Lattice Boltzmann method. Chin. Phys. **15**, 1855. doi: 10.1088/1009-1963/15/8/038 (2006)
2. Almalowi, S.J., Oztekin, A.: Flow simulations using two dimensional thermal Lattice Boltzmann method. J. Appl. Math. **2012**, 12 (2012)
3. He Y., Li Q., Wang Y, Tang G.: Lattice Boltzmann Method and its Applications in Engineering Thermo-Physics. Science in China Press, Beijing (2009)
4. Ho, C.-F., Chang, C., Lin, K.-H., Lin, C.-A.: Consistent Boundary Conditions for 2D and 3D Lattice Boltzmann Simulations, vol. 44, no. 2, pp. 137–155. CMES Tech Science Press, Duluth (2009)
5. Hou, S., Zou, Q., Chen, S., et al.: Simulation of cavity flow by the Lattice Boltzmann method. J. Compt. Phys. **118**, 329–347 (1995)
6. Barragy, E., Carey, G.F.: Stream function-vorticity driven cavity solutions using p finite elements. Comput. Fluids **26**, 453–468 (1997)
7. Botella, O., Peyret, R.: Benchmark spectral results on the lid-driven cavity flow. Comput. Fluids **27**:421–433 (1988)
8. Erturk, E., Corke, T.C., Gokcol, C.: Numerical solutions of 2-D steady incompressible driven cavity flow at high reynolds numbers. Int. J. Numer. Meth. Fluids **48**, 747 (2005)
9. Mei, R., Shy, W., Yu, D., Luo, L.-S.: Lattice Boltzmann method for 3-D flows with curved boundary: NASA, ICASE report no. 2002-17 (2002)
10. D'Humieres, D., Ginzburg, I., et al.: Multiple-relaxation-time lattice Boltzmann models in three dimensions. Philos. Trans. R. Soc Lond. A **360**, 437–451 (2002)
11. He, X., Luo, L.-S.: Lattice Boltzmann Model for the Incompressible Navier-Stokes Equation. Plenum Publishing Corporation, New York (1997)
12. Wolfram, S.: Cellular automaton fluids 1: basic theory. J. Stat. Phys. **45,** 471–526 (1986)

Localization of Rotating Sound Sources Using Time Domain Beamforming Code

Christian Maier, Wolfram Pannert and Winfried Waidmann

Abstract The motion of an acoustic source produces a Doppler shift of the source frequency which is dependent on the source's motion relative to the receiver. Some applications in acoustics involve rotating sound sources around a fixed axis in space. For example, the noise emitted by fans is of interest and because of the fast rotation, the sound sources are not easy to locate with the standard delay-and-sum beamforming code. In the time domain approach for stationary sound sources, the delay-and-sum beamforming works with shifting the microphone signals due to their different delays caused by the different distances between the source and the microphones and summing them up. This approach is adapted to a moving source, resulting in time dependent delays. The delays are calculated via an advanced time approach where the time at the receiver is calculated from the emission time τ plus a time dependent delay due to the time dependent distance $r(\tau)$. In contrast to the standard beamforming code, this time domain beamforming code allows to treat rotating sound sources as well as stationary sound sources. In this chapter the differences between the standard delay-and-sum beamforming to the rotating time domain beamforming is shown and examples are presented.

Keywords Fan · Rotating sound sources · Retarded time · Beamforming

C. Maier (✉) · W. Pannert · W. Waidmann
Department of Mechanical Engineering, University of Applied Sciences Aalen, Aalen, Germany
e-mail: Christian.Maier@htw-Aalen.de

W. Pannert
e-mail: Wolfram.Pannert@htw-Aalen.de

W. Waidmann
e-mail: Winfried.Waidmann@htw-Aalen.de

K.Z.K. Shaari and M. Awang (eds.), *Engineering Applications of Computational Fluid Dynamics*, Advanced Structured Materials 44,
DOI 10.1007/978-3-319-02836-1_4

1 Introduction

The sound emitted by moving sound sources such as a flowed airfoil or rotating fan blades are problems of technical interest. Visualising and analysing moving sound sources is much harder in comparison to stationary sound sources. The Doppler-shift and the retarded time due to the movement of the sound source have to be taken into account. In this work a time domain algorithm is presented which can be applied to rotating sound sources which are produced for example by fan blades. The theory is shown and the algorithm is proved with measurements using an acoustic camera at a rotating fan.

The standard Delay-and-Sum beamforming method can be applied in time and frequency domain [1]. However, the method is not suitable for moving sound sources. To compensate the movement of the sound source, special corrections are necessary. For this case the rotation of fans have to be compensated. The pressure field of a moving monopole is derived for a uniform flow in this approach. The approach presented below is original based on [2] and is based on the Delay-and-Sum, beamforming method in the time domain. A method to compensate rotating sound sources in the frequency domain, especially for high resolution beamforming techniques [3], is presented by Pannert [4].

2 Theory

The movement of a point source can be treated with the Greens function approach for solving the inhomogeneous wave equation.

Taking the inhomogeneous wave equation for a stationary source located at $\vec{x}$

$$\frac{1}{c^2}\frac{\partial^2 p'}{\partial t^2} - \Delta p' = q(\vec{x}, t) \tag{1}$$

where $q(\vec{x}, t)$ is a the source distribution, the solution for free space conditions without boundaries for p' can be calculated from an integral formulation

$$p'(\vec{x}, t) = \frac{1}{4\pi}\int_{\mathbb{R}^3} \frac{q(\vec{y}, t - |\vec{x} - \vec{y}|/c)}{|\vec{x} - \vec{y}|} d^3\vec{y} \tag{2}$$

with

$$r = |\vec{x} - \vec{y}| \tag{3}$$

and the retarded time τ

$$\tau = t - |\vec{x} - \vec{y}|/c \tag{4}$$

The signal which was emitted at time τ at a position $\vec{y}$ and is observed at time t at the point $\vec{x}$. For the general source distribution a concrete source distribution can be inserted. The simplest model for a moving monopole is the distribution

$$q(\vec{x}, t) = Q(t)\delta(\vec{x} - \vec{x_s}(t)) \tag{5}$$

With $\vec{x_s}(t)$ as the actual time dependent position and $Q(t)$ as the amplitude of the monopole sound source.

Figure 1 shows the situation for a moving sound source and a fixed observer position. The observer point is the microphone position (at the microphone array).

It is necessary to calculate the distance between sound source and the microphone position for every time step τ_n to calculate the time delay to the observer position [5, 6].

In the retarded time approach, the retarded emission time τ is calculated back from the receiving time t via

$$\tau = t - r(\tau)/c \tag{6}$$

and cannot be calculated analytically in general cases due to the complicated dependence of $r(\tau)$ from τ. It can numerically found as a root of Eq. (7) [6]. Algorithms that treat that problem can be found in [7] or [8].

In the advanced time approach which is applied in this work, the receiver time t can be calculated via

$$t = \tau + r(\tau)/c \tag{7}$$

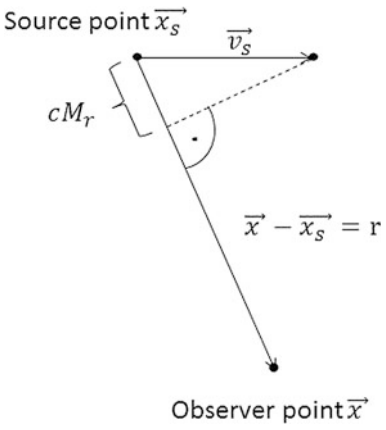

Fig. 1 Movement of the source term to a fix observation point

This is much easier, but results in unequally spaced time samples t_n when using equally spaced time samples τ_n.

In Fig. 2 the situation is shown for a moving source. An emitted signal at the time τ arrives at the observer position $\vec{x}$ at the time t. The speed of sound is c. In the case of a stationary source, the retarded time only depends on the position of the source $\vec{x_s}$. In the case of a moving source it depends on $\vec{x_s}(\tau)$. This time delay is calculated for every time step n

$$\Delta t_n(\tau_n) = t_n - \tau_n = \frac{|\vec{x} - \vec{x_S}(\tau_n)|}{\mathrm{c}}. \tag{8}$$

The condition $\tau_n < t_n$ is always fulfilled for the case that the source term moves with subsonic speed and $\Delta t_n(\tau_n)$ is always positive. Working with these time delays the motion of the source can be compensated in the received microphone signals and the moving source is imaged at a fixed position which corresponds to the position at time $\tau = 0$.

In Fig. 3, the typical set up for investigating a fan with an acoustic camera is shown. It is necessary to compensate the movement of the sound source. To compensate this movement, in this case the rotation of the fan with its blades, it is necessary to shift the time signals of every microphone for every time step at an amount, which is due to the change in distance between the moving source and the selected microphone. These shifted signals are used then to calculate the beam pattern.

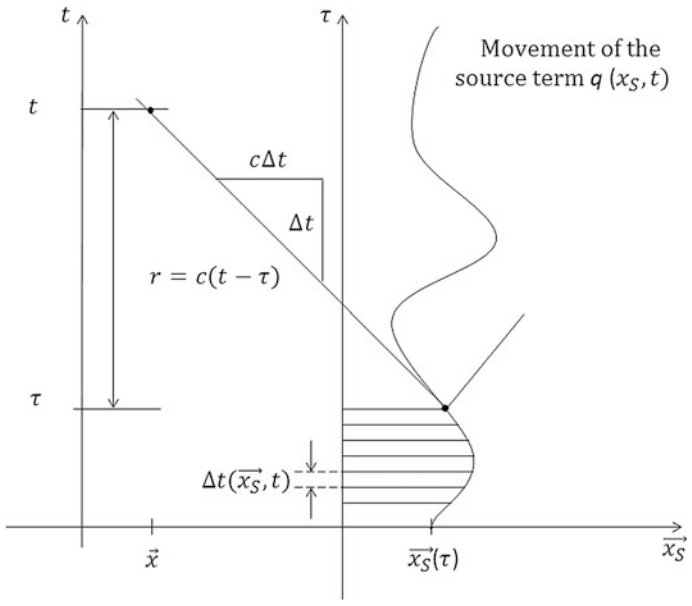

Fig. 2 Retarded time emitted from a moving sound source in the space–time

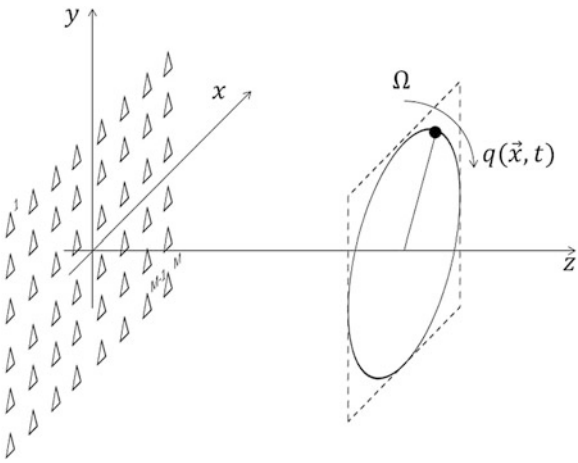

Fig. 3 Microphone array with moving sound source in front of it

In Fig. 4 simulated signals for a rotating source are shown. The pressure signal shows clearly the varying frequency due to the Doppler shift (Fig. 4a). The radial motion of the source is subsonic Fig. 4b shows the spectrum of the microphone signal in (a). The radius at which the sound source rotates is 0.65 m and the frequency of rotation is 100 Hz.

The frequency spectrum (Fig. 4b) shows the peak no longer at the position of 1500 Hz. This is the effect due to the Doppler shift; the peak is now shifted in positive and negative frequency away from the emitted 1500 Hz. Moreover, this frequency spectrum is not symmetric, because the motion between the source and the receiver also has an influence to the amplitude of the signal.

3 Measurements

Software tests with a rotating sound source were carried out to proof the programmed algorithm. This software code treats the rotating beamforming theory explained in the last section. For this tests an artificial rotating sound source was simulated in software, that rotates with 600 rpm on a circle with a radius of 0.3 m around the position $x = 0.2$ m and $y = 0.0$ m out of the middle. The distance between the sound source and the virtual microphone array is $D = 1$ m. In Fig. 5a the rotating monopole can be seen at the middle frequency 2500 Hz at the position x = 0.4 m and y = 0.0 m for a simulation time of 0 s. Figure 5b shows the same monopole sound source after 0.025 s at the position x = 0.2 m and y = 0.2 m. The monopole sound source rotates over the time and can be captured to every desired point of time.

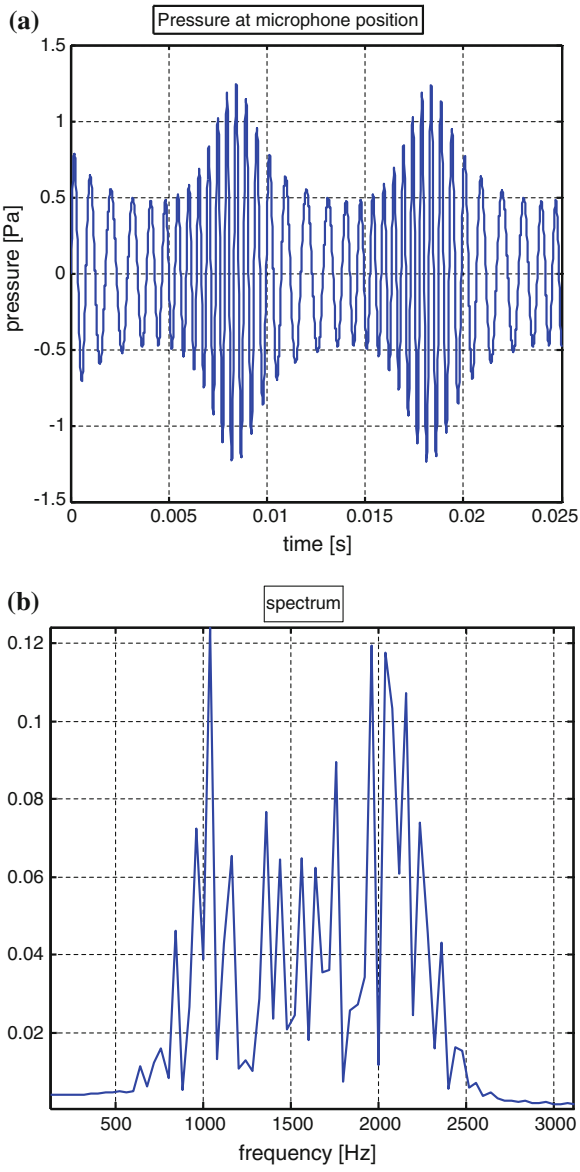

Fig. 4 Received signal from a rotating source. Distance microphone—plane of rotation in distance $D = 1$ m; rotation speed $n = 6000$/min; frequency of the source $f = 1500$ Hz. **a** shows the microphone signal and **b** the spectrum of the pressure signal

4 Results

The algorithm used for the validation is implemented in the acoustic camera. So the analysis can be done and it is possible to compare it to the standard delay-and-sum beamforming. The Delay-and Sum beamforming only locates stationary sound sources and rotating beamforming locates moving sound sources. It also shows a

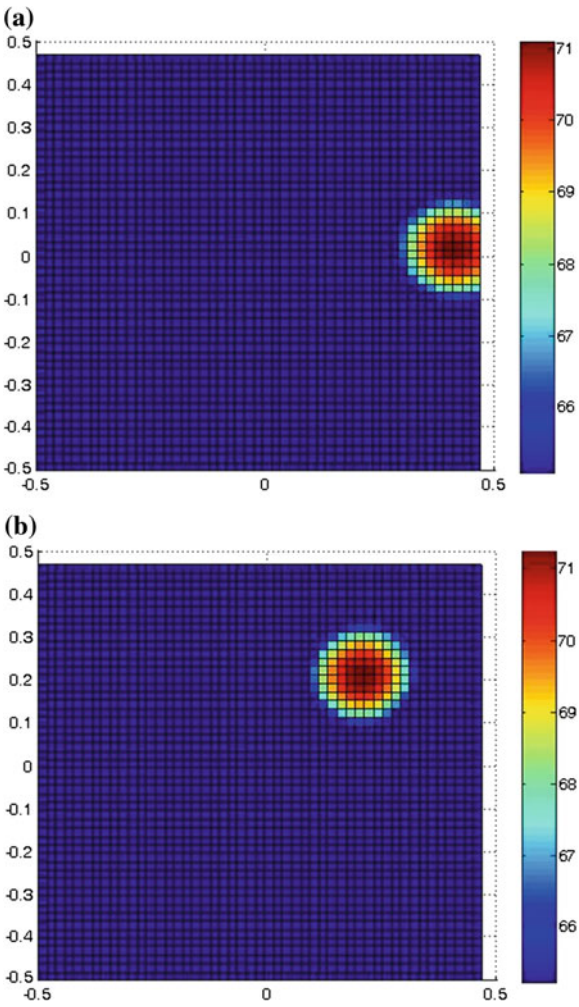

Fig. 5 Virtual software sound source rotating anticlockwise around $x = 0.2$ m and $y = 0.0$ m, **a** at time 0 s and **b** at time 0.025 s

ring shaped distribution of sound sources in the gap between the blades and the wall whereas the rotating beamforming shows the spot shaped sound sources on the blades (Fig. 6).

Figure 7 shows similar beamforming results like Fig. 6, but with the rotation compensation. Opposite to the beamforming version without rotation compensation stationary sound sources should be averaged out whereas the rotating sources are visible and, in this case, they belong to the sound emitted by the blades itself. Beside this the acoustical photo is superimposed with a frozen-image to match the sound sources to the blades of the fan.

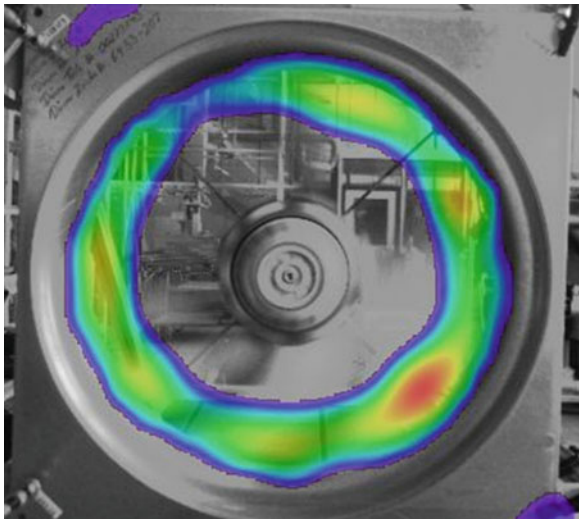

Fig. 6 Analysis of a fan with no rotation compensation. Only the stationary sound sources from the gap between blades and wall are visible

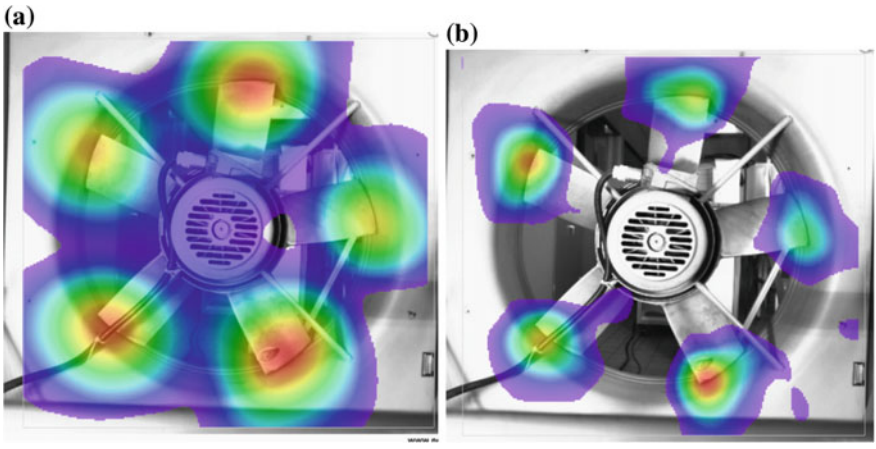

Fig. 7 Analysis with motion compensation. After an alignment of the static optical picture the moving sources at the blade tips are visible. **a** shows the Beamforming plot for 2 kHz and **b** the beamforming plot for 4 kHz

5 Conclusion

The rotating beamforming algorithm is possible to image the stationary sound sources as well as rotating sound sources. In combination with an acoustic camera it is a helpful tool for optimising fan geometries to reduce sound emission.

Moreover, with this algorithm it is possible to locate sound sources at their position on the blades. So it is possible to distinguish between the leading edge and the trailing edge of the blade and study the frequency dependence of the generated noise.

References

1. Christensen, J.J., Hald, J.: Technical Review No.1 2004—Beamforming. Brüel & Kjær Sound &Vibration Measurement A/S. http://www.bksv.com/doc/bv0056.pdf (2004). Accessed 20 Dec 2012
2. Sijtsma, P., Oerlemans, S., Holthusen, H.: Location of Rotating Sources by Phased Array Measurements. National Aerospace Laboratory, Amsterdam (2001)
3. Brooks, T.F., Humphreys, W.M.: A Deconvolution Approach for the Mapping of Acoustic Sources (DAMAS) determined from phased microphone arrays. 10th AIAA/CEAS aeroacoustics conference (2004)
4. Pannert, W.: Rotating beamforming—motion-compensation in the frequency domain and application of High-resolution beamforming algorithms. Report University of Applied Sciences Aalen (to be published in Journal of Sound and vibration in 2013)
5. Ehrenfried, K.: Skript zur Vorlesung Strömungsakustik (Script to the teaching lesson Fundamentals of Aeroacoustics). Mensch & Buch Verlag. http://vento.pi.tu-berlin.de/STROEMUNGSAKUSTIK/SCRIPT/nmain.pdf (2004). Accessed 20 Dec 2012
6. Brentner, K.S.: Numerical algorithms for acoustic integrals—the devil is in the details. 2nd AIAA/CEAS Aeroacoustics Conference (17th AIAA Aeroacoustics) http://citeseerx.ist.psu.edu/viewdoc/summary?doi=10.1.1.45.6510 (1996). Accessed 20 Dec 2012
7. Brentner, K.S., Holland, P C.: An efficient and robust method for computing quadrupole noise. 2nd international aeromechanics specialists. http://www.ingentaconnect.com/content/ahs/jahs/1997/00000042/00000002/art00007 (1995). Accessed 20 Dec 2012
8. Advanced Rotorcraft Technology, Inc.: Kirchhoff code—a Versatile CAA Tool. NASA SBIR phase I final report, contract NAS1-20366 (1995)

Effects of the Surrounding Fluid on the Dynamic Characteristics of Circular Plates

Manuel Gascón-Pérez and Pablo García-Fogeda

Abstract Recently for acoustical and spatial applications such as antennas or very light panels the influence on the dynamic characteristics of a structure surrounded by a fluid of low density has been studied. Thus, it has been shown that the air effect for the Intelsat VI C–B transmit reflector with a diameter of 3.2 m and weighting only 34.7 kg decreases the first modal frequency by 20 % with respect to the value in vacuum. It is important then, in the development of these light and large structures to have a method that estimates the effect that the surrounding fluid will have on the natural frequencies of the structure. In this way it can be avoided to test the structure in a vacuum chamber which for a large antenna or panel can be difficult and expensive. A method for the determination of the effect of the surrounding fluid on the dynamic characteristics of a circular plate has been developed. After the modes of the plate in vacuum are calculated in an analytical form, the added mass matrix due to the fluid loading is determined by a boundary element method (BEM). The BEM used is of circular rings so the number of elements to obtain an accurate result is very low. An iteration procedure for the computation of the natural frequencies of the couple fluid-structure system is presented for the case of the compressibility effect of air. Comparisons of the present method with various experimental data and other theories show the efficiency and accuracy of the method for any support condition of the plate.

1 Introduction

The influence of the surrounding fluid on the dynamic characteristics of structures has been well known for many years. References [1–8] provide good examples. However most of these works were more concerned with underwater applications,

M. Gascón-Pérez · P. García-Fogeda (✉)
Department of Aircrafts and Aerospace Vehicles, ETSIAE, UPM,
28040 Pza. Cardenal Cisneros, 3, Madrid, Spain
e-mail: pablo.garciafogeda@upm.es

K.Z.K. Shaari and M. Awang (eds.), *Engineering Applications of Computational Fluid Dynamics*, Advanced Structured Materials 44,
DOI 10.1007/978-3-319-02836-1_5

such as the sonar of a submarine and therefore the surrounding fluid was considered a liquid (negligible compressibility effects).

Spacecraft structures located in the payload compartment are submitted to an intense vibration during the launcher lift-off. These high vibration loads excite structures of a satellite such as communication reflectors, solar arrays or thin payload panels. With the advent of new technologies and the appearance of structures made of sandwich composite materials, their mass has decreased considerably thus producing an increase in the acceleration levels and the influence of the surrounding fluid on the structure has an important influence that can damage sensitive parts of the structure and the electronic equipment attached to it. For this reason, light aerospace structures are subjected to intense acoustic test in large reverberant chambers and reliable analysis methods are needed during its design to guarantee that the structure comply with all the acoustic requirements of the launcher, hence the qualification test campaign can be successfully afforded.

One effect need to be considered in order to obtain the structure dynamic response under acoustic loads due to the presence of air, is the effect of the structure surrounding fluid that transmit to the exterior domain the pressure waves generated by the plate vibration.

Fluid presence affects considerably its natural frequencies and normal modes, even in the case of light fluid, like air, when the structures are constructed with composite sandwich panels. References [9–13] provide good examples of it. Besides, these structures, mainly rectangular and circular plates, were modeled as "baffled", embedded in an infinitely rigid plane. Acoustic radiation of baffled rectangular plates has been studied in great detail obtaining the acoustic pressure distribution employing the Rayleigh integral equation. Only recent research has been focused on unbaffled plates.

There are mainly two methods capable to determine the acoustic behavior of complex geometries, Boundary Element Methods (BEM) and Finite Element Methods (FEM). The latter is a powerful tool to model general structures of arbitrary shapes and is extensively employed in structural analysis. However, the application of this method to acoustical problems necessitates the discretization of the surrounding acoustic media. This leads at high frequencies or unbounded fluid domains to algebraic systems of large size which increases the computational cost and in addition, the Sommerfield radiation condition is very difficult to impose at the external mesh boundary. To overcome the previous limitations, the BEM is an alternative method to study problems on fluid-structure interaction in which the fluid is unbounded. This method is adopted in this work to solve the integral formulation of the Helmholtz equation for the pressure field, combined with a normal mode analysis of the structural response. In this paper, the response of an unbaffled circular plate with arbitrary boundary conditions immersed in a fluid is calculated. The BEM has been used to compute the pressure jump produced by the loads generated by the plate own vibrations. This method is based on Kirchhoff's integral formulation of the Helmholtz equation for the pressure field that uses an elemental solution that satisfies the Sommerfield radiation condition. The integral equation is solved by means of a collocation technique and the finite part of the singular integral is obtained

analytically. The generalized forces due to the fluid loading are determined using the vacuum modes of the plate, obtained analytically, as base functions of the structural displacement. An iteration procedure has been developed to calculate the natural frequencies of the plate surrounded by a compressible fluid.

2 Problem Formulation

The deformation equation of the plate submerged in the fluid is [14]:

$$D\nabla^4 w(r,\theta,t) + \rho_p h \frac{\partial^2 w}{\partial t^2} = \Delta p(r,\theta,t) \tag{1}$$

With $D = \frac{E \cdot h^3}{12(1-\upsilon^2)}$ the flexural rigidity, E the elasticity modulus of material, h the plate thickness, υ the Poisson modulus and ρ_p the material density of the plate

Δp is the pressure jump across the plate, $\Delta p = p_i - p_e$ where p_i and p_e are the pressure on the upper and lower sides of the plate surface.

This pressure distribution can be obtained by solving the wave equation on the fluid domain given by

$$\frac{1}{a_\infty^2}\frac{\partial^2 p}{\partial t^2} - \Delta p = 0 \tag{2}$$

Application of the momentum equation at the surface of the plate yields the boundary condition

$$\frac{\partial p}{\partial z} = -\rho_\infty \frac{\partial^2 w}{\partial t^2} \text{ at } z = \pm 0 \tag{3}$$

At large distances from the plate, the Sommerfield radiation condition has to be satisfied. For the determination of the natural frequencies of the coupled system fluid-structure it will be assumed that the motion is harmonic for both the fluid and the structure

$$w(r,\theta,t) = \tilde{w}(r,\theta)\cdot e^{-i\omega t} \quad \text{and} \quad p(r,\theta,z,t) = \tilde{p}(r,\theta,z)\cdot e^{-i\omega t} \tag{4}$$

The deformation of the plate, when coupled with the fluid, will be expressed as a linear combination of the normal modes of the plate in vacuum

$$\tilde{w}(r,\theta) = \sum_m \sum_n W_m^n(r)\cdot \cos(m\theta)\, q_m^n \tag{5}$$

where q_m^n are the weight coefficients that indicate the contribution of the mode W_m^n to the deformation of the plate. They are unknowns and for the problem of the

computation of the natural frequencies of the coupled system fluid-structure need not to be calculated.

The functions $W_m^n(r)$ have the general expression [14]

$$W_m^n(r) = \left[A_m^n J_m(\beta_m^n r) + B_m^n I_m(\beta_m^n r)\right] \tag{6}$$

where J_m and I_m are Bessel and modified Bessel functions of mth order, A_m^n and B_m^n are unknown constants that depend of the mode order mn and of the boundary conditions of the plate edge and β_m^n is a parameter that depends on the dynamic characteristics of the plate and provides the frequencies of the plate in vacuum.

Once the assumption of harmonic motion is made Eq. (2) is expressed as

$$\Delta\tilde{p} + k^2\tilde{p} = 0 \tag{7}$$

where $k = \frac{\omega}{a_\infty}$ is the wave number.

If at the boundary condition, Eqs. (3), (4) and (5) are substituted, it is obtained

$$\begin{aligned} \left.\frac{\partial\tilde{p}(r,\theta,z)}{\partial z}\right|_{z=0} &= \rho_\infty\omega^2\tilde{w}(r,\theta) \\ &= \rho_\infty\omega^2\sum_n\sum_m W_m^n(r)\cdot\cos(m\theta)\,q_m^n \quad \text{at} \quad z=0 \\ &\quad \text{and} \quad 0<r<a \end{aligned} \tag{8}$$

where a is the radius of the plate

Then the pressure modulus can also be expanded in harmonic functions of θ

$$\tilde{p}(r,\theta,z) = \sum_m\sum_n P_m^n(r,z)\cdot\cos(m\theta) \tag{9}$$

and Eq. (8) can now be expressed as

$$\left.\frac{\partial P_m^n}{\partial z}\right|_{z=0} = \rho_\infty\omega^2 W_m^n(r)\,q_m^n \quad 0\le r\le a \tag{10}$$

By substitution of Eq. (9) at (7) the differential equation for the pressure mode P_m^n is

$$\frac{\partial^2 P_m^n}{\partial z^2} + \frac{\partial^2 P_m^n}{\partial r^2} + \frac{1}{r}\frac{\partial P_m^n}{\partial r} - \frac{m^2}{r^2}P_m^n + k^2 P_m^n = 0 \tag{11}$$

Applying Green's identities taking into account the Helmholtz equation for the pressure field and the Green`s function associated to that equation, the following integral equation for the pressure mode $P_m^n(r,z)$ is obtained [15, 16], for the case $m = 0$

$$P_m^n(r,z) = -\frac{1}{4\pi}\int_0^a \Delta P_m^n(\sigma)\frac{\partial}{\partial z}\left(\frac{e^{ik\sqrt{(r-\sigma)^2+z^2}}}{\sqrt{(r-\sigma)^2+z^2}}\right)2\pi\sigma d\sigma \tag{12}$$

And applying the boundary condition Eq. (10) it is obtained

$$\rho_\infty \omega^2 W_m^n(r)\, q_m^n = -\frac{1}{4\pi}\int_0^a \Delta P_m^n(\sigma)\frac{\partial^2}{\partial z^2}\left(\frac{e^{ik\sqrt{(r-\sigma)^2+z^2}}}{\sqrt{(r-\sigma)^2+z^2}}\right)_{z=0} 2\pi\sigma d\sigma \tag{13}$$

$$\text{Let} \quad \mathrm{K}(r-\sigma,z,k) = \frac{\partial^2}{\partial z^2}\left(\frac{e^{ik\sqrt{(r-\sigma)^2+z^2}}}{\sqrt{(r-\sigma)^2+z^2}}\right)\Bigg|_{z=0} \tag{14}$$

be the Kernel of the integral equation. The solution to Eq. (13) will be obtained approximately by applying a collocation method.

The plate is divided into N circular rings. Be $\Delta r_j = r_{j+1} - r_j$ the thickness of the jth ring. At each ring a circle at the radii $\bar{r}_j = \frac{r_{j+1}+r_j}{2}$ is placed where Eq. (13) is fulfilled.

Then this equation can be expressed for the collocation method

$$\rho_\infty \omega^2 W_m^n(\bar{r}_j)\, q_m^n = -\frac{1}{2}\sum_{i=1}^{N} \Delta P_m^n(\sigma_i)\int_{r_i}^{r_{i+1}} \mathrm{K}(\bar{r}_j-\sigma,0,k)\sigma d\sigma \tag{15}$$

So finally we end up with a linear system of algebraic equations to determine the pressure mode jump at each ring $\Delta P_m^n(\sigma_i)$.

To improve the stability of the collocation method the N rings are divided so all of them have the same area. Therefore the values of r_i are obtained in such a manner that the area of each ring be equal to $\frac{\pi a^2}{N}$.

When evaluating the integral

$$\Lambda_{ij} = -\frac{1}{2}\int_{r_i}^{r_{i+1}} \mathrm{K}(\bar{r}_j-\sigma,0,k)\sigma d\sigma \tag{16}$$

special care must be taken of the singularity when $\sigma \to \bar{r}_j$. To avoid this singularity the Kernel function is split into a regular part and a singular part

$$\mathrm{K} = \mathrm{K}_r + \mathrm{K}_s \tag{17}$$

The singular part is integrated analytically and the regular part is integrated numerically.

The singular part is

$$K_s = -\frac{1}{R^3} - \frac{k^2}{2R} \tag{18}$$

where $R = \sqrt{(r-\sigma)^2 + z^2}$

And

$$K_r = K - K_s \tag{19}$$

Be Λ_{sij} the value of the singular integral

$$\Lambda_{sij} = \frac{1}{2}\int_{r_i}^{r_{i+1}} \left(\frac{1}{R^3} + \frac{k^2}{2R}\right)\sigma d\sigma$$

Taking Mangler's principal value [17] is obtained that

$$\Lambda_{sij} = -\frac{1}{4}\left[\frac{\bar{r}_j}{(r_{i+1}-\bar{r}_j)^2} + \frac{\bar{r}_j}{(\bar{r}_j - r_i)^2}\right] + \frac{k^2}{4}\left[2\bar{r}_j + \bar{r}_j\, Ln\left[\left(\frac{r_{i+1}}{\bar{r}_j} - 1\right)\left(1 - \frac{r_i}{\bar{r}_j}\right)\right]\right] \tag{20}$$

Thus finally the system of Eq. (15) is expressed as

$$\rho_\infty \omega^2 W_m^n(\bar{r}_j)\, q_m^n = \sum_{i=1}^{N} (\Lambda_{sij} + \Lambda_{rij}) \Delta P_m^n(r_i) \quad j = 1....N \tag{21}$$

where Λ_{rij} is the numerical integration of K_r.

In matrix form this system of equations can be expressed as

$$[\Lambda_{ij}]\{\Delta P_m^n(r_i)\} = \rho_\infty \omega^2 \{W_m^n(\bar{r}_j)\} \tag{22}$$

So finally the modal pressure jump is given by

$$\{\Delta P_m^n(r_i)\} = \rho_\infty \omega^2 [\Lambda_{ij}]^{-1} \{W_m^n(\bar{r}_j)\} \tag{23}$$

The next step is to solve Eq. (1). After substitution of Eqs. (4), (5) and (9) this equation is expressed as

$$D\tilde{\nabla}^4 W_m^n(r) - \rho_p h \omega^2 W_m^n(r) = \Delta P_m^n(r) \tag{24}$$

where $\tilde{\nabla}^4$ is a differential operator of the form $\tilde{\nabla}^4 = \left(\frac{d^2}{dr^2} + \frac{1}{r}\frac{d}{dr} - \frac{m^2}{r^2}\right)^2$

By multiplying Eq. (24) by the mode W_u^v and integration over the surface of the plate, the following system is obtained

$$\left[[K] - \omega^2 \left([M] + [M_F] \right) \right] \{q\} = \{0\} \tag{25}$$

where the elements of the three matrices are

$$K_{mu}^{nv} = D \left\lfloor \nabla^4 W_m^n \right\rfloor [\Delta S] \left\{ W_u^v \right\} \tag{26}$$

$$M_{mu}^{nv} = \rho_p h \left\lfloor W_m^n \right\rfloor [\Delta S] \left\{ W_u^v \right\} \tag{27}$$

$$M_{Fmu}^{nv} = \rho_\infty \left\lfloor W_m^n \right\rfloor \left[\left[\Lambda_{ij} \right]^{-1} \right]^T [\Delta S] \left\{ W_u^v \right\} \tag{28}$$

where $[\Delta S]$ is a diagonal matrix containing the surface area of each ring. Since in this method all the rings have the same area, this matrix can be expressed as $[\Delta S] = \frac{\pi a^2}{4N} [I]$.

It should be noted that the matrix $[M_F]$ for compressible cases will depend on the natural frequencies through the wave number $k = \frac{\omega}{a_\infty}$. Thus, the solution to Eq. (25) for the determination of the natural frequencies ω becomes a nonlinear eigenvalue problem since $[M_F(\omega)]$. An iteration procedure needs to be used to obtain the natural frequencies of the system. The iteration scheme developed is as follows:

1. First the natural frequencies of the system are computed assuming that the surrounding fluid is incompressible. For this case the matrix $[M_F]$ is independent of ω and the computation of the natural frequencies becomes a standard method of computation of eigenvalues.
2. From the solution of incompressible case a set of N frequencies $\omega_{j\,incomp.}$ can be obtained for the coupled incompressible fluid-structure system.
3. For each frequency of step 2. A wave number is accordingly defined and a mass matrix $\left[M_F\left(k_j\right)\right]$ can be calculated.
4. For other values of the wave number k the fluid mass matrix can be obtained by linear interpolation between each two computed matrices $\left[M_F\left(k_j\right)\right]$ and $\left[M_F\left(k_{j+1}\right)\right]$.
5. Starting with the lowest wave number available k_1, the natural frequencies of the system $[-\omega^2 ([M] + [M_F(k_1)]) + [K]] \{q\} = \{0\}$ are computed. Let the lowest natural frequency computed be ω_1^i. If $\left|\frac{\omega_1^i}{a_\infty} - k_1\right| < \varepsilon$, where ε is a small number, then we proceed to the computation of the next natural frequency of the system. If the above condition is not satisfied then step five is repeated taking now a new mass matrix for the fluid close to the wave number $\frac{\omega_1^i}{a_\infty}$ of the set obtained at step four.

For each frequency the above procedure converges in two or three iterations. It should be noted that for a compressible fluid the natural frequencies are obtained one by one while for incompressible fluid all of them are obtained at the same time. Once the natural frequencies of the coupled fluid-structure are determined, the normal modes can be computed by determining the eigenvector $\{q_i\}$ and expressed as a linear combination of the normal modes of the structure in vacuum.

3 Results

For the case of a plate immersed in water (incompressible fluid), shown in Tables 1, 2 and 3 the frequencies f_{lm}^n and f_{vm}^n are compared with the results of other authors with f_{lm}^n the frequency associated to the mode W_m^n of the plate in contact with water, and f_{vm}^n the corresponding frequency in vacuum both in Hz.

It can be observed that for the first mode the natural frequencies are similar, and for the second and third mode the results present differences between the three cases. This can be due to the different boundary conditions, because in the cases of

Table 1 Natural frequencies for free edge circular aluminum plate (in vacuum and liquid), radius $a = 7.5$ cm, thickness $h = 3$ mm

	Present method	Gallego-Juárez [7]		Amabili-Kwak [1]	Vacuum frequency f_{v0}^n
		Exp	Calc		
f_{l0}^1	566	565	527	667	1,181
f_{l0}^2	3,908	2,700	2,684	3,336	5,045
f_{l0}^3	10,018	6,533	6,875	8,351	11,515

Table 2 Natural frequencies for clamped circular aluminum plate (in vacuum and liquid) radius $a = 7.5$ cm, thickness $h = 3$ mm

	Present method	Lamb [5]
f_{l0}^0	500	500
f_{v0}^0	1,327	1,327

Table 3 Natural frequencies for free edge circular steel plate (in vacuum and liquid), radius $a = 17.5$ cm, thickness $h = 2$ mm

	Present method	Amabili-Dalp-Sant [3]	Amabili-Kwak [1]	Vacuum frequency f_{vm}^n
f_{l0}^1	65.4	67.8	78	147
f_{l0}^2	475	314	393	627

Table 4 Natural frequencies for clamped circular aluminum plate (in vacuum and liquid), radius $a = 10$ cm, thickness $h = 3$ mm

f_{v0}^0	f_{l0}^0	f_{v0}^1	f_{l0}^1	f_{v0}^2	f_{l0}^2
746.2	247.5	2,905	2,116	6,508	5,472

Table 5 Natural frequencies for a free edge circular aluminum plate (in vacuum and liquid), radius $a = 10$ cm, thickness $h = 3$ mm

f_{v0}^1	f_{l0}^1	f_{v0}^2	f_{l0}^2	f_{v0}^3	f_{l0}^3
664.5	283.4	2,838	2,121	6,477	5,497

Gallego-Juárez [7] and Amabili-Kwak [1], the plate is situated in a hole of a rigid wall that separates the fluid on the lower and upper sides of the plate, and even in the case of Gallego-Juárez [7] the fluid domain is not infinite because is immersed in a tank of finite dimensions. In this case the results for the present method coincides with those obtained by Lamb [5].

It can be observed that for the first mode the natural frequencies are similar, and for the second mode the results present differences between the three cases.

Tables 4 and 5 show the results for a clamped and free edge aluminum plate, radius $a = 10$ cm, thickness $h = 3$ mm, of the frequencies in liquid and in vacuum. It can be observed the high reduction of the frequency with respect to its value in vacuum that for the first mode is about three times, and for the second and third mode this reduction decreases.

For the case of the plate immersed in air (compressible fluid), two boundary conditions are considered: clamped plate and free edge plate. The plate is made of two skins of carbon fiber and a core of honeycomb with the following properties:

Radius $a = 1$ m. Thickness $h = 1$ cm. Elasticity modulus $E = 9 \times 10^9$ Pa.

Density $\rho_p = 139\ \frac{\text{kg}}{\text{m}^3}$. Poisson modulus $\upsilon = 0.3$.

In Figs. 1 and 2, the fluid mass coefficient as function of the wave number $k = \frac{\omega}{a_\infty}$ are presented. The coefficient is defined as $C_{mf} = \frac{M_f}{4\pi a^3 \rho_\infty}$ where M_f is the diagonal term of the fluid mass matrix that is responsible of the reduction of the frequency with respect to the vacuum value. C_{mf} presents a maximum for intermediate values of the wave number k and for high values tends to reach a zero value, so this fluid mass coefficient can be interpreted as the function transfer that gives the effect of the fluid over the plate (jump pressure) associated to the deformation mode of the plate. This fluid mass coefficient is constant with the radius plate a, because the fluid mass matrix is proportional to the cube of the radius of the plate.

Figures 3, 4, 5 and 6 show the frequency parameter which is defined as $C_\omega = \omega \cdot a^2 \sqrt{\frac{\rho_m}{D}}$, as function of the radius of the plate a, for the modes 1 and 2.

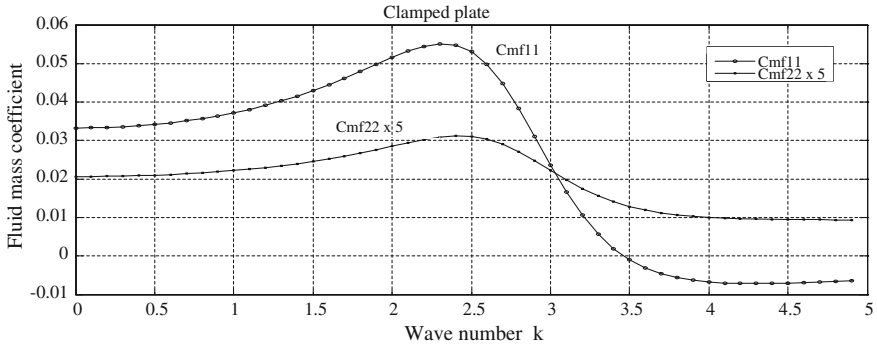

Fig. 1 Fluid mass coefficient versus reduce frequency k for a clamped plate

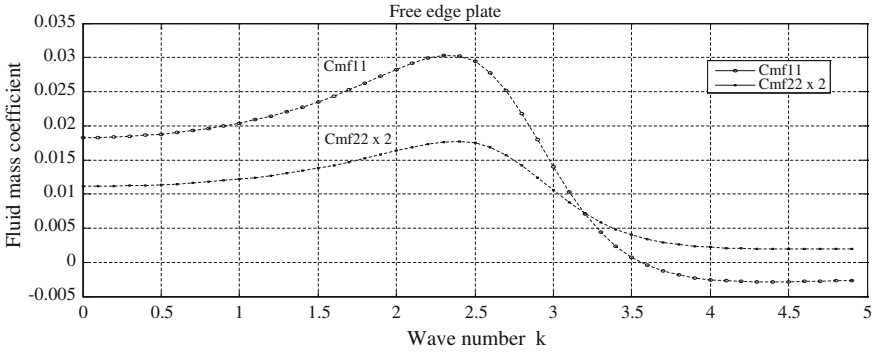

Fig. 2 Fluid mass coefficient versus reduce frequency k for a free edge plate

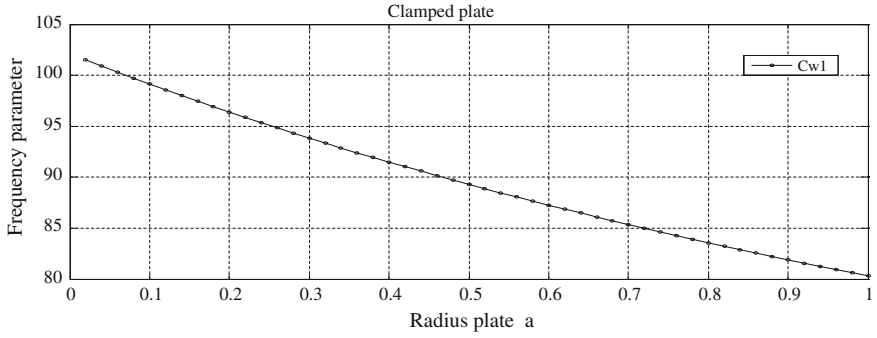

Fig. 3 Frequency parameter $C_{\omega 1}$ versus radius of the plate for a clamped plate

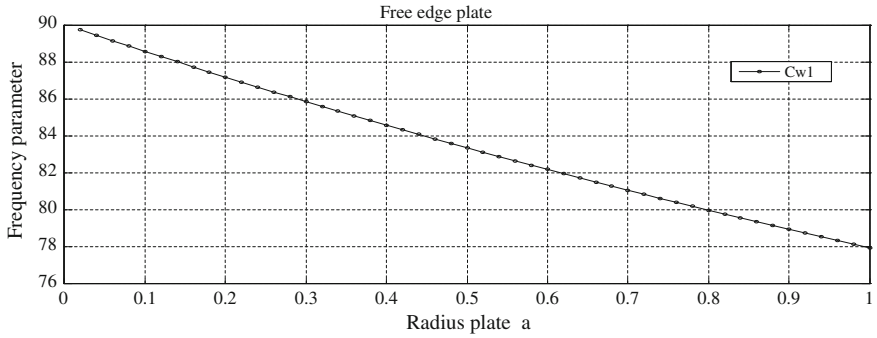

Fig. 4 Frequency parameter $C_{\omega 1}$ versus radius of the plate for a free edge plate

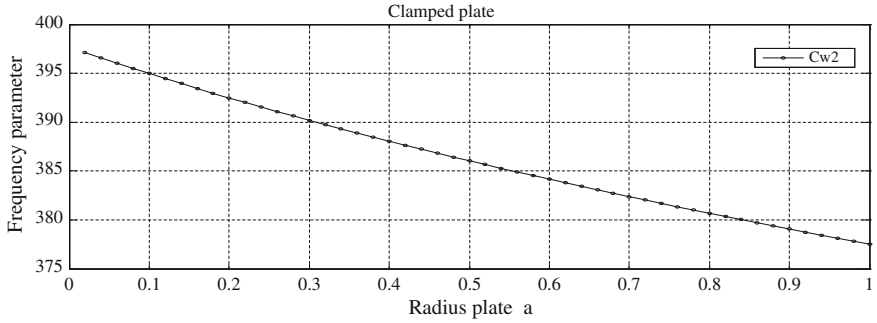

Fig. 5 Frequency parameter $C_{\omega 2}$ versus radius of the plate for a clamped plate

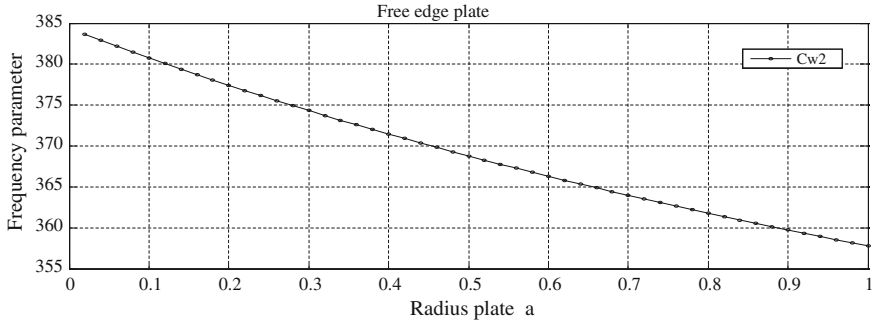

Fig. 6 Frequency parameter $C_{\omega 2}$ versus radius of the plate for a free edge plate

Figures 7, 8, 9 and 10 show the frequency parameter which is defined as C_{ω}, as function of the relative density $\frac{\rho_{\infty}}{\rho_{\infty 0}}$ of the fluid, with $\frac{\rho_{\infty}}{\rho_{\infty 0}} = 0$ for vacuum, for the modes 1 and 2.

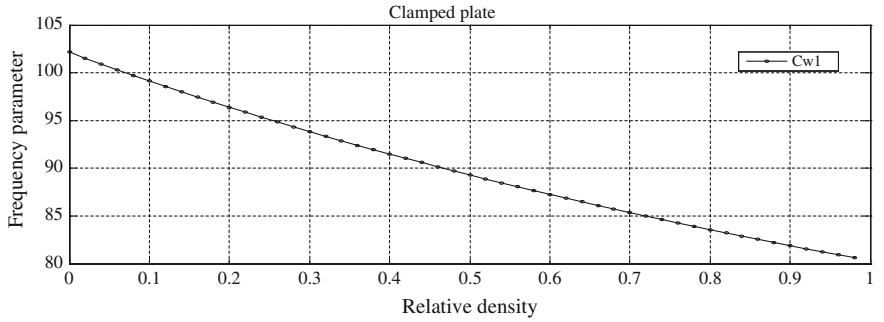

Fig. 7 Frequency parameter $C_{\omega 1}$ versus relative density for a clamped plate

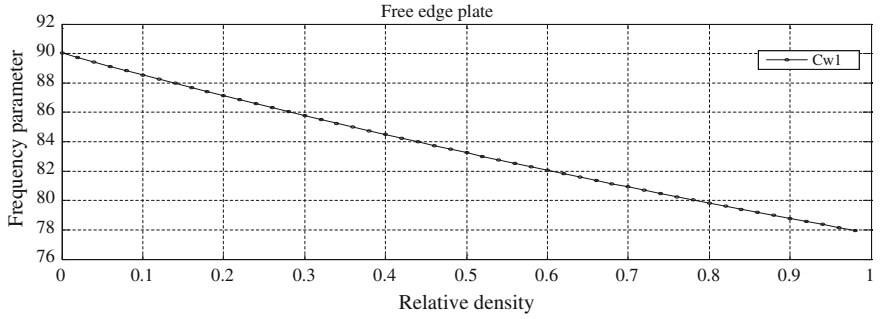

Fig. 8 Frequency parameter $C_{\omega 1}$ versus relative density for a free edge plate

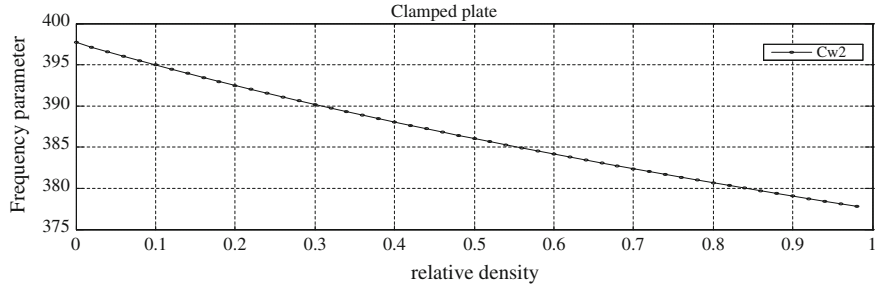

Fig. 9 Frequency parameter $C_{\omega 2}$ versus relative density for a clamped plate

Tables 6 and 7 illustrate the results of the natural frequencies (in Hz) in air (incompressible and compressible) and in vacuum for the same clamped and free edge plate.

It can be observed that compressibility effects modify about a 2 % the frequencies of the plate with respect to the incompressible fluid assumption. For the first order mode however the influence of compressibility is negligible.

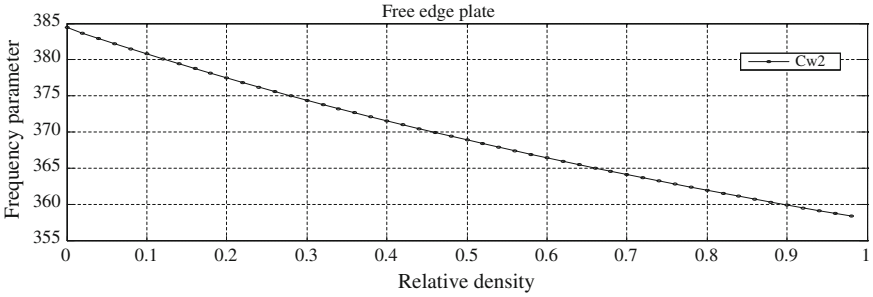

Fig. 10 Frequency parameter $C_{\omega 2}$ versus relative density for a free edge plate

Table 6 Natural frequencies for a clamped circular honeycomb plate (in vacuum and air incompressible and compressible), radius $a = 1$ m, thickness $h = 1$ cm

f^0_{v0}			$k=0$ f^0_{a0} $k\neq 0$		f^1_{v0}	$k=0$ f^1_{a0} $k\neq 0$		f^2_{v0}
				$k=0$ f^1_{a0} $k\neq 0$				
39.6	31.59	31.37	154.1	146.82	144.57	345.3	333.16	339.4

Table 7 Natural frequencies for a free edge circular honeycomb plate (in vacuum and air incompressible and compressible), radius $a = 1$ m, thickness $h = 1$ cm

f^1_{v0}	$k=0$ f^1_{a0} $k\neq 0$		f^2_{v0}	$k=0$ f^2_{a0} $k\neq 0$		f^3_{v0}	$k=0$ f^3_{a0} $k\neq 0$	
35.30	30.75	30.63	150.6	140.79	136.52	343.7	332.46	337.10

4 Conclusions

A method has been presented for the computation of the natural frequencies of a circular plate surrounded by a compressible fluid of arbitrary density. This method is valid for any type of support condition of the plate and use as input modes those calculated analytically for the vacuum case. The method has been validated with existing tests and with other numerical methods for the cases where compressibility of the fluid is negligible in particular for the case that the fluid is water. In the case of air and light structures, the reduction in frequency has a considerable effect and must be considered. The compressibility effects does not affect very much the results obtained in comparison with respect the incompressible case.

References

1. Amabili, M., Kwak, M.K.: Free vibrations of circular plates coupled with liquids: revising the Lamb problem. J. Fluids Struct. **10**, 743–761 (1996)
2. Amabili, M., Pascualini, A., Dalpiaz, G.: Natural frequencies and modes of free edge circular plates vibrating in vacuum or in contact with liquid. J. Sound Vib. **188**(5), 685–699 (1995)

3. Amabili, M., Dalpiaz, G., Santolini, C.: Free vibration of free edge circular plates immersed in water. In: Proceedings of the 12th International Modal Analysis Conference, vol. 2251, p. 349 (1994)
4. Kwak, K.: Vibration of circular plates in contact with water. J. Appl. Mech. **58**(2), 480–483 (1991)
5. Lamb Horace, F.R.S.: On the vibrations of an elastic plate in contact with water. Proc. R. Soc. Lond. **98**, 205–216 (1920)
6. McLachlan, N.W.: The accession to inertia of flexible discs vibrating in a fluid. Proc. Phys. Soc. Lond.**44**, 546 (1932)
7. de Montero Espinosa, F., Gallego Juárez, J.A.: On the resonance frequencies of water loaded circular plates. J. Sound Vib. **94**(2), 217–222 (1984)
8. Peake, W.H., Thurston, E.G.: The lowest resonant frequency of a water-loaded circular plate. J. Acoust. Soc. Am. **26**, 166–168 (1954)
9. Atalla, N., Nicolas, J., Gauthier, C.: Acoustic radiation of an unbaffled vibrating plate with general elastic boundary conditions. J. Acoust. Soc. Am. **99**(3), 1484–1495 (1966)
10. Berry, A., Guyader, J.L., Nicolas, J.: A general formulation for the sound radiation from rectangular, baffled plates with arbitrary boundary conditions. J. Acoust. Soc. Am. **88**(6), 2792–2802 (1990)
11. Fowler, J., Lagerquist, N., Leve, H.: Effect of air in modal tests. In: Proceedings of the 5th International Modal Analysis Conference, London (1987)
12. Iglesia, F., García Fogeda, P., López Díez, J., et al.: Effects of the surrounding fluid on the dynamic characteristics of rectangular plate. Mach. Vib. **5**, 52–61 (1996)
13. Lomas, N.S., Hayek, S.I.: Vibration and acoustic radiation of elastically supported rectangular plates. J. Sound Vib. **52**(1), 1–25 (1977)
14. Leissa, A.W.: Vibration of plates, NASA SP 160. U.S. Government Printing Office, Washington DC (1969)
15. Junger, M.C., Feit, D.: Sound, structures and their interaction. M.I.T Press, Cambridge (1972)
16. Skudrzyk, E.: The Foundations of Acoustics. Springer-Verlag, New York (1971)
17. Mangler, K.W.: Improper Integrals in Theoretical Aerodynamics. Aeronautical Research Council, London (1952)

CFD Modelling of the Coanda Based Thrust Vectoring Nozzle

A. Suñol, D. Vucinic and S. Vanlanduit

Abstract The paper presents the CFD study of a Coanda-effect based nozzle, developed within the European FP7 project ACHEON. The ACHEON nozzle is able to provide a directional thrust without any movement of mechanical parts, by utilizing the Coanda effect to divert a jet from the symmetry axis. The deviation of the jet produces an oriented thrust vector due to the existence of a perpendicular component to the main propulsive direction. The studied nozzle is envisaged to be applied to UAVs. The directional thrust control—its deviation from the symmetry axis—is achieved by the relative mass flow variations between the two inlet jets. The geometry of the nozzle forces the resulting jet to follow the desired trajectory, thus by controlling in this way the thrust direction exerted by the nozzle. The influence of the selected parameters on the control of the thrust direction has been studied using CFD. In particular, the dependency of the thrust change in respect to the inlet conditions is analysed for different scenarios, with special focus on the thrust magnitude and its direction. The following parameters affecting the flow field of the nozzle have been studied: (a) the ratio of inlet velocities, (b) the Reynolds number at the throat and (c) the geometrical ratio throat/cylinder. Significant dependences between the identified parameters have been observed.

List of Symbols

ACHEON	Aerial Coanda High Efficiency Orienting-jet Nozzle
CFD	Computational Fluid Dynamics
c_T	Thrust coefficient
D_{th}	Throat diameter
HOMER	High-speed Orienting Momentum with Enhanced Reversibility
j	Mass velocity
k	Turbulent kinetic energy
p	Static pressure
q	Dynamic pressure

A. Suñol (✉) · D. Vucinic · S. Vanlanduit
Vrije Universiteit Brussel, Brussels, Belgium
e-mail: anna.sunyol.jimenez@gmail.com

K.Z.K. Shaari and M. Awang (eds.), *Engineering Applications of Computational Fluid Dynamics*, Advanced Structured Materials 44,
DOI 10.1007/978-3-319-02836-1_6

r	Radius
Re	Reynolds number
s	Throat slot
S	Inlet surface
SST	Shear Stress Transport model
SA	Spallart–Almaras model
T	Thrust force
v	Flow velocity
ε	Turbulent dissipation rate
μ	Dynamic viscosity
ρ	Flow density
θ_T	Thrust angle
θj	Separation point

1 Introduction

The ACHEON nozzle is a HOMER nozzle (High-speed Orienting Momentum with Enhanced Reversibility [1–4]). This nozzle is designed to provide directional control without the movement of mechanical parts, taking advantage of the geometry of the nozzle to divert the jet to the desired direction due to the Coanda effect. The Coanda effect is the tendency of a fluid to adhere to a curved surface because of the reduced pressure caused by the high velocities [5]. There is a recent interest of using the aerodynamic effects as control elements, avoiding consequently moving parts and electronic circuits. The principles utilized for creating controllable elements are relying on the fluid behaviour, and are named Fluidic elements. Fluidic elements are based on the (a) jets interaction, (b) the Coanda effect or (c) the vortex element arising in the jet transition from a laminar to a turbulent regime [5]. The ACHEON nozzle characteristics are based on the first two above mentioned effects: jet interaction and Coanda effect. Newman's theory [4] was applied during the conceptual design of the ACHEON nozzle, where the Coanda adhesion to a curved surface is explained as the direct consequence of the forces equilibrium present in the fluid. Higher jet velocities create a lower pressure region, which creates a tendency to attach the fluid stream to the nearest wall. If the wall is curved, the centrifugal forces take over by acting in the opposite direction in respect to the pressure forces. As the jet comes from the slot, the pressure present in the contact region with the curved wall increases—adverse pressure gradient, and gradually equates to the ambient pressure. When the pressure has reached and equals the value of the pressure force and the centrifugal force, the jet detaches [2, 4]. Taking into account these conclusions, a cylindrical surface is selected for the ACHEON geometry. By varying the inlet conditions, and thus the pressure of the jet, the angle of detachment is expected to change, and this effect would provide the necessary control for the jet deviation. Consequently, the ACHEON nozzle is conceived as an analogic fluidic element, rather than as a digital

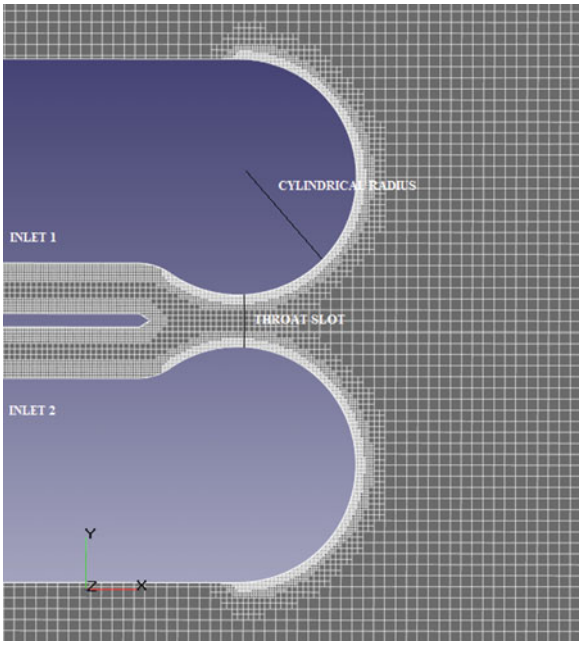

Fig. 1 ACHEON geometry and mesh

fluidic element, providing a range of possible thrust directions. Figure 1 shows the selected geometry for the ACHEON nozzle. The second aerodynamic effect on which the ACHEON nozzle relies is the interaction between two jets. From the literature study [2], it was concluded that, due to entrainment, two parallel jets tend to mix and behave similarly to a single jet after passing through transient phase, and flowing through the converging and a merging regions. The jet with higher momentum tends to entrain the one with lower momentum, due to its lower pressure.

The presented research aims to set the basis for the study of the controllability of the ACHEON nozzle, defined as the ability to deviate the direction of the thrust resulting from the variation of the inlets conditions. In this paper, the resulting thrust force and its direction are computed for the different, systematically selected scenarios. The parameters affecting the behaviour of the jet are identified, and their influence is investigated. From literature, the parameters to study are: the Reynolds number at the throat [6], which is controlled by the mean velocity at the inlets; the Reynolds number along the cylindrical surface, which is controlled by the ratio of velocities at the inlets; and the ratio slot/radius of the cylinder [2, 4].

2 Numerical Scheme

In each simulation, solely one of the parameters is varied, aiming to study the isolated influence for each analysed parameter. The varied parameters are the mean mass velocity, calculated by Eq. (1), the mass velocity ratio and the geometrical

Table 1 Numerical parameters applied

Boundary conditions	
Inlets	
Mean normal mass velocity (kg/m^{2}s)	20, 30, 45, 60, 123
Mass velocity ratios	1, 1.33, 1.8, 2.5
Turbulence intensity (%)	10
Initial conditions (transient analysis)	
Velocity, temperature, turbulence	0
Physical processes	
Turbulence modelling	k-ε, SST and SA
Numerical scheme	
Implicit/explicit	Implicit
CFL number	3
Spatial discretization	2nd order forward

ratio s/R. The CFD calculations were conducted using the Flow Vision software [7]. Table 1 shows the numerical parameters applied in this study. Due to the complexity of modelling the fluidic effects involved, it becomes important that the numerical scheme is carefully setup. An existing specific study of the Coanda effect on a cylindrical surface has been taken as reference, which involves the development of an analytical description of the attached flow [8] and the computational study, based on grid size and turbulence models applied [9]. Because the geometry of the nozzle is close to be 2D, the use of 2D CFD model can be justified. The negative pressure gradient, which the boundary layer is facing, has a major influence in locating the point of the jet detachment. Consequently, a fine grid is applied for the walls of the ACHEON nozzle, and more specifically, for the cylindrical walls parts. The selected mesh, shown in Fig. 1, is the one which provides mesh-independence on thrust in magnitude and direction. In [9], the selected numerical scheme solves the viscous sub-layer to accurately predict the separation point. In the calculations performed in this research, a cell size of 6.25 mm (y+ value depending on the simulated scenario) provides independence of results, only varying 1.25 % if using a coarser mesh.

The turbulent model applied for the simulations plays a major role. Literature shows the importance of correctly predicting the Coanda effect, especially on high curvature walls [10–13]. Traditional k-ε model shows a highly sensitive behaviour, failing on the prediction of the detachment point. The effect of streamline curvature is a known mechanism for failure of isotropic models [14]. The k-ω model is more accurate simulating the near wall layers, but fails for the flows with pressure induced separation [14]. Both Spalart–Allmaras (SA) and Shear Stress Transport (SST) model have been found in a good agreement with the experimental data coming from the circulation control simulations [11], which involves similar aerodynamic effects such as high curvature, Coanda effect and entrainment. In order

to select the turbulent model, simulations based on k-ε, SA and SST k-ω turbulent models were performed and the results were compared.

$$\bar{J} = j_{i1} + j_{i2} = \rho_{i1} v_{i1} + \rho_{i2} v_{i2} \tag{1}$$

3 Influence of Ratio of Inlet Velocities, Reynolds Number and Geometrical Ratio s/R

At the throat of the nozzle, both jets interact and merge, following a similar behaviour as a single jet. The jet with higher momentum entrains the one with lower momentum. Consequently, the difference of velocity of both jets affects the deflection of the jet. Different numerical simulations have been performed applying identical mean mass velocity (20 kg/m^{2}s), identical geometrical ratio s/R(0.37) and different mass velocity ratios (1, 1.33, 1.8 and 2.5).

The Reynolds number at the throat, represented in Eq. (2) is one of the important parameters affecting the physics of the ACHEON nozzle. The Reynolds number has a large influence on the ratio of centrifugal and radial pressure forces and the energy of the boundary layer. Numerical simulations imposing same ratio of velocities but different mean mass velocities ($\bar{J}$) were performed. The non-dimensional parameter c_T, defined in Eq. (3), is utilized for comparison of the inlet velocities and the thrust obtained. Different numerical simulations have been performed applying different mean mass velocity (20, 30, 45, 60 and 123 kg/m^{2}s), identical geometrical ratio s/R (0.37) and identical mass velocity ratios (1.33).

The last considered parameter was geometrical. The ratio s/R influences the behaviour of the jet, as mentioned in [2]. In order to acquire a qualitative knowledge of the influence on the generated thrust force, simulations of geometries with different combinations of the ratio s/R were conducted. A variation in the dimension s would induce changes in the Reynolds number at the throat which, as already proved, has an influence on the magnitude and direction thrust. In order to avoid influences on the Reynolds number at throat, geometries with radius of 80, 110 and 122 mm and a constant throat of 46 mm were considered. Two effects were expected. On the one hand, if conditions at the throat are maintained, a larger diameter of the cylinder implies a lower negative pressure gradient, as represented by the Bernoulli's equation of continuity (Eq. 4). A lower adverse pressure implies a delay of the detachment of the jet, which leads to a higher deviation of the jet from the symmetry axis, and thus a larger angle of thrust force. On the other hand, a lower s/R ratio implies a lower difference of pressure of the jet near the throat, as a consequence of combining Bernoulli's equation and Bernoulli's equation of continuity, which results in Eq. (5) [15]. A lower difference of pressure at the throat implies a lower Coanda effect and consequently moving further the detachment point. Due to the advance of the detachment point, the deviation of the thrust from the symmetric axis is higher. As a result of these two effects, a higher radius should

Table 2 Simulated scenarios

Mass flow ratio influence simulations	
Mean normal mass velocity (kg/m^{2}s)	20
Mass velocity ratios (–)	1, 1.33, 1.8, 2.5
Geometrical ratio s/R (–)	0.37
Reynolds number influence simulations	
Mean normal mass velocity (kg/m^{2}s)	20, 30, 45, 60, 123
Mass velocity ratios (–)	1.33
Geometrical ratio s/R (–)	0.37
s/R ratio influence simulations	
Mean normal mass velocity (kg/m^{2}s)	20
Mass velocity ratios (–)	1.33
Geometrical ratio s/R (–)	0.575, 0.43 and 0.37

involve a higher jet deviation. To validate this, different numerical simulations have been performed applying identical mean mass velocity (20 kg/m^{2}s), different geometrical ratio s/R (0.575, 0.43 and 0.37) and identical mass velocity ratios (1.33).

The different scenarios simulated are defined in Table 2.

$$Re = \frac{\rho v D_{th}}{\mu} \tag{2}$$

$$c_T = \frac{T}{q_i S_i} \tag{3}$$

$$\frac{dp}{dr} = \rho \frac{v^2}{r} \tag{4}$$

$$p = p_\infty - \frac{\rho v^2 s}{R} \tag{5}$$

4 Results

The simulation of the ACHEON nozzle with geometrical ratio s/R 0.37, mean mass velocity of 30 kg/m^{2}s and mass velocity ratio 1.3 agree well in terms of jet angle with the same simulation published in [9]. As predicted from literature a difference in mass flows creates the desired entrainment and diverts the jet from the symmetry axis. The ratio 1.25 at mean mass flow of 20 kg/m^{2}s, the lowest analysed, already induces a 25° thrust angle. Consequently, the nozzle sensitivity is high. Figure 2 shows the jet deflection at different mass velocity ratios. It is significant to mention that the direction of the jet is not the same as the direction of the thrust. In the considered

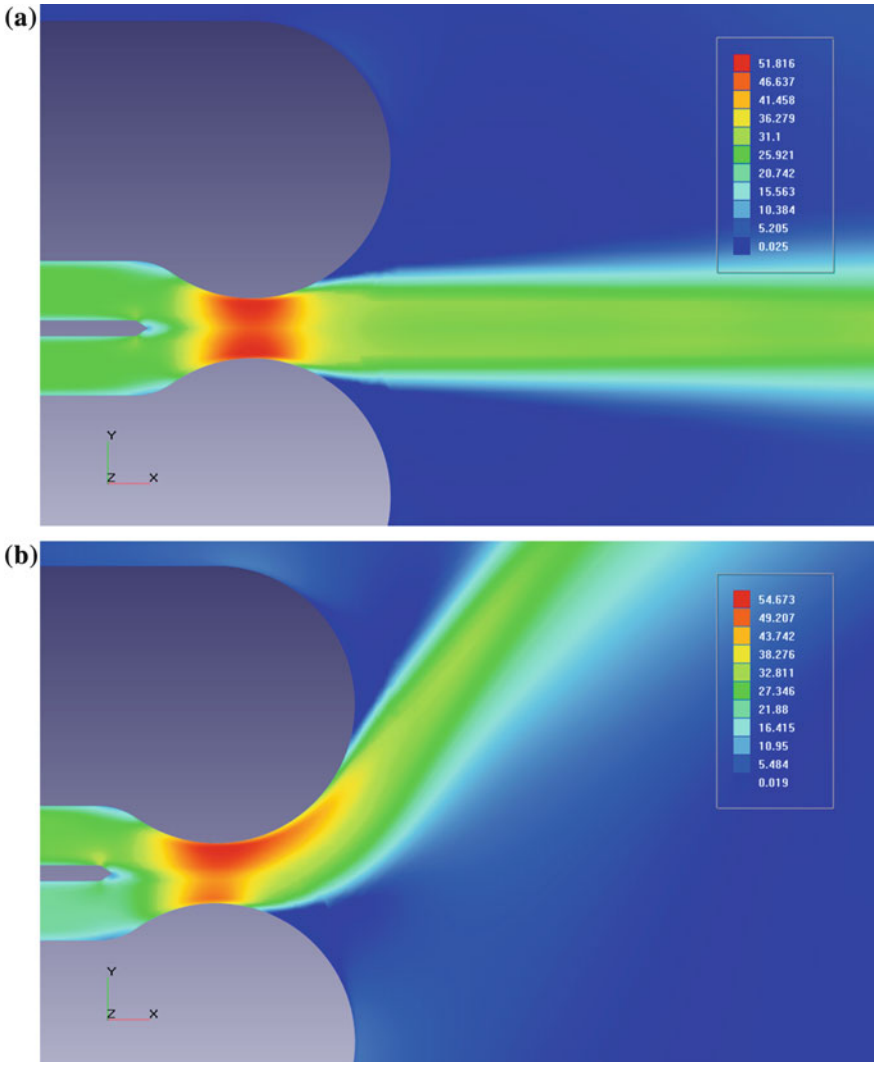

Fig. 2 Influence of ratio of inlet velocities represented by the velocity map (m/s). Respectively, **a** 1, **b** 1.33, **c** 1.8 and **d** 2.5 at 20 kg/m^{2}s

scenarios (ratios of inlet velocities from 1 to 5), the magnitude of force is reduced until a 10 % compared to the symmetric conditions; and a vertical jet provides a thrust direction of 45°. The reason of this difference is that the force exerted by the jet is not just the momentum at the throat but also the distribution of pressure on the cylindrical walls, which has a major influence on the total force direction.

As predicted from literature, the results show a clear disagreement between SA-SST and k-ε models, while SA and SST models show similar results. The angle

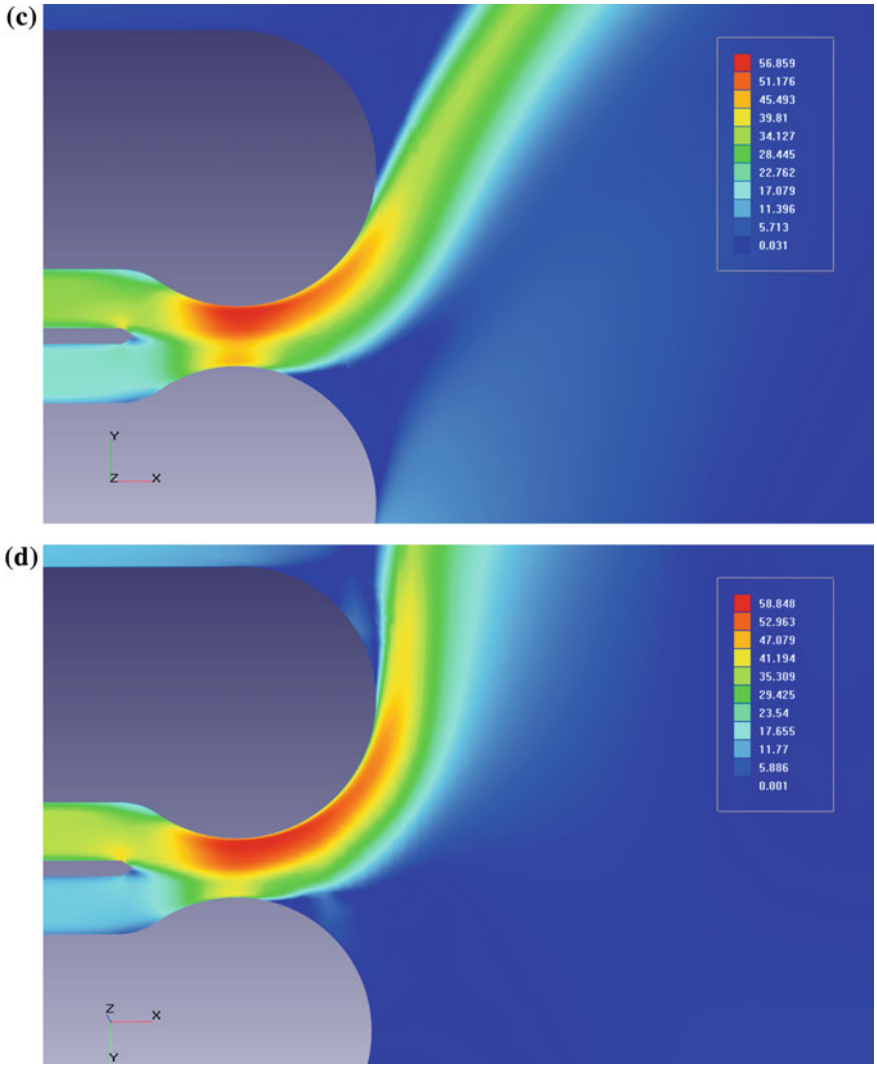

Fig. 2 (continued)

of detachment has been calculated from the pressure distribution on the cylindrical surface as the point where the pressure on the wall is the same as the pressure outside the jet, and represented in Fig. 3 for a mean mass flux of 30 kg m/s at inlets and a ratio of inlet velocities of 1.33. The x axis of the graph represents the angular distance from the throat. Due to a lower computational time, the SA model was selected.

Regarding the influence of Reynolds number at throat, a severe dependence is found. At higher Reynolds, the detachment is delayed, while the angle of the thrust

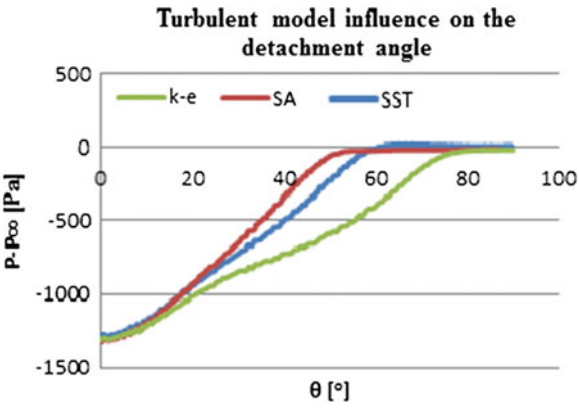

Fig. 3 Influence of turbulent model on the detachment angle

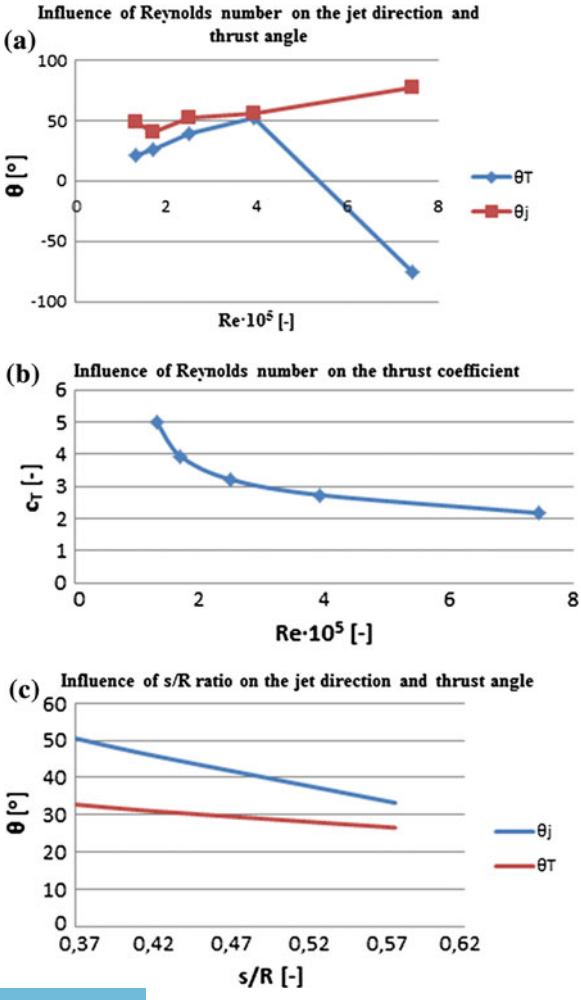

Fig. 4 Graphical representation of the influence of the variables on the thrust magnitude and angle. **a** Influence of Reynolds number on the angle of detachment and the angle of thrust, **b** Influence of Reynolds number on the thrust coefficient, **c** Influence of s/R ratio on the angle of detachment and the angle of thrust

is significantly increased. The increase of the angle of detachment is not proportional to the increase of the angle of thrust force (Fig. 4a). The delay of the angle of separation is explained considering that a more turbulent boundary layer involves that the separation occurs later. The increase of the angle of thrust is explained by the increase of pressure force, due to higher velocity. As the pressure is negative, the jet creates a suction force on the wall, providing a perpendicular component and decreasing the force in x direction. Consequently, as a result of the horizontal component of the suction force, a higher Reynolds number at throat also involves lower thrust coefficients (Fig. 4b).

Finally, considering the influence of the geometric ratio s/R, Fig. 4c shows that at larger radius of the cylinder, the detachment point is postponed as expected, as a consequence of the lower adverse pressure. At the same time, the results show an increase of the angle of thrust with the increase of radius, but significantly lower than the increase of the angle of detachment. This difference in the mentioned increase can be explained by the decrease of pressure at the throat, which implies lower centrifugal forces at the wall and, consequently, less flow deviation.

5 Conclusions

The influence of the main parameters which affect the deflection and thrust of the nozzle has been investigated computationally. The studied parameters are: Reynolds number at the throat, ratio of velocities at the inlets and the geometric ratio R/s. The main conclusions resulting from the performed simulations are:

- High sensitivity to a difference in inlet mass flows, a 1.33 mass flow ratio already produces a 25° thrust angle.
- High influence of the turbulence model in the computational results. The k-ε model is proved to be not adequate to model the flow separation, both from literature and obtained results, while SST and SA model agree well.
- Since SST and SA models agree well and SA is computationally faster since it is a one equation model, SA is found to be the most appropriate turbulence model.
- High dependence on Reynolds number at throat. At higher Reynolds the angle of the thrust is significantly increased, due to a more energized boundary layer. In addition, the thrust coefficient decreases with higher Reynolds numbers at throat.
- Larger s/R ratios imply lower jet angles, thus increasing the radius imply higher sensitivity.

As part of the future research of the ACHEON project, an experimental validation will be performed. A PIV experiment in the whole plane of symmetry of the ACHEON nozzle is envisaged. The principal difficulty of PIV to study the whole model is on how to visualize the inner part of the nozzle, as the material of the model must be optically accessible. A similar study has already been conducted at VUB labs, during the study of Upper Human Airways [16]. A negative model was

prototyped applying Stereo-lithography. This negative model was put into a mould and transparent liquid silicone (Silicone Elastomer Sylgard 184) was casted, covering half of the model. After the curing process, the negative model was removed, obtaining a half transparent model of the nozzle. The process was repeated, obtaining two halves of the prototype. A finishing process was needed, in order to obtain a good accuracy after the re-assembly and to assure the desired surface quality [17]. Such model was employed for a PIV study, which utilized water as fluid. In a PIV experiment which measures an inner flow, the material used must match the index of refraction of the fluid, avoiding refraction and reflection of the laser sheet as it passes through the material. Since the working fluid will be air for the ACHEON experimental set up, another material must be selected.

In order to minimize the time required for the setup, an open fluid flow circuit is envisaged. Seeded gas will be accumulated in a container, and two blowers will direct the flow in the nozzle. The size of the model will be maintained by obtaining the complete kinetic and dynamic similarity [18].

Acknowledgments The presented work in this paper was performed as part of the Aerial Coanda High Efficiency Orienting-jet Nozzle (ACHEON) project, supported by European Commission through the 7th Framework Programme, and which is gratefully acknowledged.

We would like to acknowledge the data provided by the ACHEON consortium partners, whose results have been considered as guidance for the performed simulations.

Special thanks go to Maharshi Subhash for his valuable help in turbulence modeling and boundary layer analysis and to the Flow Vision team for their support in setting up the CFD simulations.

References

1. ACHEON: ACHEON project. http://ACHEON.eu/project/ (2013)
2. Trancossi, M.: An overview of scientific and technical literature on Coanda effect applied to nozzles. SAE Technical paper 2011-01-2591 (2011). doi:10.4271/2011-01-2591
3. Trancossi, M., Dumas, A.: A.C.H.E.O.N.: Aerial Coanda high efficiency orienting-jet nozzle. SAE Technical paper 2011-01-2737 (2011). doi:10.4271/2011-01-2737
4. Trancossi, M., Dumas, A.: Coanda synthetic jet deflection apparatus and control. SAE Technical paper 2011-01-2590 (2011). doi:10.4271/2011-01-2590
5. Olivotto, C.: Fluidic elements based on Coanda effect. Anniversary Session "Celebrating 100 year of the First Jet Aircraft Invented by Henri Coanda". COMOTI and Henri Coanda Association, Bucharest (2010)
6. Miozzi, M., Lalli, F., Romano, G.P.: Experimental investigation of a free-surface turbulent jet with Coanda effect. In: 15th International Symposium on Applications of Laser Techniques to Fluid Mechanics, Lisbon (2010)
7. Aksenov, A., Korenev, D., et al.: "Drop-Test" FSI simulation with Abaqus and flow vision based on the direct 2-way coupling approach. In: Abaqus Users, Newport, USA (2008)
8. Trancossi, M., Vucinic, D., Dumas, A.: Mathematical modeling of Coanda effect. In: SAE 2013 Aero Tech Congress and Exhibition Proceedings, Montreal, Quebec, Canada (2013)
9. Subhash, M., Dumas, A.: Computational study of Coanda adhesion over curved surface. In: SAE 2013 Aero Tech Congress and Exhibition Proceedings, Montreal, Canada (2013)

10. Dumitrache, A., Frunzulica, F., Ionescu, T.C.: Mathematical modelling and numerical investigations on the Coanda effect. In: Awrejcewicz, J. (ed.) Nonlinearity, Bifurcation and Chaos—Theory and Applications (2012). ISBN:978-953-51-0816-0
11. Jones, G.S., Lin, J.C., Allan, B.G., et al.: Overview of CFD Validation Experiments for Circulation Control Applications at NASA. In: Proceedings of the IPLC 2008: International Powered Lift Conference, London, UK, 22–24 July 2008
12. Drăgan, V.: A new mathematical model for high thickness Coanda effect wall jets. Rev. Air Force Acad. **1**(23), 25–45 (2013)
13. Djojodiradjo, H., Abdulhamid, M.F., Basri, S., et al.: Numerical simulation and analysis of Coanda effect. IIUM Eng. J. Spec. Issue Mech. Eng. **12**, 63–75 (2011)
14. Menter, F.R., Kuntz, M., et al.: Ten years of industrial experience with the SST turbulence model. In: Proceedings of the Fourth International Symposium on Turbulence, Heat and Mass Transfer, vol 4. Begell House Inc (2003)
15. Houghton, E.L., Carpenter, P.W.: Aerodynamics for Engineering Students, pp. 508–510. Butterworth-Heinemann, Oxford (2003)
16. Brouns, M., Verbanck, S., Van Beeck, J., Vanlanduit, S., Vanherzeele, J., Lacor, C.: PIV on the flow of a simplified upper airway model. In: 13th International Symposium of Applications of Laser Techniques to Fluid Mechanics (2006)
17. Brouns, M.: Numerical and experimental study of flow and deposition of aerosols in the upper human airways. Doctoral thesis (2007)
18. Barlow, J.B., Rae, W.H., Pope, A.: Low-Speed Wind Tunnel Testing, 3rd edn. Wiley, New York (1999)

Numerical Investigation of the Flow Over Delta Wing and Reverse Delta Wing

Hani Ludin@ Jamaluddin, Ashraf A. Omar and Waqar Asrar

Abstract This study aims to give some thoughts and initial understanding of passive wake vortex alleviation by introducing add-ons devices onto the aircraft, which are delta wing (DW) and reverse delta wing (RDW). However, as a preliminary investigation, the study has treated these devices separately from the aircraft in order to clearly visualize the wake vortex formation behind the wing as a standalone. Simulations were performed using RANS turbulence model. The results were obtained and quantified at measurement section locations downstream, of x/c = 1.359 and x/c = 3.418 measured from leading edge point of the model. Comparison between numerical and experimental results has shown good agreement in term of aerodynamic forces for RDW, whereas the comparison is not so good for DW as far as the prediction of drag coefficient is concerned. Although the simulations capture vortex roll-up trends, the size of the vortex is not predicted correctly by RANS turbulence model. Overall, it can be concluded from the results that the wake vortex generated from DW exhibit higher tangential velocity magnitude and circulation than the one generated from RDW at a particular angle of attack (AOA) between 20° and 30°.

1 Introduction

This study aims to gain an insight and initial understanding of add on devices which may be used for passive wake vortex alleviation. These add-ons devices fitted on aircraft wings have the shape of a delta wing (DW) or a reverse delta wing (RDW).

H. Ludin@ Jamaluddin · W. Asrar
Department of Mechanical Engineering, International Islamic University Malaysia,
P. O. Box 10, 50728 Kuala Lumpur, Malaysia

A.A. Omar (✉)
Department of Aeronautical Engineering, University of Tripoli, P. O. Box 13154
Tripoli, Libya
e-mail: aao@aerodept.edu.ly

K.Z.K. Shaari and M. Awang (eds.), *Engineering Applications of Computational Fluid Dynamics*, Advanced Structured Materials 44,
DOI 10.1007/978-3-319-02836-1_7

However, as a preliminary investigation, this study has treated these devices separately from the aircraft in order to clearly visualize the wake vortex formation behind them as a standalone.

Numerical simulations were performed for both DW and RDW at various angles of attack to investigate the characteristics of the vortices generated downstream. These vortices are investigated in terms of velocity vectors with its magnitude, tangential velocity distribution and streamlines.

2 Overview of Related Previous Work

The following section will present some of the recent studies that have been conducted on the vortical flow behaviour downstream of a delta wing (DW) and a reverse delta wing (RDW).

2.1 Delta Wing (DW)

The delta wing is a wing of a triangular planform, named after the Greek uppercase letter delta (Δ). This type of wing was intentionally designed to be used for supersonic flights after the design of highly swept wings airplanes. Delta wings are used on many different types of airplanes around the world; hence, the delta wing is an important aerodynamic configuration [1].

A lot of investigations were conducted concerning the behavior of vortices generated from delta wing. Zhu and Jia [2] have conducted numerical simulation of incompressible Navier–Stokes and Euler equations of the vortical flow about a delta wing. They found out that for delta wings at moderate or high angle of attack, its leeward and windward side boundary layers flow outward, separate from the wing leading edge and join to form a shear layer which rolls up into vortices above the wing, then convecting and stretching, the vortices were concentrated into the so-called leading-edge vortex on the leeward side of the delta wing.

Another trend of researches was more focused on understanding of the leading edge vortices behavior on delta wings, where researchers have focused on the delay of vortex breakdown. Experiments have proved that a trailing edge fan can enhance the vortical flow and offset vortex breakdown by nearly half of the wing's length [3]. Srigrarom and Lewpiriyawong [4] have studied the effect of perturbation to the breakdown of the leading-edge vortices over delta wing by means of installing hemisphere-like bulges on the delta wing along the projection of the vortices. The results had showed that the best outcome of perturbing the vortex core occurs in the case of 65° angle of attack (AOA).

Several numerical approaches have been conducted as well along with experiments. Gurr et al. [5] has simulated delta wing of a generic aircraft configuration using Detached-Eddy Simulation (DES) under unsteady flow condition. He

concluded that DES method is much better suited to near-future requirements in the simulation of such practicality-relevant flows for which unsteady effects play a major role. Further numerical computations were carried out by Heinrich and Stefan [6] using DES turbulence model. The results obtained showed good agreement with wind tunnel measurements.

Schiavetta et al. [7] have presented in detail by the use of Computational Fluid Dynamics (CFD) that a shock vortex interaction is responsible of the sudden movement of vortex breakdown location as the angle of incidence of delta wing is increased. Huixue and Zhichun [8] have recently simulated the phenomenon of vortex breakdown over a delta wing using Navier–Stokes equations. The results indicated that vortex breakdown location moves upstream with the increase of incidence angle, where the kinetic energy of leading edge vortex is transformed into kinetic energy of small vortices and turbulent kinetic energy during the process of vortex breakdown.

2.2 Reverse Delta Wing (RDW)

The main difference between a reverse delta wing and a regular delta wing is that the flow direction on RDW planform tends to move inward from the leading edge towards the trailing edge apex point, while for DW; it tends to move outward from leading edge apex point towards the tip and trailing edge. Figure 1 illustrates the difference of planform flow direction between the two configurations.

Gerhardt [9] has observed significant differences between a regular delta wing and a reverse delta wing, where he concluded that certain aerodynamic characteristics can be exploited for efficient supersonic flight. The performance of reverse delta wing has showed that at supersonic speeds, the boundary layer at the wing surface exhibits laminar flow starting at the leading edge, continuing for some

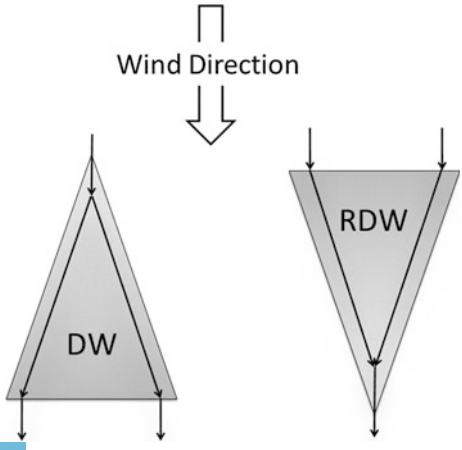

Fig. 1 Flow over delta wing (DW) and reverse delta wing (RDW)

fraction of the chord of the wing and terminating at a transition boundary line, where it then becomes turbulent. The large region of laminar flow on a reverse delta wing allows the lowest drag, which gives it favorable aerodynamic characteristics.

Urquhart et al. [10] studied the ground effect of the reversed delta wing surface craft. He revealed that the wake vortex flow structure illustrates complex interaction of the vortices with the ground, providing experimental validation of classical wing ground effect theory.

Wind tunnel tests have been performed by Elsayed et al. [11] to investigate the aerodynamics of the reverse delta wing using Particle Image Velocimetry (PIV). The test results conclude that RDW can be used as a wake vortex alleviation add-on device that may excite some instability through stable laminar or unstable wave phase or through modifying the vortex rollup process as a result of interaction with the turbulent phase, which may lead to rapid diffusion of vorticity that can enhance vortex decay.

Another study on a reverse delta wing (RDW) has been carried out by Altaf [12] and Altaf et al. [13] to investigate the wake vortices generated downstream, and their dependence on angle of attack and roll, at a Reynolds number, $Re_c = 3.82 \times 10^5$. The results obtained from the RDW model have been analyzed against the regular delta wing (DW) in term of vortex core radius, tangential velocity and circulation. It was concluded from the investigation that as angle of attack increases, vortex core radius, tangential velocity and circulation increase. Moreover, the results have also showed that, a reverse delta wing vortex exhibited lower magnitude of tangential velocity, circulation and vorticity than a regular delta wing vortex at a particular angle of attack.

3 Numerical Setup

The process of setting-up the problem, from developing a 3D CAD model up to post-processing the results is described in the following sections.

4 3D CAD Model

The 3D CAD model was developed using a commercial CAD modeler and pre-processing software called “STAR-Design”. The geometry of the 3D CAD model is illustrated in Fig. 2.

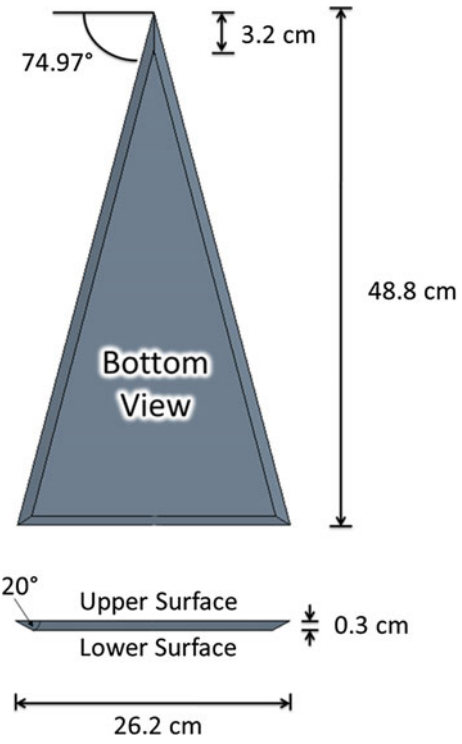

Fig. 2 Delta wing geometry

4.1 Meshing, Convergence Criteria and Physics Setup

Solution convergence is highly dependent on the quality of the mesh, as well as the equations used to model the physics of the problem. Fortunately, meshing the model of delta wing and reverse delta wing are quite uncomplicated due to their simple geometry. Merely, chamfers on the edges of the model were to be taken care of to avoid high skewness angle on the transition between the upper and lower surfaces. This can be done by distributing smaller cell size on the model, as shown in Fig. 3.

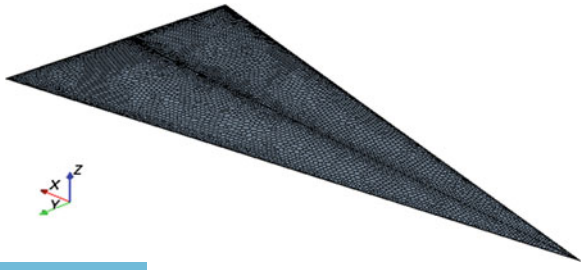

Fig. 3 Surface mesh on delta wing

Table 1 Mesh properties of DW and RDW

Mesh property	Parameter
Mesh type	Polyhedral dominant
Boundary layers	Prisms
Number of prism layers	3
Prism layers stretching	1.4 %
Prism layers thickness	0.001557 m
Minimum y^+	18.12
Maximum y^+	54
Cell size	Max: 0.07785 m Min: 0.002595 m
Growth rate	1.1 %
Total no. of cells	>174,000

There are key sensitive parameters that play significant roles in maximizing mesh quality and solution validity, where some can affect computational time and efficiency. The mesh around the DW and the RDW was generated using unstructured polyhedral dominant cells with prism boundary layers of y^+ ranging from 18.12 (minimum y^+ of the first point above model surface) to 54 (maximum y^+ of last point above model surface), which covers the logarithmic overlap region, where both viscous and turbulent region are resolved. Table 1 summarizes the key parameters used for meshing the DW and RDW.

The mesh density was kept fine enough on the model as well as at the wake which covers a measurement section distance of up to 167 cm, measured from the leading edge or the apex point of delta wing. Consequently, the total number of cells of more than $\sim$174,000 cells should represent adequate mesh density to simulate the flow. Moreover, the quality of the mesh was examined to ensure solution convergence is achieved. Table 2 summarizes overall mesh quality in term of skewness angle, face validity, and volume change, which are reported to be very good.

In order to evaluate solution convergence of both DW and RDW, it is usually sufficient to monitor the solution based on the residuals of the governing equations, especially when dealing with basic turbulence models of steady, single phase flow and under subsonic speed. Therefore, the residuals of turbulent kinetic energy (Tke) and turbulent dissipation rate (Tdr) of less than 1×10^{-2} should be sufficient, and as long as the continuity, X-momentum, Y-momentum and Z-momentum residuals reaches below 1×10^{-4} for the solution to be characterized as converged. In

Table 2 Mesh quality report of DW and RDW

Mesh property	Parameter
Maximum boundary skewness angle	82.5°
Maximum skewness angle	86.8°
Minimum face validity	1
Minimum volume change	0.004

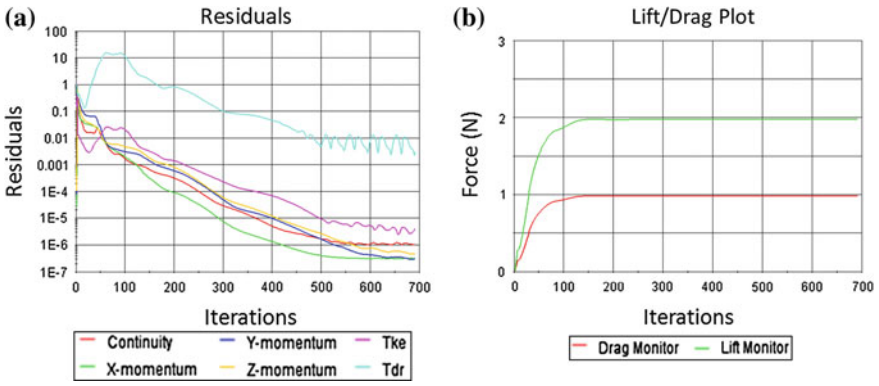

Fig. 4 Residual plot of RDW at α = 25°. **a** Residual plot. **b** Aerodynamic forces plot

addition to that, the aerodynamic forces lift and drag have been taken into account and monitored for additional convergence judgement. Figure 4 shows a sample residuals history in (a) and aerodynamic forces convergence in (b) of reverse delta wing at α = 25° when the solution become converged.

Basic physics of air flowing over an object at a subsonic speed has been used. The model has been examined in three dimensional space (3D) where it remains stationary and air with density of 1.18415 kg/m^3 blowing upstream at a constant speed of 12 m/s. In addition, second order segregated incompressible flow condition has been chosen under subsonic speed. The segregated flow model solves the flow equations (one component for velocity, and one for pressure) in a segregated or uncoupled manner, which uses a second order convection scheme to discretize the flow. Reynolds-Averaged Navier–Stokes (RANS) equations with K-Epsilon turbulence model have been used to model and predict the turbulence in the near-wake, downstream of the model. K-Epsilon model have been in use for several decades, and it has become the most widely used model for industrial applications.

5 Comparison Between Numerical and Experimental Results of DW and RDW

Wind tunnel tests of delta wing and reverse delta wing have been carried out by Altaf et al. [13], where some of the experimental results are brought up in this section for the purpose of comparison with the numerical results presented earlier. This comparison is carried out in terms of aerodynamic coefficients, maximum cross-flow velocity, tangential velocity distribution and circulation distribution.

5.1 Aerodynamic Coefficients

Lift and drag coefficients, C_L and C_D, have been computed numerically for both delta wing (DW) and reverse delta wing (RDW) at several angles of attack (α) and compared against experimental data measured by Altaf et al. [13]. As shown in Fig. 5, the experimental and numerical aerodynamic coefficients show similar trends, where C_L and C_D increase as the angle of attack increases. Furthermore, both numerical and experimental results show lower drag and lift coefficients for reverse delta wing (RDW) compared to delta wing (DW).

Furthermore, Table 3 summarizes some quantitative differences between experimental and numerical data of C_L and C_D at angles of attack of 25° and 30°. The comparison shows minimal difference error as 0.43 % which is excellent, and maximal difference error as 25.7 %.

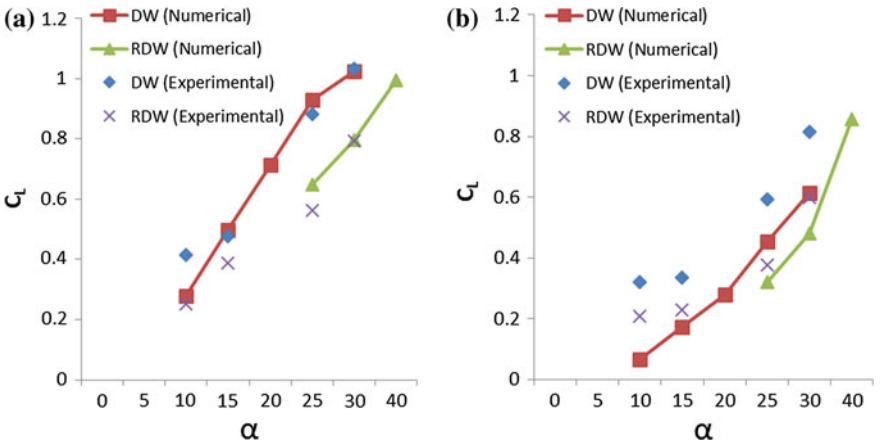

Fig. 5 Comparison between experimental and numerical aerodynamic coefficients of DW and RDW. **a** C_L versus α. **b** C_D versus α

Table 3 Aerodynamic coefficients comparison between numerical and experimental data of delta wing and reverse delta wing at α = 25° and 30°

	A (°)	Experimental		Numerical		Percent error %	
		DW	RDW	DW	RDW	DW	RDW
C_L	25	0.88	0.56	0.93	0.65	5.33	15.38
	30	1.03	0.79	1.03	0.80	0.64	0.43
C_D	25	0.59	0.38	0.45	0.32	23.40	13.3
	30	0.81	0.60	0.61	0.48	25.7	19.63

5.2 Vortex Roll-Up and Maximum Cross-Flow Velocity of DW

The numerical cross-flow velocity contours and vectors of delta wing have been compared against the experimental results, at measurement sections of x/c = 1.395 and x/c = 3.418 and angles of attack of 10 and 20°, in term of vortex roll-up and maximum magnitude of cross flow velocity. As can be seen from Figs. 6 and 7, the numerical cross-flow velocity contours at x/c = 1.395 shows acceptable agreement with the experimental results in terms of vortex roll-up and maximum cross–flow velocity magnitude compared to x/c = 3.418. This increase in difference error in numerical calculations is due to fast dissipation of energy as we go further

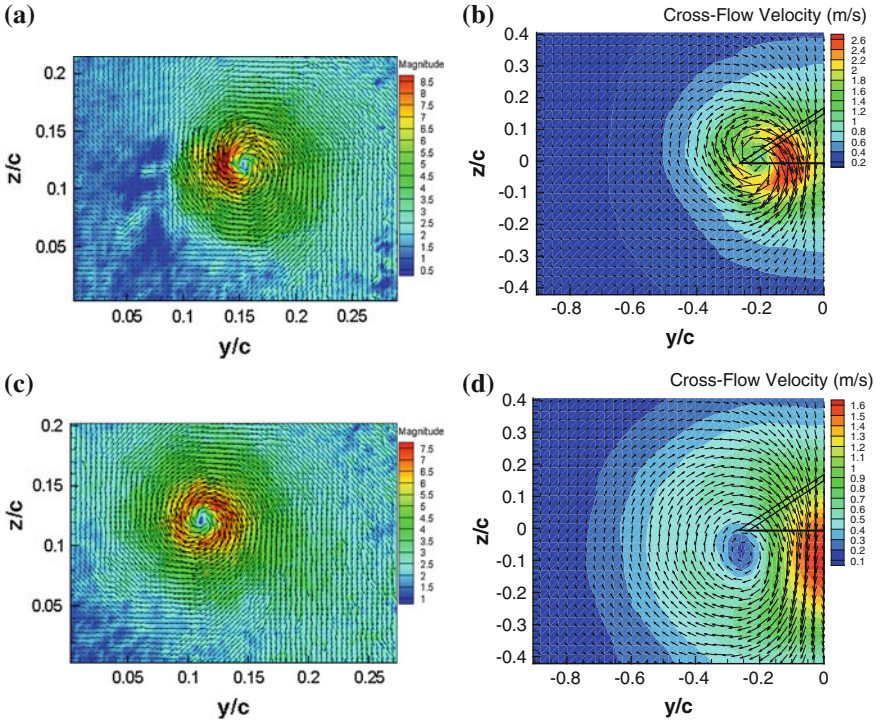

Fig. 6 Comparison between experimental and numerical delta wing vortex in term of cross-flow velocity magnitude at α = 10°. **a** Experimental delta wing vortex at x/c = 1.395 Altaf et al. [13]. **B** Numerical delta wing vortex at x/c = 1.395. **c** Experimental delta wing vortex at x/c = 3.418 Altaf et al. [13]. **d** Numerical delta wing vortex at x/c = 3.418

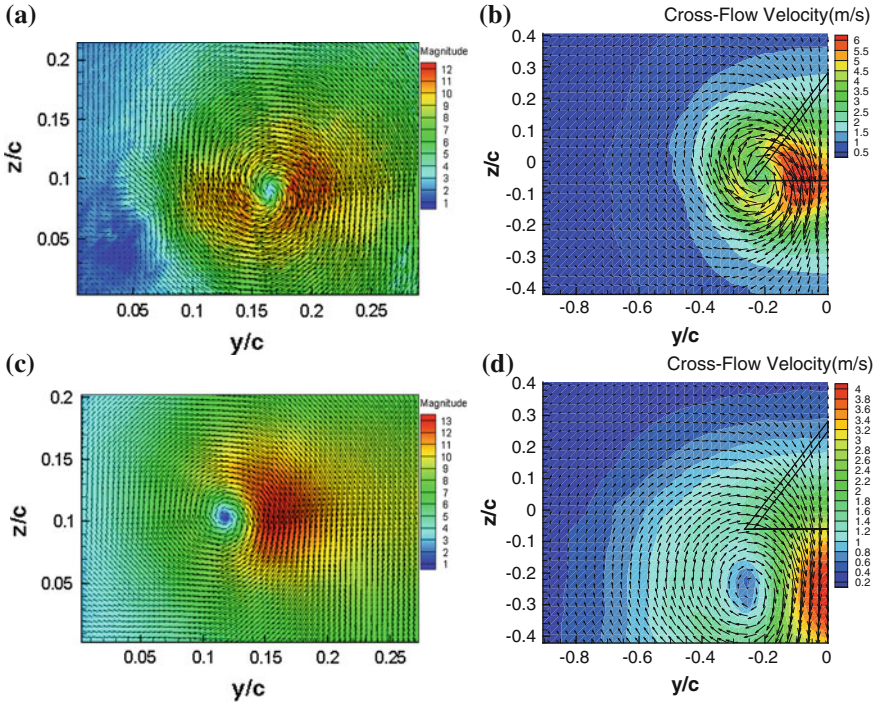

Fig. 7 Comparison between experimental and numerical delta wing vortex in term of cross-flow velocity magnitude at α = 20°. **a** Experimental delta wing vortex at *x/c* = 1.395 Altaf et al. [13]. **b** Numerical delta wing vortex at *x/c* = 1.395. **c** Experimental delta wing vortex at *x/c* = 3.418 Altaf et al. [13]. **c** Numerical delta wing vortex at *x/c* = 3.418

downstream which is attributed to the turbulence model used being limited in modelling eddies and flow circulations to some extent.

5.3 Tangential Velocity and Circulation Distributions of DW

Tangential velocity and circulation distribution around delta wing vortex core has been calculated and plotted in term of radial distance and compared against experimental results at 25° and 30° angle of attack.

As can be seen from Fig. 8, both experimental and numerical results show similar trend where peak magnitude of normalized tangential velocity tends to increase as the angle of attack increases.

Moreover, in terms of peak magnitude of tangential velocity distribution, the difference error between experimental and numerical results tends to increase further downstream for the same reason explained in the previous sections. Similarly, it can be noted from Fig. 9 that the peak circulation increases as the angle of attack increases.

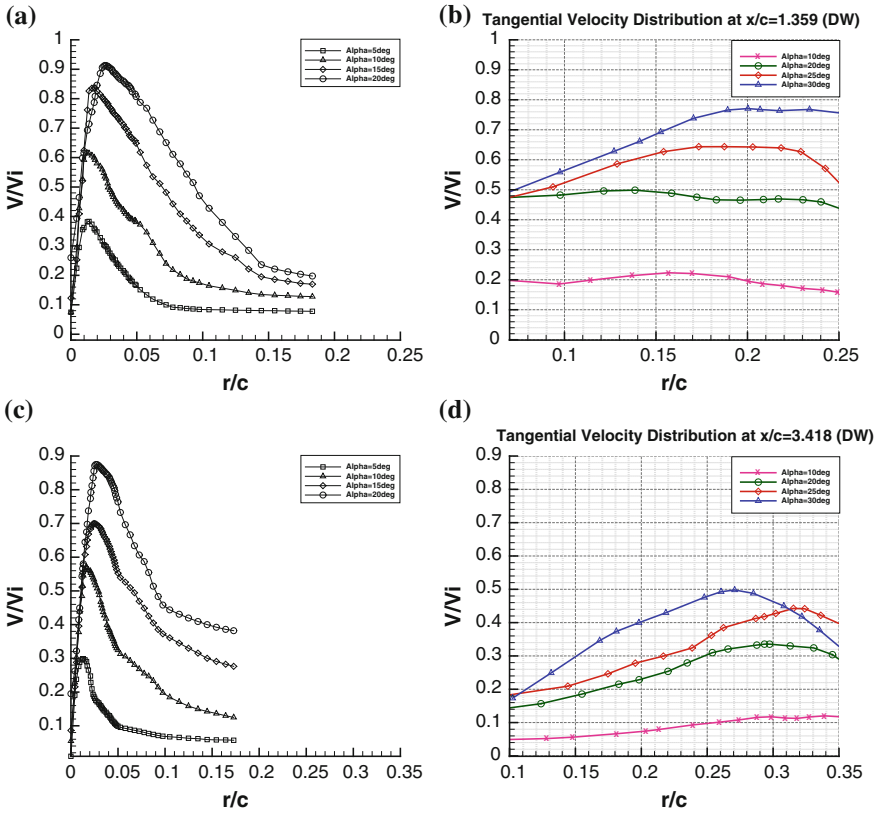

Fig. 8 Comparison between experimental and numerical tangential velocity distribution of delta wing. **a** Experimental tangential velocity distribution of delta wing at x/c = 1.395 Altaf et al. [13]. **b** Numerical tangential velocity distribution of delta wing at x/c = 1.395. **c** Experimental tangential velocity distribution of delta wing at x/c = 3.418 Altaf et al. [13]. **d** Numerical tangential velocity distribution of delta wing at x/c = 3.41

However, the difference error increases at farther measurement sections with noticeable percentages due to inadequate modelling of flow circulations associated with the RANS turbulence model.

5.4 Streamlines

Figures 10, 11, 12, 13, 14, 15 and 16 show the streamlines of the flow path on the wake of DW and RDW, where particles are being seeded from the surface of the model.

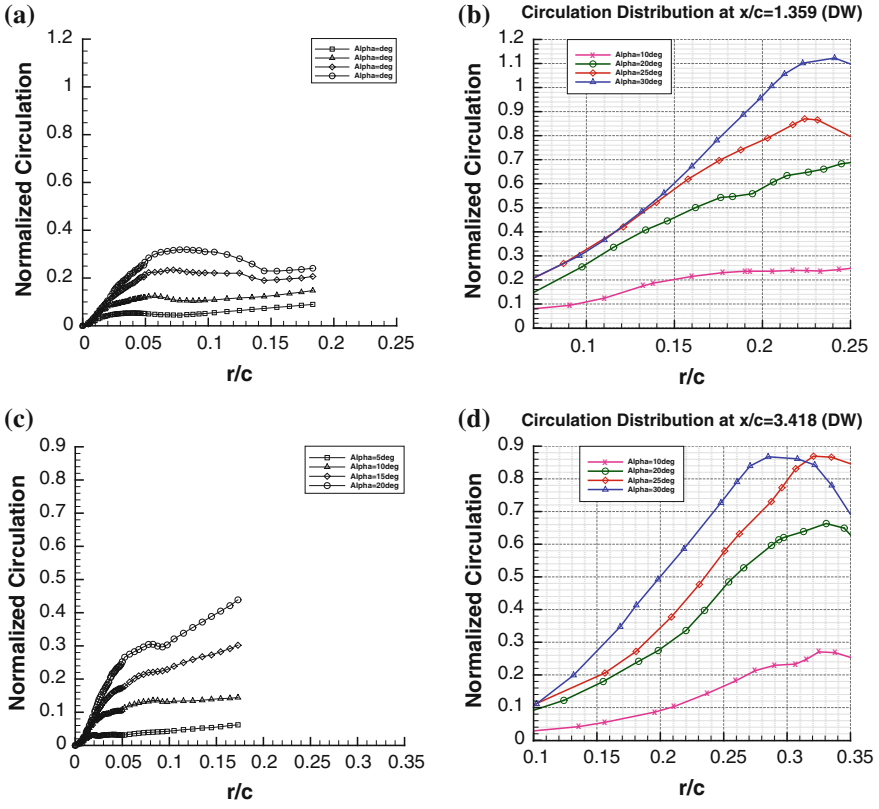

Fig. 9 Comparison between experimental and numerical circulation distribution of delta wing. **a** Experimental circulation distribution of delta wing at x/c = 1.395 Altaf et al. [13]. **b** Numerical circulation distribution of delta wing at x/c = 1.395. **c** Experimental circulation distribution of delta wing at x/c = 3.418 Altaf et al. [13] **d** Numerical circulation distribution of delta wing at x/c = 3.418

For the DW, as seen from Figs. 10, 11, 12 and 13, there are formations of vortex tubes along the upper side edges of the DW. These vortex tubes start forming smaller at the apex point of the leading edge, and grow as they go further downstream. Moreover, as the AOA increases, the flow becomes more violent, where eddies and vortices become much stronger and more durable.

In Figs. 14 and 15, the streamlines of the RDW show that circular flow starts from the leading edge tip points with weaker vortex tubes compared to the vortex tubes generated by the DW. However, in Fig. 16, vortex tubes seem to be more steady and uniform as the AOA increases to 40°.

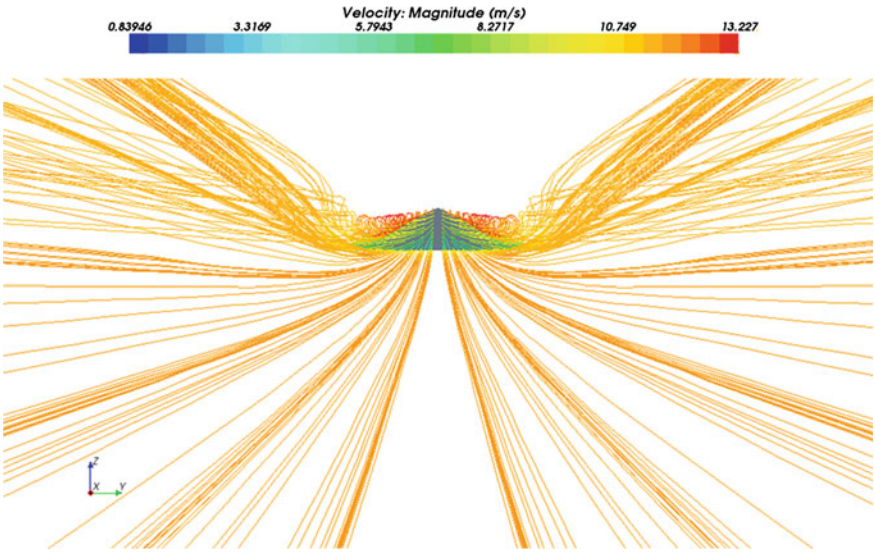

Fig. 10 Delta wing streamlines at α = 10°

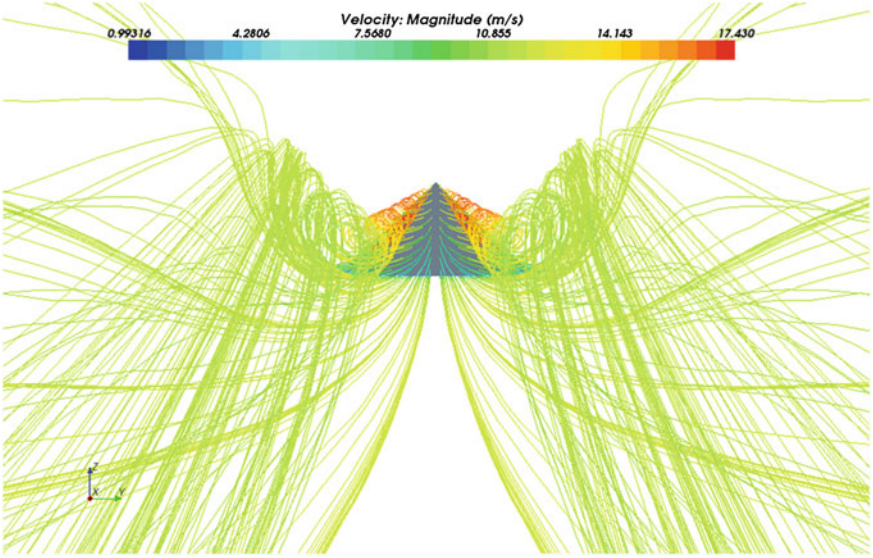

Fig. 11 Delta wing streamlines at α = 20°

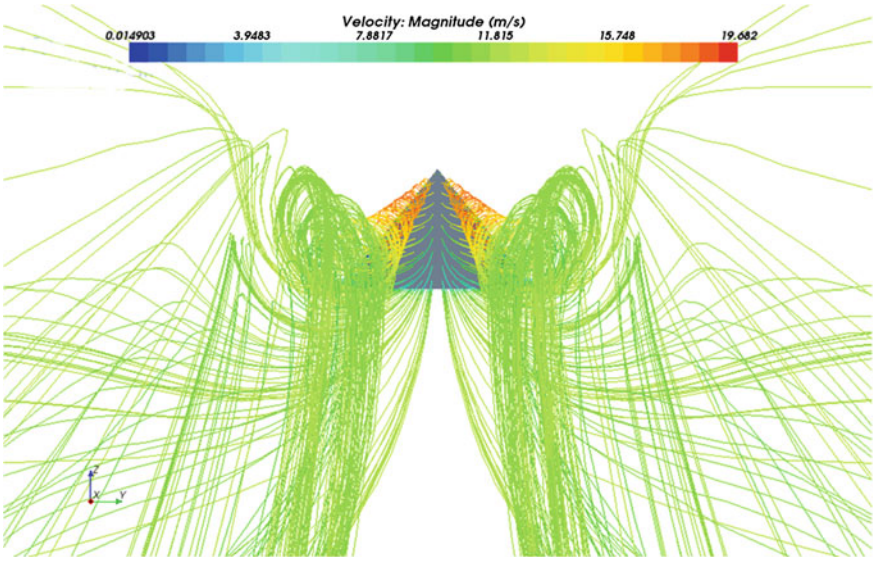

Fig. 12 Delta wing streamlines at α = 25°

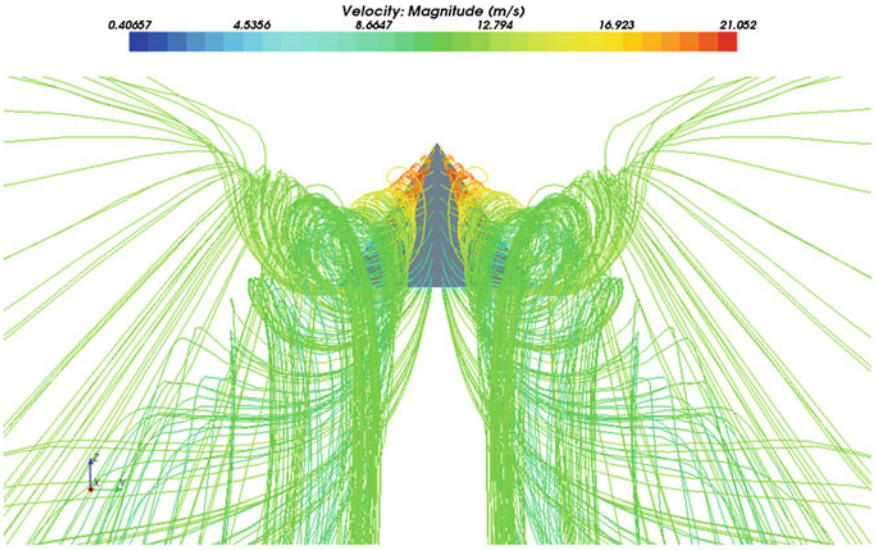

Fig. 13 Delta wing streamlines at α = 30°

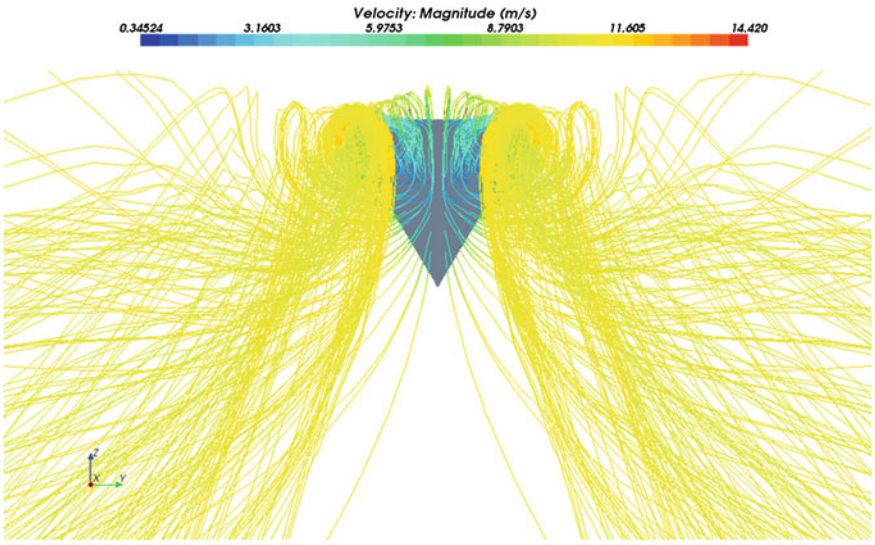

Fig. 14 Reverse delta wing streamlines at α = 25°

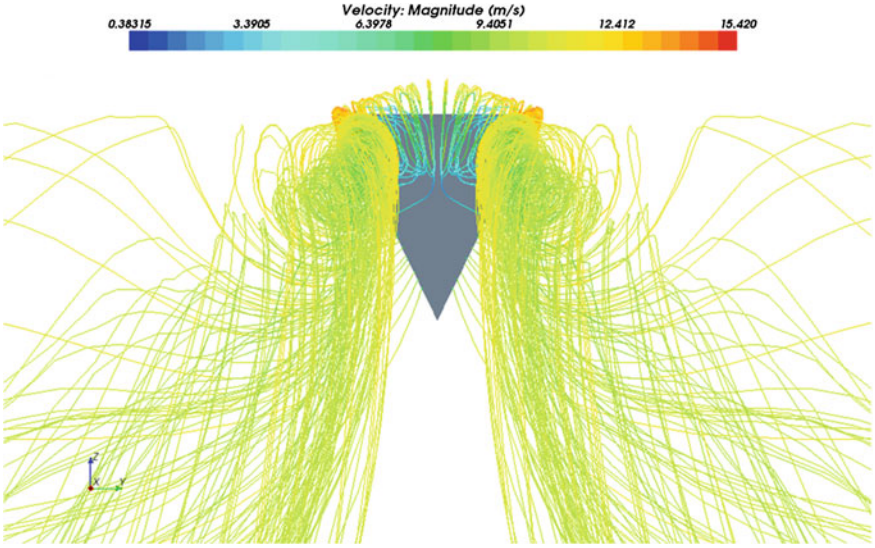

Fig. 15 Reverse delta wing streamlines at α = 30°

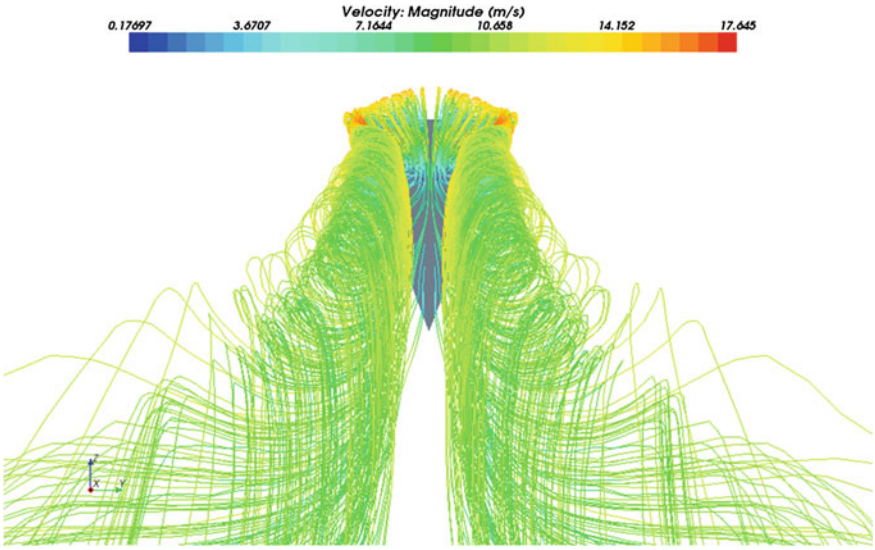

Fig. 16 Reverse delta wing streamlines at α = 40°

6 Summary

Wake vortex structure and its characteristics of both delta wing (DW) and reverse delta wing (RDW) were studies numerically by using commercial CFD code.

Comparison between numerical and experimental results has shown good agreement in terms of aerodynamic forces for RDW, whereas the comparison is not so good as far as the prediction of drag coefficient is concerned. However, as RANS turbulence model is limited to modeling eddies and flow circulations, vortex size were not predicted correctly. As a result, there were significant increases in difference error in term of maximum cross flow velocity magnitude and peak tangential velocity.

The results have shown that as the angle of attack increases, the tangential velocity magnitude, vorticity magnitude and circulation increase for both the DW and the RDW vortices. In addition, peak values of tangential velocity of both the DW and the RDW indicate direct dependency on the angle of attack, whereby they increase as AOA increases. However, the RDW vortex exhibited a lower magnitude compared to the DW vortex for AOA between 20 and 30°.

Overall, the results have shown that the DW generates more favorable (e.g. stronger) wake vortices than the RDW. As a result, these wake vortices may play a significant role in the attenuation of wake vortices generated from aircraft wing tip and minimize hazard to the following aircraft.

References

1. Anderson, J.D.: Fundamentals of Aerodynamics, 3rd edn., pp. 230–401. McGraw Hill, Singapore (2001)
2. Zhu, Z.Q., Jia, J.B.: Numerical simulation of incompressible Navier–Stokes and Euler equations to the vortical flow about a delta wing. Acta Mech. **122**, 21–31. Springer, Berlin (1996)
3. Zhou, J., Jeff, M., Hochstein, J., Mo, J. D.: The effect of downstream suction on the delta wing leading-edge vortex. In: Proceeding of the Eighth Asian Congress of Fluid Mechanics, Shenzhen, China (1999)
4. Srigrarom, S., Lewpiriyawong, N.: Controlled vortex breakdown on modified delta wings. J. Vis. 10(3), 299–307 (2007)
5. Gurr, A., Rieger, H., Breitsamter, C., Thiele, F.: Detached-eddy simulation of the delta wing of a generic aircraft configuration. In: Hans-Josef, R. (eds.) New Results in Numerical and Experimental Fluid Mechanics V: Notes on Numerical Fluid Mechanics and Multidisciplinary Design (NNFM), vol. 92, pp. 463–470. Springer (2006)
6. Heinrich, L., Stefan, L.: Unsteady CFD analysis of a delta wing fighter configuration by delayed detached Eddy simulation. In: Shia-Hui, P., Werner H. (eds.) Advances in Hybrid RANS-LES Modelling, vol. 97, pp. 37–44. Springer (2008)
7. Schiavetta, L.A., Boelens, O.J., Crippa, S., Cummings, R.M., Fritz and Badcock, K.J.: Shock effects on delta wing vortex breakdown. J. Aircr. **46**(3), 903–911 (2009)
8. Huixue, D., Zhichun, Y.: Vortex Breakdown over Delta Wing and Its Induced Turbulent Flow. Northwestern Polytechnical University, Xi'an (2010)
9. Gerhardt, H.A.: Supersonic Natural Laminar Flow Wing. Northrop Grumman Corporation, Los Angeles (1996) (Patent No. 5538201)
10. Urquhart, S.R., Prince, S.A., Khodagolian, V.: Aerodynamic study of reversed-delta wing surface craft in ground effect. 44th AIAA Aerospace Science Meeting and Exhibit, Reno, Nevada (2006)
11. Elsayed, O.A., Asrar, W., Omar, A.A.: Reverse delta wing trailing vortex characteristics by particle image velocimetry (PIV). In: 3rd international symposium on advanced fluid/solid science and technology in experimental mechanics, Tainan, Taiwan (2008)
12. Altaf A.: A study of the reverse delta wing using particle image velocimetry (PIV). M. Sc. thesis. International Islamic University Malaysia (IIUM), Kuala Lumpur, Malaysia (2011)
13. Altaf, A., Omar, A.A., Asrar, W., Ludin, H.B.: A Study of the Reverse Delta Wing. J. Aircr. **48**(1), 277–286 (2011). doi:10.2514/1.C031101

Numerical Modeling and Research of 3D Turbine Stage

Galina Ilieva Ilieva

Abstract The current study deals with a methodology for numerical modeling, research and analysis of flow parameters distribution in a 3D turbine stage with twisted rotor blade. The object under consideration is the forth stage of one of two low pressure turbine aggregates, working in Kozloduy Nuclear Power Plant, Bulgaria. A logical sequence for modeling of 3D viscous, compressible and turbulent flow in turbine stage, with moving twisted rotor blade, is accessed, as a result of the performed research works. Approaches how to attain high quality mesh grid and overcome convergence problems were established. The elaborated methodology was applied for research of boundary layer development; radial gap effects on flow aerodynamics in turbine stages; erosion effects over turbine blades working in wet steam; roughness influence over turbine blade surface, etc.

1 Introduction

Thermal turbo-machines are widely applied in modern aviation, marine ships, and energetic industry. Flow in turbo-machines is characterized by complexity and many features caused by 3D and unsteady effects, real physical fluid properties (compressibility, turbulence effects and viscosity) and complex stator and rotor blade geometry. During the operational process of each turbo unit, multiple-characteristic phenomena of detached boundary layer, vortices structures, secondary flows, energy losses in radial and axial clearances, shock waves phenomena, erosion, high streamlines curvature are observed.

All mentioned specifics contribute to mechanical and thermal stresses, which significantly affect turbines reliability and efficiency. Complete and accurate modeling of fluid flow in turbine components is essential for purposes of taking

G.I. Ilieva (✉)
Departamento de Engenharia Electromecânica, Universidade da Beira Interior,
R. Marquês D'Ávila e Bolama, 6201-001 Covilhã, Portugal
e-mail: galinaili@yahoo.com

K.Z.K. Shaari and M. Awang (eds.), *Engineering Applications of Computational Fluid Dynamics*, Advanced Structured Materials 44,
DOI 10.1007/978-3-319-02836-1_8

certain activities to increase the efficiency of the machine. Precise modeling, research and analysis of the fluid flow characteristics is important and one very relevant task of the modern theory of thermal turbo-machines.

In the beginning of the 20th century turbo-machines were designed on the assumption for 1D flow in stator and rotor channels. The most used and widespread equation for flow modeling was the Bernoulli's equation. Problems for flow research in turbine stages have been investigated by Helmtsman, Reynolds, Gyugonio [1].

Theory and practice development, in the area of turbine's aerodynamic, proved that 1D methods are unsatisfactory, that is why researchers proceeded to 2D modeling to attain flow characteristics in turbine aggregates. For modeling purposes an ideal model of infinitely large number of infinitely thin profiles had been applied.

On the subsequent development of 2D mathematical models worked Wu [73], Stepanov, Simonov, Zhukovsky, Vavra, Steynits, Goldstein and others.

Determination of parameters considering the flow characteristics in 3D aspect, is related to solving a system of nonlinear, partial differential equations (PDEs) with derivatives on the three coordinates x, y, z and time t. Three-dimensional problem is considered in two ways: transform the 3D unsteady equations system to two systems of 2D equations for stationary fluid and to calculate pure 3D flow in turbine stages.

Problem of 3D flow aerodynamics in turbo-machines can be solved using different approaches. Some of these approaches are Wu's method for flow parameters distribution on surfaces S1 and S2 [2–4]; the streamlines curvature method [5–8].

Also Wu's method is applied to flow modeling in turbine stages in recent years [2, 3]. Research of flow aerodynamics in surfaces S1 and S2, based on the method of streamlines curvature method is described in [5–7, 9].

In the mathematical model of Stepanov and Sirotkin [10], flow equations are averaged in space-time coordinates. Flow in rotational fluid surfaces with a variable thickness **h**, is transformed to a rotation surface S1′. Instead of a set of surfaces S2 is implemented the averaged meridional plane S2′.

Recently, approaches are related to solve Euler's [11–13] and Navier-Stokes [8, 14–17] set of equations. Navier-Stokes equations are averaged by Reynolds [18, 19, 21–24] or by Favre, for stationary [19, 25, 26] or non-stationary [11, 27–29] flow in turbine stages.

Numerical approaches used to solve a set of flow equations are Finite Elements Methods (FEM) [22, 30–32], Control Volume Method (CVM) [18, 23, 26, 29]. They are applied in many software codes such as FLUENT [33–37], ANSYS-CFX [28], CFX [15].

Basic CFD solvers applied for solving flows in turbine stages are Segregated Solver [18, 22, 30] and Coupled (Implicit or Explicit) Solver [30, 39, 40]. Flow equations can be discretized by First Order Upwind (FOU) [21], Second Order Upwind (SOU) [41, 42], Semi-Implicit Method for Pressure-Linked Equations (SIMPLE) [29, 38], SIMPLE-Consistent (SIMPLEC) [5, 17, 39, 40].

In turbulence models, several approaches have been done by previous researchers such as Spallart Allmaras (SA) [22], Standard k-ε model [33, 43], Reynolds Stress Turbulence Model (RSM) [43], Wilcox Turbulence Model (κ-ω model) [20, 21, 37, 44, 45], Renormalized Group Model (RNG k-ε) [46, 47], Shear-Stress Turbulence (SST) model [22, 28]. For 3D flow in turbine stages, Standard k-ε [46] is appropriate. RSM is applicable for modeling effects of additional vortices presence and shear stress effects over fluid particles [43]. In the current research Standard k-ε, RNG and RSM turbulence models are used [46].

Boundary zones and boundary conditions definition is a complex procedure, including great number of modeling features [46, 47]. Boundary zone type and boundary conditions are discussed and presented in details in [46].

Nowadays schemes for boundary conditions set-up are: total and static inlet pressure, inlet temperature, outlet static pressure and temperature, turbulent parameters and flow direction [45, 48]. At the streamlined walls are set zero velocity components [49]. Another possibility is pressure, speed and turbulence intensity at inlet and turbulence intensity and pressure at the outlet [16] or by Acton and Cargill scheme, presented in [50].

Different approaches can be applied for stator-rotor interaction modeling "frozen rotor" [51], "Sheared Cell" [52], MPI (Message Passing Interface) [30], Through Flow, Passage Average and other described in [53]. In [54] overlapping elements are applied in the area of interaction between stator and rotor stages. Interrelated and overlapping elements are described and applied to the analysis in [55–58].

The models do not include changeable fluid properties and boundary conditions update for each iteration and in each flow cell in the interaction area during the iterative procedure. Therefore, new schemes were proposed such as "Sliding Mesh" [37, 38, 52] in two-dimensional and "Mixing Plane" [59] in the three-dimensional aspect. Performed studies by Laumert et al. [60] for unsteady, 3D interaction between stator and rotor blades [60, 61] are of a great interest.

Based on a literature survey, it is obvious that 3D flow simulations have to be performed and addressed to: fluid physical properties and effects of their variation on flow aerodynamic; vortices structures and how they affect the overall efficiency performance; an exact choice of turbulence model; study of vortices and pressure pulsation effects, due to pressure change in downstream direction, aerodynamic behavior and efficiency of new radial and axial seals.

An actual and important problem, related to the process of numerical modeling of 3D flow in turbine stages, is to take into account all geometry and aerodynamic features. This will contribute to detailed research of turbine aggregates, working under variable conditions, also to consider specific criteria and approaches for increasing efficiency of turbine aggregates.

2 Research Algorithm

2.1 Mathematical Model

The mathematical model implemented in ANSYS Fluent gives an opportunity for modeling of a wide variety of flows. The set of equation is as follows:

(a) Continuity equation:

$$\frac{\partial \rho}{\partial t} + \frac{\partial(\rho Vx)}{\partial x} + \frac{\partial(\rho Vy)}{\partial y} + \frac{\partial(\rho Vz)}{\partial z} = 0. \tag{1}$$

(b) Rheology equation:

$$\tau_{ij} = -P\delta_{ij} + \mu\left(\frac{\partial ui}{\partial xj} + \frac{\partial uj}{\partial xi}\right) + \delta_{ij}\lambda\frac{\partial ui}{\partial xi}. \tag{2}$$

(c) Momentum equations:

$$\begin{aligned}&\frac{\partial(\rho Vx)}{\partial t} + \frac{\partial(\rho VxVx)}{\partial x} + \frac{\partial(\rho VyVx)}{\partial y} + \frac{\partial(\rho VzVx)}{\partial z} = \\ &\rho g_x - \frac{\partial P}{\partial x} + Rx + \frac{\partial}{\partial x}\left(\mu_e\frac{\partial Vx}{\partial x}\right) + \frac{\partial}{\partial y}\left(\mu_e\frac{\partial Vx}{\partial y}\right) + \frac{\partial}{\partial z}\left(\mu_e\frac{\partial Vx}{\partial z}\right) + T_x;\end{aligned} \tag{3}$$

$$\begin{aligned}&\frac{\partial \rho Vy}{\partial t} + \frac{\partial(\rho VxVy)}{\partial x} + \frac{\partial(\rho VyVx)}{\partial y} + \frac{\partial(\rho VzVy)}{\partial z} = \\ &\rho g_y - \frac{\partial P}{\partial y} + Ry + \frac{\partial}{\partial x}\left(\mu_e\frac{\partial Vy}{\partial x}\right) + \frac{\partial}{\partial y}\left(\mu_e\frac{\partial Vy}{\partial y}\right) + \frac{\partial}{\partial z}\left(\mu_e\frac{\partial Vy}{\partial z}\right) + Ty;\end{aligned} \tag{4}$$

$$\begin{aligned}&\frac{\partial \rho Vz}{\partial t} + \frac{\partial(\rho VxVz)}{\partial x} + \frac{\partial(\rho VyVz)}{\partial y} + \frac{\partial(\rho VzVz)}{\partial z} = \\ &\rho g_z - \frac{\partial P}{\partial y} + Rz + \frac{\partial}{\partial x}\left(\mu_e\frac{\partial Vz}{\partial x}\right) + \frac{\partial}{\partial y}\left(\mu_e\frac{\partial Vz}{\partial y}\right) + \frac{\partial}{\partial z}\left(\mu_e\frac{\partial Vz}{\partial z}\right) + Tz.\end{aligned} \tag{5}$$

(d) Energy equation for stagnation conditions:

$$\begin{aligned}&\frac{\partial}{\partial t}(\rho CpTo) + \frac{\partial}{\partial x}(\rho VxCpTo) + \frac{\partial}{\partial y}(\rho VyCpTo) + \frac{\partial}{\partial z}(\rho VzCpTo) = \\ &\frac{\partial}{\partial x}\left(K\frac{\partial To}{\partial x}\right) + \frac{\partial}{\partial y}\left(K\frac{\partial To}{\partial y}\right) + \frac{\partial}{\partial z}\left(K\frac{\partial To}{\partial z}\right) + W_v + E_k + Q_v + \Phi + \frac{\partial P}{\partial t},\end{aligned} \tag{6}$$

All mathematical terms included in Eqs. (3), (4), (5) and (6) are described in [46, 62].

A detailed review of turbulence models is presented in [46, 62].

2.2 *Structure of the Global Logical Sequence for Geometry and Numerical Modeling*

Figure 1 presents methodology flowchart for geometry and numerical modeling of flow in 3D turbine stages with complex geometry.

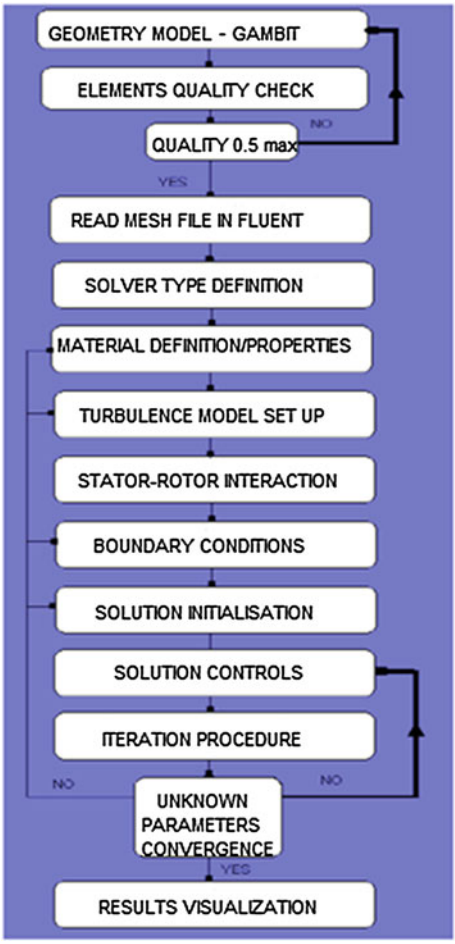

Fig. 1 Global logical sequence for *numerical modeling* of 3D compressible, viscous and turbulent flow in turbine stage of a complex geometry

2.3 Geometry Modeling of 3D Turbine Stage with Twisted Rotor Blade

Key steps in geometry modeling and approaches to obtain high quality grid mesh are as follows.

2.3.1 Key Points Coordinates Introduction from *.tur File and Construction of Basic Lines Which Forms Stator and Rotor Profiles, Inlet and Outlet Parts of Blade Sections

It is advisable for concave and convex sides to be consisted of minimum three lines [46, 47].

Profile contours must be approximated without any sharp edges. The main aim is to obtain high quality mesh; refined boundary layer mesh and furthermore blades streamed without vortex structures formations.

2.3.2 Stator and Rotor Blade Volumes

Decomposition method is an approach that helps to avoid problems during the procedure of fluid zones discretization, mainly at leading and trailing blade edges. This is the most appropriate method for turbine blades with twisted rotor blades [47].

2.3.3 Boundary Layer Modeling for Stator and Rotor Blades

For purposes of boundary layer mesh, a definite number of rows (depending on the flow conditions and some preliminary calculations based on the Schlichting's theory) with a smooth transition in the elements height, is recommended. First row elements height must be as small as possible. This leads to a possibility for visualization of all specific features and detection of boundary layer separation point also.

2.3.4 Discretization of Stator and Rotor Blades

The discretization steps are as follows:

- Discretization of hub section with elements of an appropriate shape and application of next options (Spacing/Interval Count in Mesh Faces panel);
- Discretization of hub base lines and those in radial direction with appropriate values for Grading/Successive Ratio/Ratio and Spacing/Interval Size options in Mesh/Edges panel;
- "Cooper" discretization scheme application. It is appropriate for a regular distribution of element volumes in radial direction; elements with negative volumes and highly stretched elements are surpassed.

2.3.5 Boundary Zones Definition for Stator and Rotor Blades

Before mesh file to be read in FLUENT, the boundary types must be specified for turbo volumes. The boundary zones are of the types: "wall", "pressure-inlet", "pressure-outlet", and "periodic".

2.3.6 Elements Quality Check

Finite elements quality factor must be a maximum value of 0.7, according to GAMBIT theory references [39, 40, 63]. The present research proves that it's better to obtain quality mesh factor 0.5 or the best option is 0.3. Negative element volumes Fig. 2a, skewed elements Fig. 2b, sharp edges along streamed profiles, could be surpassed in different ways, which is described in [46, 47].

2.4 Numerical Modeling of 3D Flow in a Turbine Stage

Numerical modeling procedure and its main steps are described in details in [46].

Working fluid is saturated steam, according to the official exploitation documentation.

Boundary zones that were imposed are: "Pressure Inlet", "Pressure Outlet", "Periodic" and "Wall". Boundary conditions are: total and static pressure, static temperature, flow direction at turbine stage inlet, static pressure and temperature at

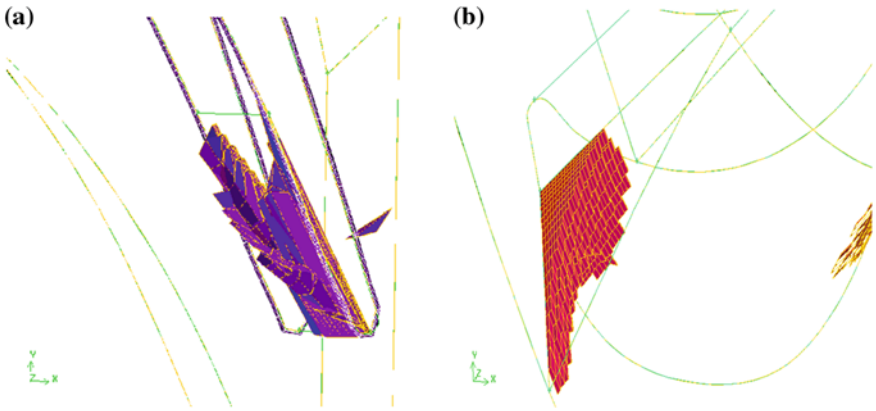

Fig. 2 **a**, **b** Finite elements with negative volumes in the trailing edge of stator blade (**a**), and stretched elements in twisted rotor blade (**b**)

stage outlet and turbulence parameters. Boundary conditions values were preliminary calculated in the process of 2D modeling by control sections in radial direction [47].

The chosen solver is Coupled Solver with imposed initial value for the Courant-Friedrich-Levy (CFL) number of 5. During the solution procedure, CFL number has been gradually decreased as follows: 2, 1.5, 1, 0.75, 0.5, 0.25. Options for residuals smoothing-"Iteration smoothing" and "Smooth factor", were set to 1 and 0.1.

Initially, solution was obtained with implemented First Order Upwind convective scheme, after the discretization scheme was switched to Second Order Upwind, in order to obtain physically correct solution.

It is well-known that after each iteration the values obtained for the unknown variables should become closer and closer together and thus converge. Due to strong non-linear equations, unsteady solution, separation and other aerodynamic effects, the solution is unstable; that is why a set of relaxation factors is used to remove the steep oscillations. For all under-relaxation factors, calculations were performed, with initial values equal to the default values included in FLUENT. After a gradual decrease, the final value for each under-relaxation factor was set to be 0.5.

Convergence is assumed to be obtained when the scaled residuals are in the range of 10^{-4} for all the unknown parameters; the exceptions are energy and turbulence parameters, which are 10^{-6}.

All relaxation factors and discretization schemes, as well as the approaches to overcome different divergence problems and access convergence, are described and discussed in more details in [46, 47].

Numerical results that were obtained, their detailed verification and validation are presented in [46].

2.4.1 Numerical Modeling of 3D Turbine Stage with Radial Gap

The aim of this research is determination of parameters distribution in turbine stage with twisted rotor blade and radial gap 0.005 m.

Geometry for turbine stage was obtained in GAMBIT. One of the main problems is related to discretization of the radial gap. Presence of bad quality elements (high skewness and negative volumes) must be avoided with very refined mesh.

Grid mesh options—"Spacing/Interval Count" in "Mesh Faces" panel and "Grading/Successive Ratio/Ratio & Spacing/Interval Size" in "Mesh/Edges" panel were applied.

Working fluid is water steam with physical properties according to the working conditions of the turbine stage.

Boundary zones that were imposed are: "Pressure Inlet", "Pressure Outlet", "Periodic" and "Wall". Rotor blade shroud is defines as "Wall".

Stator-rotor interaction is modeled with "Mixing Plane" model.

For exact physical performance of the turbulent effects in the flow, k-ω turbulence model is activated. This model is proved to be appropriate for modeling of flows in turbine stages with high adverse pressure gradients [62, 64], in case of

presence of regions with intensive separation and swirls. Also, Shear Stress Turbulent Model (SST) turbulent model could be applied [16, 43].

All flow equations are solved with Coupled Solver and appropriate set of relaxation and convergence approaches. Discretization scheme is Second Upwind Order, all under-relaxation factors are set to value of 0.5.

Residuals for the unknown parameters are set to be 10^{-4}; the exceptions are energy and turbulence parameters, which are 10^{-6}.

Problem formulation, boundary zones and boundary conditions are presented in [46, 65, 66].

2.4.2 Numerical Modeling for 3D Turbine Stage with Roughness

The current study deals with determination of flow parameters distribution and energy conversion efficiency in a turbine stage with definite roughness.

Wall roughness is implemented in FLUENT with roughness function ΔB, which is valid for all values and types of roughness. For constant roughness, ΔB depends on both the Ks+ (dimensionless roughness height) and roughness height—Ks. The model for ΔB calculation includes three regimes; they are a function of Ks+. These models are based on the Nikuradze's curve and are adapted by Cebeci, for calculation of ΔB, depending on the flow regime. All equations are explained in FLUENT theory.

At first, the iteration procedure is started in case of a zero roughness Ks. After calculations for Ks = 0, a new iteration procedure is started with next roughness height value. Working fluid is compressible, viscous and turbulent. According to the FLUENT theory references, a discretization mesh, representing boundary layer over turbine blades must have first row of elements with height higher than the roughness height.

All results obtained are presented in details in [46].

2.4.3 Erosion and Its Impact on Turbine Blades—Numerical Modeling

The main goal of this research is related to modeling and evaluation of the erosion effects on turbine stage working in two phase flow. For this purpose, Discrete Phase Model (DPM) has been applied.

The working fluid is wet steam, turbulent, compressible and viscous, with physical properties in function of the working conditions.

Boundary zones that were setup for the turbine stage are "pressure inlet", "pressure outlet", "periodic", "wall" and "fluid". The total gauge pressure, static pressure, static temperature, turbulence parameters and flow direction were imposed as "pressure inlet" boundary conditions. Static pressure, static temperature, flow direction and

turbulence parameters were implied as the outflow ("pressure-outlet") boundary conditions. Periodic boundary conditions were imposed to the side wall boundary zones. No-slip boundary conditions for hub, shroud, blade surfaces were applied. All values for the imposed boundary conditions are shown in [46].

FLUENT predicts the trajectory of a discrete phase particle by integrating the force balance on the particle, which is written in a Lagrangian reference frame. This force balance equates the particle inertia with the forces acting on the particle [62].

The primary inputs for the discrete phase calculations are: velocity, trajectory and temperature of the water droplets; mass flow rate, etc. These initial conditions provide starting values for all of the dependent discrete phase variables that describe the instantaneous conditions of an individual particle.

For the numerical simulation of wet steam flow, the general assumptions are as follows: ignore the speed slipping between droplets and steam; interaction forces among water droplets are equal to zero; the quantity of condensation phase is maximum 10–12 %.

The particles were set to be of type—"water-liquid". Droplets are with spherical shape and their diameter distribution is of type "uniform".

Numerical simulations were performed with water drops diameters of 1, 5, 15, 20 and 25 microns. Experimentally, droplets' maximum diameter for the conditions and velocities under consideration is found to be 15–25 microns [34]. Particles of size 150–200 microns could be only found in a very small area in the vortex immediately after the trailing edge where a fragmentation of the wet film is to be observed.

The total mass flow rate of wet steam for the turbine stage, according to the working documentation, is 2.97 kg/s. The total mass flow of the imposed secondary phase is 0.133 kg/s, equal to 4.478 % wetness. This value is responding to the real wetness measured in the turbine stage during working regimes.

In the current research boundary conditions, concerning the secondary phase, are implemented.

The Navier-Stokes equations set has been solved applying density based solver, fully implicit approach. Second order discretization scheme is used.

For all under-relaxation factors, calculations were performed with initial values that were equal to the default values included in FLUENT. After a gradual decrease, the final value for each under-relaxation factor was set to be 0.5.

Again, convergence is assumed to be obtained when the scaled residuals are in the range of 10^{-4} for all the unknown parameters; the exceptions are erosion, energy and turbulence parameters, which are 10^{-6}.

All other specific modeling features are fully described in [46].

3 Numerical Results

3.1 Results for 3D Real Fluid Flow in Turbine Stage with Rotating Twisted Rotor Blade in FLUENT

The main target of this research is to define the flow parameters distribution in a 3D turbine stage. For the purposes of the turbulence modeling, Standard k-ε turbulence model, RNG k-ε, Standard k-ω, for the case of research on radial gap, and RSM (Reynolds Stress Model) models are applied depending on the flow conditions.

The Standard k-ε model gives quite good values, especially for the turbulent kinetic energy, in the core flow [33, 43].

In [67] results show that the advantage of using the RSM in regions of flow separation, however the main flow features were still enough good, captured by the k-ε model.

The RNG model gives the highest prediction of lift and maximal lift angle [68].

The k-ω turbulence models are appropriate for flows characterized by high adverse pressure and intensive separation. This model allows for a more accurate near wall treatment with an automatic switch from a wall function to a low-Reynolds number formulation based on grid spacing [35, 69, 70].

In the current study is found that depending on the specific flow feature, under consideration, different turbulence model have to be applied.

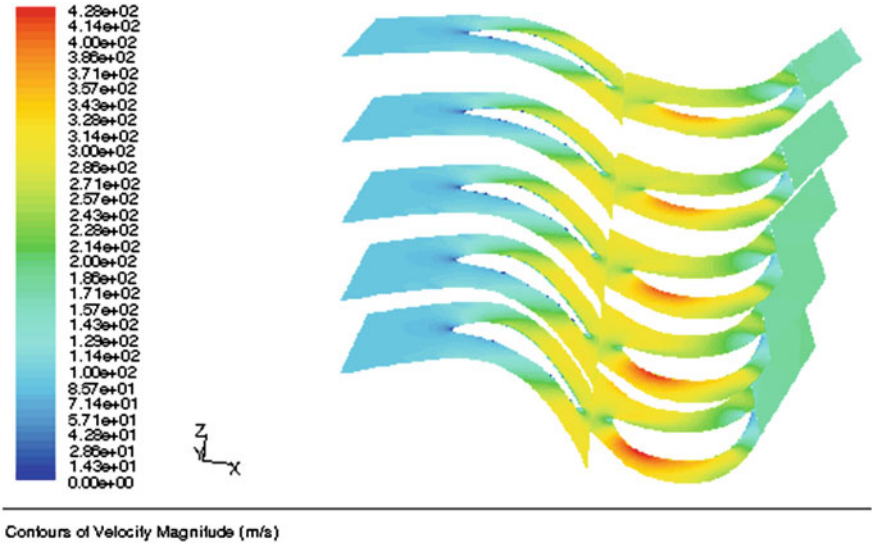

Fig. 3 Flow velocity field distribution in control sections, in radial direction

3.2 Results for Flow Parameters Distribution—Rotating Rotor Blade (1500 rpm) and Applied Standard k-ε Turbulence Model

Figure 3 shows velocity field distribution in case of rotating rotor blade and activated Standard κ-ε turbulence model.

Figure 4 shows vorticity magnitude values, in radial direction, in the turbine stage under consideration.

3.3 Results for Flow Parameters Distribution in Case of Rotating Rotor Blade

Numerical results are shown on Figs. 5a–d and 6.

In Fig. 7 are shown vortices, in radial direction, due to a difference between the pressure field values for hub and shroud sections in turbine stage. The area occupied by this vortex is bigger than the one, formed in case of Standard k-ε turbulence model, Fig. 4.

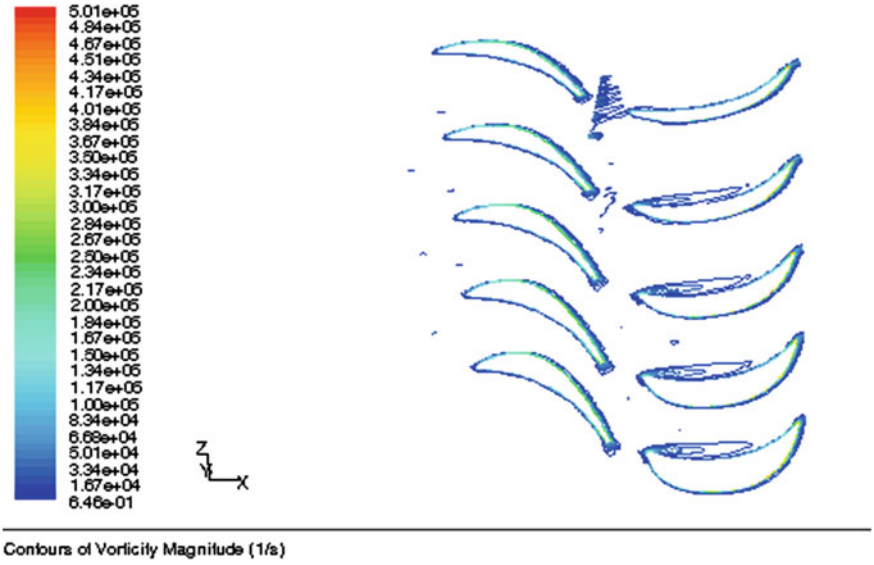

Fig. 4 Vorticity magnitude values in control sections, in radial direction

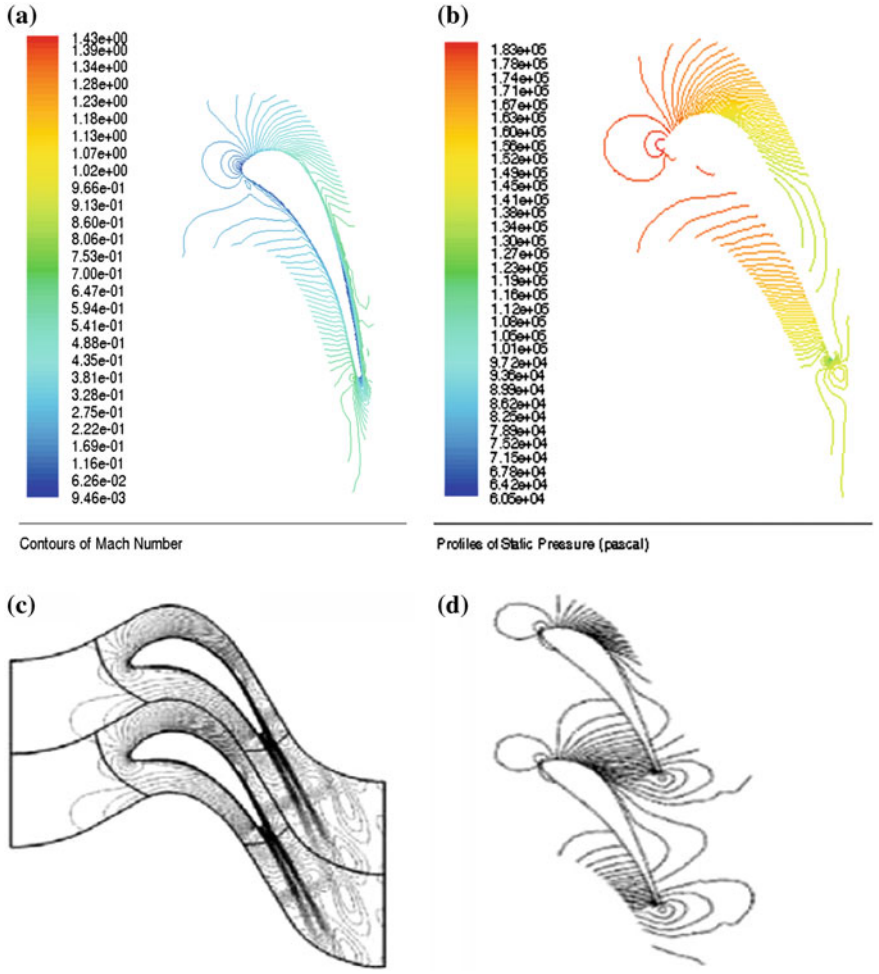

Fig. 5 **a**–**d** Mach number contours (**a**) and static pressure contours (**b**) of stator blade hub section, in comparison with the ones after Bo Chen (2008), and Cinella (2004) (**c**, **d**), presented in [46]

3.4 Results for Flow Parameters Distribution in Case of Rotating Rotor Blade (1500 rpm) and Applied RNG k-ε Turbulence Model

The RNG model is acceptable for study both the shear stress and streamlines curvature effects. The model presents the vortices structure at the trailing edge, and also provides results for aerodynamic features at the leading edge.

In case of applied RSM model, a relative decrease of 1.308 % for turbine stage efficiency is observed. This is a result of taking into account of all pulsations and

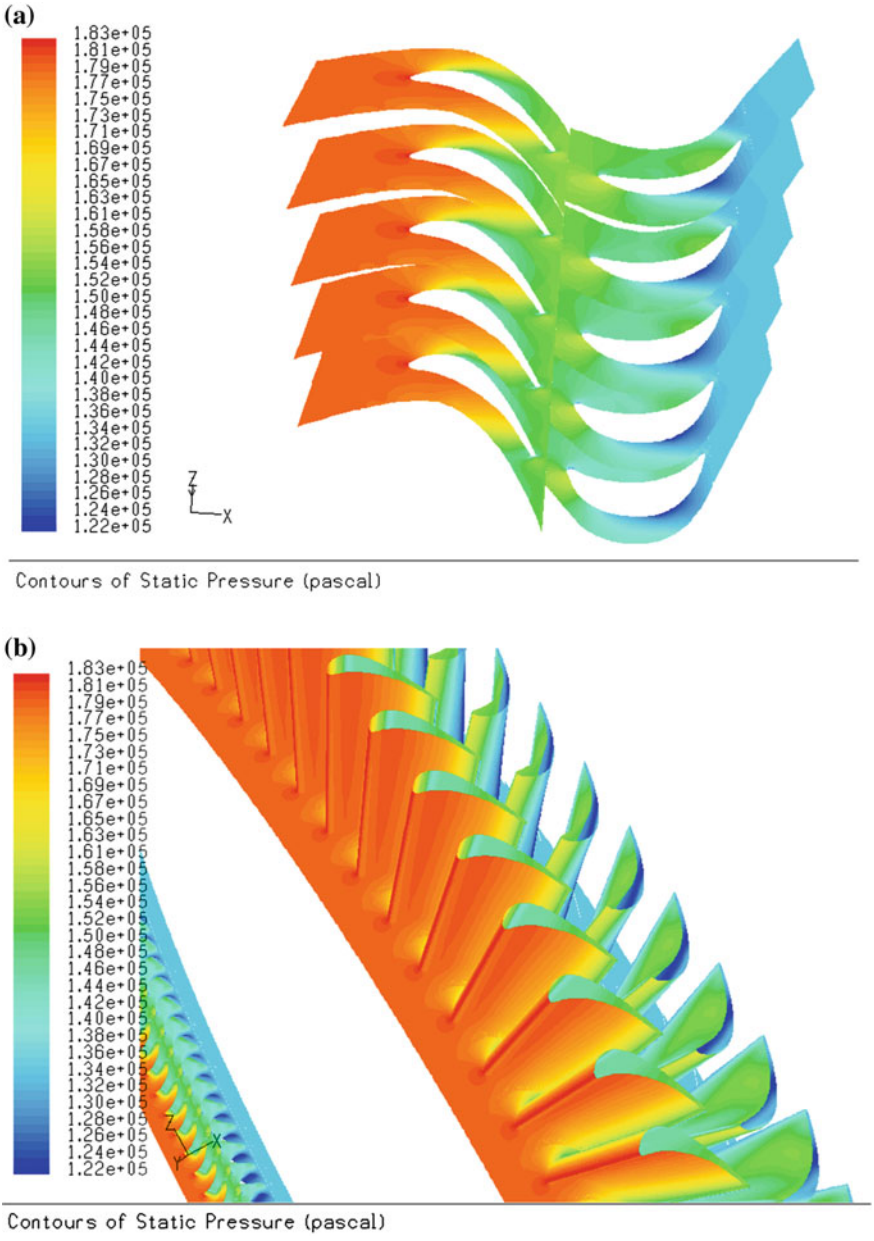

Fig. 6 Static pressure distribution—by control sections (**a**), in the entire turbine stage (**b**) in case of rotating rotor blade

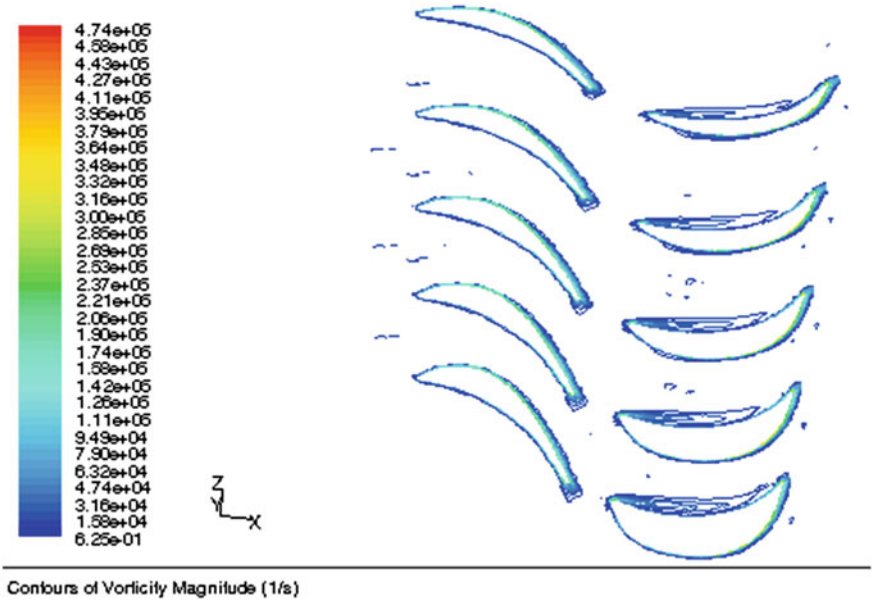

Fig. 7 Vorticity magnitude values by control sections, in radial direction

vortex structures near the wall regions, boundary layer separation, viscosity and compressibility effects.

The RNG κ-ε turbulence model leads to increased values for turbulent intensity and less values for turbulent viscosity. This is a prerequisite for decrease of the left hand side term values in the momentum equations. This causes relative increase of stage efficiency with 0.147 %, in a comparison with the case of implemented RSM turbulence model.

3.5 Results Obtained for the Radial Gap Influence Over Flow Parameters Distribution in 3D Turbine Stage

Figure 8a, b visualizes secondary flows, obtained due to presence of radial gap and pressure differences between hub and shroud sections. Figure 8c, d shows good agreement with the results obtained for the researched blade. This approach can be used for research on new labyrinth seals.

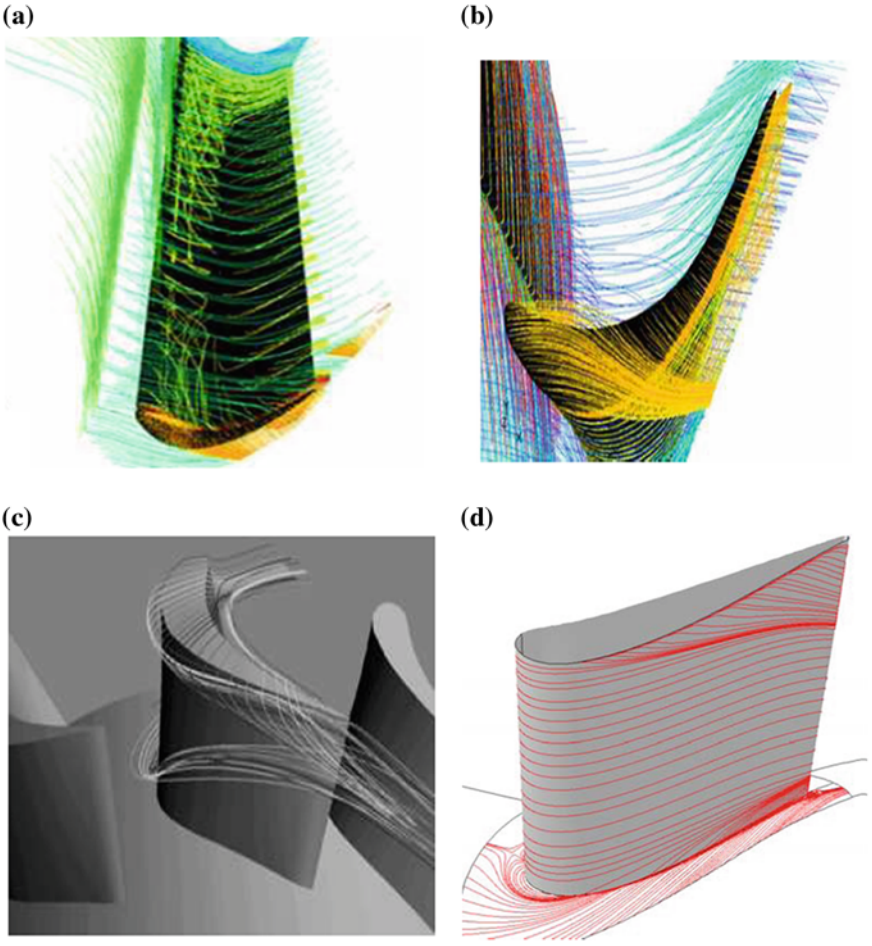

Fig. 8 **a**–**d** Secondary flows in the turbine stage under consideration (**a**, **b**); validation after Hamed et al. [71] (**c**) [46]; validation after Mumic (**d**) [64]

3.6 Results Obtained for Research on Erosion Affecting Turbine Blades Working in Wet Steam Conditions

Figure 9a, b presents results for erosion on blade surfaces in case of water droplets with mass flow rate m_1 = 0.133 kg/s and d_1 = 25 microns (a), and d_2 = 5 microns (b). Erosion effects are observed, mainly on the stator's leading edge and concave surface Fig. 9a, and along the leading and trailing edge of the rotor blade, Fig. 9b. Those effects are as a result of droplets trajectories, changes of blade's geometry, droplets' diameter, and impact pressure of the droplet over the surfaces, droplets' velocity and angle of impact. Also, higher droplets diameter leads to

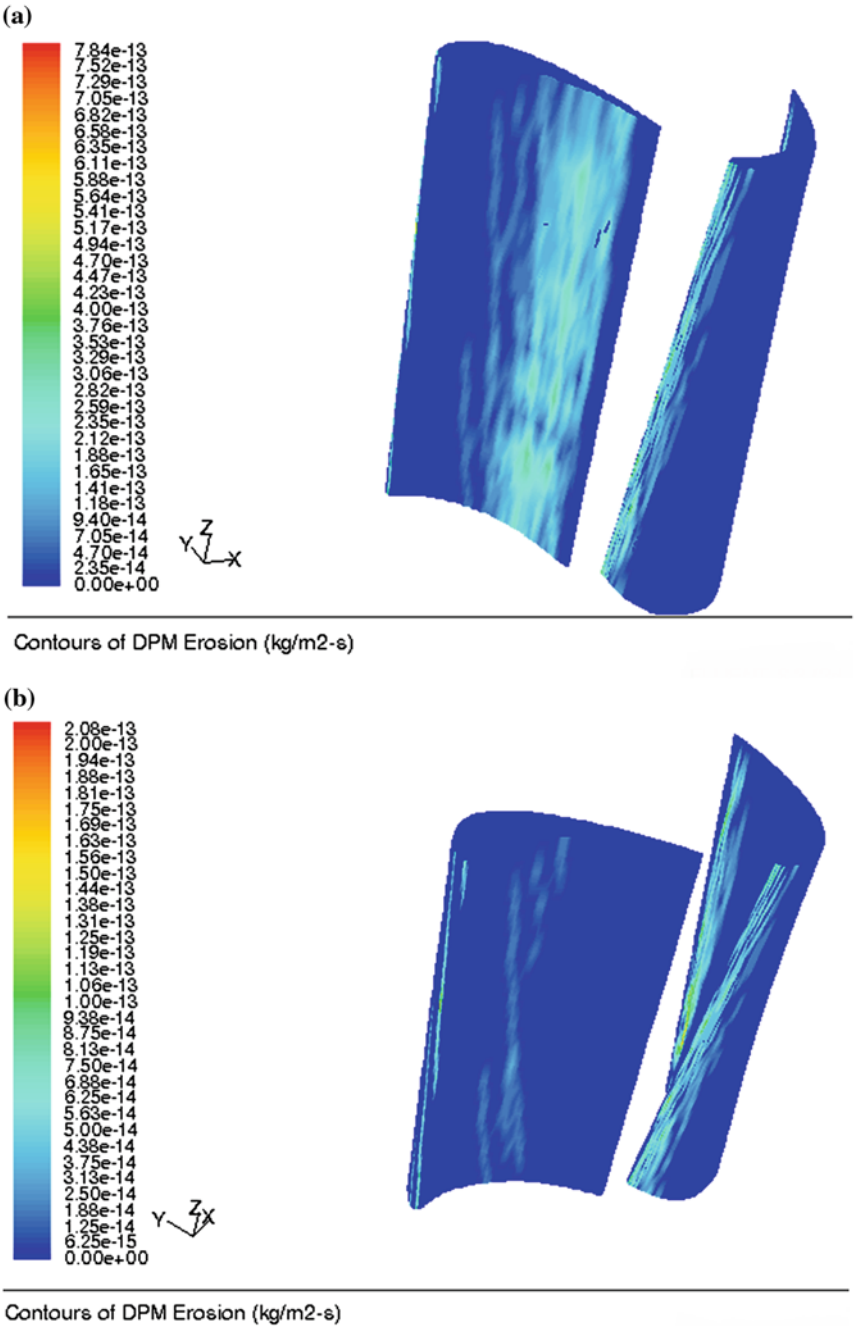

Fig. 9 **a**, **b** Turbine surfaces erosion effects—diameter d_1 = 0.025 mm and mass flow rate 0.133 kg/s (**a**); droplets' diameter d_2 = 0.005 mm (**b**)

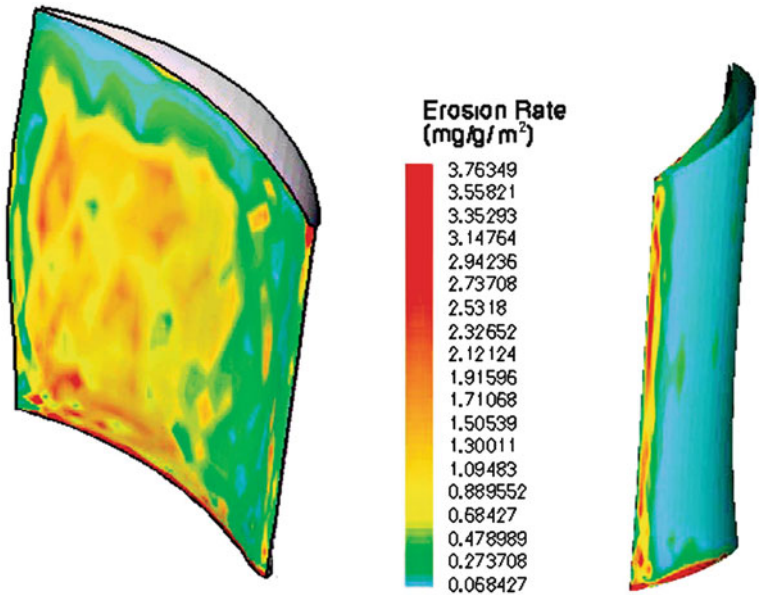

Fig. 10 Erosion effects on turbine blade after Hamed et al. [71]

increased erosion over the blade surfaces as it's shown in Fig. 9b. Verification of the obtained results is presented in Fig. 10.

In Fig. 11a are visualized liquid particles' traces and concentration on the blade surfaces, verification of the results after research of Hamed et al. [71] is shown in Fig. 11b.

Efficiency in energy conversion, in comparison with case without water droplets, is decreased with 3.77 % [46].

Roughness, as a result of erosion caused by water droplets, provokes different problems: blade surface roughness, certain energy losses; deteriorated aerodynamic performance and erosion effects [72] also profile geometry changes, worse aerodynamic behavior and efficiency decrease.

The current study shows that erosion and decrease in efficiency depend on water droplets diameter, their velocity, impact angles, mass flow rate; profile shape change in radial direction.

The approach can be applied for a study on the erosion effects in turbine aggregates, working in wet steam conditions and for research on methods implemented for decrease of erosion effects and their effectiveness.

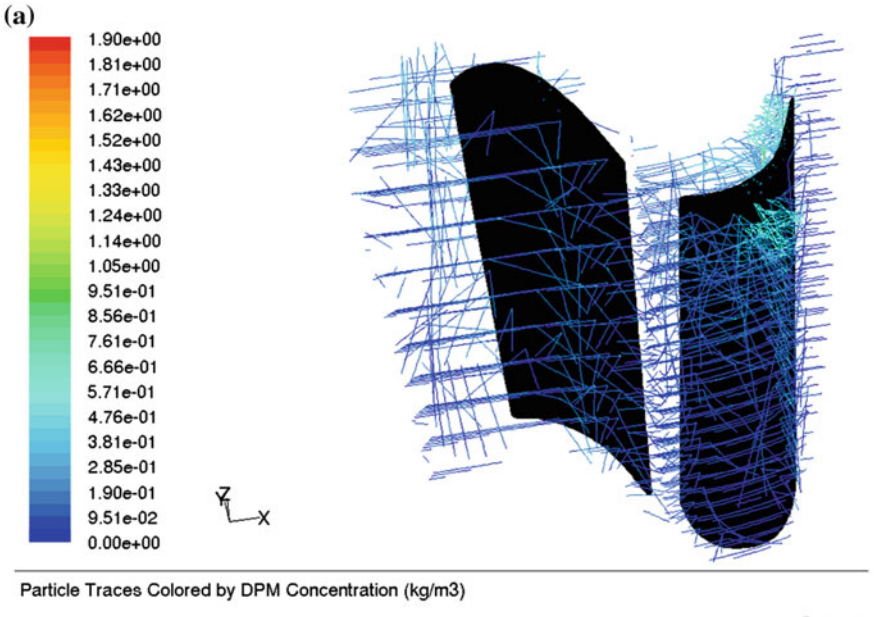

Fig. 11 Liquid particles' traces, coloured by discrete phase model concentration in kg/m^3 (**a**); liquid particle traces in the research of Hamed et al. (**b**) [71]

4 Conclusions

1. As a result of the performed global research, a logical scheme with specific approaches to surpass presence of bad elements and solution convergence problems, and perform a numerical modeling of specific features in turbine

stages, was elaborated. The logical sequence was applied for numerical modeling of 3D viscous, compressible and turbulent flow in turbine stage with rotating twisted rotor blade.
2. The logical sequence was successfully applied to perform: static pressure distribution along streamed profiles; research of aerodynamic and specific flow features at stator and rotor outlets; radial gap influence over flow parameters distribution; research on wet-steam conditions and roughness impact over blade surfaces; study on erosion effects over turbine blades; analysis of boundary layer growth along turbine blades and predicting it's separation. This methodology is applied for teaching purposes of students in Technical University—Varna.
3. The logical sequence can be applied as important and very useful methodology to attain all parameters needed for complex research and energy efficiency evaluation; study on strength, thermal stresses and modal analysis in turbo aggregates and their elements; research on exploitation in nominal and variable operating regimes; modernization and reconstruction of turbo-machines.

Acknowledgments The research work, presented herein, is a small part of dissertation thesis, accomplished in Technical University-Varna, Bulgaria. Specific codes, elaborated for the purposes of flow analysis are not shown and discussed here. I am gratefull to my supervisor Prof. Dr. Rumen Yossifov for his patience, support and precious ideas during my study.

References

1. Хауторн, У.Р.: „Аэродинамика турбин и компрессоров", Изд. „Машиностроение", М., 1968 (in Russian)
2. GRAPE 2-D Grid Generator for Turbomachinery: User's manual and documentation, Version 104, 24 Oct 1997
3. Fridh, J.: Experience from through-flow calculations with SCAM-T for a two-stage axial turbine-the streamline curvature method-version 1. Technical report January 2002 SNEA project P12457-2 (2002)
4. Sonoda, T., Arima, T., Olhofer, M., et al.: A study of advanced high-load transonic turbine airfoils. J. Turbomach. **128**(4), 650–657 (2006)
5. Wilkinson, D.H.: A numerical solution of the analysis and design problems for the flow past one or more aerofoils or cascades. Aeronautical Research Council Report and Memorandum, No 3545 (1968)
6. Wilkinson, D.H.: Calculation of blade-to-blade flow in a turbomachine by streamline curvature. Aeronautical Research Council Report and Memorandum, No 3704 (1972)
7. Wilkinson, D.H.: Stability, convergence and accuracy of two-dimensional streamline curvature method using quasi-orthogonals. IMechE Thermodynamics and Fluid Dynamics Convention 1970, Paper 35
8. Кириллов, А.И., Рис, В.В., Смирнов, Е.М., Ходак: „Расчет трехмерных турбулентных течений в турбомашинах на основе решения параболизованных уравнений Навые Стокса", А.Е., 1987г (in Russian)
9. Novak, R.A., et al.: A nearly three-dimensional interablade computing system for turbomachinery. ASME Papers 76-FE-19 and 76-FE-20, Parts I and II (1976)

10. Сироткин, Я.А., Степанов, Г.Ю.: „Установившееся осесимметричное вихревое течение невязкой жидкости в многоступенчатых турбомашинах", Изв. АН СССР, МЖГ № 6, 1981г (in Russian)
11. Kachel, C.E., Denton, J.D.: Experimental and numerical investigation of the unsteady surface pressure in a three stage model of an axial high pressure turbine. J. Turbomach. **128**(2), 261–272 (2006)
12. Oksuz, O.: Aerodynamic optimization of turbine cascades using an euler/boundary-layer solver coupled genetic algorithm. Doctoral thesis (2002)
13. Schaffarczyk, A.P., Pawlak, M., Richert, F.: New model for calculating intensities of turbulence in the wake of wind-turbines. DEWEK Lecturers Notes (2001)
14. Oyama, A., Liou, M.-S., Obayashi, S.: Transonic axial-flow blade shape optimization using evolutionary algorithm and three-dimensional Navier-Stokes solver. AIAA 2002-5642 (2002)
15. Zobeiri, A., Kueny, J.-L., Farhat, M., Avellan, F.: Pumpturbine rotor-stator interactions in generating mode: pressure fluctuation in distributor channel. In: 23rd IAHR Symposium—Yokohama, Oct 2006, vol. 1, Issue 10 (2006)
16. Holley, B.M., Becz, S., Langston, L.S.: Measurement and calculation of turbine cascade endwall pressure and shear stress. J. Turbomach. **128**, 232–239 (2006)
17. Pasinato, H.D., Kyle, D., et al.: Assessment of Reynolds-averaged turbulence models for prediction of the flow and heat transfer in an inlet vane-endwall passage. J. Fluids Eng. ASME **126**, 305–315 (2004)
18. Bonfiglioli, A., Sergio Campobasso, M.: Computing three-dimensional turbomachinery flows with an implicit fluctuation splitting scheme. In: Conference on Modeling Fluid Flow (CMFF'06), The 13th International Conference on Fluid Flow Technologies Budapest, Hungary, 6–9 September 2006
19. Biswas, D.: Studies on unsteady laminar-turbulent transition caused by wakes in turbine rotor-stator interaction based on a hybrid-LES model. In: 35th AIAA Fluid Dynamics Conference and Exhibit, 6–9 June 2005. Toronto, Ontario Canada, AIAA 2005-4770 (2005)
20. Doi, H., Alonso, J.J.: Fluid/structure coupled aeroelastic computations for transonic flows in turbomachinery. In: Proceedings of the ASME Turbo Expo 2002, 3–6 June 2002. Amsterdam, The Netherlands (2002)
21. Yang, H., Nuernberger, D., Kersken, H.-P.: Toward excellence in turbomachinery computational fluid dynamics: a hybrid structured-unstructured reynolds averaged Navier-Stokes solver. J. Turbomach. **128**, 390–402 (2006)
22. Yan, J., Gregory-Smith, D.: CFD Simulations of 3-Dimensional flow in turbomachinery applications. Presented at Turbomachinery Flow Prediction VIII ERCOFTAC WorkshopLac Clusaz, France, March 2000
23. Gier, J., Stubert, B., Brouillet, B., de Vito, L.: Interaction of shroud leakage flow and main flow in a three-stage LP turbine. In: Proceedings of the ASME Turbo Expo 2002, 3–6 June 2002. Amsterdam, The Netherlands (2002)
24. Laumert, B., Matensson, H., Fransson, T.H.: Investigation of the flowfield in the transonic VKI BRITE EURAM turbine stage with 3D steady and unsteady N-S computations. ASME Paper, 2000-GT-0433
25. Ameri, A.A.: Heat transfer and flow on the blade tip of a gas turbine equipped with a mean-camberline strip. NASA/CR-2001-210764 2001-GT-0156 (2001)
26. Anziam, J., Wu, Y.H., Wiwatanapataphеey, B., et al.: An exponentially fitted enthalpy control volume algorithm for coupled fluid flow and heat transfer. ANZIAM J. **42**(E), C1580, C1598 (2000). http://anziamj.austms.org.au/V42/CTAC99/Wu2
27. Craft, T.J., Launder, B.E., Suga, K.: A non-linear eddy-viscosity model including sensitivity to stress anisotropy. In: Proceedings of the Tenth Symposium on Turbulent Shear Flows, pp. 23-19–23-24, 173 (1995)
28. Innovative Turbulence Modeling: SST Model in ANSYS-CFX: Technical brief, ANSYS-CFX (2005)

29. Uzol, O., Brzozowski, D., Chow, Y.C., et al.: A database of PIV measurements within a turbomachinery stage and sample comparisons with unsteady RANS. J. Turbul. **8**(10), 1–20 (2007)
30. Iahr, W.G., Ruprecht, A., Bauer, C., et al.: The behaviour of hydraulic machinery under steady oscillatory conditions. Unsteady forces on the blading of an axial turbine caused by stator-rotor interaction. http://www.ihs.uni-stuttgard.de
31. Jaime Fernandez-Castaneda, S.A., Corral, R.: Surface mesh generation by means of Steiner triangulations. Industria de Turbo Propulsores. AIAA J. **39**(1), 176–180 (2001)
32. Hughes, T.J.R., France, L.P., Hulbert, G.M.: A new finite element formulation for fluid dynamics the Galerkin/least-squares method for advective-diffusive equations. Comput. Methods Appl. Mech. Eng. **73**, 173–189 (1989)
33. Buntić Ogor, I., Dietze, S., Ruprecht, A.: Numerical simulation of the flow in turbine-99 draft tube. In: Proceedings of the Third IAHR/ERCOFTAC Workshop on Draft Tube Flow, Porjus, Sweden, 8–9 Dec 2005
34. Xie, D., Yu, X., Li, W., et al.: Numerical simulation of water droplets deposition on the last-stage stationary blade of steam turbine. Energy Power Eng. **2**, 248–253 (2010). doi:10.4236/epe.2010.24036, http://www.SciRP.org/journal/epe. Accessed Nov 2010
35. Menter, F.R.: Zonal two equation k-w turbulence models for aerodynamic flows. In: AIAA Paper #93-2906, 24th Fluid Dynamics Conference, July 1993
36. GAMBIT 2 Tutorial Guide, December 2001
37. Yao, J., Jameson, A., Alonso, J.J., et al.: Development and validation of a massively parallel flow solver for turbomachinery flows. J. Propul. Power **17**(3), 659–668 (2001)
38. Fernández Oro, J., Argüelles Díaz, K., Santolaria Morros, C., et al.: Unsteady flow analysis of the stator-rotor interactions in an axial flow fan. In: Proceedings of the ASME FEDSM'03 4th ASME_JSME Joint Fluids Engineering Conference Honolulu, 6–10 July 2003. Hawaii, USA, FEDSM 2003-4 5394 (2003)
39. Huitao, Y.: Investigations of flow and film cooling on turbine blade edge regions. A dissertation by Huitao Yang, August 2006, 46 (2006)
40. Song, B., Ng, W.F.: Performance and flow characteristics of an optimised supercritical compressor stator cascade. J. Turbomach. **128** (2006)
41. Lefebvre, M., Arts, T.: Numerical aero-thermal predictions of laminar/turbulent flows in a two-dimensional high pressure turbine linear cascade. http://euroturbo.org
42. Takemitsu, N.: An analytical study of the standard k–ε model. J. Fluid Mech. **112**(6), 192–198 (1990)
43. Menter, F.: Turbulence modeling for turbomachinery applications. QNET-CFD Meeting, Lucerne (2002)
44. Lapwort, L., Shahpar, S., Neittaanmäki, P., Rossi, T., Korotov, S., O˜nate, E., Périaux, J., Knörzer, D. (eds.): Jyvakyl "Design of Gas Turbine Engines Using CFD". In: European Congress on Computational Methods in Applied Sciences and Engineering ECCOMAS 2004, 24–28 July 2004
45. Lampart, P., Gardzilewicz, A., Yershov, S., et al.: Investigations of flow characteristics of an HP turbine stage including the effect of tip leakage and windage flows using a 3D Navier-Stokes solver with source/sink-type boundary conditions. In: Proceedings of the 2000 International Joint Power Generation Conference, 23–26 July 2000. Miami Beach, Florida, IJPGC2000-15004 (2000)
46. Ilieva, G.I.: Modelling, research and analysis of 3D real flow in turbine stages with complex geometry. Dissertation thesis, Technical University-Varna (2009)
47. Ilieva, G.I., Iosifov R.D.: Geometry modeling features for 3D turbine cascade with twisted rotor blade in GAMBIT. Acta Univ. Pontica Euxinus **2**(5), 7–12 (2005). ISSN:1312-1669
48. Sakai, N., Harada, T., Imai, J.: Numerical study of partial admission stages in steam turbine. JSME **2**(49), 212–217 (2006)
49. Yershov, S.V., Rusanov, A.: Numerical simulation of 3D viscous turbomachinary flow with high-resolution ENO scheme and modern turbulence model. CFD for Turbomachinery Applications 1–3 Sept 2001, Gdansk Poland (2001)

50. Acton, E., Cargill M.: Non-reflecting boundary conditions for computations of unsteady turbomachinery flows. In: Proceedings of the 4th International Symposium on Unsteady Aerodynamics and Aeroelasticity of Turbomachines and Propellers, pp. 211–228. http://www.springerlink.com
51. Brost, V., Ruprecht, A., Maihöfer, M.: Rotor-stator interactions in an axial turbine, a comparison of transient and steady state frozen rotor simulations. http://www.ihs.uni-stuttgart.de
52. Hohn, W., Gombert, R., Kraus, A.: Unsteady aerodynamical blade row interaction in a new multistage research turbine. Part 2: numerical investigation. In: Proceedings of the IGTI'01 ASME TURBO EXPO 2001, 04–07 June 2001. New Orleans, Louisiana, USA (2001)
53. Sleiman, M.: Simulation of 3-D viscous compressible flow in multistage turbomachinery by finite element methods. A thesis in the Department of Mechanical Engineering, Mohamad Sleiman (1999)
54. Рай, М.М.: „Моделирование взаимодействия ротора и статора турбины на основе решения трехмерных уравнений Навье-Стокса. Часть 1. Метод расчета", Аэрокосмическая техника № 3, 1990 (Journal of Propulsion and Power 1989 №3 pp. 305–311) (in Russian)
55. Rai, M.M.: A conservative treatment of zonal boundaries for Euler equation calculations. J. Comput. Phys. **62**, 472–503 (1986)
56. Rai, M.M.: An implicit conservative zonal boundary scheme for Euler equation calculations. Comput. Fluids **14**(3), 295–319 (1986)
57. Rai, M.M.: A relaxation approach to patched grid calculations with the Euler equations. J. Comput. Phys. **66**, 99–131 (1986)
58. Rai, M.M.: Navier-Stokes simulations rotor-stator interaction using patched and overlaid grids. J. Propul. Power **3**, 387–396 (1987)
59. Gier, J., Ardey, S., Eymann, S., Reinmöler, U., Niehuis, R.: Improving 3D flow characteristics in a multistage LP turbine by means of endwall contouring and airflow design modification Part 2: numerical simulation and analysis. In: Proceedings of the ASME TURBO EXPO 2002, 3–6 June 2002. Amsterdam, The Netherlands, GT-2002-30353
60. Laumert, B., Mårtensson, H., Fransson, T.H.: Investigation of unsteady aerodynamic blade excitation mechanisms in a transonic turbine stage. Part II: analytical description and quantification. ASME J. Turbomach. **124**, 419–428 (2002)
61. Laumert, B., Mårtensson, H., Fransson, T.H.: Investigation of unsteady aerodynamic blade excitation mechanisms in a transonic turbine stage. Part I: phenomenological identification and classification. ASME J. Turbomach. **124**, 410–418 (2002)
62. FLUENT 5 User's Guide, Volume 2, Fluent Incorporated, July 1998
63. GAMBIT 2 User's Guide, December 2001
64. Mumic, F.: Computational analysis of heat transfer and fluid flow in the gap between a turbine blade tip and the casing. http://www.vok.Ith.se
65. Ilieva, G.I.: Numerical modeling and investigation of 3D real flow in turbine stage with tip clearance—special features and approaches, convergence of numerical procedure. Part I. In: Proceedings of the TU-VARNA 2008 (2008). ISSN:1311-896X
66. Ilieva, G.I.: Numerical modeling and investigation of 3D real flow in turbine stage with tip clearance—special features and approaches, convergence of numerical procedure. Part II. Numerical results. In: Proceedings of the TU-VARNA 2008 (2008). ISSN:1311-896X
67. Villalpando, F., Reggio, M., Ilinca, A.: Assessment of turbulence models for flow simulation around a wind turbine airfoil. Model. Simul. Eng. **2011**(Article ID 714146), 8p (2011). http://dx.doi.org/10.1155/2011/714146
68. Jošt, D., et al.: Numerical flow simulation and efficiency prediction for axial turbines by advanced turbulence models. IOP Conf. Ser. Earth Environ. Sci. **15**, 062016 (2012). doi:10.1088/1755-1315/15/6/062016
69. Menter, F.R.: Two-equation Eddy-viscosity turbulence models for engineering applications. AIAA J. **32**(8), 1598–1605 (1994)

70. Cleak, J.G.E., Gregory-Smith, D.G.: Turbulence modeling for secondary flow prediction in a turbine cascade. J. Turbomach. **114**(3), 590–598 (2008) (Jul 01, 1992) (9pp). doi:10.1115/1.2929183History. Accessed 06 Feb 1991; Online 09 June 2008
71. Hamed, A.A., Tabakoff, W., Rivir, R.B., et al.: Turbine blade surface deterioration by erosion. J. Turbomach. **127**, 445 (2005)
72. White, L.C.: Modern Power Station Practice. British Electricity International, Pergamon Press, London, 1–659 (1992)
73. Wu, C.H., Beck, P.: A general theory of three-dimantional flow in subsonic turbomachines of axial-, radial-, and mixed-flow types. National Advisory Committee for Aeronautics, Technical Note, no. 2604, Washington D.C.(1952)

Unsteady Interaction Effects Between an Airship and Its Air-Jet Propulsion System

Galina Ilieva, José Páscoa, Antonio Dumas and Michele Trancossi

Abstract An airship able to travel from ground to 15 km altitude is being developed on course of the European Research Project MAAT—Multibody Advanced Airship for Transportation. The airship has a cylindrical shape when completely inflated at the pressure altitude. Based on an initial research for the airship shape and aerodynamic features at given altitudes, propulsion needs were analyzed by means of numerical simulations for different flow conditions and propulsion concepts. The propulsion system is comprised of two rows of air-jets, at top and bottom of the airship, that expel cold air in order to provide propulsion thrust. Herein, we will present the steady and unsteady results of the computations regarding the interaction of the air-jets with the airship. Then, a detailed analysis on the vortex shedding from the airship is presented when it in subjected to only horizontal movement, this is further enhanced by computing the near vehicle flow when it is subject to the incoming wind. We will also present details about the total required thrust power for the various working conditions. The outcome of the research highlights the main advantages of the system to attain feasible high altitude airships.

1 Introduction

The hybrid airships include the best from classic airship technology and conventional fixed-wing lifting technology. They combine the principle of buoyancy with a lifting body for additional payload capacity.

G. Ilieva (✉) · J. Páscoa
Departamento de Engenharia Electromecânica, Universidade da Beira Interior,
R. Marquês D'Ávila e Bolama, 6201-001 Covilhã, Portugal
e-mail: galinaili@yahoo.com

A. Dumas · M. Trancossi
Department of Science and Methods for Engineering, University Modena e Reggio-Emilia,
Via Amendola, 2 Pad. Morselli, 42122 Reggio Emilia, Italy

K.Z.K. Shaari and M. Awang (eds.), *Engineering Applications of Computational Fluid Dynamics*, Advanced Structured Materials 44,
DOI 10.1007/978-3-319-02836-1_9

There are many projects, and research works, related to the study and implementation of new shapes, more feasible from an energy point of view, for airships and their associated propulsion technologies [1].

One of the ongoing projects is related to an innovative shape and propulsion system design, it is the MAAT project—Multibody Advanced Airship for Transportation, supported by the 7th Framework Program. This project, that comprises 12 research institutions, introduces the idea to use a cruiser (PTAH—Photovoltaic Transport Aerial High) altitude system/feeder (ATEH—Aerial Transport Elevator Network feeder) concept to allow transport of people and goods [2].

The cruiser is an air-vehicle operating at stratospheric altitudes, controlled by buoyancy. In particular the feeder is an airship which transports people from ground to the cruiser and from the cruiser to the ground. In this case the cruiser is designed for long, non-stop flight at economical altitudes and also to operate mainly at stratospheric altitudes. The feeder is designed as a main balloon with vertical control by buoyancy, also with the ability of vertical climbing with a strong resistance to winds. It has the ability to drift and has an additional propulsive system, which is intended for stabilization and approaching operations near the cruiser and of the airport hub (at least vertical take-off and landing capacity must be guaranteed). For this novel airship concept a new envelope and propulsion concept design are envisaged [3, 4].

To propel an airship through the air, some kind of power source and a way of applying it, is required. At the end of the eighteenth century the only available power sources were horsepower, steam power and manpower. Various ways of applying these were used: oars, paddles and flapping wings among them, but the only way which worked was the airscrew (propeller) [1, 5]. The real “Age of The Airship” became possible in 1883, when Gottlieb Daimler built the World’s first four stroke petrol internal combustion engine.

Most of classical airships relied on internal combustion engines running on Otto or Diesel cycles. However, the internal combustion engines are heavier than turbine engines, even if presenting lower fuel consumption for small sized engines.

Over the years both the internal combustion and turbine engines have evolved and nowadays they present very good reliability, in particular turbo shaft engines.

Recently, the possibility of solar powered air vehicles established a new era in the airship industry. The solar airships are foreseen as an easier way to achieve a given altitude than heavier-than-air aircraft, since there is no need to distribute the propulsion power to create a lift. In this way the power budget is strongly reduced [6, 7].

Propellers are one of the most widely used thrusters, but many exploitation problems were observed through the years. These problems are, namely, their bad performance at low Re number, blade tip vortices, etc. But, stern mounted propellers reduce boundary layer separation by suction. However this is only a feasible approach at very low Reynolds numbers [8, 9]. Mainly because the suction effect of a stern-mounted propeller affects the flow in the aft portion of the airship hull, which is accelerated. The resulting suction force on the body is oriented downstream, which causes an additional propeller induced pressure drag. On the other

hand, when a stern propeller is working in the airship wake, the axial velocity is decreased. This leads to reduction in required power by the propeller to produce a certain thrust. For reducing propeller blade tip losses and directing its thrust, a ducted fan is used.

Stern mounted propellers could be used as a propulsive element, but they are usually not acting alone, in particular because they do not offer the flexibility to provide wider maneuverability. Also, at very low speeds the control surfaces are considered ineffective, since they cease to produce dynamic lift to control the attitude of the airship. Most of the time tilting rotors are preferred as a stand alone or in combination with stern propellers [1].

Ducted fans are more efficient in producing thrust than a conventional propeller, especially at higher rotational speeds [10, 11]. Also, ducted fans present lower noise and safer handling for ground crews.

The hybrid airship concept use lifting gas to obtain static lift. Airships can operate in Vertical Take-Off and Landing conditions (VTOL). Powerful engines, that use thrust vectoring technology, for change in direction, are included on most current airships. The aim is to overcome both low speed maneuverability and changes in incoming wind stream.

VTOL is obtained mainly by vectorized thrusters [12, 13]. However, propellers for VTOL and cruise operation, for example, are used in some projects [14].

Among one of the less conventional means of propulsion for airships is the cycloid rotor moving around a horizontal axis, perpendicular to the direction of a normal flight [15]. The cycloid propeller can provide thrust force in any direction and also to help hover. This consists of several blades rotating around a horizontal axis, perpendicular to the direction of normal flight [16–20]. The angle of the individual blades, to the tangent of the circle of the blades path, is varied by a pitch control mechanism. This is designed so that the periodic oscillation of the blades, about their span axis, may be changed both in amplitude and in phase angle. The net force vector acting on the axis of the cycloidal rotor may be varied in magnitude and direction by the movement of the eccentricity point that controls the blades pitch. Thus, the air vehicle has very good maneuverability and fast response.

Another airship alternative propulsion concept is related to the so called fish-like movement in air, obtained by dielectric elastomers [21–24]. The bending of the fish-like body increases the velocity drastically and introduces a relevant contribution to the propulsion.

One of the nowadays concepts is the idea for propulsion based on air-jets. In the area of airship propulsive systems there has been a big variation of concepts proposed during the years, at all [1].

In the most recent years unsteady flows around vehicles are also being increasingly, mainly due to the availability of reliable numerical codes. There are many reasons for considerably unsteady effects, but one of the most important is that the unsteady flows present properties that can be exploited for control of advanced flight vehicles. In addition all flying vehicles must maneuver from one point to another and as a result all they experience unsteady conditions.

For vehicles that depend on the surrounding fluid for maneuvering, such as airships, the vortices generated in the flight time are convected downstream. For subsonic flow, as is the flow in the current case, flow property information from the downstream convected fluid is transferred back upstream. Therefore, the past history of the motion of the vehicle is needed to determine its instantaneous states and one need of an unsteady solution.

CFD is an effective tool for the unsteady analysis of complex flows, and it is routinely used in the design process of more efficient air vehicles and propulsion system components. Its success is due to the flexibility in the investigation different working conditions, and on the capability in analyzing overall and detailed information about the flow field.

Unsteady calculations analysis can help to better understand and research on the specific flow features, in case of the gust response on an airship. This is very important to assess the aero-elasticity and stability control requirements. Unsteady analysis will give detailed information about vortex structures development, and forces and moments acting one airship's hull, which play a significant role on the static and dynamic analysis. Having forces for different time steps, during the flight, one can obtain also the power budget.

The present work is focused on implementation and analysis of unsteady performance of the air-jets propulsion concept for an innovative airship. The main part of this study is concerned on the air-jets interaction, effects and needs for a High Altitude Airship (HAA). The numerical analysis is performed in FLUENT.

2 Problem Formulation

The objective of the current study concerns the implementation of unconventional propulsion system for an airship with an innovative shape and VTOL capability. It is attained by performing a numerical modeling on its steady and unsteady aerodynamic and propulsion performance.

It is preferable for airships with VTOL and horizontal cruise flight capability to have vectorized thrust. Thrusters must have high efficiency and capable of rapid changes in thrust according to the flight needs. A HAA airship needs to be light and have an efficient propulsion system that can operate with little or no oxygen. This is important when an airship operates, in the thin atmosphere, at very high altitudes and for extended periods of time [25].

All the above mentioned requirements are covered by the present innovative propulsion system, based on the air-jets concept. The underlying idea is to apply a set of air-jets, distributed in circular row around both the top and lower side parts of the feeder's structure. The air-jets work with an ambient air that is blown in by fans, through two main inlets, Fig. 1. These two inlets are connected with a central tube, which let the maneuverability of the airship to be increased. The air, accelerated by the fans, passes through a set of pipe ducts located within the airship body. The pipe ducts are designed with variable cross-section along their length. The main purpose

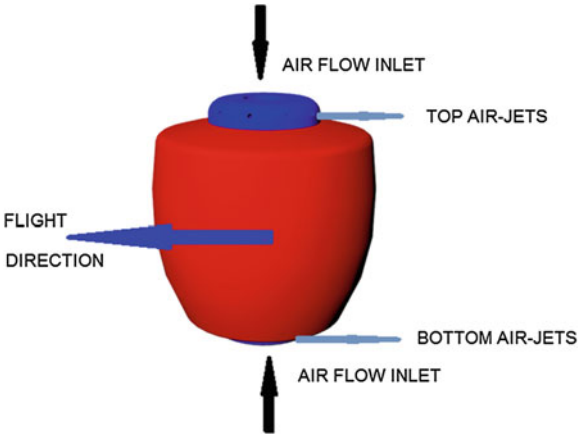

Fig. 1 Air-jets propulsion concept

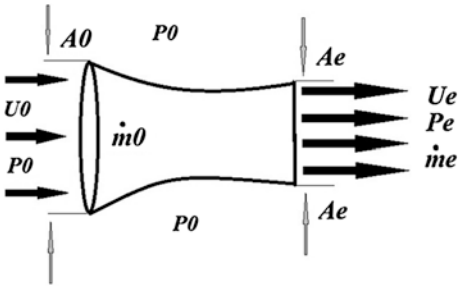

Fig. 2 Air-jets working principle

for that is to achieve a high mass flow rate at lower air flow velocity, thus reducing losses. The air is blown from a set of pipe channels into the ambient atmosphere at increased velocity. These air-jets generate thrust to drive the airship in horizontal direction. Both the number and sequence of the working air-jets depend on the flight direction and on power requirements for the current flight regime.

Figure 2 shows the physical principal on which is based the air-jets propulsion concept. This physical principle, in combination with the known Coanda effect [26], lead to increase of lift force and also to a boundary layer separation point shift, as it is pointed in [27].

Thrust generated by each air-jet is given by $T = \dot{m} \cdot ue + Ae \cdot (pe - p0)$. Propulsive efficiency is given by $\eta_{prop} = 1/(1 + ue/u0)$, where Ae-cross sectional area for air-jet outlet, [m^2]; $\dot{m}$-mass flow rate through the air-jet channel, [kg/s]; p0-ambient pressure, [Pa]; pe-achieved pressure at air-jet channel outlet, [Pa]; u0-incoming air velocity at air-jet inlet, [m/s]; ue-velocity at air-jet outlet, [m/s]; T-generated thrust, [N]; η_{prop}-propulsive efficiency, [-].

The fitting of the aerodynamic configuration with the power-source must be accomplished in a way that maximizes the performance at specific design condition. For that purpose, we need of an unsteady analysis to predict the interaction features between the airship's hull and its propulsion elements.

The ambient conditions affect strongly the aero-dynamic performance of bodies. A detailed research on the interaction of air-jets, design shape and incoming flow for the case of specified conditions is needed. Advances in aerodynamic performance related to the interaction between the airship and the working air-jets can be made, in particular if the complex vortices generation and turbulent separation flow phenomena can be understood, modeled and then included in the design process. The prediction of the unsteady flow field is an affordable item, and is required by the reduced margin of efficiency increase for the working air-jets, stability control and propulsion components.

In order to have a deeper insight on the phenomena concerning the evolution of the vortices, and on the effect of unsteadiness on the global power needs, a very accurate analysis, based on unsteady solution calculation was done.

The main purpose of this study is to initiate a detailed unsteady research on air-jet performance, by working with high mass flow rates to reach high efficiency at a low flow speed.

3 Numerical Simulation

The HAA's geometry is shown on Fig. 1. Maximum diameter is *Dmax* = 87 m and maximum height is *Hmax* = 96 m, calculated volume is $V = 412{,}013\ m^3$. Reference area used for *drag force* calculation is $Aref = 6{,}968.302\ m^2$. Air inlets at top and bottom parts of the feeder's structure have a diameter in function of the needed mass flow and number of working air-jets, five meters. For each air-jet (in case of eight acting air-jets) the outlet diameter is 2 m.

To discretize the *airship* geometry and fluid domain, a hybrid mesh is created with included boundary layer grid, Fig. 3a. The boundary layer mesh is formed by 20 rows of structural elements, with factor of growth 1.1. The first row of elements is at height of 0.0001 m. This provides an opportunity to observe streaming and separation effects over the envelope surfaces and obtains drag coefficient changes for each time step. The total number of elements that were used for flow domain approximation is more than 1,300,000.

The level of discretization ensures a detailed description of all flow features. This is very important in the near wall zones, especially where the working air-jets interact with the incoming air flow and with the *airship*'s hull.

Boundary zones, for both the steady and unsteady analysis, are "pressure far field", "mass flow inlet", "wall" and "fluid". The boundary conditions for "pressure far field" are a static pressure 12,112 Pa, static temperature 216.65 K and the Mach number is 0.1016. Turbulent intensity (2–5 %) and the length scale (0.8 for the airship hull and 0.02 for the air-jets' outlets) are defined for both the pressure far field and the mass flow inlet boundary zones.

The working fluid is considered viscous and turbulent, all physical properties are in a function of the flight altitude [28].

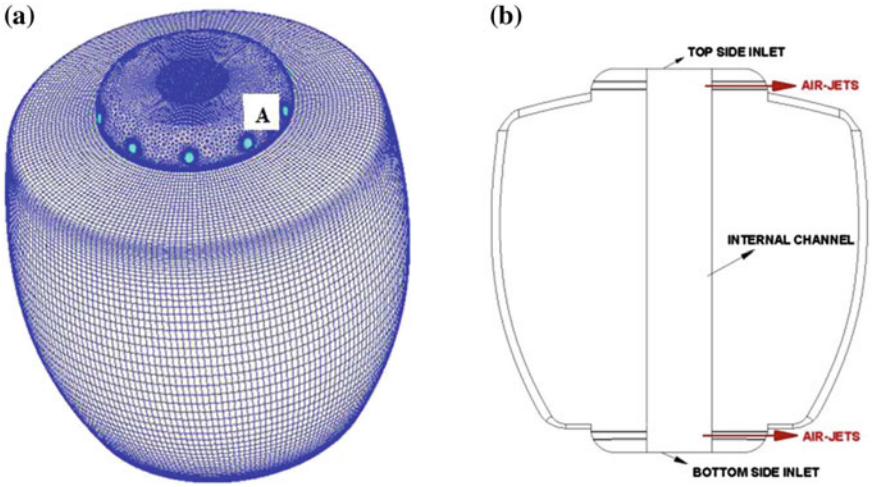

Fig. 3 **a**, **b** *Airship*'s design shape geometry and mesh around the walls (A-air-jets at the *top side*) (**a**), positioning of the air-jet channels (**b**)

Calculations were performed for an imposed airship velocity of 15 km/h and for wind speed, corresponding to the MAAT project requirements [2]. Mass flow rate, set as boundary condition at each air-jet outlet, is such that ensures needed thrust at the altitude under consideration. Mass flow rate and air-jets velocity are specified after numerical simulations, which have been performed for power requirements, according to the computed drag coefficient.

Solution of RANS equations with a Realizable k-ε closure turbulence model, valid adjacent to the walls, is based on a density-based solver, described in [29].

The Realizable k-ε model offers improved performance and solutions for boundary layers under strong adverse pressure or separation; it also resolves steep gradients near walls [30]. The term "realizable" means that the model satisfies certain mathematical constraints on the Reynolds stresses in a way that is consistent with the physics of turbulent flows. The Realizable k-ε turbulence model shows very good agreement between the numerical and experimental results in cases of strong separation [29]. Also, similarly to the k-ω SST (Shear Stress Transport) model, the Realizable k-ε model managed to capture the flow separation effects [31]. This model has been extensively validated for a wide range of flows [15, 32].

It is well known that when the boundary layer separates from a surface forms a free shear layer and is highly unstable. This shear layer eventually will roll into a discrete vortex and detach from the surface under consideration. The vortex shedding occurs at a discrete frequency and is a function of the Reynolds number.

In order to perform unsteady solution, we need of a correct choice for time step size and to define a maximum number of iterations per time step. The shape under consideration is close to a cylinder. The shedding Strouhal number, St = f D/V, in this case is approximately equal to 0.21, when the Reynolds number is greater than 1,000.

To capture the shedding correctly, we must have from 20 to 25 time steps in one shedding cycle. Knowing both the air flow velocity and the feeder's body diameter, we can calculate the cycle time and time step size. The obtained values are as follows: 7 and 0.3 s. The maximum number for iterations per time step is 200.

Spatial discretization is based on a finite-volume method [33]. The solution approach is density-based method, with application of an implicit linearization of the flow equations.

A cell-centered layout is adopted, in which the flow variables (pressure p and velocity components u, v and w) are defined at a center of each cell. The discretization scheme chosen for each equation was Second-Order upwind; the quantities at the cell faces were computed using a multidimensional linear reconstruction approach. In this approach, higher-order accuracy is achieved at the cell faces through a Taylor series expansion of the cell-centered solution about the cell centroid.

During the unsteady simulations, each time step is including 200 iterations to ensure all convergence criteria for the given conditions and at the subsequent time iteration loop. The final solution, including the number of iterations to obtain convergence in steady-state mode, was obtained after around 23,000 iterations.

It is well-known that after each iteration, the values obtained for the unknown variables should become closer and closer together and thus converge. Due to strong non-linear equations, unsteady solution, separation and other aerodynamic effects, the solution is unstable; that is why a set of relaxation factors is used to remove the steep oscillations. For all under-relaxation factors, calculations were performed with initial values that were equal to the default values included in FLUENT. After a gradual decrease, the final value for each under-relaxation factor was 0.5.

Convergence is assumed to be obtained when the scaled residuals are in the range of 10^{-4} for all the unknown parameters; the exceptions are energy and turbulence parameters, which are 10^{-6}.

The obtained results and specific flow features, in case of steady and unsteady flow, are shown and discussed furthermore in the following sections.

4 Numerical Results and Discussions

Unsteady computations, based on a numerical modeling of eight acting jets, four at the top part and four at the lower part of the airship structure, are presented and discussed.

For the current numerical simulation, the air-jets are working at an imposed exit velocity of 260 m/s, corresponding to a mass flow rate for each of them of 203 kg/s. The overall concept for distribution of weights, buoyancy and required propulsion needs, also the ways to overcome the problems related to the impact of air-jet working parameters (mass flow rate and velocity) on the dimensions distribution, is already described in [25].

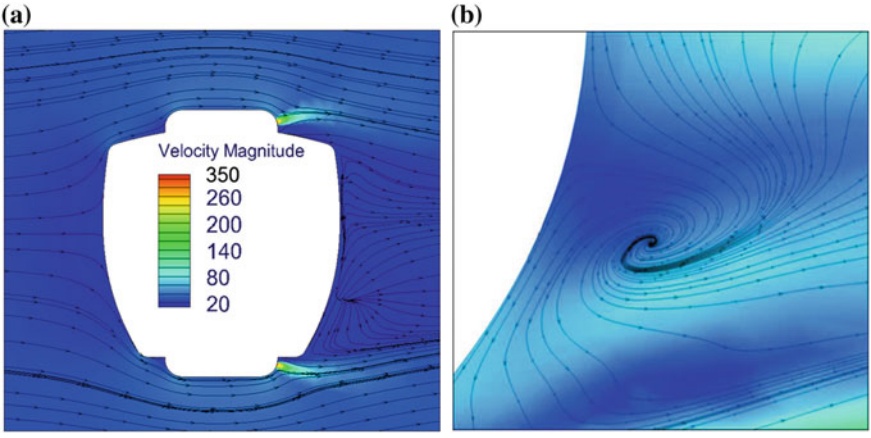

Fig. 4 **a**, **b** Velocity field distribution for the core flow with lateral velocity of 92 km/h and vertical velocity of 15 km/h, steady solution at time $t = 0$ s (**a**), unsteady solution at time $t = T$ s (**b**)

On the basis of the performed steady computations it is obvious that the airship body is affected by the incoming wind flow and by the air-jets behavior, leading to momentum decrease and boundary layer separation at the lateral walls, Fig. 4a.

From the unsteady solution it is shown that a vortex has developed for one time period, Fig. 4b. The vortex structure leads to worse aerodynamic performance, possible stability and control problems, Fig. 4b.

Air-jets, located at the top and bottom parts of airship hull interact with the incoming flow and generate vortex structures. The generated vortices cause worse aerodynamic performance and drag increase. This gives a rise to the thrust needs and to a necessity of a strong system for flight control.

In order to visualize the flow features around and at the rear airship part, three control sections were introduced, Fig. 5. Flow particle streamlines and vortices, at time t = 0 s, are presented for each control section, at both the upper and lower parts of the feeder's body, Fig. 5. Figures 6a–f, 7a–f, 8a–f and 9a–f show increased circulation zone around the airship, due to the interaction among the acting air-jets, air stream flow, and the separated boundary layer. This will cause significant losses in momentum and can involve pressure changes. The pressure differences are a reason vortex structures to appear. On Figs. 6f, 7f, 8f and 9f eddies at the bottom side increase their diameter due to shift in the minimum pressure area and strive to equalization. As it is shown on Figs. 6a–f, 7a–f, 8a–f and 9a–f, wakes are developing with time in upstream direction and at a definite distance. Some of them disappear and new vortex structures arises. In the same time, vortices magnitude (at given places) decrease from one to another control section and in upstream direction during one time period, Fig. 10a, b.

Vortex structures, which are formed due to the interaction between the two central air-jets and the incoming flow, at the bottom part of airship hull, have higher

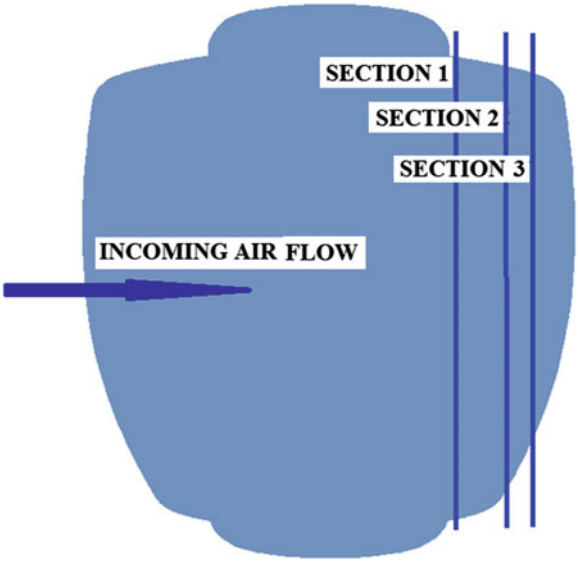

Fig. 5 Control sections created at the rear part of the *airship* hull for visualization of flow field features

vorticity than those raised due to the sideward air-jets. The vorticity change lead to irregularity in pressure distribution around the hull and will introduce stability problems. A change in vorticity means that there is additional force acting on the body under consideration.

The air flow past the airship hull interacts with the working air-jets and creates alternating vortices at air-vehicle's top and bottom sides, Figs. 6a–f, 7a–f, 8a–f and 9a–f. There retreat to a distance from the airship vertical axis, in upward flow direction, inducing a separated boundary layer flow in interaction with the incoming flow, as it is well visible on Figs. 6e–f, 7e–f, 8e–f and 9e–f. The circulation phenomena will result in variable lateral forces and moments acting on the ATEN airship hull.

Due to pressure differences around the airship, it will tend to move toward the low-pressure zone.

At time t = 0 s (steady simulation) the drag coefficient obtained is 0.745 and the corresponding *drag force* is 3,42,164.185 N. In case of unsteady calculations were observed periodic changes in both the drag coefficient and power budget values. Variations in drag values (from 0.7325 to 0.755) lead to a strong change in power required for propulsion needs, during one time period. These changes were found to be in the range of $(1.785–1.84) \times 10^7$ W.

Changes in propulsive power budget as a function of time will help to provide better design and performance of the overall propulsion system.

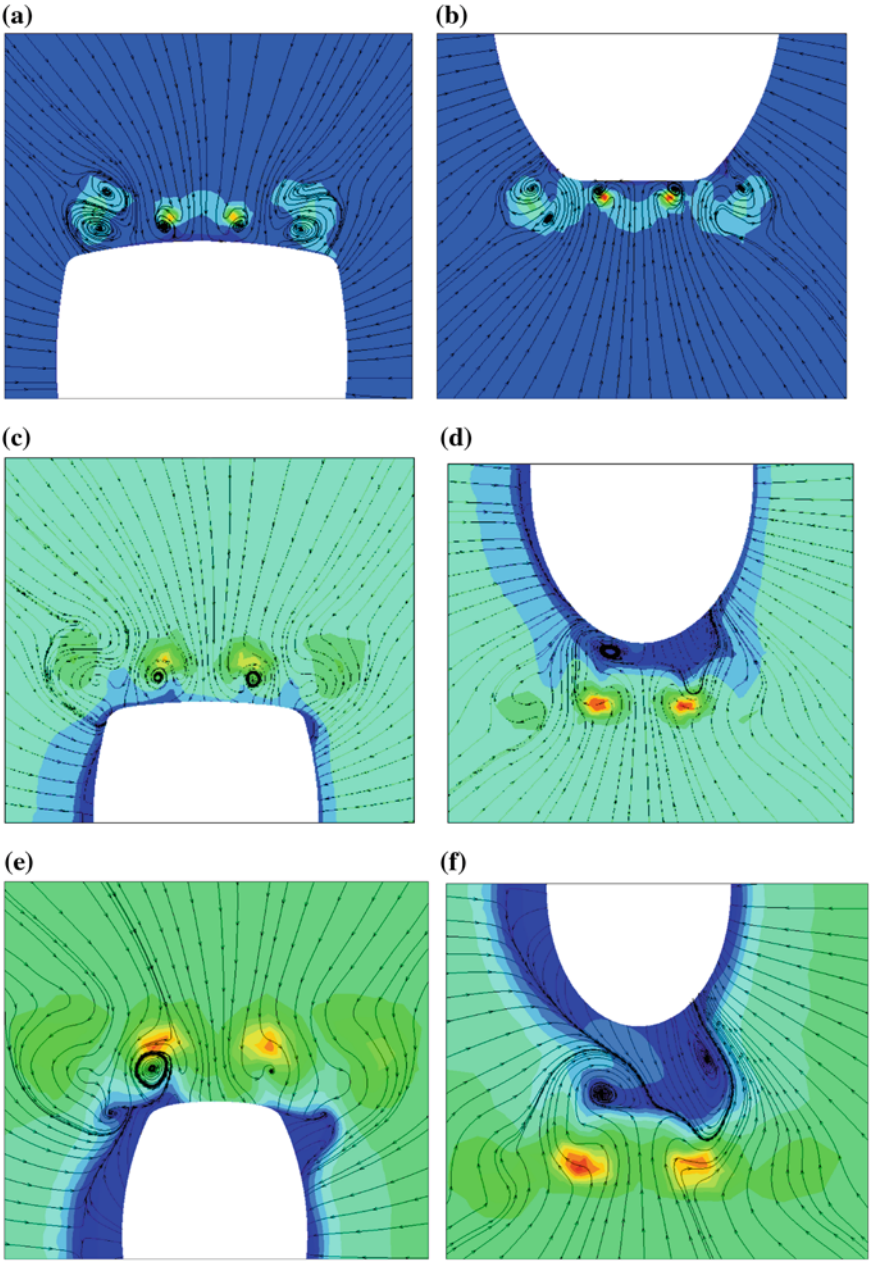

Fig. 6 **a–f** Streamlines and vortex structures (t = 0 s), obtained due to interaction between the working *air-jets* and the incoming air flow: *section 1-top* (**a**) and *bottom side* (**b**), *section 2-top* (**c**) and *bottom side* (**d**), *section 3-top* (**e**) and *bottom side* (**f**)

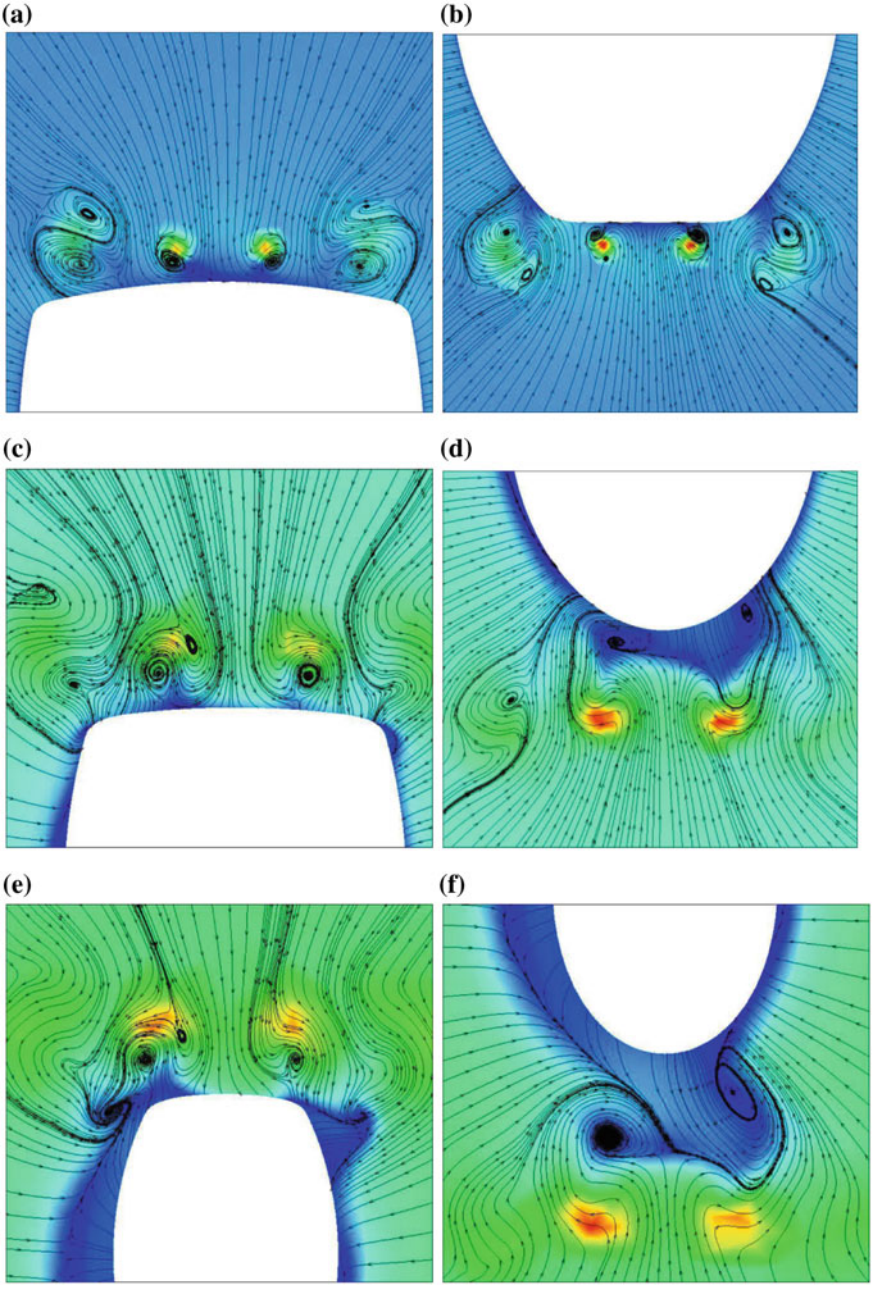

Fig. 7 **a–f** Streamlines and vortex structures (t = 1/4T), obtained due to interaction between the working air-jets and the incoming air flow: *section 1-top* (**a**) and *bottom side* (**b**), *section 2-top* (**c**) and *bottom side* (**d**), *section 3-top* (**e**) and *bottom side* (**f**)

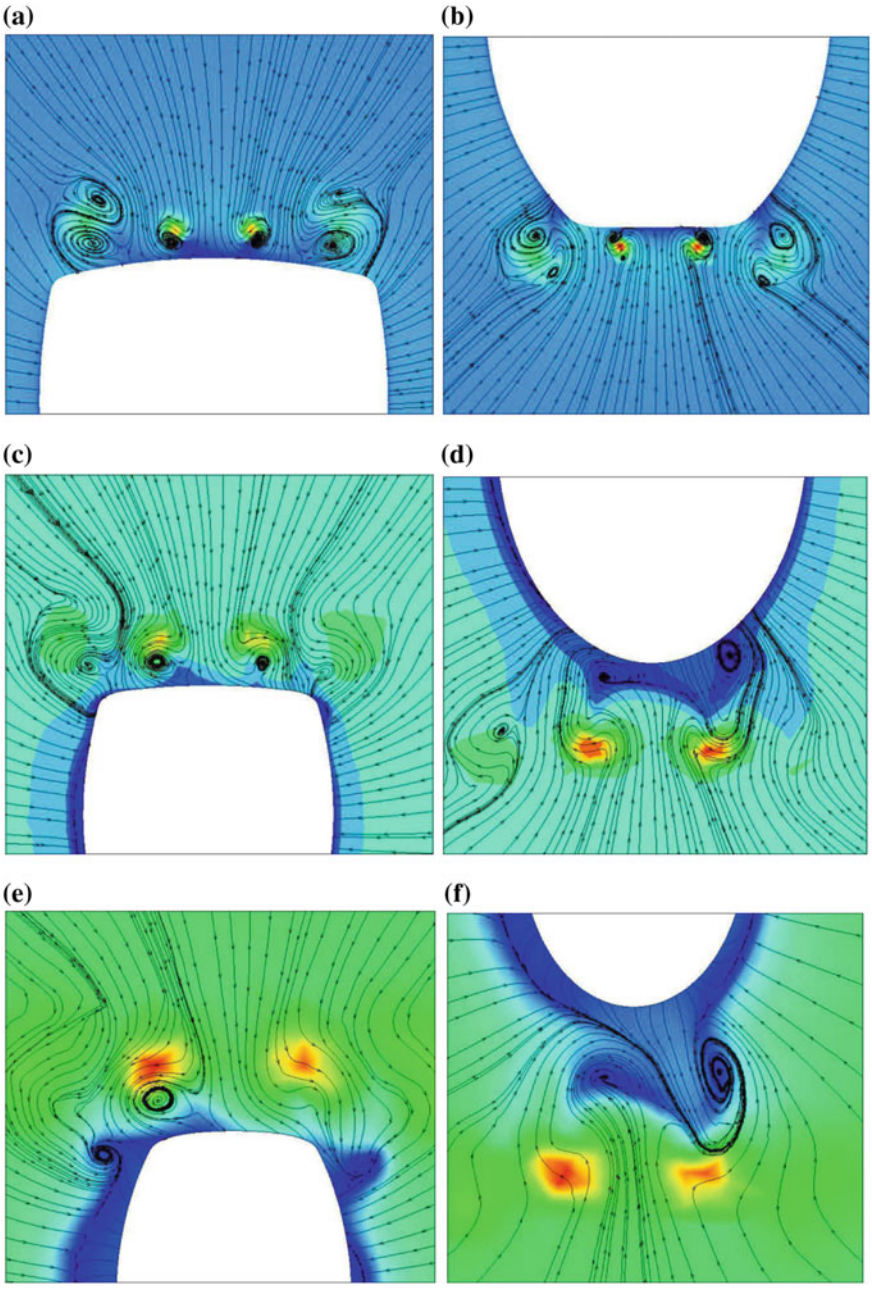

Fig. 8 **a–f** Streamlines and vortex structures (t = 1/2T), obtained due to interaction between the working air-jets and the incoming air flow: *section 1-top* (**a**) and *bottom side* (**b**), *section 2-top* (**c**) and *bottom side* (**d**), *section 3-top* (**e**) and *bottom side* (**f**)

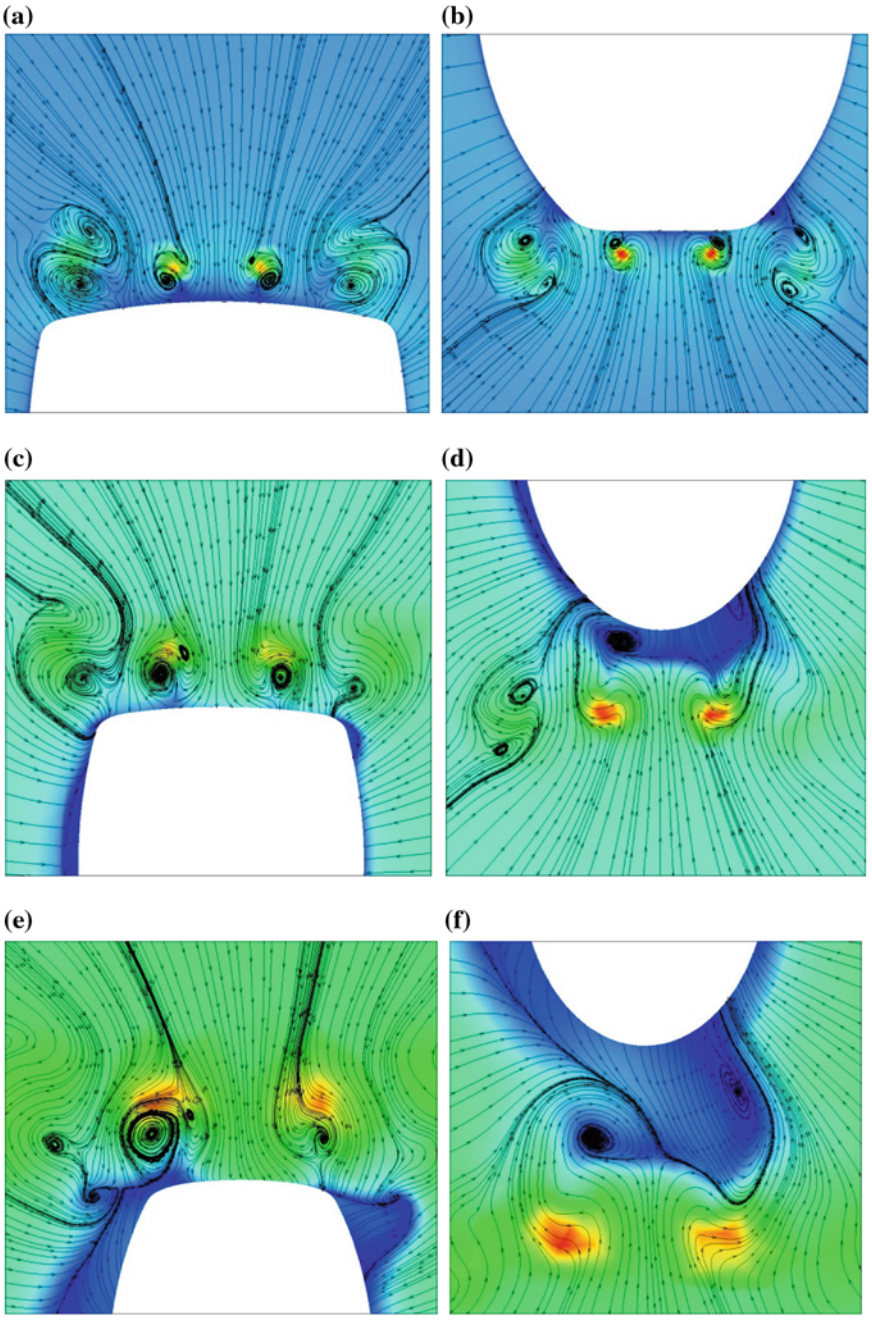

Fig. 9 **a–f** Streamlines and vortex structures ($t = T$), obtained due to interaction between the working air-jets and the incoming air flow: *section 1-top* (**a**) and *bottom side* (**b**), *section 2-top* (**c**) and *bottom side* (**d**), *section 3-top* (**e**) and *bottom side* (**f**)

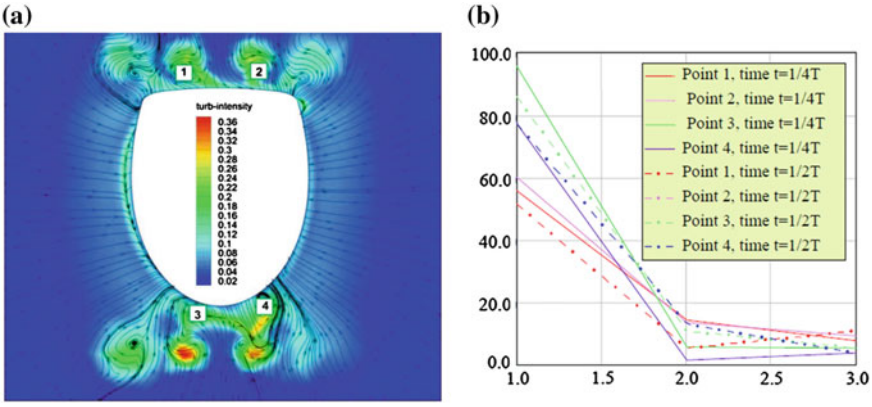

Fig. 10 **a**, **b** Four specific places to extract vorticity levels, originated due to interaction effects between the air-jets and the incoming flow (**a**), vorticity in 1/s at time $t = 1/4T$, $t = 1/2T$, shown on "y" axis for each control section on "x" axis, (**b**)

5 Conclusions

Lighter-than-air (LTA) vehicles represent a unique and promising platform for many applications that involve a long duration airborne presence. As LTA vehicles achieve their lift through buoyancy, they require much less power than a traditional aircraft. This leads to the possibility of using renewable energy sources, based on innovative propulsion systems, which would permit a controlled flight to be maintained almost indefinitely.

As a result of an aerodynamic study, presented in [25], and research on problems referred to overall performance, an innovative propulsion system with implemented air-jets concept was assessed. The propulsion system leads to airship weight reduction at all. It is very important for decrease of the gross power needed for propulsion.

The air-jets system is environmentally friendly and can operate with a reduced amount or absence of oxygen and contributes for fast change of the vectorized thrust. Also, the propulsion system leads to airship weight reduction at all. It is very important for decrease of gross power needed for propulsion. The thrusters have high efficiency and the possibility to fast change for thrust according to the flight needs.

In order to overcome the aerodynamic problems related to the airship, in particular regarding the propulsion system performance, an additional unsteady analysis was performed.

Unsteady computations have shown that the development of vortex structures and the increase of vortices in time take place for the airship under consideration. It is also observed that strong changes in both the drag coefficients and required power budget, were introduced. The additional vortex structures provoke less aerodynamic performance and stability problems. The obtained results for this research can be

used as a basis for a study on the frequency of vortex shedding and see if it is close to the natural frequency of some mode of vibration of the cylinder body (the shape of the airship under consideration is very close to a cylinder).

All the obtained results, and the solutions pointed out for better and efficient performance of the propulsion system, provide opportunities for future development of the research work, which is related to innovative propulsion concepts for airships.

Acknowledgments The results presented were obtained inside the MAAT Project (Multibody Advanced Airship for Transport), project grant number 285602, financed by the European Commission under the 7th Framework Program.

References

1. Ilieva, G., Páscoa, J.C., Dumas, A., Trancossi, M.: A critical review of propulsion concepts for modern airships. Cent. Eur. J. Eng. **2**, 189–200 (2012). ISSN: 2081-9927, doi:10.2478/s13531-011-0070-1. Received on 17-12-2011, accepted for publication on 18-02-2012
2. Dumas, A., Madonia, M., Giuliani, I., Trancossi, M.: MAAT cruiser/feeder project: criticalities and solution guidelines. In: SAE AEROTECH 2011, SAE Technical Paper 2011-01-2784 (2011). doi:10.4271/2011-01-2784
3. Ilieva, G., et al.: MAAT-Promising innovative propulsive concept for future airship's transport. Aerosp. Sci. Technol. (2014). doi:10.1016/j.ast.2014.01.014
4. Ilievam, G., Pascoa, J.C., Dumas, A., Trancossi, M.: Numerical analysis of aerodynamic performance and propulsion needs for an innovative airship. In: Proceedings MEFTE 2012 IV Conferencia Nacional em Mecanica dos Fluidos, Termodinamica e Energia, Lisbon, Portugal, Paper No 57, 11p (2012)
5. The Development of an Airship. www.barrygray.pwp.blueyonder.co.uk/Tutoring/Airships.html, 05 Jan 2012
6. Klesh, A.T., Kabamba, P.T.: Solar-powered aircraft: energy-optimal path planning and perpetual endurance. J. Guidance Control Dyn. **32**(4) (2009). doi:10.2514/1.40139
7. Iverson, Z., Achuthan, A., Marzocca, P., Aidun, D.: Optimal design of hybrid renewable energy systems (hres) using hydrogen storage technology for data center applications. Renew. Energy **52**, 79–87 (2003)
8. Lutz, T., Leinhos, D., Wagner, S.: Theoretical investigations of the flow field of airships with a stern propeller. In: Proceedings International Airship Convention and Exhibition, Bedford, England, pp. 1–12 (1996)
9. Lutz, T., Funk, P., Jakobi, A., Wagner, S.: Calculation of the propulsive efficiency for airships with stern thruster. In: 14th AIAA Lighter-Than-Air Technical Committee Convention and Exhibition, Akron, Ohio, USA, 15–19 July 2001
10. de Piolenc, F.M., Wright, G.E.: Ducted Fan Design: Millenial Year Edition-2001, vol. 1. Mass Flow, West Covina, CA (2001)
11. Turner, R.C.: Notes on ducted fan design. Technical Report 895, Aeronautical Research Council Current Papers (1966)
12. Kothman, T.: The Kothmann multi-use airship. US Patent 6648272b1 (2003)
13. Rademacher. A.T.: Very large luxury airship. AIAA J. **43**(1), 283–286 (2006)
14. Buerge, B.: Polar family of airships for surveying and cargo (2011). www.airshipstothearctic.com/docs/pr/14_Brandon_Buerge.pdf, cited on 16 Jan 2011
15. Kim, S.J., Yun, C.Y., Kim, D., Yoon, Y., Park, I.: Design and performance tests of cycloidal propulsion systems. In: 44th AIAA/ASME/ASCE/AHS Structures, Structural Dynamics, and Materials Conference, Norfolk, VA, AIAA Paper 2003-1786, April 2003

16. Iosilevskii, G., Levy, Y.: Experimental and numerical study of cyclogiro aerodynamics. AIAA J. **44**(12), 2866–2870 (2006)
17. Hwang, I.S., Kim, S.J.: Aerodynamic performance enhancement of cycloidal according to blade pivot point movement and preset adjustment. KSAS Int. J. **9**(2), 58–63 (2008)
18. Benedict, M., Ramasamy, M., Chopra, I.: Improving the aerodynamic performance of micro-air-vehicle-scale cycloidal rotor: an experimental approach. J. Aircr. **47**(4) (2010). doi:10.2514/1.45791
19. Benedict, M., Jarugumilli, T., Lakshminarayan, V., Chopra, I.: Experimental and computational studies to understand the role of flow curvature effects on the aerodynamic performance of a MAV-scale cycloidal rotor in forward flight. AIAA 2012-1629 Paper, 53rd AIAA/ASME/ASCE/AHS/ASC Structures, Structural Dynamics and Materials Conference 20th AI, Honolulu, Hawaii, 23–26 April 2012
20. Pascoa, J., Ilieva, G., Dumas, A., Trancossi, M.: Overcoming stopovers in cycloidal rotor propulsion integration on air vehicles. In: Proceeding of International Design Engineering Technical Conferences and Computers and Information in Engineering, at Chicago, Illinois, USA, 12–15 Aug 2012
21. Barrett, D.S., et al.: Drag reduction in fish-like locomotion. J. Fluid Mech. **392**, 183–212 (1999)
22. Jordi, C, Michel, S., Fink, E.: Fish-like propulsion of an airship with planar membrane dielectric elastomer actuators. Bioinspir. Biomim. **5** (2010). doi:10.1088/1748-3182/5/2/026007
23. Silvain, M, Bormann, A., Jordi, C., Fink, E.: Feasibility studies for a bionic propulsion system of a blimp based on dielectric elastomers. Proc. SPIE **6927**, 69270S–69270S-15. doi:10.1117/12.777588
24. Triantafyllou, G.S., et al.: Optimal thrust development in oscillating foils with application to fish swimming. J. Fluids Struct. **7**(2), 205–224 (1993)
25. Ilieva, G., Pascoa, J., Dumas, A., Trancossi, M.: Numerical research on efficiency performance of the propulsion system for an innovative airship. In: Proceedings of the ASME, DETC/CIE 2012, Paper No70927 (2012)
26. Dumas, A., Pascoa, J., Trancossi, M., Tacchini, A., Ilieva, G., Madonia, M.: ACHEON project: a novel vectoring jet concept. In: Proceedings of the ASME 2012 International Mechanical Engineering Congress and Exposition, IMECE 2012, Houston, Texas, USA. IMECE2012—87638, 9–15 Nov 2012
27. Trancossi, M., Dumas, A.: CFD based design of a nozzle able to control angular deflection. In: Proceedings of IMECE2011, ASME International Mechanical Engineering Congress and Exposition, Denver, Colorado, USA IMECE2011-12359, 11–17 Nov 2011
28. www.aerospaceweb.org. Design Scripts Atmosphere, cited on 17 Jan 2011
29. Castelli, M.R., Cioppa, P., Benini, E.: Numerical simulation of the flow field around a 30° inclined flat plate. World Acad. Sci. Eng. Technol. **63**. http://waset.org/publications/5926, 29 March 2012
30. Bakker, A.: Lecture Series on Applied Computational Fluid Dynamics Lecture 10, Fluent Inc. http://www.bakker.org/dartmouth06/engs150/10-rans.ppt, 2002
31. Furbo, E., Harju, J., Nilsson, H.: Project 9 evaluation of turbulence models for prediction of flow separation at a smooth surface. Report in Scientific Computing Advanced Course June (2009). http://www.it.uu.se/edu/course/homepage/projektTDB/vt09/project9/Report_vt09_09_new.p
32. Shih, T.H., Liou, W.W., Shabbir, A., Yang, Z., Zhu, J.: A new k-ε eddy-viscosity model for high Reynolds number turbulent flows-model development and validation. Comput. Fluids **24** (3), 227–238 (1995)
33. www.ansys.com. Documentation for ANSYS, cited on 22 Nov 2011

Numerical Investigation on the Nanofluid Flow and Heat Transfer in a Wavy Channel

M.A. Ahmed, M.Z. Yusoff and N.H. Shuaib

Abstract In this article, laminar convective heat transfer of copper-water nanofluid in isothermally heated wavy -wall channel is numerically investigated. The governing continuity, momentum and energy equations in body-fitted coordinates are discretized using finite volume approach and solved iteratively using SIMPLE algorithm. The study covers Reynolds number and nanoparticle volume concentration in the ranges of 100–800 and 0–5 % respectively. The effects of nanoparticles volume concentration and Reynolds number on velocity and temperature profiles, the local Nusselt number, the local skin-friction coefficient, average Nusselt number, pumping power and heat transfer enhancement are presented and analyzed. Results show that there is a significant enhancement in heat transfer by addition of nanoparticles. This enhancement increase with concentration of particles but the required pumping power also increases. The present results display a good agreement with the literature.

List of Symbols

a	Wavy amplitude, mm
A	Dimensionless wavy amplitude, (A = a/H)
C_f	Skin-friction coefficient
C_p	Specific heat, J/kg K
D_h	Hydraulic diameter, mm ($D_h = 2H$)
Dp	Dimensionless pressure drop, ($Dp = \Delta p/\rho_f u_{in}^2$)
f	Friction factor
h	Heat transfer coefficients, (W/m^2 °C)
H	Separation distance between wavy walls, mm

M.A. Ahmed
Mechanical Engineering Department, College of Engineering,
University of Anbar Ramadi, Anbar, Iraq

M.A. Ahmed · M.Z. Yusoff (✉) · N.H. Shuaib
Centre for Advanced Computational Engineering (CACE),
College of Engineering, Universiti Tenaga Nasional, Jalan IKRAM-UNITEN,
43009 Kajang, Selangor, Malaysia
e-mail: zamri@uniten.edu.my

K.Z.K. Shaari and M. Awang (eds.), *Engineering Applications of Computational Fluid Dynamics*, Advanced Structured Materials 44,
DOI 10.1007/978-3-319-02836-1_10

L_s	Length of smooth wall, mm
L_w	Length of wavy wall, mm
J	Jacobian of transformation
K	Thermal conductivity, W/m °C
Nu	Nusselt number
p	Pressure, Pa
P	Dimensionless pressure
Pr	Prandtl number
Re	Reynolds number
T	Temperature, °C
u, v	Velocities components, m/s
U, V	Dimensionless velocity component
x, y	2D Cartesian coordinates, m
X, Y	Dimensionless Cartesian coordinates
ζ, η	Body-fitted coordinates
α_f	Thermal diffusivity, m^2/s
α_ϕ, α_P	Relaxation factors
β_{11}, β_{12}	Transforming coefficients
β_{21}, β_{22}	Transforming coefficients
φ	Volume concentration of particles, %
ϕ	General variable
μ	Dynamic viscosity, Ns/m^2
ρ	Density, kg/m^3
θ	Dimensionless temperature
Δp	Pressure drop, Pa
eff	Effective
f	Base fluid
in	Inlet
l	Average value
nf	Nanofluid
p	Particles
w	Wall
x	Local value
c	Contravariant velocity

1 Introduction

The wavy-wall channel is one of the enhancement techniques that used to improve the thermal performance of heat exchangers. The heat transfer enhancement in such channel may be achieved by bulk fluid mixing and re-initiation of thermal boundary layer. As the fluid enters a wavy channel, the re-circulation zones occur in trough

(crest) of lower (upper) wall of wavy channel and hence improve the mixing of cold fluid with the hot fluid near to the walls of wavy channel.

The disturbed fluid in wavy channel lead to reduce the thickness of thermal boundary layer and increase the temperature gradient near the walls of channel. Because of the importance of heat exchangers in many industrial applications and to design more efficient devices, research on additional techniques for heat transfer enhancement has become essential. For this purpose and due to the poor thermal conductivity of traditional fluids such as water, ethylene glycol and oil, using nanofluids as a cooling fluids in these devices instead of conventional fluids can improve thermal conductivity of fluids and consequently further improvement in the performance of heat exchangers.

Many numerical and experimental studies in the past have been carried out to investigate the heat transfer enhancement in wavy passages using conventional fluids. O'Brien and Sparrow [1] experimentally investigated on the convective heat transfer in triangular-corrugated duct. They were found that the enhancement in heat transfer was around 2.5 over the straight channel but with a grater pumping power requirements. Sparrow and Comb [2] performed experiments to determine flow and heat transfer characteristics in triangular-corrugated duct using water as working fluid. They were observed that heat-transfer coefficient for the smaller spacing between the walls of channel was slightly higher than that for the larger spacing, and the pressure drop penalty was higher as well. Ali and Ramadhyani [3] have been experimentally investigated on the forced convection flow of water flow through triangular-corrugated channel. It was observed that the channel with larger spacing provides better performance than that of smaller spacing. Wang and Vanka [4] numerically investigated on the convective heat transfer in wavy passages. The governing transport equation, in term of curvilinear orthogonal coordinates, have been solved using two-stage fractional step procedure. It was found that the average Nusselt number is slightly increased in steady flow regime. In transitional flow regime, there was a significant increase in heat transfer, but there was a companied by increasing in the friction factor. Fabbri [5] performed a numerical study on the laminar heat transfer flow through composed, smooth and corrugated, walls channel using finite element model. Results showed that the enhancement in heat transfer of the optimum corrugated profile increases as Prandtl and Reynolds numbers increases. Wang and Chen [6] numerically studied on the convection heat transfer in a sinusoidal-wavy channel over the Reynolds number range of 100–700. The governing transport equations in terms of curvilinear coordinates were solved using spline alternating direction implicit method. It was found that there was a slightly augmentation in heat transfer at smaller value of amplitude-wavelength ratio, while at larger amplitude-wavelength ratio, there was a significant enhancement in the rate of the heat transfer. Comini et al. [7] have been numerically studied on the convective heat transfer in wavy channels. The numerical result displayed that the friction factor as well as Nusselt number increase as aspect ratios decreases. Naphon and Kornkumjayrit [8] studied on the convective heat transfer of air flow through channel with one-sided corrugated plate using commercial CFD program. The results displayed that the corrugated walls had a significant influence on the heat

transfer augmentation. Zhang and Che [9] numerically investigated the influence of corrugation profile for cross-corrugated plates on thermalhydraulic performance using air as working fluid. The Reynolds number values range of 1,000–10,000. It was found that Nusselt number as well as friction factor were about 1–4 times higher for the trapezoidal-corrugated channel than for the elliptic-corrugated channel.

In this paper, a numerical investigation on the laminar convective heat transfer of copper-water nanofluid in a sinusoidal-wavy channel with phase shift of 0° is carried out for Reynolds number range of 100–800 and nanoparticles volume fraction range of 0–5 %. The governing equations are transformed Cartesian coordinates into body-fitted coordinates and these equations are solved using finite volume method. The effects of nanoparticles volume concentration and Reynolds number on velocity vectors, temperature contours, velocity and temperature profiles, the local skin-friction coefficient, the local Nusselt number, average Nusselt number, pumping power and heat transfer enhancement are presented and analyzed.

2 Problem Description and Mathematical Formulation

2.1 Physical Domain and Assumptions

Figure 1 shows the geometry of the present study. It consists of a two parallel plates forming channel with average space between the plates (H) of 10 mm and the phase shift between these walls is 0°. The channel wall is composed of a smooth-adiabatic wall and a wavy-heated wall. The length of each plain (smooth) section that located upstream and downstream of the wavy section is L_s (L_s = 4H), the length of wavy section is L_w (L_w = 12H) and the wave-amplitude is A (A = 0.2H). On the other hand, nanofluid is a homogenous mixture of water and copper nanoparticles with diameter of 100 nm. It can be assumed as Newtonian fluid.

2.2 Computational Domain

In order to develop the computational mesh of the present geometry, the two Poisson equations proposed in Thompson et al. [20] are adopted. The two-dimensional Poisson equations in physical space (x, y) can be written as:

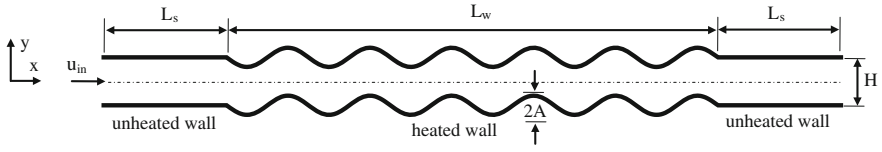

Fig. 1 Schematic of the physical model of wavy channel

$$\frac{\partial^2 \zeta}{\partial x^2} + \frac{\partial^2 \zeta}{\partial y^2} = P(\zeta, \eta) \tag{1}$$

$$\frac{\partial^2 \eta}{\partial x^2} + \frac{\partial^2 \eta}{\partial y^2} = Q(\zeta, \eta) \tag{2}$$

where P(ζ, η) and Q(ζ, η) are the control functions which are used to cluster points near the given boundaries. The above equations are transformed to the computational space (ζ, η) by interchanging the dependent and independent variables and then can be expressed as:

$$\beta_{11} \frac{\partial^2 x}{\partial \zeta^2} - 2\beta_{12} \frac{\partial^2 x}{\partial \zeta \eta} + \beta_{22} \frac{\partial^2 x}{\partial \eta^2} + J^2 \left(P \frac{\partial x}{\partial \zeta} + Q \frac{\partial x}{\partial \eta}\right) = 0 \tag{3}$$

$$\beta_{11} \frac{\partial^2 y}{\partial \zeta^2} - 2\beta_{12} \frac{\partial^2 y}{\partial \zeta \eta} + \beta_{22} \frac{\partial^2 y}{\partial \eta^2} + J^2 \left(P \frac{\partial y}{\partial \zeta} + Q \frac{\partial y}{\partial \eta}\right) = 0 \tag{4}$$

In Eqs. (3) and (4), β_{11}, β_{12}, β_{22} and J are geometry factors and can be defined as:

$$\begin{aligned} \beta_{11} &= x_\eta^2 + y_\eta^2, \quad \beta_{22} = x_\zeta^2 + y_\zeta^2, \\ \beta_{12} &= x_\zeta x_\eta + y_\zeta y_\eta, \quad J = x_\zeta y_\eta - x_\eta y_\zeta \end{aligned} \tag{5}$$

Equations (3) and (4) are solved numerically using Successive Line Over-Relaxation algorithm to determine the values of (x, y) at each point of computational grid [21]. The computational grid which is developed in current study is shown in Fig. 2.

2.3 Governing Equations

The general form of non-dimensional governing equations for two-dimensional, steady, laminar and incompressible flow in Cartesian coordinates can be written as (Table 1):

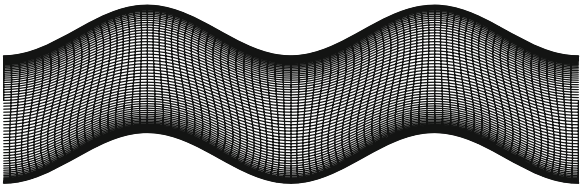

Fig. 2 Computational domain of present study

$$\frac{\partial(\rho\, u\, \phi)}{\partial x} + \frac{\partial(\rho\, v\, \phi)}{\partial y} = \frac{\partial}{\partial x}\left(\Gamma \frac{\partial u}{\partial x}\right) + \frac{\partial}{\partial y}\left(\Gamma \frac{\partial u}{\partial y}\right) + S_\phi(x, y) \tag{6}$$

Due to the complex geometry (i.e. wavy boundaries) of present study, the governing equations are transformed to a body-fitted coordinate system, and the these equations can be written as [22, 23]:

$$\begin{aligned}\frac{1}{J}\frac{\partial(\rho\, U^c\, \phi)}{\partial \zeta} + \frac{1}{J}\frac{\partial(\rho\, V^c\, \phi)}{\partial \eta} = \frac{1}{J}\frac{\partial}{\partial \zeta}\left[\frac{\Gamma_\phi}{J}\left(\beta_{11}\phi_\zeta - \beta_{12}\phi_\eta\right)\right] \\ + \frac{1}{J}\frac{\partial}{\partial \eta}\left[\frac{\Gamma_\phi}{J}\left(\beta_{22}\phi_\eta - \beta_{12}\phi_\zeta\right)\right] + S_\phi(\zeta, \eta)\end{aligned} \tag{7}$$

where U^c and V^c are contravariant velocity components and it can be defined as

$$U^c = UY_\eta - VX\eta,\; V^c = VX_\zeta - UY_\zeta \tag{8}$$

Table 1 A summary of the governing equations

Equation	ϕ	Γ_ϕ	$S_\phi(x, y)$	$S_\phi(\zeta, \eta)$
Continuity	1	0	0	0
x-Momentum	u	μ	$-\frac{\partial p}{\partial x}$	$-y_\eta \frac{\partial p}{\partial \zeta} + y_\zeta \frac{\partial p}{\partial \eta}$
y-Momentum	v	μ	$-\frac{\partial p}{\partial y}$	$x_\eta \frac{\partial p}{\partial \zeta} - x_\zeta \frac{\partial p}{\partial \eta}$
Energy	T	$\frac{\mu}{\mathrm{Pr}}$	0	0

3 Numerical Algorithm

3.1 Discretization of Governing Equations

The governing equations in body-fitted coordinate system are discretized using finite volume method. The diffusion term is discretized using central scheme and the convection term is discretized by power-law scheme. A collocated grid arrangement, in which all physical variables such as velocity, temperature and pressure are stored at the center of control volume, is used (Fig. 3.). The final discretized equation is

$$A_P^\phi\, \phi_p = \sum_{nb} A_{nb}^\phi\, \phi_{nb} + S_\phi\, J\, \Delta\zeta\, \Delta\eta - \left[\left(\frac{\Gamma_\phi}{J}\beta_{12}\, \phi_\eta\, \Delta\eta\right)_w^e + \left(\frac{\Gamma_\phi}{J}\beta_{12}\, \phi_\zeta\, \Delta\zeta\right)_s^n\right] \tag{9}$$

In above equation, the terms within the brackets are originated from approximating the diffusion terms on the non-orthogonal grid [24]. The coefficients A involve the

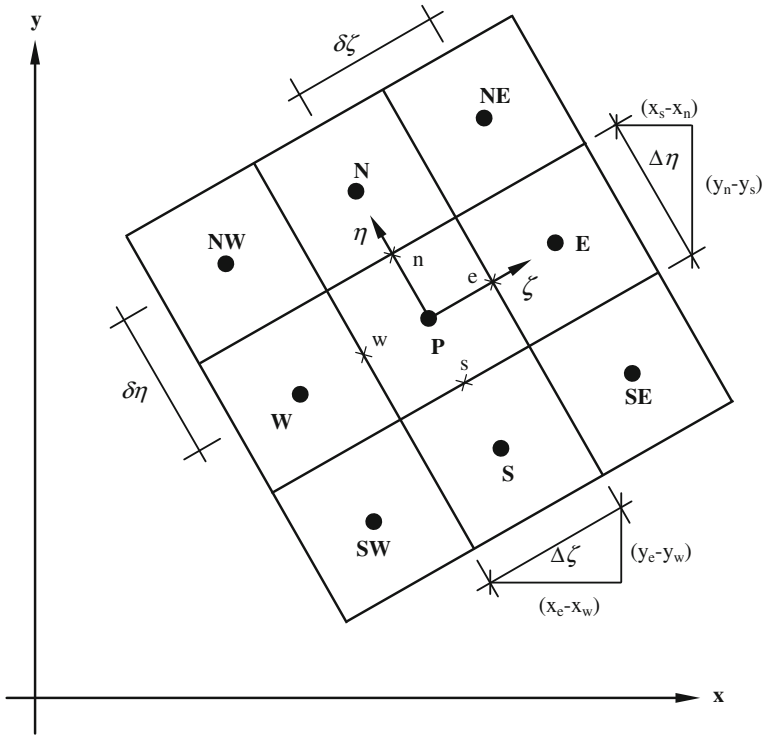

Fig. 3 Control volume in computational domain of non-orthogonal grid

flow rate F and diffusion conductivity D and these coefficients can be defined as follows [25]:

$$
\begin{aligned}
A_E &= D_e \max\,[0,\ (1-0.1\,|Pe_e\,|)^5] + \max\,[-F_e,\ 0],\\
A_W &= D_w \max\,[0,\ (1-0.1\,|Pe_w\,|)^5] + \max\,[F_w,\ 0]\\
A_N &= D_n \max\,[0,\ (1-0.1\,|Pe_n\,|)^5] + \max\,[-F_n,\ 0],\\
A_S &= D_s \max\,[0,\ (1-0.1\,|Pe_s\,|)^5] + \max\,[F_s,\ 0]\\
A_P &= A_E + A_W + A_N + A_S,\\
Pe_i &= \frac{F_i}{D_i};\ (\mathrm{i} =\ \ \mathrm{e},\ \mathrm{w},\ \mathrm{n},\ \mathrm{s})
\end{aligned}
\tag{10}
$$

where

$$F_e = (\rho\, U^c\, \Delta\eta)_e,\ F_w = (\rho\, U^c\, \Delta\eta)_w,\ F_n = (\rho\, V^c\, \Delta\zeta)_n,\ F_s = (\rho\, V^c\, \Delta\zeta)_s$$

$$D_e = \left(\frac{\beta_{11}}{J}\ \Gamma\ \frac{\Delta\eta}{\Delta\zeta}\right)_e,\ D_w = \left(\frac{\beta_{11}}{J}\ \Gamma\ \frac{\Delta\eta}{\Delta\zeta}\right)_w,\ D_n = \left(\frac{\beta_{22}}{J}\ \Gamma\ \frac{\Delta\zeta}{\Delta\eta}\right)_n,\ D_s = \left(\frac{\beta_{22}}{J}\ \Gamma\ \frac{\Delta\zeta}{\Delta\eta}\right)_s \tag{11}$$

The discretised Eq. (9) is iteratively solved using Tri-Diagonal Matrix Algorithm (TDMA) [25]. The system is numerically modeled in a FORTRAN.

3.2 Pressure Correction Equation

The pressure field can be obtained by coupling of the velocity and pressure equations on a collocated non-orthogonal grid using the SIMPLE algorithm [25]. To illustrate the algorithm, the velocity components u and v can be obtained from

$$u_p^* = \frac{1}{A_P^u}\sum_{nb} A_{nb}^u\, u_{nb}^* + b_u + \left(B_P^u\,\frac{\partial p^*}{\partial\zeta} + C_P^u\,\frac{\partial p^*}{\partial\eta}\right) \tag{12}$$

$$v_p^* = \frac{1}{A_P^v}\sum_{nb} A_{nb}^v\, v_{nb}^* + b_v + \left(B_P^v\,\frac{\partial p^*}{\partial\zeta} + C_P^v\,\frac{\partial p^*}{\partial\eta}\right) \tag{13}$$

$$B_p^u = -\frac{1}{A_P^u}\left(\frac{\partial y}{\partial\eta}\right)_p \Delta\zeta\,\Delta\eta,\quad C_p^u = \frac{1}{A_P^u}\left(\frac{\partial y}{\partial\zeta}\right)_p \Delta\zeta\,\Delta\eta \tag{14}$$

$$B_p^v = \frac{1}{A_P^v}\left(\frac{\partial x}{\partial\eta}\right)_p \Delta\zeta\,\Delta\eta,\quad C_p^v = \frac{1}{A_P^v}\left(\frac{\partial x}{\partial\zeta}\right)_p \Delta\zeta\,\Delta\eta \tag{15}$$

and b_u and b_v are residues from S_u and S_v, respectively, after the pressure gradient terms have been removed from them [24]. The pressure gradient terms in Eqs. (12) and (13) are determined by

$$\frac{\partial p^*}{\partial\zeta} = \frac{(p_e^*)_p - (p_w^*)_p}{\Delta\zeta},\ \frac{\partial p^*}{\partial\eta} = \frac{(p_n^*)_p - (p_s^*)_p}{\Delta\eta} \tag{16}$$

$$u = u^* + \left(B^u\,\frac{\partial p'}{\partial\zeta} + C^u\,\frac{\partial p'}{\partial\eta}\right),\quad v = v^* + \left(B^v\,\frac{\partial p'}{\partial\zeta} + C^v\,\frac{\partial p'}{\partial\eta}\right) \tag{17}$$

where P' is the pressure correction which can be related to the correct pressure P and the guessed pressure P^* as follows:

$$P = P^* + P' \tag{18}$$

The correction of contravariant velocity components U^{c*} and V^{c*} can be defined as

$$U^c = U^{c*} + \left(B^u y_\eta - B^v x_\eta\right) \frac{\partial p'}{\partial \zeta} + \left(C^u y_\eta - C^v x_\eta\right) \frac{\partial p'}{\partial \eta} \tag{19}$$

$$V^c = V^{c*} + \left(C^v x_\zeta - C^u y_\zeta\right) \frac{\partial p'}{\partial \eta} + \left(B^v x_\zeta - B^u y_\zeta\right) \frac{\partial p'}{\partial \zeta} \tag{20}$$

It has to be noted that the last two terms of Eqs. (19) and (20), based on the approximation of Rhie and Chow [24], are ignored if the computational grid is nearly orthogonal. Therefore, these equations can be rewritten as:

$$U^c = U^{c*} + B \frac{\partial p'}{\partial \zeta}, \; V^c = V^{c*} + C \frac{\partial p'}{\partial \eta} \tag{21}$$

where

$$B = B^u y_\eta - B^v x_\eta, \;\; C = C^v x_\zeta - C^u y_\zeta \tag{22}$$

The discretised continuity equation can be written as follows

$$\left(\rho \Delta\eta U^c\right)_e - \left(\rho \Delta\eta U^c\right)_w + \left(\rho \Delta\zeta V^c\right)_n - \left(\rho \Delta\zeta V^c\right)_s = 0 \tag{23}$$

Substituting the corrected face contravariant velocities into above equations gives

$$A_P P'_P = A_E P'_E + A_W P'_W + A_N P'_N + A_S P'_S + S_m \tag{24}$$

where

$$A_E = \left(\rho \Delta\eta B\right)_e, \;\; A_W = \left(\rho \Delta\eta B\right)_w, \;\; A_N = \left(\rho \Delta\zeta C\right)_n, \;\; A_S = \left(\rho \Delta\eta C\right)_s \tag{25}$$

and S_m is the mass imbalance over the control volume and it can be expressed as

$$S_m = \left(\rho \Delta\eta U^{c*}\right)_e - \left(\rho \Delta\eta U^{c*}\right)_w + \left(\rho \Delta\zeta V^{c*}\right)_n - \left(\rho \Delta\zeta V^{c*}\right)_s \tag{26}$$

3.3 Interpolation of the Face Velocities

The velocity interpolation is performed to calculate the face velocities of control volume on a collocated non-orthogonal grid. For this purpose and to avoid the

unreal pressure oscillation, the momentum interpolation method which is proposed by Rhie and Chow [24] is adopted in this study. The discretised u-momentum equation at the nodes P and E can be written as:

$$u_p = \frac{1}{(A_P^u)_P}\left(\sum_{nb} A_{nb}^u u_{nb} + b_u\right)_P + \frac{1}{(A_P^u)_P}\left(B_P^u \frac{\partial p}{\partial \zeta} + C_P^u \frac{\partial p}{\partial \eta}\right)_P \tag{27}$$

$$u_E = \frac{1}{(A_P^u)_E}\left(\sum_{nb} A_{nb}^u u_{nb} + b_u\right)_E + \frac{1}{(A_P^u)_E}\left(B_P^u \frac{\partial p}{\partial \zeta} + C_P^u \frac{\partial p}{\partial \eta}\right)_E \tag{28}$$

In similar manner, the velocity at the east face can be written as:

$$u_e = \frac{1}{(A_P^u)_e}\left(\sum_{nb} A_{nb}^u u_{nb} + b_u\right)_e + \frac{1}{(A_P^u)_e}\left(B_P^u \frac{\partial p}{\partial \zeta} + C_P^u \frac{\partial p}{\partial \eta}\right)_e \tag{29}$$

The first term and the $1/(A_P^u)_e$ in the second term of the above equation are linearly interpolated as follows:

$$\begin{aligned}\frac{1}{(A_P^u)_e}\left(\sum_{nb} A_{nb}^u u_{nb} + b_u\right)_e = {} & f_e^+ \frac{1}{(A_P^u)_E}\left(\sum_{nb} A_{nb}^u u_{nb} + b_u\right)_E \\ & + (1 - f_e^+)\frac{1}{(A_P^u)_P}\left(\sum_{nb} A_{nb}^u u_{nb} + b_u\right)_P\end{aligned} \tag{30}$$

$$\frac{1}{(A_P^u)_e} = f_e^+ \frac{1}{(A_P^u)_E} + (1 - f_e^+)\frac{1}{(A_P^u)_P} \tag{31}$$

where f_e^+ is a linear interpolation factor and it can be defined as:

$$f_e^+ = \frac{\Delta\zeta_P}{2\,\delta\zeta_e} \tag{32}$$

Re-arranging Eqs. (27) and (28), gives:

$$\frac{1}{(A_P^u)_P}\left(\sum_{nb} A_{nb}^u u_{nb} + b_u\right)_P = u_p - \frac{1}{(A_P^u)_P}\left(B_P^u \frac{\partial p}{\partial \zeta} + C_P^u \frac{\partial p}{\partial \eta}\right)_P \tag{33}$$

$$\frac{1}{(A_P^u)_E}\left(\sum_{nb} A_{nb}^u u_{nb} + b_u\right)_E = u_E - \frac{1}{(A_P^u)_E}\left(B_P^u \frac{\partial p}{\partial \zeta} + C_P^u \frac{\partial p}{\partial \eta}\right)_E \tag{34}$$

Substituting Eqs. (33) and (34) in Eq. (30), gives:

$$\frac{1}{(A_P^u)_e}\left(\sum_{nb} A_{nb}^u u_{nb} + b_u\right)_e = f_e^+ \left[u_E - \frac{1}{(A_P^u)_E}\left(B_P^u \frac{\partial p}{\partial \zeta} + C_P^u \frac{\partial p}{\partial \eta}\right)_E\right] + (1 - f_e^+)\left[u_p - \frac{1}{(A_P^u)_P}\left(B_P^u \frac{\partial p}{\partial \zeta} + C_P^u \frac{\partial p}{\partial \eta}\right)_P\right] \tag{35}$$

Substituting Eq. (35) in Eq. (29), gives:

$$u_e = f_e^+ \left[u_E - \frac{1}{(A_P^u)_E}\left(B_P^u \frac{\partial p}{\partial \zeta} + C_P^u \frac{\partial p}{\partial \eta}\right)_E\right] + (1 - f_e^+)\left[u_p - \frac{1}{(A_P^u)_P}\left(B_P^u \frac{\partial p}{\partial \zeta} + C_P^u \frac{\partial p}{\partial \eta}\right)_P\right] + \frac{1}{(A_P^u)_e}\left(B_P^u \frac{\partial p}{\partial \zeta} + C_P^u \frac{\partial p}{\partial \eta}\right)_e \tag{36}$$

Re-arranging the above equation, gives:

$$u_e = \left[f_e^+ u_E + (1 - f_e^+) u_p\right] + \frac{1}{(A_P^u)_e}\left(B_P^u \frac{\partial p}{\partial \zeta} + C_P^u \frac{\partial p}{\partial \eta}\right)_e - f_e^+ \frac{1}{(A_P^u)_E}\left(B_P^u \frac{\partial p}{\partial \zeta} + C_P^u \frac{\partial p}{\partial \eta}\right)_E - (1 - f_e^+) \frac{1}{(A_P^u)_P}\left(B_P^u \frac{\partial p}{\partial \zeta} + C_P^u \frac{\partial p}{\partial \eta}\right)_P \tag{37}$$

The velocities at the other faces such west, north and south faces can be obtained using similar procedure.

3.4 Under-Relaxation

In order to slow down the updating of the dependent variables at each iteration to achieve a better convergence behavior, the under- relaxation is applied. Therefore, the under-relaxation factor can be introduced to the discretised equation (Eq. 9) as follows [25]:

$$\frac{A_P^\phi}{\alpha_\phi}\phi_P = \sum_{nb} A_{nb}^\phi \phi_{nb} + S_\phi J \Delta\zeta \Delta\eta - \left[\left(\frac{\Gamma_\phi}{J}\beta_{12}\phi_\eta \Delta\eta\right)_w^e + \left(\frac{\Gamma_\phi}{J}\beta_{12}\phi_\zeta \Delta\zeta\right)_s^n\right] + \frac{1 - \alpha_\phi}{\alpha_\phi} A_P^o \phi_P^o \tag{38}$$

where α_ϕ is the under-relaxation factor. Equation (38) can be written as:

$$\frac{A_P^\phi}{\alpha_\phi}\,\phi_P = \sum_{nb} A_{nb}^\phi\,\phi_{nb} + S_\phi^r - \left[\left(\frac{\Gamma_\phi}{J}\beta_{12}\,\phi_\eta\,\Delta\eta\right)_w^e + \left(\frac{\Gamma_\phi}{J}\beta_{12}\,\phi_\zeta\,\Delta\zeta\right)_s^n\right] \tag{39}$$

where

$$S_\phi^r = S_\phi\,J\,\Delta\zeta\,\Delta\eta + \frac{1-\alpha_\phi}{\alpha_\phi}\,A_P^o\,\phi_P^o \tag{40}$$

The under-relaxation is also applied for the pressure correction equation as follows:

$$P^{new} = P^* + \alpha_P\,P' \tag{41}$$

where α_p is the under-relaxation factor for the pressure correction equation. However, the values of under-relaxation factors which are used in the current study are 0.7 for momentum and energy equations and 0.2 for pressure.

4 Boundary Conditions

The corresponding boundary conditions that are used to solve the governing equation based on the non-dimensional expressions are given by:

i. Channel inlet:

$$U = \frac{3}{2}\left[1 - \frac{\eta}{(H/2)}\right]^2,\ V = 0,\ \theta = 0,\ -\frac{H}{2} \le \eta \le \frac{H}{2} \tag{42}$$

ii. Along the smooth walls:

$$U = 0,\ V = 0,\ \theta = 1 \tag{43}$$

iii. Along the wavy walls:

$$U = 0,\ V = 0,\ \frac{\partial\theta}{\partial\eta} \tag{44}$$

iv. Channel outlet:

$$\frac{\partial U}{\partial\zeta} = 0,\ \frac{\partial V}{\partial\zeta} = 0,\ \frac{\partial\theta}{\partial\zeta} = 0 \tag{45}$$

5 Physical Properties of Nanofluids

The properties of nanofluid can be expressed as follows:

i. Density:
The effective density of the nanofluid can be expressed as [26]:

$$\rho_{nf} = (1 - \varphi)\,\rho_f + \varphi\,\rho_p \tag{46}$$

ii. Heat capacity:
The heat capacity of nanofluid is defined as [26]:

$$(\rho C_P)_{nf} = (1 - \varphi)(\rho C_P)_f + \varphi\,(\rho C_P)_p \tag{47}$$

iii. Dynamic viscosity:
The effective dynamic viscosity of the nanofluid is given by [27]:

$$\frac{\mu_{nf}}{\mu_f} = \frac{1}{(1 - \varphi)^{2.5}} \tag{48}$$

iv. Thermal conductivity:
The effective thermal conductivity of nanofluid can be determined using the model proposed by Patel et al. [28], as follows:

$$\frac{k_{eff}}{k_f} = 1 + \frac{k_p A_p}{k_f A_f} + c\,k_p\,Pe\frac{A_p}{k_f A_f}, \tag{49}$$

where

$$\frac{A_p}{A_f} = \frac{d_f}{d_p}\frac{\varphi}{(1 - \varphi)}, \tag{50}$$

and c is the empirical constant and

$$Pe = \frac{u_p d_p}{\alpha_f}, \tag{51}$$

where u_p is the Brownian motion velocity of the particles which is defined as:

$$u_p = \frac{2k_p T}{\pi\,\mu_f\,d_p^2} \tag{52}$$

6 Performance and Non-dimensional Parameters

After solving the governing equations, the flow and thermal fields of nanofluid in wavy channel are obtained. The local Nusselt number at the walls of wavy wall can be calculated as [4]:

$$Nu_x = -\frac{k_{nf}}{k_f}\left[\frac{1}{J}\left(X_\zeta^2 + Y_\zeta^2\right)^{1/2}\frac{\partial\theta}{\partial\eta}\right]_{\zeta,w} \tag{53}$$

The average Nusselt number can be obtained by integrating the local Nusselt number over the walls of the wavy wall as follows:

$$Nu_L = \frac{1}{L_w}\int_{L_s}^{L_s+L_w} Nu_x\, d\zeta \tag{54}$$

The local skin-friction coefficient at the wavy wall can be calculated as:

$$C_{fx} = \frac{2}{\mathrm{Re}}\left[\frac{1}{J}\left(X_\zeta\frac{\partial U}{\partial\eta} - Y_\zeta\frac{\partial V}{\partial\eta}\right)\right]_{\zeta,w} \tag{55}$$

The friction factor can be defined as:

$$f = \Delta p\,\frac{D_h}{L_w}\frac{2}{\rho_{nf}\,u_{in}^2} \tag{56}$$

The required pumping power can be expressed as:

$$Pumping\ power = H\,u_{in}\,\Delta P \tag{57}$$

The non-dimensional parameters which are used in current study can be defined as follows:

$$X = \frac{x}{D_h},\ Y = \frac{y}{D_h},\ U = \frac{u}{\mathrm{u_{in}}},\ V = \frac{v}{\mathrm{u_{in}}},\ \theta = \frac{T - T_{in}}{T_w - T_{in}} \tag{58}$$

$$P = \frac{p}{\rho_{nf}u_{in}^2},\ \mathrm{Re} = \frac{\rho_{nf}u_{in}D_h}{\mu_{nf}},\ \mathrm{Pr} = \frac{\mu_{nf}C_{Pnf}}{K_{nf}} \tag{59}$$

7 Code Validation and Grid Independence Test

To validate the code that developed in present study, the average Nusselt number for the convective heat transfer of water ($\varphi = 0\ \%$) flow in sinusoidal-wavy channel is obtained and compared with previous numerical results of Heidary and Kermani [16], see Fig. 4a. Moreover, the average Nusselt number for copper-water nanofluid flowing between two parallel plates has been calculated and compared with previous numerical results of Santra et al. [13] as shown in Fig. 4b. The results are in good agreement. The accuracy of numerical result are generally dependent on the grid size. To test the grid independence, the non-dimensional streamwise velocity as well as the non-dimensional temperature were calculated for different grid size at Re = 500 and $\varphi = 5\ \%$ as displayed in Fig. 5a, b. The grid size of

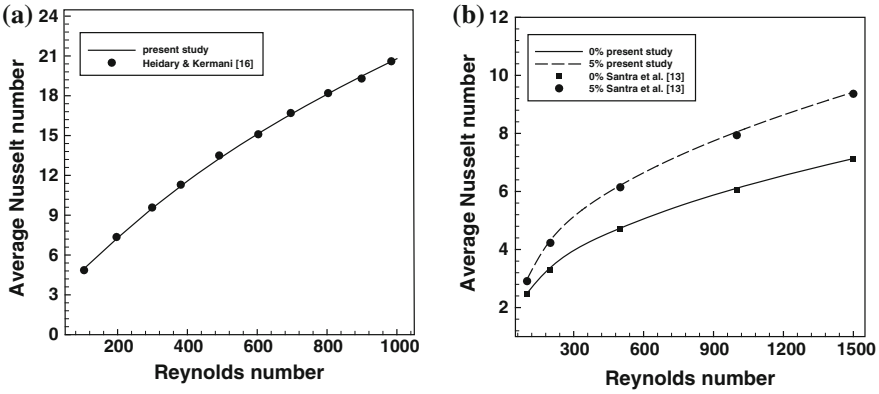

Fig. 4 Comparison of the results for **a** water flow in a wavy-wall channel, **b** copper-water nanofluid flow in a straight channel

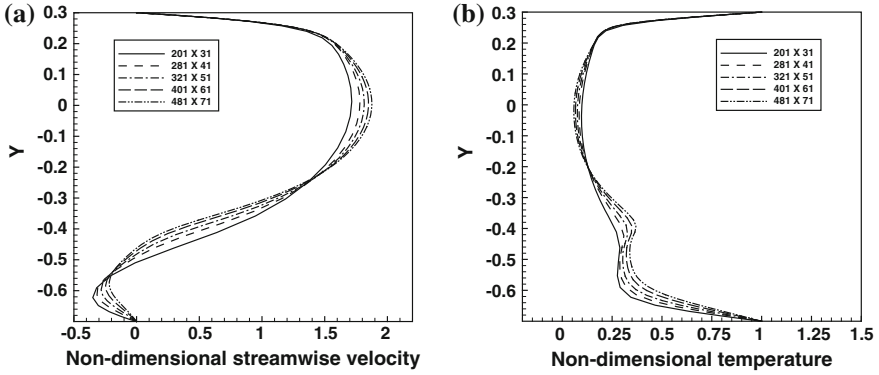

Fig. 5 Grid independence test at Re = 500, $\varphi = 5\ \%$ and X = 10.5: **a** Non-dimensional streamwise velocity **b** Non-dimensional temperature

401 × 61 can be considered grid-independent and is therefore used throughout all computations. In current study, the computation is terminated when the sum of absolute residual for each parameter over computational domain is less than 1×10^{-5}.

8 Results and Discussion

Laminar convective heat transfer of nanofluid in a wavy channel has studied numerically over Reynolds number ranges of 100–800 and nanoparticles volume concentration of 0–5 %. Figure 6 shows the velocity vectors and temperature contours for Reynolds number of 100, 300, 500 and 800 and nanoparticles volume concentration is 5 %. In general, it can be seen that the velocity vectors as well as temperature contours are asymmetric about x-axis because of the top and bottom walls of wavy channel are in the same phase (i.e. the phase shift between top and bottom walls of wavy channel is 0°). When the nanofluid flow in a wavy channel, the nanofluid must turn to pass through this channel and hence reversal flow appear

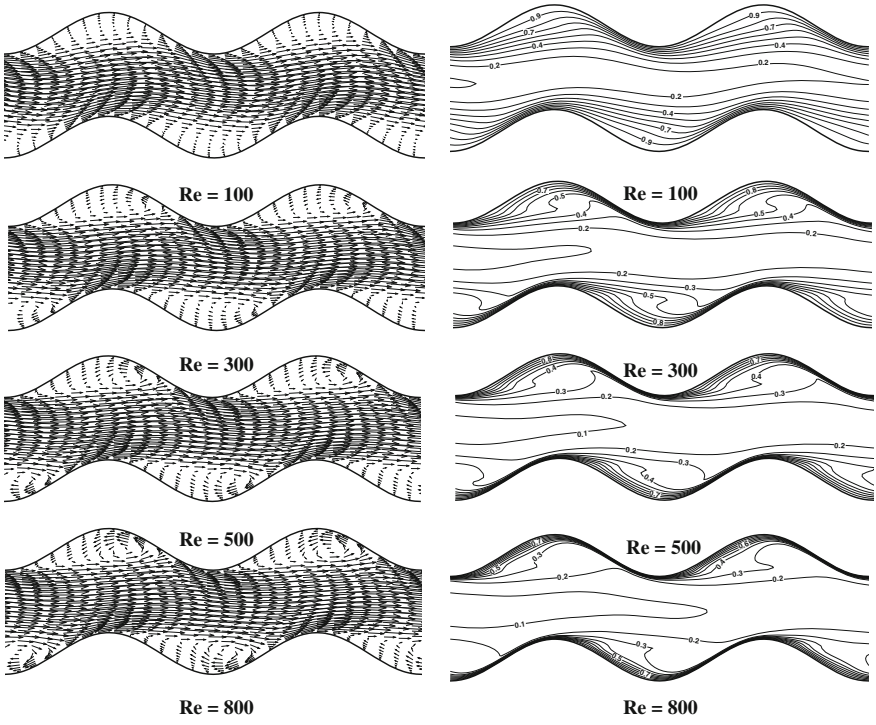

Fig. 6 Velocity vectors (*left*) and temperature contours (*right*) for different Reynolds numbers at $\varphi = 5\%$

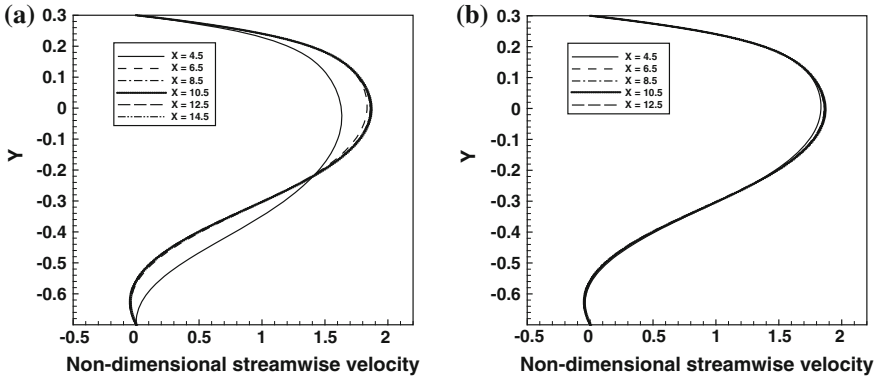

Fig. 7 Variation of non-dimensional streamwise velocity at troughs along the length of the wavy channel for $\varphi = 5\%$ at **a** Re = 100, **b** Re = 800

in trough (crest) of lower (upper) wall. When Reynolds number increases, the velocities for recirculation regions which are in opposite direction to the main flow increase in magnitude. However, the size of recirculation regions increase with increasing in Reynolds number. From temperature contours it can be clearly seen that when Reynolds number increases, thermal boundary layer thickness deceases and the temperature gradient at the walls of wavy channel increases due to improve the mixing of core fluid with the fluid close to the walls of channel. The non-dimensional streamwise velocity distribution at different locations (troughs) along the length of the wavy channel for Reynolds numbers of 100 and 800 at $\varphi = 5\ \%$ are plotted in Fig. 7a and b. In general, the velocities at the upper and lower walls of the wavy channel are equal to zero due to the non-slip condition is stated at the walls of the channel. It can be observed that the maximum velocity is detected in the upper part of the wavy channel while the minimum velocity, i.e. negative velocity, is detected in the lower part of the channel. In other word, the peak value of the velocity profile is shifted from the centerline of the wavy channel to the upper part of the way channel. Furthermore, the flow attains periodically fully developed profile downstream of the first wave. This behavior is similar to that reported by Bahaidarah et al. [29]. Moreover, the negative velocity in trough of the wavy channel, i.e. re-circulation regions increases in magnitude as Reynolds number increases from 100 to 800. This is can be clearly observed from Fig. 6.

Figure 8a and b show the non-dimensional temperature distribution in the spanwise direction at troughs along the length of the wavy channel for Reynolds numbers of 100 and 800 at $\varphi = 5\ \%$. Basically, it is found that the magnitude of non-dimensional temperature at the upper and lower heated-walls of wavy channel is equal to one ($\theta = 1$) as stated in the boundary conditions. At Re = 100, the temperature of the fluid in the trough of the lower wall is higher than that in the crest of the upper wall due to the slow down the velocity of the fluid in the re-circulation regions. Also, the temperature increases when the lengthwise (X)

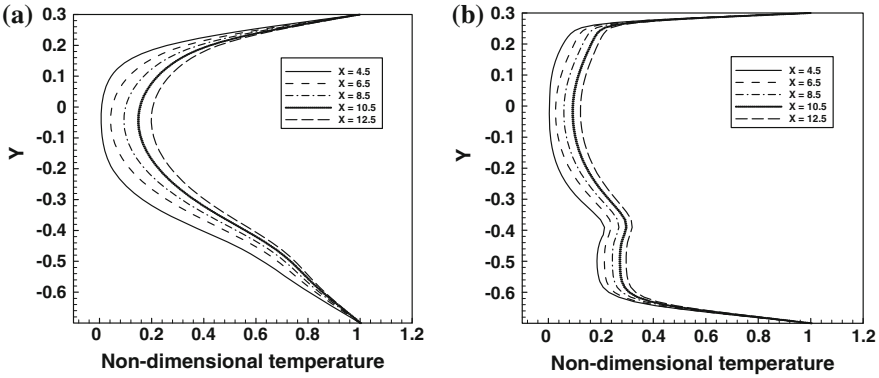

Fig. 8 Variation of non-dimensional temperature at troughs along the length of the wavy channel for $\varphi = 5\%$ at **a** Re = 100 **b** Re = 800

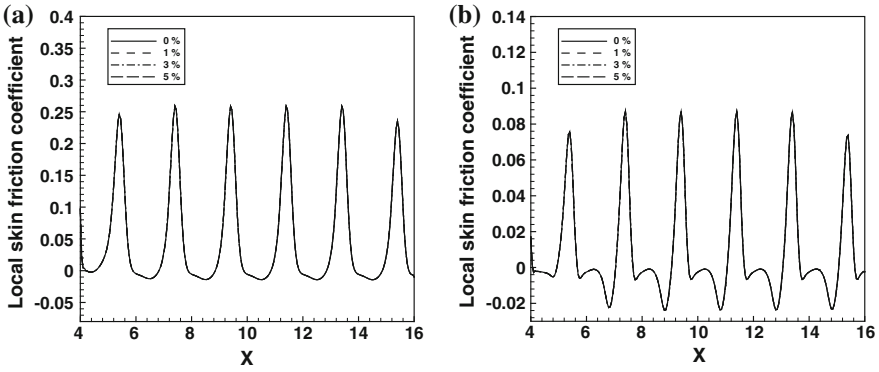

Fig. 9 Local skin friction coefficient distribution along lower wavy-wall for different nanoparticle volume concentration at **a** Re = 100 **b** Re = 800

increases. As Reynolds number increases, Re = 800, the temperature (temperature gradient) deceases (increases) especially in the trough of the lower wall of wavy channel due to improve the fluid mixing. Figure 9 depicts the distribution of the local skin-friction coefficient along the bottom wall of wavy channel for different nanoparticles volume concentrations for Re = 100 and 800. It should be noted that the local skin-fiction coefficient has a maximum value which is located at crest of the wavy wall. This is because the velocity gradient has a maximum value at this location. While the skin-friction coefficient has a minimum value at the trough of the wavy wall due to low velocity gradient in the reversal flow regions. It is also found that the skin-friction coefficient has a negative value due to reversal flow that appear in trough of wavy channel. Furthermore, as expected, the skin-friction

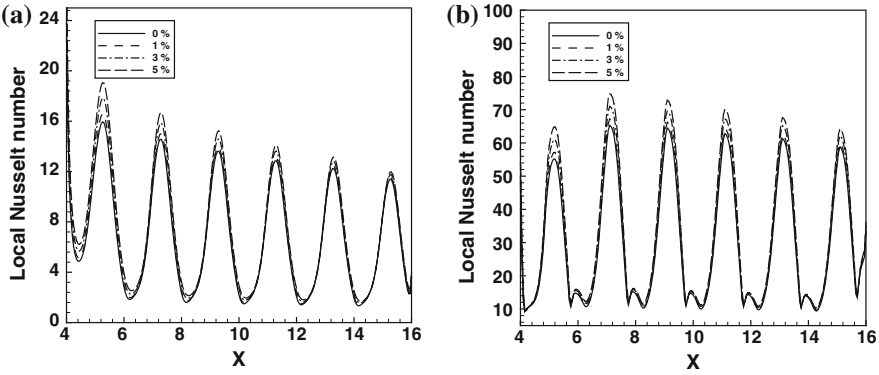

Fig. 10 Local Nusselt number distribution along lower wavy-wall for different nanoparticle volume concentration at **a** Re = 100 **b** Re = 800

coefficient at Re = 100 is higher than that at Re = 800 because of the skin-friction coefficient is inversely proportional to Reynolds number, see Eq. 55. Moreover, nanoparticles volume concentration has no effect on the local skin-friction coefficient. Figure 10 gives the distribution of the local Nusselt number along the bottom wavy-wall for different nanoparticles volume concentration at Re = 100 and 800. The maximum local Nusselt number occur upstream of the wave-crest, while the minimum value occur downstream of the wave-crest. This is because the velocity as well as the temperature gradients upstream of the wave-crest are higher than that downstream of the wave-crest. Also, it can be noted that the local Nusselt number, especially the peak values, increase as the volume concentration of nanofluid increases due to improve thermal conductivity of nanofluid.

The average Nusselt number versus Reynolds number at different values of nanoparticles volume concentrations has been presented in Fig. 11. It should be noted that at a specific concentration of the solid particles, the average Nusselt number increases as Reynolds number increases. This because when Reynolds number increases, the fluid mixing in channel is improved due to re-circulation regions that appear in wavy channel and hence the temperature gradient at wall also increases. On other hand, the average Nusselt number increases with increasing in the volume concentration of solid particles at particular Reynolds number because of the addition nanoparticles to the base fluid can improve thermal conductivity of base fluid and consequently improve heat transfer rate. Figure 12 displays the variation of pumping power with Reynolds number for different nanoparticles volume concentrations. It is observed that the required pumping power increases when Reynolds number increase at a particular nanoparticles volume concentrations. Also, the pumping power increases with nanoparticles volume concentrations due to increase the density and viscosity of nanofluid. This is consistent with numerical results of Manca et al. [30]. Figure 13 shows the average Nusselt number for nanofluid flow in a wavy channel over the average Nusselt number for water

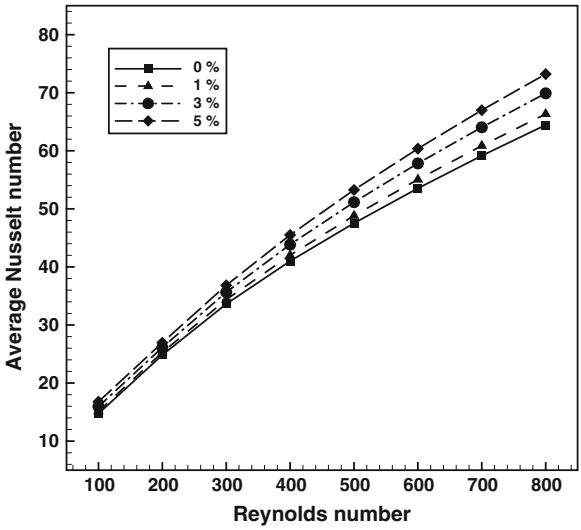

Fig. 11 Average Nusselt number versus Reynolds number for different nanoparticle volume concentration

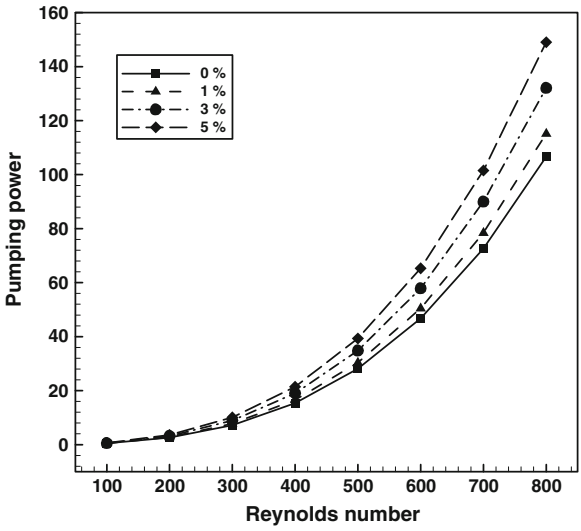

Fig. 12 Pumping power versus Reynolds number for different nanoparticle volume concentration

(conventional fluid) flow in a plain channel (conventional channel) versus Reynolds number at different volume concentrations of nanoparticles. It is found that the enhancement in average Nusselt number increases with Reynolds number and with the nanoparticles volume concentration as well. As mentioned above, nanoparticles suspension and using wavy-wall increase the enhancement in heat transfer due to the enhance thermal conductivity as well as the fluid mixing.

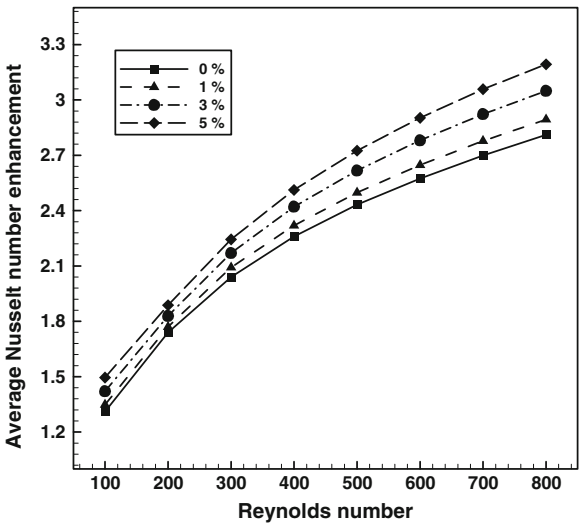

Fig. 13 Average Nusselt number enhancement versus Reynolds number for different nanoparticle volume concentration

9 Conclusions

In this study, laminar flow and heat transfer of copper-water nanofluid in a sinusoidal-wavy channel is numerically investigated over Reynolds number range of (100–800) and nanoparticle volume concentration range of (0–5 %). The phase shift between the upper and lower walls of wavy channel is 0°. The non-dimensional governing continuity, momentum and energy equations in terms of curvilinear coordinates are solved using finite volume method. The effects of nanoparticles volume concentration and Reynolds number on the velocity and temperature profiles, the local skin-friction coefficient, the local Nusselt number, average Nusselt number, pumping power and heat transfer enhancement are presented and discussed. Results show that the local Nusselt, the average Nusselt number as well as the average Nusselt number enhancement are significantly increase with the nanoparticle volume concentration, but the required pumping power increases as well. Also, it is found that the nanoparticles volume concentration has no effect on the local skin-friction coefficient. It can be recommended that the using nanofluid in a wavy channels is a suitable way to design more compact heat exchangers with a higher heat transfer performance.

Acknowledgments The authors would like to sincerely thank the Ministry of Higher Education (MOHE) of Malaysia for the provision of a grant with code no. 20110106FRGS to support this work.

References

1. O'Brien, J.E., Sparrow, E.M.: Corrugated duct heat transfer, pressure drop, and flow visualization. ASME J. Heat Transf. **104**, 410–416 (1982)
2. Sparrow, E.M., Comb, J.W.: Effect of interwall spacing and fluid flow inlet conditions on a corrugated-wall heat exchanger. Int. J. Heat Mass Transf. **26**, 993–1005 (1983)
3. Ali, M., Ramadhyani, S.: Experiments on convective heat transfer in corrugated channels. Exp. Heat Transf. **5**, 175–193 (1992)
4. Wang, G., Vanka, S.P.: Convective heat transfer in periodic wavy passages. Int. J. Heat Mass Transf. **38**, 3219–3230 (1995)
5. Fabbri, G.: Heat transfer optimization in corrugated wall channels. Int. J. Heat Mass Transf. **43**, 4299–4310 (2000)
6. Wang, C.C., Chen, C.K.: Forced convection in a wavy-wall channel. Int. J. Heat Mass Transf. **45**, 2587–2595 (2002)
7. Comini, G., Nonino, C., Savino, S.: Effect of aspect ratio on convection enhancement in wavy channels. Numer. Heat Transf. Part A **44**, 21–37 (2003)
8. Naphon, P., Kornkumjayrit, K.: Numerical analysis on the fluid flow and heat transfer in the channel with V-shaped wavy lower plate. Int. Commun. Heat Mass Transf. **34**, 62–71 (2007)
9. Zhang, L., Che, D.: Influence of corrugation profile on the thermalhydraulic performance of cross-corrugated plates. Numer. Heat Transf. Part A **59**, 267–296 (2011)
10. Xuan, Y., Li, Q.: Heat transfer enhancement of nanofluids. Int. J. Heat Fluid Flow **21**, 58–64 (2000)
11. Xuan, Y., Li, Q.: Investigation on convective heat transfer and flow features of nanofluids. J. Heat Transf. **125**, 151–155 (2003)
12. Kulkarni, D.P., Namburu, P.K., Ed Bargar, H., et al.: Convective heat transfer and fluid dynamic characteristics of SiO_2 ethylene glycol/water nanofluid. Heat Transf. Eng. **29**, 1027–1035 (2008)
13. Santra, A.K., Sen, S., Charaborty, N.: Study of heat transfer due to laminar flow of copper-water nanofluid through two isothermally heated parallel plates. Int. J. Therm. Sci. **48**, 391–400 (2009)
14. Kolade, B., Goodson, K.E., Eaton, J.K.: Convective performance of nanofluids in a laminar thermally developing tube flow. J. Heat Transf. **131**, 1–8 (2009)
15. Kalteh, M., Abbassi, A., Avval, M.S., et al.: Eulerian-Eulerian two-phase numerical simulation of nanofluid laminar forced convection in a microchannel. Int. J. Heat Fluid Flow **32**, 107–116 (2011)
16. Heidary, H., Kermani, M.J.: Effect of nano-particles on forced convection in sinusoidal-wall channel. Int. Commun. Heat Mass Transf. **37**, 1520–1527 (2010)
17. Ahmed, M.A., Shuaib, N.H., Yusoff, M.Z., et al.: Numerical investigations of flow and heat transfer enhancement in a corrugated channel using nanofluid. Int. Commun. Heat Mass Transf. **38**, 1368–1375 (2011)
18. Ahmed, M.A., Shuaib, N.H., Yusoff, M.Z.: Numerical investigations on the heat transfer enhancement in a wavy channel using nanofluid. Int. J. Heat Mass Transf. **55**, 5891–5898 (2012)
19. Ahmed, M.A., Shuaib, N.H., Yusoff, M.Z.: Effects of geometrical parameters on the flow and heat transfer characteristics in trapezoidal-corrugated channel using nanofluid. Int. Commun. Heat Mass Transf. **42**, 69–74 (2013)
20. Thompson, J.F., Thames, F.C., Mastin, C.W.: Automatic numerical generation of body-fitted curvilinear coordinate system for field containing any number of arbitrary two-dimensional bodies. J. Comput. Phys. **15**, 299–319 (1974)
21. Cebeci, T., Shao, J.P., Kafyeke, F., et al.: Computational Fluid Dynamics for Engineers, 1st edn. Horizons, California (2005)
22. Bose, T.K.: Numerical Fluid Dynamics. Narosa Publishing House, London (1997)

23. Tannehill, J.C., Anderrson, D.A., Pletcher, R.H.: Computational Fluid Mechanics and Heat Transfer, 2nd edn. Taylor & Francis, New York (1997)
24. Rhie, C.M., Chow, W.L.: Numerical study of the turbulent flow past an airfoil with trailing edge separation. AIAA J. **21**, 1525–1532 (1983)
25. Versteeg, H.K., Malalasekera, W.: An Introduction to Computational fluid Dynamics the Finite Volume Method, 2nd edn. Longman Scientific and Technical, Harlow (2007)
26. Xuan, Y., Roetzel, W.: Conceptions for heat transfer correlation of nanofluids. Int. J. Heat Mass Transf. **43**, 3701–3707 (2000)
27. Brinkman, H.C.: The viscosity of concentrated suspensions and solutions. J. Chem. Phys. **20**, 571–581 (1952)
28. Patel, H.E., Pradeep, T., Sundarrajan, T., et al.: A micro-convection model for thermal conductivity of nanofluid. Pramana-J. Phys. **65**, 863–869 (2005)
29. Bahaidarah, H.M.S., Anand, N.K., Chen, H.C.: Numerical study of heat and momentum transfer in channels with wavy walls. Numer. Heat Transf. Part A **47**, 417–439 (2005)
30. Manca, O., Nardini, S., Ricci, D.: A numerical Study of nanofluid forced convection in ribbed channels. Appl. Therm. Eng. **37**, 280–292 (2012)